INTRAVASCULAR DETECTION OF MICROVESSEL INFILTRATION IN ATHEROSCLEROTIC PLAQUES: AN INTRALUMINAL EXTENSION OF ACOUSTIC ANGIOGRAPHY

K. Heath Martin

A dissertation submitted to the faculty at the University of North Carolina at Chapel Hill in partial fulfillment of the requirements for the degree of Doctor of Philosophy in the Department of Biomedical Engineering in the School of Medicine.

Chapel Hill
2016

Approved by:

Paul A. Dayton

Xiaoning Jiang

David S. Lalush

Timothy C. Nichols

Yueh Lee

ABSTRACT

K. Heath Martin: Intravascular Detection of Microvessel Infiltration in Atherosclerotic Plaques: An Intraluminal Extension of Acoustic Angiography.
(Under the direction of Paul A. Dayton)

Cardiovascular disease is the leading cause of death worldwide, surpassing both stroke and cancer related mortality with 17.5 million deaths in 2014 alone. Atherosclerosis is the build-up of fatty deposits within arteries and is responsible for the majority of cardiovascular related deaths. Over the past decade, research in atherosclerosis has identified that a key limitation in the appropriate management of the disease is detecting and identifying dangerous fatty plaque build-ups before they dislodge and cause major cardiovascular events, such as embolisms, stroke, or myocardial infarctions. It has been noted that plaques vulnerable to rupture have several key features that may be used to distinguish them from asymptomatic plaques. One key identifier of a dangerous plaque is the presence of blood flow within the plaque itself since this is an indicator of growth and instability of the plaque. Recently, a superharmonic imaging method known as "acoustic angiography" has been shown to resolve microvasculature with unprecedented quality and could be a possible method of detecting blood vessel infiltration within these plaques.

This dissertation describes the material and methods used to move the application of "acoustic angiography" to a reduced form factor typical of intravascular catheters and to demonstrate its ability to detect microvasculature. The implementation of this approach is described in terms of the contrast agents used to generate superharmonic signals, the dual-frequency transducers to image them, and the hardware needed to operate them in order to

establish how these design choices can impact the quality of the images produced. Furthermore, this dissertation demonstrates how image processing methods such as adaptive windowing or automated sound speed correction can further enhance image quality of vascular targets. The results of these chapters show how acoustic angiography may be optimized using engineering considerations both in signal acquisition and post processing. Overall, these studies demonstrate that acoustic angiography can be performed using a catheter-deployable dual-frequency transducer to detect microvasculature through superharmonic imaging methods.

To Christina

ACKNOWLEDGEMENTS

The work presented in the following pages would not have been possible without the help of my committee members, the foremost being my advisor and committee chair, Paul Dayton. Thank you for seeing in me what others did not and for guiding me through my graduate career with a stable lab-life and advice tempered by experience. I would also like to thank Dr. Jiang for his constant and continual involvement with my project through our bi-weekly meetings where we continually sought improvement in our approach. Of course I must recognize the work of Jianguo Ma, a former student of Dr. Jiang, whose success in his own dissertation predicated much of mine. I would also like to thank all my labmates that tore apart the stereotype of the lab being a cold and calloused workplace and for the insightful comments that aided me in completing my dissertation. I would also like to thank Bob Kruger and Dick Lam for their time, funding, and providing me another project to keep things interesting during my later research. I am greatly appreciative of the funding I was awarded by the Dean's Doctoral fellowship from NCSU that enabled my initial research with the Dayton lab. Thank you also to my teachers, from elementary to now – it takes special people to teach and I'm privileged to have you in my life (Mrs. Champion, Mrs. Frost, Dr. Hyun, Dr. O'Brien, the late Dr. Paul, and Dr. Marone were exceptionally influential). Finally, a very deep and heart-filled thank you goes out to my family who encouraged me to take the chance on a getting higher education. I love you all and I am grateful that I have you in my life, especially my wife Christina. With this chapter coming to an end, I look forward to starting the next adventure with you.

TABLE OF CONTENTS

LIST OF TABLES

LIST OF FIGURES

LIST OF ABBREVIATIONS

2D	Two Dimensional
3D	Three Dimensional
AAA	Abdominal Aortic Aneurysm
A/D	Analog to Digital
ADC	Analog to Digital Converter
A-line	Amplitude Line
ARF	Acoustic Radiation Force
ARFI	Acoustic Radiation Force Impulse
AWG	Arbitrary Waveform Generator
B-mode	Brightness Mode
BW	Bandwidth
BW_f	Fractional Bandwidth
CAM	Chorioallantoic Membrane
CCL	Creative Common License
CE	Contrast Enhancement
CE-IVUS	Contrast Enhanced Intravascular Ultrasound
CMAP	Speed-of-Sound Map
CNR	Contrast to Noise Ratio
CPS	Cadence Contrast Pulse Sequencing
cRGD	Cyclo-Arg-Ala-Gly-Asp-D-Tyr-Cys
CSI	Contrast Specific Imaging

CT	Computed Tomography
CTA	Computed Tomography Angiography
CTR	Contrast to Tissue Ratio
D/A	Digital to Analog
DC	Direct Current
DF	Dual-Frequency
DSPC	1,2-Distearoyl-sn-Glycero-3-Phosophocholine
DSPE	1,2-Distearoyl-sn-Glycero-3-Phosphoethanolamine
f_c	Center frequency
FDA	Food and Drug Administration
FPGA	Field-Programmable Gate Array
FOBRL	Francis Owens Blood Research Laboratory
FSIL	Frequency Selective Isolation Layer
FWHM	Full-width, half-maximum
GUI	Graphical User Interface
HDL	High Density Lipoprotein
HIFU	High Intensity Focused Ultrasound
HMG-CoA	3-Hydroxy-3-Methyglutarl-Coenzyme-A
HPF	High-Pass Filter
IACUC	Institutional Animal Care and Use Committee
ICAM-1	Intracellular Adhesion Molecule – 1
IMT	Intima-Media Thickness
I/O	Input/Output

IVUS	Intravascular Ultrasound
KLM	Krimholtz-Leedom-Matthaei
LAD	Left Anterior Descending Artery
LCx	Left Circumflex Artery
LDL	Low Density Lipoprotein
LED	Light Emitting Diode
LPF	Low-Pass Filter
LTI	Linear, Time Invariant
MB	Microbubbles
MCA	Microbubble Contrast Agents
MI	Mechanical Index
MIP	Maximum Intensity Projection
MOSFET	Metal Oxide Semiconductor Field Effect Transistor
MPE	Maximum Permissible Exposure
MR	Magnetic Resonance
MRI	Magnetic Resonance Imaging
MV	Minimum Variance
NM	Nuclear Medicine
NMOS	N-Type Metal Oxide Semiconductor
OCT	Optical Coherence Tomography
PA	Photoacoustics
PAM	Photoacoustic Mammography
PAT	Photoacoustic Tomography

PBS	Phosphate Buffered Saline
PC	Personal Computer
PCB	Printed Circuit Board
PCCA	Phase Change Contrast Agents
PCF	Phase Coherence Factor
PCI	Percutaneous Coronary Intervention
PCIe	Peripheral Component Interconnect Express
PEG	Polyethylene-Glycol
PET	Positron Emission Tomography
PMN-PT	Lead Magnesium Niobate-Lead Titanate
PMOS	P-Type Metal Oxide Semiconductor
PNP	Peak Negative Pressure
PSF	Point Spread Function
PVDF	Polyvinylidene Fluoride
RCA	Right Coronary Artery
RF	Radiofrequency
RFH	Rapacz Familial Hypercholesterolemic
RMS	Root-Mean-Square
ROI	Region of Interest
sem	Standard Error of the Mean
SMA	SubMiniature version A
SNR	Signal to Noise Ratio
SOS	Speed-of-sound

SPECT	Single-Photon Emission Computed Tomography
THI	Tissue Harmonic Imaging
TLRH	Transmit-Low, Receive-High
TNR	Tissue to Noise Ratio
US	Ultrasound
USDA	United States Department of Agriculture
VEGFR-2	Vascular Endothelial Growth Factor Receptor – 2
VH	Virtual Histology

CHAPTER 1

INTRODUCTION

1.1 Motivation

Atherosclerotic cardiovascular disease is a leading cause of death worldwide which can manifest without warning [1]. Acute coronary syndromes are postulated to be initiated by atherosclerotic plaque ruptures in up to 75% of cases [2, 3]. For this reason, detection of atherosclerotic plaques prone to rupture is one of the most active areas of research in cardiology and biomedical imaging [4].

Intravascular ultrasound (IVUS) uses standard brightness mode (B-mode) imaging which is the current imaging gold standard to determine plaque composition. Tissues containing heterogeneous density and compressibility such as plaques, media, and smooth muscle layers are detectible on B-mode images, but tissue lacking these variations in material properties do not scatter ultrasound well enough to cause measurable reflections. A multitude of plaque characteristics exist that, if detected, can indicate whether the plaque is at a higher risk of causing a future ischemic event, however current IVUS imaging methods cannot detect these symptoms of a vulnerable plaque [5].

Recently, a new way of visualizing vessels using ultrasound has been developed and used to image tumor vasculature in response to therapy [6]. This technique, termed acoustic angiography, has resulted in high resolution and contrast three dimensional imaging of vascular networks previously unobtainable when using ultrasound. Acoustic angiography has only

recently been developed because it uses wide-band separation between the operating frequencies of two different elements that cannot normally be achieved using conventional transducer designs. A low frequency element is used to generate nonlinear harmonics using high pressures while another high frequency element (4-10x higher) is used to receive only the nonlinear signals generated by microbubbles. This produces contrast only images with a very high specificity that can clearly resolve vessel networks when the system is operated to acquire 3D volumes. Dual-frequency transducers are the only type of ultrasound devices that have previously demonstrated the ability to produce acoustic angiography images.

Current intravascular ultrasound transducers are poorly optimized for nonlinear contrast imaging strategies such as those used in acoustic angiography based on their inherent high frequency design. However, a dual-frequency IVUS transducer could surpass this limitation to enable assessment of plaque risk of rupture by using contrast specific imaging (CSI) to detect the presence of microvessels within a plaque. Translation of acoustic angiography into the IVUS environment has not yet been performed but could result in identifying vulnerable atheroma by detecting neovascularization within the plaques associated with the deadly disease of atherosclerosis.

1.2 Dissertation scope and objectives

The goal of this dissertation is to develop, optimize, and determine the clinical relevance of acoustic angiography in an intravascular platform using a newly developed dual-frequency transducer. Chapter 2 begins by giving background information regarding the severity of atherosclerosis and how the disease is currently managed today. Microbubble contrast agents are introduced in the next chapter as theranostic agents capable of both therapy and diagnostics. It is then followed by Chapter 4 which is an introduction to dual-frequency transducers. This chapter

also highlights important finding gleaned from dual-frequency transducers used in previous works while also providing detailed fabrication and operation strategies that are unique to these ultra-broad bandwidth devices. In Chapter 5, a prototype dual-frequency IVUS transducer design is discussed and preliminary results are gathered using *in vitro* setups. Chapter 6 is focused on optimizing the hardware and operating electronics to improve the image quality and ease of use of the prototype device while Chapter 7 provides a series of experiments that quantify the behavior of this approach in clinically relevant models included *ex vivo* and small animal *in vivo* studies to assess image quality metrics. While the previous three chapters were concerned with optimizing the acquisition of the data using a dual-frequency probe, Chapter 8 reviews advanced post-processing methods that can be applied to these datasets. Beamforming methods are introduce for intravascular acoustic angiography as well as automated error correction algorithms to estimate the appropriate speed of sound needed to perform image reconstruction. Finally, Chapter 9 discusses the conclusions derived from this work, areas of future research, and other applications for dual-frequency IVUS probes.

CHAPTER 2

CLINICAL BACKGROUND OF ATHEROSCLEROSIS

Atherosclerosis is a pathological build-up of a lipid burden in arteries that can result in ensuing cardiac events such as stroke or myocardial infarction. Atherosclerosis is associated with a large portion of reported sudden deaths in the United States as well as world-wide. While the etiology of the atherosclerosis is still being studied, the epidemiology of the disease as well as the consequences of leaving the matter untreated necessitates further advances in its field of study to preserve global health. A background of atherosclerosis outlining the phases of development, diagnosis, and treatment will be covered in this chapter. Finally, the relationship of microvasculature with vulnerable plaques will be defined in terms of lesion assessment and treatment response.

2.1 Dysfunction of normal vasculature due to atherosclerosis

Atherosclerosis impedes the function of normal, healthy arteries preventing them from exchanging metabolites and waste products from regions of tissue that they would normally supply (Figure 2.1). Arteries are composed of 3 basic layers that serve different functions – the intima, media, and adventitia. The outermost layer is the adventitia or *tunica externa* and is composed mainly of connective tissue and provides a support function for the artery. Owing to its composition of mostly collagen and elastin fibers, the adventitial layer is tough and durable to give protection to the remaining, inner two layers which are considerably more delicate. The adventitia of larger arteries also functions similar to basement membranes found in other organs

given they support a delicate network of vessels (*vasa vasorum*) and nerves (*nervi vasorum*). The *vasa vasorum* is a microvascular network that provides blood flow to diffusion limited regions of larger arteries while the *nervi vasorum* are primarily used to control vasoconstriction and vasodilation performed by the smooth muscle cells located in the media. The majority of *vasa vasorum* originates form the adventitia, but some *vasa vasorum* comes from the intimal or medial layers [7]. *Vasa vasorum* is present only in larger arteries and typically will not be found in healthy human vasculature with a lumen less than 0.5 mm in diameter [8] or in vessels having a wall thickness less than 29 cells [9, 10]. While it is still undetermined if their role is causal or reactive, *vasa vasorum* proliferation is enhanced in regions affected by cardiovascular diseases such as atherosclerosis and the detection of enhanced microvascular networks would be a valuable diagnostic tool as an indicator of imminent rupture [8].

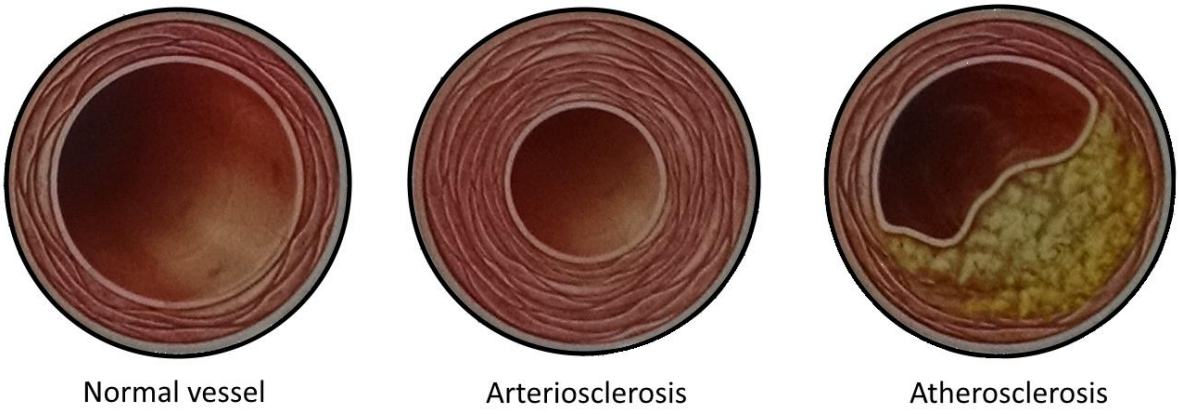

Figure 2.1: Comparative anatomy of cardiovascular disease states. The artery is composed of 3 distinct layers that may be affected differently depending upon cardiovascular health. Figure reused with permission from [11] (Copyright © 2014 Wolters Kluwer Health)

The media or *tunica media* is the middle layer of an artery and is oftentimes the thickest layer of an artery. The layer is populated by a lamella of smooth muscle cells responsible for adjusting the size of the blood vessel. Vascular patency is important for maintaining proper

systemic blood pressure and can also be used to regulate blood flow to specific regions. Smaller arteries may only have a single layer of smooth muscle cells, but larger arteries will have multiple layers connected with elastic tissue arranged in varying orientations. The elastic tissues in the media not only connect individual sheets of muscle, but also provide pulsation dampening which gives smaller arteries a nearly time-invariant blood velocity. Additionally, elastin has roles that exist outside structural support such as the prevention of over-proliferation of smooth muscle cells [12].

Finally, the innermost layer is the intima or *tunica intima* and is composed mainly of endothelial cells. Except in the largest arteries, the intima is composed of a single layer of cells attached with a delicate connective layer. The intima is in direct contact with blood flow and is the principal site for molecular imaging strategies since microbubbles cannot extravasate (see Chapter 3 for more discussion). The intimal layer of arteries is the primary site affected by atherosclerosis where the buildup of plaque burden occurs within the arteries.

Atherosclerotic related cardiovascular disease is a principal cause of death worldwide and is a disease which can manifest without warning [1]. Acute coronary syndromes are postulated to be initiated by atherosclerotic plaque ruptures in up to 75% of cases [2, 3]. For this reason, detection of atherosclerotic plaques prone to rupture is one of the most active areas of research in cardiology and biomedical imaging [4]. The imaging of coronary atherosclerosis and developing methods to noninvasively assess the instability of atheromatous plaques is critically important to reduce patient mortality due to cardiovascular disease. Furthermore, the identification of vulnerable plaques that may detach would enhance patient treatment and reduce the risk of complications such as myocardial infarction [13-17]. Computed tomography, magnetic resonance angiography, and gray scale intravascular ultrasound are currently utilized in

atherosclerotic plaque assessment, but all of these methods provide limited information in regards to degree of stenosis or plaque morphology [18].

Atherosclerosis is often considered in light of its consequences, namely coronary blockages that cause heart attacks in unhealthy individuals. The disease is one that culminates over several decades and is a silent killer that manifests itself in a sudden thrombolytic event which causes the most significant impacts on health. Thrombosis formation is a result of atherosclerotic lesions building up and exposing their inner core to the blood where the body's natural thrombolytic cascade begins and forms a clot. When the thrombosis dislodges, it becomes an embolism and travels downstream in the circulatory system where it occludes the vessel. At this point, the embolism cannot travel further and will block blood flow to regions normally supplied by the artery. Atherosclerosis mediated embolisms are the principal cause of deadly complications such as heart attacks and stroke and it is very difficult to detect plaques prone to rupture when they are relatively safe to treat.

While atherosclerosis is considered a systemic disease that affects the cardiovascular system, the most dangerous plaques tend to develop in specific locations of the arterial anatomy. It is important to note that the plaques that are frequently studied are those that cause the more severe complications since they impact patient health severely and researchers acknowledge that there may be a bias on underreporting plaques that do not cause significant medical issues [19]. The propensity of plaques to form in the aorta, coronary, carotid, and femoral arties is higher than in other regions of the cardiovascular system [20]. The spatial distribution of acute coronary occlusions in 208 patients have identified that the majority of occlusions happen within the proximal third of the right coronary (RCA), left anterior descending (LAD), and left circumflex (LCx) arteries [21]. A graphical depiction of the frequency of occlusions is given in

Figure 2.2 which summarizes the findings of Wang *et al*. The coronary sites within 25 mm of the ostium contained at least 50% of the observed occlusions.

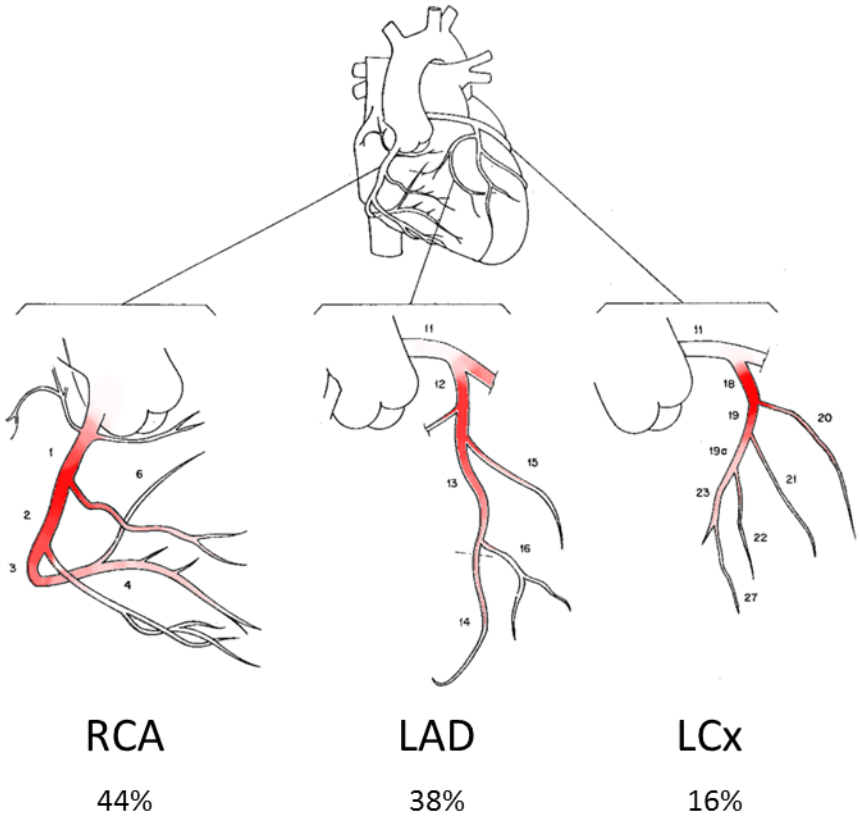

Figure 2.2: Spatial distribution of coronary occlusions indicates that the vast majority of lesions prone to rupture develop in the proximal portions of the right coronary (RCA), left anterior descending (LAD), and left circumflex (LCx) arteries. The percentage of all occlusions identified in the study of 208 patients is given per artery. Image modified and reused with permission from [21] (Copyright © 2004 Wolters Kluwer Health, Inc.)

The formation of plaques is promoted based on the rheological conditions of the artery. As blood flows through an artery, the velocity profile through the lumen varies spatially as well as temporally in larger arteries. Near the center of the vessel, blood velocities are typically at their highest as predicted by the Poiseuille model for pressure driven flow through a tube. While this model is not satisfactory to model hemodynamics due to its simplicity, it does demonstrate

that the velocity of the blood flow through the artery approaches zero near the vessel wall. Conservation of energy requires that shear stress develops at the wall-fluid interface and this shear stress has been studied with respect to atherogenesis. It was observed in the carotid bifurcation that regions having lower wall shear stress (τ_{wss}) have a positive correlation with plaque formation [22]. Computational fluid dynamics have studied patient derived blood flow simulations and have confirmed that low τ_{wss} promotes plaque formation and that certain blood flow patterns such as flow separation can additionally increase propensity for lesions to form [23]. Figure 2.3 illustrates an example of the complex flow profiles that can be found in the carotid bifurcation. While under-stressed regions of the endothelium promotes atherogenesis and lipid culmination, it has been observed that high regions of τ_{wss} can destabilize plaque bodies and is a likely route to plaque rupture [24].

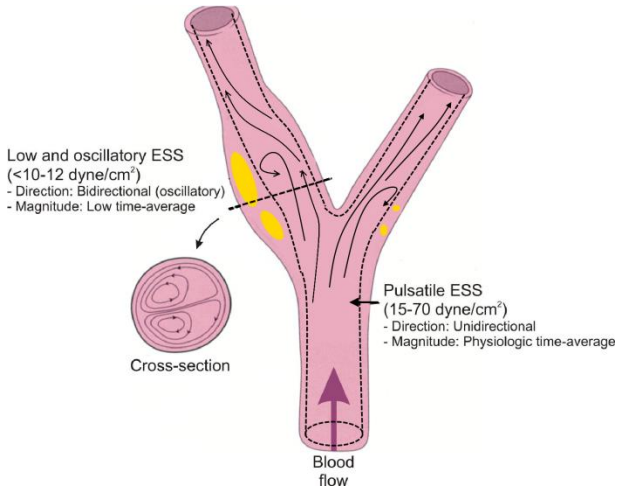

Figure 2.3: Spatial variations of atheroma formation at the carotid bifurcation. Regions of flow separation correspond to areas of low wall shear stress and lipid accumulation (yellow) in the sub-intimal space. Blood flow stream lines are depicted in solid black arrows and show regions of flow detachment. ESS – Endothelial Wall Shear Stress. Illustration modified and reused with permissions from [25] (Copyright © 2007 Elsevier).

2.2 Plaque classification

The American Heart Associate has established a classification system used to describe plaques based on morphology and associated risks. This classification system is the result of a mid-1990s Committee on Vascular Lesions of the Council on Arteriosclerosis that reviewed histological sectioning of numerous plaques types [26-28]. In this classification system, plaques are numbered using Roman numerals with letter suffixes to designate specific variations from the general histological motif of the current plaque level. The table below (Table 2.1) summarizes the AHA classification system and gives a brief description of plaque features that describe the plaques within that category while Figure 2.4 provides an illustration of the morphologies within a given type. An overview of the different plaque types will be highlighted briefly.

Table 2.1: Descriptive summary of the AHA plaque classification system.

AHA Atherosclerotic Plaque Classification	
Type	Description
Non atherosclerotic	
0	Normal, healthy artery
I	Adaptive thickening due to mechanical stresses. Present from birth. Intimal macrophage foam cell accumulation.
II	Intimal xanthoma: Fatty streaks visible and infiltration of SMC with foam cells
III	Pre-atheroma: Extracellular lipid in small, isolated pools appear. Intermediate lesion.
Atherosclerotic	
IV	Atheroma: Lipid pool or necrotic core encapsulated by fibrous tissue, potentially symptom producing
V	Fibroatheroma: Thick fibrous cap covering a lipid/necrotic core
VI	Complicated lesion: Fissures, ulcers, or other indications of previous damage present
b	Subtype indicating the presence of calcification within the lesion
c	Subtype indicating the lipid core has been replaced with fibrous tissue

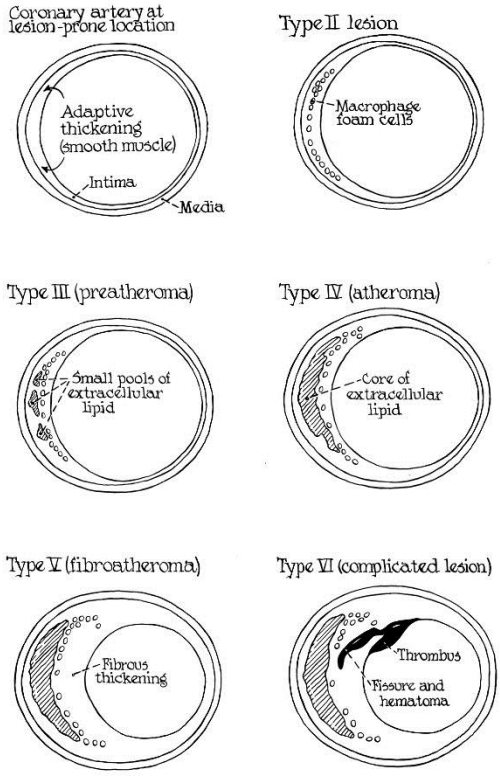

Figure 2.4: Graphical summary of the AHA plaque classification system. Figure reprinted with permission from [28] (Copyright © 1995, Wolters Kluwer Health, Inc.).

The first type of plaque identified in the AHA classification system is Type I lesions. Commonly referred to as initial lesions, Type I "plaques" are typically comprised of regions of adaptive wall thickening with the presence of a few lipid-filled macrophages (foam cells) in the intima. Adaptive wall thickening refers to hypertrophy of vascular tissue in response to the mechanical stresses imparted on the vessel wall due to blood flow and are found from birth onward. The defining feature that distinguishes Type I lesions from adaptive thickening is the presence of foam cells in the intimal regions of the vessel wall which marks the beginnings of atherosclerosis. Type II lesions (intimal xanthomas) have an escalated amount of lipid in the form of streaks, which are bands of foam cells. Smooth muscle cells are noticeably more proliferated at this stage and contain some foam cell infiltration. Type III lesions are classified

as “pre-atheroma” or intermediate lesions because they represent the stages between those that are typically asymptomatic and those that cause complications (Type IV+). Lipid accumulation appears not only within foam cells, but also in the extracellular space of the vessel wall in small, isolated pools. Until this point, all listed classifications of atherosclerotic lesions were considered non-atherosclerotic and are generally not symptom producing. Type IV lesions are atheroma and are potentially symptom producing lesions. The plaque is formed by a lipid or necrotic core that is encapsulated with connective tissue. If the encapsulating material is breached, the core of the plaque is considered ruptured and exposes thrombogenic material to the blood to promote the formation of a blood clot and possible embolism. Because of the lesions intimal disorganization and predisposition to sudden advancement to ischemic events, the Type IV plaque is classified as an advance lesion and at risk for future complications. If the encapsulating material is considerably thick, the plaque may be classified as Type V. The Type V lesion may also be referred to as a fibroatheroma or sub-classified to Type Vb (if calcifications are present) or Type Vc (if the lipid pool is minimal or absent). If any signs of rupture, hemorrhage or ulceration occurs in the plaque, it is immediately classified into the final category, Type VI. Type VI lesions are considered complicated lesions and may be sub-categorized based on any identified feature including (a) surface disruption, (b) bleeding, or (c) thrombosis. In contrast to other lesions, Type VI lesions are very obstructive and oftentimes are detected due to the symptoms that they cause. Ruptured and healed plaques are stentotic with the majority of them (75%) reducing lumen diameters by 50% or more [29].

Recently, Virmani has proposed a modification to the AHA classification system to include possible causes of thrombosis other than rupture such as endothelial erosion and the exposure of calcified nodules to the lumen of the vessel [30]. This modified classification was

formed in response to growing evidence that suggests that other origins of atherothrombosis manifests itself in poor clinical outcomes. In one study, 75% of patients with acute myocardial infarction occurred due to plaque ruptures and the remaining 25% were caused by plaque erosion [31].

2.3 The vulnerable plaque and implications of intraplaque blood flow

While disease progression of atherosclerosis is still under investigation, lesions with certain characteristics are more prone to rupture and are considerably more dangerous than others. Muller was the first to describe these lesions as "vulnerable plaques" referring to their likelihood to cause future coronary thrombosis [32]. Since then, clinicians and researchers have been identifying key features of vulnerable plaques that may be used to distinguish them from plaques that under changes in stress or rheological environment will not rupture and thus considered stable. Transient ischemic events are a severe complication arising from untreated vulnerable plaques and there is an unmet need of identifying these plaques early, before complications can arise. Both morphological and functional differences exist between stable and unstable (vulnerable plaques).

The characteristics that define a vulnerable plaque results from the pathological course preceding those plaques that have been found to rupture. A graphical summary is given from Vancraeynest *et al*. (Figure 2.5).

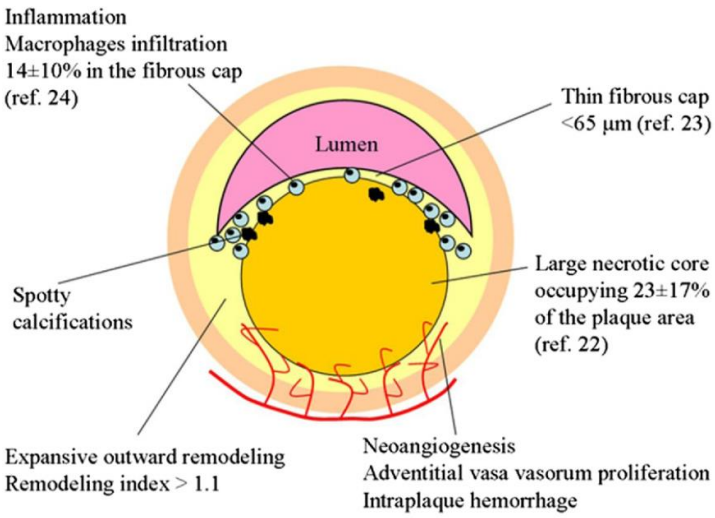

Figure 2.5: Identifying features of a vulnerable plaque. Figure reprinted with permission from [5] (Copyright © 2011, Elsevier).

Of the several characteristics said to identify a vulnerable plaque, several of them may be detected using contrast enhanced ultrasound methods. Active areas of inflammation are common in vulnerable plaques and it has been shown that molecularly targeted microbubbles can be used to selectively enhance areas of inflammation from atherosclerosis using ultrasound [33]. Areas of platelet aggregation are also a characteristic found in vulnerable plaques [1] which are possible targets for molecular imaging by using GPIIb IIIa binding receptors [34]. Intraplaque blood flow in the form of complex ulcerations, hemorrhage, or neoangiogenesis also signifies a lesion that is either at risk for rupture or has already ruptured and healed. Current imaging methods have difficulty detecting this blood flow, especially in coronary arteries. Methods like contrast enhanced ultrasound have a great potential for detecting this complication *in vivo* and has already shown improvement of plaque visualization in carotid lesions using transcutaneous contrast enhanced ultrasound [35]. By designing an IVUS transducer capable of contrast specific imaging, vessels other than the carotid arteries could be imaged to classify and assess plaque vulnerability and would be a valuable addition to current percutaneous interventions.

2.4 Imaging modalities

Intravascular ultrasound is one of the leading technologies used in the assessment of atherosclerosis disease progression. While other modalities can image the vessel lumen with the aid of contrast, no other imaging modality can resolve the small structure composition of plaques and endothelial structure in real time. Some of the competing technologies are in the fields of X-ray, nuclear medicine, magnetic resonance (MR) or optics, but there are also several other ultrasound based modalities that provide assessment of the vascular health of a patient. A review of all these modalities will be discussed in context of assessing vascular health describing their use, benefits, and disadvantages.

2.4.1 X-ray

X-ray based approaches are invaluable tools for clinicians assessing vascular health by visualizing vast regions of the body. They provide a large field of view, can be noninvasive, and have excellent resolution. However, these approaches have limited application in disease models such as atherosclerosis which is characterized by complications associated with plaques growing inside the vessel. While they can provide a detailed view of the lumen of the vessel, the majority of atherosclerotic vessels do not exhibit narrowing of the vessel lumen until the final stage of the disease. Instead, as plaque continues to build up, the arteries compensate by dilating outward such that blood flow remains largely unchanged in a process known as Glagov remodeling [36]. While it is true that stenotic vessels are at a greater risk for complications compared to non-stenotic vessels, the frequency of non-stenotic vessels is much greater in the population and thus imaging of the blood lumen alone cannot provide a means of detecting the disease for the majority of those afflicted by it [1].

X-ray angiography is performed by injecting a radio-opaque contrast agent into the lumen of the vessel and then imaging a patient with x-rays to track the flow of the contrast. Dynamic and real-time information can be extracted by analyzing the flow of radio-contrast agents directly using x-ray fluoroscopy and provides a wide field of view that is very useful for interventional procedures. Cardiac interventions such as tracking guidewire advancement or confirming coronary blood flow after angioplasty are almost exclusively performed using this imaging modality. Fluoroscopy provides detailed 2D projections which may be combined with 3D morphological information by advancing the gantry that houses the receiving equipment around the patient in a rotational angiography procedure. Computed tomography angiography (CTA) create 3D volumes of the patient's vasculature in a similar manner by injecting a dye systemically in a peripheral artery instead of catheter delivery as done in the previously described approach. X-ray angiography requires contrast and ionizing radiation, but has excellent resolution, can be done in real time, and can image a large area quickly making it the workhorse of the interventional radiology department.

Nuclear medicine is a field of medicine that uses radiolabeled isotopes to selectively image areas of disease. The method is performed by injecting a radioactive isotope into the patient, typically designed to accumulate at regions of interest such as markers of disease. The injected marker will spontaneously decay to a lower energy level which typically produces high energy (140-512 keV) ionizing radiation that can be detected with gamma cameras to form images. Three dimensional imaging in nuclear medicine is primarily performed with single photon emission computed tomography (SPECT) using rotating gamma cameras or with positron emission tomography (PET) using a detection ring to measure simultaneous pairs of positrons. SPECT and PET can image a variety of diseases by conjugating radioactive labels such as

technetium-99m or fludeoxyglucose (FDG) to binding ligands, peptides, monoclonal antibody fragments, or cellar receptors that would enhance uptake of the material into tissue to preferentially target specific areas within the body. Nuclear medicine has numerous applications in the field of cardiology. Some of the more popular methods include radionuclide ventriculography and myocardial perfusion which allow physicians to measure cardiac output and identify regions of cell viability within the heart tissue, respectively. Imaging atherosclerotic lesions have been studied with SPECT to identify regions of enhanced lipid uptakes in diseased arteries, sites of endothelial damage, and macrophage accumulation [37]. Likewise, similar studies in carotid, femoral, and iliac arteries have been conducted to track inflammation in atherosclerosis using PET imaging of ^{18}F-FDG [38]. Nuclear medicine approaches are extremely valuable diagnostic tools that can be implemented in assessing plaque functionality in atherosclerosis, but image quality degrades substantially when trying to image coronary vessels due to the high mobility of the heart and tidal blood volume [37].

2.4.2 Magnetic Resonance

Similar to CTA, magnetic resonance angiography (MRA) can create excellent images of blood vasculature either with or without contrast agents by magnetically inducing decaying nuclear spins (typically hydrogen). Several methods exist to image blood flow, but MRA is most different from CTA in that images of vessels are gathered using non-ionizing magnetic fields by gathering spectral information in k-space. MRA can visualize vessels with or without the aid of contrast agent making it an attractive option for patients with kidney disease, but without contrast the technique is sensitive to flow making it more difficult to image smaller vessels that have lower flow rates. The resolution obtained using MR techniques depends upon how well sampled the image is in k-space. Thus, higher resolution MRA images take longer to acquire

making them subject to motion artifacts which must be accounted for in moving structures like coronary vessels. Additionally, the MR equipment used to obtain vascular images are expensive to purchase, operate, and maintain [39]. MRA approaches have improved over the past decade and provide an alternative to ionizing imaging approaches with spatial and temporal resolutions coming close to those achieved through X-ray methods [40].

2.4.3 Ultrasound

Intravascular ultrasound is commonly performed by inserting a catheter in a large peripheral vein and then guiding it to the target location. Once in place, an ultrasound transducer is passed within the catheter to image the surrounding structure by using conventional pulse-echo B-mode imaging to reveal the internal structure of the vessel. Because the ultrasound transducer is located very close to the target to be imaged, ultrasound attenuation is low allowing for the use of high frequency sound waves which give better axial and lateral resolution (typically ~40 MHz single elements, ~20 MHz for arrays). B-mode images using such frequencies allow visualization of vessel structures such as endothelium, media, and adventitia in healthy vessels and can also image plaques to determine composition based on morphology. Traditional IVUS imaging is frequently used to determine the accuracy of stent placement for coronary interventions and can determine if a vessel is hemorrhaging from vessel dissection post-balloon angioplasty.

Intravascular ultrasound has many specializations that can compete with the presented dual-frequency transducer design presented herein. Of these specializations, several seek to better characterize plaques based on the composition of the plaque. One such commercially available tool is Virtual Histology (VH) provided by Volcano. VH incorporates spectral analysis of raw radiofrequency (RF) data in order to determine composition of the area by categorizing tissue in one of four categories (fibrofatty, fibrous tissue, necrotic core, or dense calcium) and it

has been shown that VH correlates well with traditional histology following atherectomy [41]. However, VH and other methods like it have room to improve since (1) the broad categorization of plaque composition is limited to only 4 categories, (2) these categories do not fully describe the characteristics of a vulnerable plaque, and (3) must be gated to occur only during the R-wave portion of the cardiac cycle [1, 42]. Other composition determining methods have been developed such as integrated backscatter IVUS and iMAP, but are similar to VH because they perform spectral analysis to identify tissue types in plaques [43-45].

While the previously discussed methods seek to characterize plaques based on their composition, analysis of plaques may be based on their mechanical properties to provide additional information into the behavior of the plaque. Elastography in ultrasound is a method of imaging the stiffness of tissue and can be performed in a number of ways. One such way is by using acoustic radiation force (ARF) using 2 different pulse types – one pulse to push tissue and another to track the motion of the tissue upon release of the pushing pulse [46]. Tissue properties such as viscoelasticity and stiffness can be estimated from this type of imaging and can be used to map the relative mechanical properties of a plaque highlighting areas of concern. This method is a major advancement in determining deformation behavior of tissue types using IVUS and was initially developed as displacement tracking of vessel walls under diastole compared to systole [47, 48]. However, ARF imaging is computationally expensive and processing of individual images is usually performed offline and thus not real-time, although there are studies that use graphical processing units to significantly decrease processing time, leading to real-time ARF imaging at lower resolutions [49]. Elastography is a promising field of research in assessing the vulnerability of atherosclerotic lesions by determining the varying degrees of stiffness of the tissue and thus provides valuable information on the morphology of the plaque. However, to

accurately identify a vulnerable plaque, one needs to know both the morphology and the activity [1]. Active plaques exhibit inflammation, invasion of foam cells and macrophages, have higher metabolic activity, and undergo angiogenesis in the plaque. The critical need to assess the activity level of plaques is left largely unanswered by most *in vivo* imaging modalities presenting an opportunity for contrast agent use in IVUS.

Microbubble contrast agents (MCAs) have already been used to identify molecular markers associated with intravascular inflammation [50] and new transducers in IVUS are being developed for the sole purpose of detecting contrast flow in microvessels such as the *vasa vasorum* which are considered possible etiologic factors associated with a growing, active plaque requiring treatment. Much research has already been performed studying MCAs in molecular imaging. Thus, the remaining challenge behind using contrast in IVUS is detecting the presence of an agent while suppressing surrounding tissue signal. Numerous approaches exist to create a contrast only image that would be competitive to acoustic angiography. These contrast detection methods can broadly be categorized into single pulse or multiple pulse detection strategies.

Multiple pulse contrast detection can be performed on a limited bandwidth transducer and is currently the preferred method used by commercial vendors in transcutaneous contrast imaging. The most basic contrast imaging technique is pulse inversion which sums the traces recorded by a pair of inverted waveforms in order to cancel out the linear reflectors, such as tissue, while retaining the even harmonics generated by nonlinear scatterers, such as contrast agents [51]. Although easy to implement, pulse inversion imaging is not ideal to create images with high contrast to tissue ratio (CTR) since it has been shown that tissues can produce harmonic signal in the first harmonic which composes the majority of the signal content used to create pulse inversion imaging [52, 53].

Single element transducers for second harmonic and subharmonic imaging have been developed to have high transmission efficiency at the fundamental frequency, f_c, while maximizing reception sensitivity at $2f_c$ or $0.5f_c$ [54, 55]. However, strong fundamental signals are present due to the combined channel sensitivity so filtering and pulse inversion are required to make contrast-only images [56]. Other pulse inversion approaches in IVUS have been studied and compared to chirp reversal contrast imaging by Maresca [57]. The use of pairs of either up-sweeping or down-sweeping chirps delivers more energy into the tissue, but requires match filtering of the received signal to compress the rather long transmitted pulse length to retain decent axial resolution. This matched filtering is not perfect and usually results in poorer resolution than other approaches (as noted by Maresca, ultrasonic pulse inversion could resolve a 200 μm channel that chirp reversal imaging could not). Radial modulation in IVUS imaging has also been demonstrated to detect contrast agents using a 20 MHz IVUS commercial catheter *in vitro* by (likely) exploiting non-thickness mode excitations exhibited by a commercial catheter [58]. Care has to be used when using radial modulation since the low frequency pulse used to modulate microbubbles can cause distortion of properties that varies with depth [59]. This can be corrected for if nonlinearity parameters can be obtained, but presents a problem in environments with multiple structures each having different nonlinearity as seen in the layers that compose a vessel.

2.4.4 Optical

The final imaging modality to discuss would be those pertaining to optical imaging. Optical based approaches are attractive because the wavelength of light is extremely small giving them resolution on the order of several microns [60]. Additionally, some biological tissue can selectively absorb different wavelengths of light much like infrared spectroscopy is used to

identify chemical structures in analytical chemistry. Near infrared spectroscopy has been used to identify and help characterize plaques using this patented idea [61]. Lipid rich plaques have been noted to be characterized especially well using this technique [62]. However, using light as the source for imaging also presents a limiting depth since it is subject to a higher degree of scattering. Since the wavelengths of the light source are so small, small scatterers such as individual red blood cells can severely limit the depth at which this imaging technique may be used (~ 1 mm). Optical coherence tomography (OCT) is yet another way of using light to image the endothelial layer of plaques but also makes a trade-off between higher resolution and reduced depth of penetration that is common to most coherent imaging.

Lastly, researchers have explored combining different modalities together to get the best picture of how vessel diseases such as atherosclerosis behave. The finer resolution of OCT is used in the near-field while the depth of penetration of IVUS is exploited to look at deeper structures that cannot be seen with optical based approaches [63]. Hybrid OCT/IVUS catheters are promising, but are difficult to manufacture since the specialized needs of two separate imaging modalities must be combined in a limited amount of space. Additionally, this type of system may be better at assessing fine morphological features such as the presence of a thin fibrous cap, but would have trouble detecting *vasa vasorum* and intraplaque neovascularizations since they typically originate from the adventitial layer of the vessel and would likely be too deep to image using either modality.

2.5 Vascular response to statin therapy

Patients diagnosed with atherosclerosis or those with prior history of cardiovascular disease may be prescribed lipid lowering treatments either for treatment of disease or prevention of it. Low cholesterol diets can help some patients with atherosclerosis, but not others especially

if anabolism of cholesterol is hyperactive. Coupled with dietary and activity level precautions, patients are often prescribed a class of drugs called statins. Statins help reduce cholesterol levels by inhibiting the rate limiting enzyme of cholesterol synthesis in the liver, 3-hydroxy-3-methyglutarl-coenzyme-A reductase (HMG-CoA reductase). Statins such as lovastatin produced by the fungus *Aspergillus terreus* prevent this enzyme from creating 3R-mevalonate which is one of the first reagents needed toward synthesis of cholesterol [64].

When plaques are detected and statins administered for treatment, the ideal outcome is regression of the plaque to a small, stable level. Thus, it is likely to suspect that statin therapy alters the physical composition of the plaque itself. Analysis of clinical outcomes of patients undergoing statin therapy compared to those that do not suggests that plaques are targeted by the therapy; the growth of plaques is retarded, and in some cases, regression of the plaques may occur [65]. Statins lower levels of low density lipoprotein (LDL) concentration and may increase high density lipoprotein (HDL) concentration not only systemically, but also within the plaque [66, 67]. This intraplaque decrease in cholesterol levels indicate that plaques are at a lower risk of causing future cardiac events becoming more "stabilized."

One hallmark of plaque vulnerability this course of study wishes to leverage is the presence or absence of neovascularizations in the plaque as an indicator of increased susceptibility to plaque rupture. The presence of blood vessels in a plaque has already been identified to precede plaque growth and reacts to anti-angiogenic therapies [68]. While not anti-angiogenic in nature, *vasa vasorum* has similarly shown response to statin therapies with decreasing vascular density in plaques undergoing reduced progression or regression [69, 70]. It is possible that the loss of vascularity in plaques could be used as an indicator of growth inhibition and effective treatment in response to statin therapies.

Since the proposed transducer is designed to visualize microvessel contrast flow, specifically originating inside the plaque, future *in vivo* validation must be considered. It has been suggested that a minimum of 19.7 months of statin treatment are required to identify plaque regression in atherosclerosis [65]. Based on the previously discussed literature, we expect to see *vasa vasorum* reduction near the conspicuous plaque, meaning the signal of interest should go away in response to effective statin therapies. Studies with measurands that reduce over time can be difficult to perform since conducting the study incorrectly could have the same results as the expected longitudinal outcome from treatment. Additionally, statins are contraindicated with patients with liver disease. Since the primary site of elimination of most contrast agents are the lungs for gas core release and the liver for shell material removal [71, 72], it is unclear if the injection of a phospholipid shell contrast agent will cause liver dysfunction for the animals or patient undergoing statin therapy. A secondary form of measurement is proposed by following the precedent set by contrast enhanced ultrasound examination of carotid plaques. A review of the benefits associated with this approach is given by Feinstein, some of which are not applicable upon translation to IVUS such as enhanced delineation of intima-media thickness (IMT), which is normally easy to see in IVUS without contrast since higher frequencies are used [35, 73]. However, contrast enhancement for complex lesions such as those with dissections or ulcers could be improved by using a transducer designed to image contrast agents [74].

CHAPTER 3

CURRENT STATUS AND PROSPECTS FOR MICROBUBBLES IN ULTRASOUND THERANOSTICS

Microbubble contrast agents are capable of performing diagnostic and therapeutic behaviors based on their application and design when manufacturing them. The first section of this chapter will provide a brief discussion of the advantages of microbubbles combined with ultrasound. The following section will give a detailed description on how the design of the microbubble material impacts its utility in theranostics and will be followed by a section that details the physics of how microbubbles behave when insonified. The chapter will then conclude by providing both diagnostic and therapeutic applications of microbubble contrast agents (MCAs) as well as address some of the current challenges of using MCAs.

Theranostics refers to the combination of diagnostic and therapeutic approaches, typically for assessing response to therapy. Although it is possible for an agent to be used simultaneously for imaging and therapy, by definition, theranostics is fundamentally the combination of a diagnostic test with a therapeutic approach. Thus, theranostics can involve either application of a diagnostic technique followed by a therapeutic, or vice versa [75]. Theranostic approaches are a key aspect in the drive toward personalized medicine, where the tailoring of decisions and

---

KHM authored the review paper with edits performed by PAD.

treatment practices for individual patients is based on diagnostic information specifically from that patient. In this chapter, we illustrate how microbubbles can be used for imaging, for therapy, or for both simultaneously. Because of this broad application, microbubbles combined with acoustics may be one of the most universal theranostic tools.

3.1 Introduction

3.1.1 Advantages of ultrasound

Ultrasound is already one of the most widespread diagnostic modalities, routinely used in cardiology and obstetrics, but also commonly used for imaging soft tissues [76]. The utility of the ultrasound platform is further enabled by recent advances in electronics. Rapidly shrinking and more powerful application-specific integrated circuits have led to ultrasound being one of the most portable imaging modalities. Many ultrasound manufacturers now offer imaging systems which are the size of laptop computers, and some of the latest devices are only slightly larger than smart phones. In contrast, the sizes of other clinical imaging systems such as MRI, CT, SPECT, and PET are substantially larger and therefore remain less portable and accessible. Although ultrasound does not provide the large region volumetric imaging that is provided by these other modalities, its acquisition rates exceed that of MRI and nuclear imaging technologies by several fold. This high-frame rate provides an advantage in therapeutic applications with real-time feedback, which can be cumbersome with other imaging techniques. Another advantage of ultrasound is the significant soft-tissue contrast obtained in its images, although tissue attenuation severely limits the resolution and contrast of ultrasound for deep tissue applications. Furthermore, ultrasound imaging delivers no ionizing radiation, and thus is considered one of the safest imaging modalities [77]. Although the safety of ultrasound contrast agents still needs to be examined for many applications, initial evaluations of contrast ultrasound in cardiology suggest

that adverse effects resulting from contrast use are very rare [78-80]. Furthermore, ultrasound contrast may play an important role in patient populations where MRI and CT contrast agents are contraindicated (such as renally compromised patients) [81]. Along with the inherent safety and portability of ultrasound imaging, the equipment cost is significantly lower in comparison with other imaging modalities. With these advantages, the future role of the microbubble platform in both diagnostics and therapeutics is highly promising.

3.1.2 Advent of microbubbles for medical imaging

Ultrasound image formation relies on the reception and interpretation of acoustic reflections scattered by blood and tissue. However, the scattering components associated with blood are weak, and thus blood flow in tissues and small vessels is challenging to image. Gramiak and Shah are credited with the first publication of the contrast ultrasound technique as they described the application of bubbles produced by rapid intracardiac saline injections to enhance delineation of aortic blood flow [82]. It was not until over two decades later, with the marketing of Albunex, Mallinckrodt Medical, Inc., St. Louis, MO, that microbubbles became commercially available for use as an ultrasound contrast agent [83].

3.2 Microbubble composition

3.2.1 Encapsulating shell

Initial studies of gas bubbles for acoustic enhancement utilized unencapsulated microbubbles that were generated *in situ*. Because of the solubility of air in blood, unencapsulated microbubbles dissolved in seconds [84], and could not traverse the pulmonary vasculature [85, 86]. First generation contrast agents utilized a stabilizing albumin shell which improved circulation time substantially over unencapsulated microbubbles. The shell reduces the

rate at which the gaseous core diffuses into the surrounding media [87]. Microbubbles are normally injected intravenously as suspensions meaning they are exposed to aqueous solutions during clinical use. As such, shells composed of amphiphilic molecules help ensure microbubbles can achieve thermodynamic stability with a hydrophobic gas core. Various compositions have since been used to provide an encapsulating shell, including proteins, lipids, and polymers. The commercially produced contrast agents Optison (Mallinckrodt, San Diego, CA) and Definity (DuPont Pharmaceuticals Co., North Billerica, MA) are currently the only two Food and Drug Administration (FDA) approved agents in the United States still in production. Optison and Definity utilize albumin and phospholipid encapsulation, respectively, to provide their stabilizing shell material for the inner gas core [88].

The diversity of encapsulating material composition, thickness, stiffness, charge, and surface area enables tailoring of bubble design for custom applications [89]. Shell material choice is important in microbubble formulation and design because the shell functions as a scaffold for ligand binding, prevents core gases from diffusing, and influences biocompatibility. Phospholipid shells are widely used because they are easily modifiable for ligand-binding and targeting applications. The polar heads of these phospholipids are frequently the site of conjugation to make targeted microbubbles [90]. Direct modifications of the microbubble shells have been used in specialized applications to explore novel methods of enhancing microbubble function [90-95].

Polyethylene glycol (PEG) chains of varying length attached to the shell of the microbubble act as steric brushes, reducing microbubble aggregation and immune recognition while also providing an attachment point for bioconjugates [90, 96, 97].

3.2.2 Gas core

The composition of the gas core also determines the stability of the microbubble. Commercial formulations of the inner gas core have included air (Albunex), sulfur hexafluoride (Sonovue, Bracco SpA, Milan, Italy), or perfluorocarbons (Definity, Lantheus Medical Imaging, North Billerica, MA).The transition from air to high molecular weight fluorinated gas cores has improved microbubble stability. Gases with lower blood solubility and higher molecular weight take longer to diffuse across the microbubble shell allowing for longer persistence times [98].

3.2.3 Microbubble size control

Most lipid and protein encapsulated microbubbles are formed through either mechanical agitation or sonication to produce a suspension of encapsulated bubbles. These methods result in microbubble populations that are polydisperse. The acoustic response of microbubbles varies with respect to many parameters but the largest contributor is diameter [99, 100]. Acoustic scattering cross section is a function of size, and microbubbles of decreasing diameter naturally oscillate at higher resonant frequencies. By tailoring microbubble size distribution, imaging sensitivity can be optimized [101-104]. Microbubble size also plays a significant role in therapeutic effects, as size is proportional to drug loading, and smaller microbubbles require lower pressure magnitudes to cause shell rupture [105]. Microbubble size is also related to cavitation magnitude and corresponding changes in blood–brain barrier permeability during microbubble-enhanced focused ultrasound treatment [106, 107].

Microbubble preparations with custom or narrow size distributions are generally obtained in one of four ways: microfluidics [108, 109], electrohydrodynamic atomization [110], filtering [111], or differential centrifugation [102]. In microfluidics and electrohydrodynamic atomization, microbubbles are produced with uniform diameters by precisely controlling the

flow rates of the encapsulating (usually lipid) phase that sheaths around the inner phase (usually high molecular weight gas). Microfluidics uses flow-focusing devices driven by pressure along with advantageous channel geometries to direct and control flow while electrohydrodynamic atomization utilizes electric fields to pull droplets from a fluid cone. In contrast to the previous two techniques, differential centrifugation and filtering do not create microbubbles at a given size but instead refine a polydisperse population into sorted samples. Both methods are generally of higher throughput than either microfluidic or electrohydrodynamic techniques. Some groups have utilized filtering to refine microbubble populations, although this method can be challenging due to the fact that most microbubbles are very susceptible to destruction at high shear rates or pressure changes [112], and soft-shelled microbubbles are deformable and thus may not be efficiently sorted by specific pore sizes. Centrifugal sorting is commonly used in microbubble size refinement as it can be performed on large batches of microbubbles using common laboratory equipment.

3.3 Microbubble behaviour

3.3.1 Acoustic response

The gas core of a microbubble has a compressibility that is several orders of magnitude greater than an equivalent volume of blood. It is this combination of high compressibility coupled with the low density of the core that provides a substantial impedance mismatch between microbubbles and surrounding blood or tissue, and thus makes microbubbles excellent ultrasound contrast agents [113]. When exposed to an ultrasound pulse, microbubbles oscillate in response to the acoustic pressure waves (Figure 3.1) [84, 114].

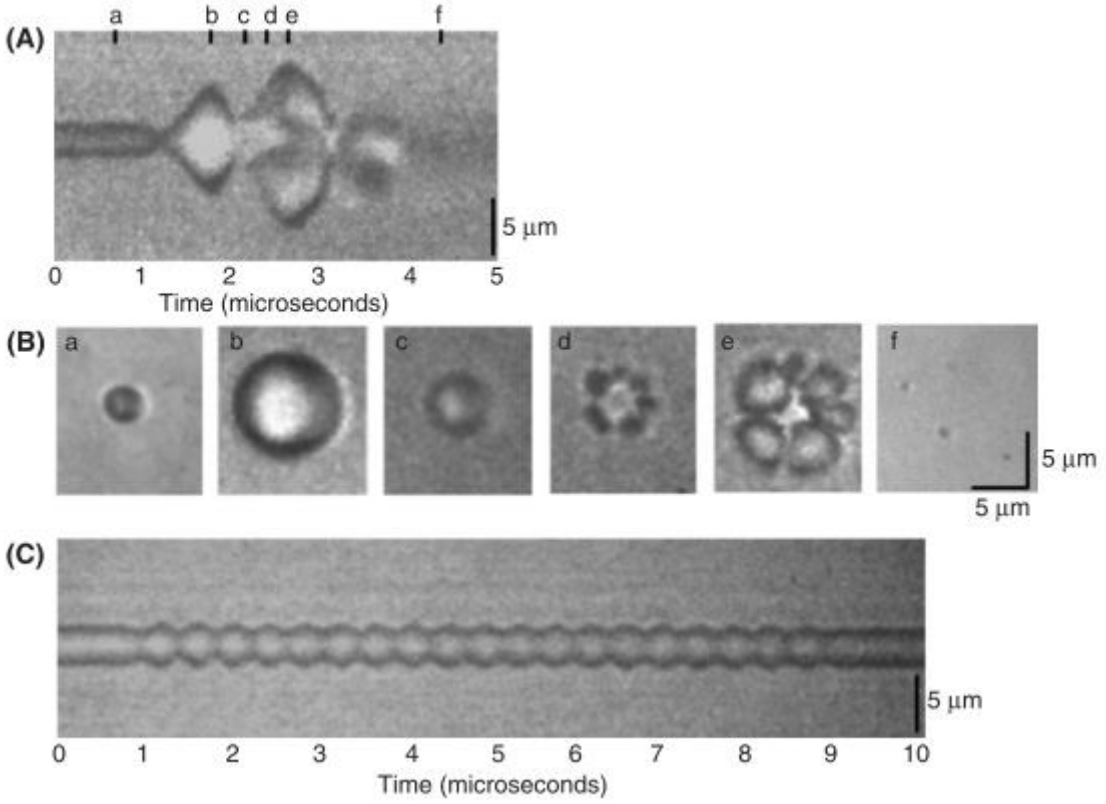

Figure 3.1: High-speed optical photography of acoustically excited microbubbles illustrating microbubble fragmentation as well as stable oscillation. (A) Diameter versus time streak photography showing a 3-µm bubble in response to two cycle insonation at approximately 1.5 MHz and 1200 kPa. The microbubble is observed to expand and contract substantially and then fragment (B). Standard two-dimensional framing photography acquired simultaneously to the diameter versus time image presented in (A); (C) 20-cycle insonation of a 3.5-µm bubble at approximately3.5 MHz and 200 kPa, showing stable, linear, low-amplitude oscillation.

At low acoustic pressures, most microbubbles oscillate stably, scattering sound energy as they resonate. At high acoustic pressures, large cycles of expansion and contraction can result in instability that results in fragmentation of the shell and consequential microbubble destruction with diffusive loss of the gas core. Microbubble destruction can also result in the release of any incorporated payload, facilitating the use of microbubbles as a therapeutic agent [105, 115]. Microbubble behavior depends on many factors, including acoustic frequency and pressure, bubble size, and physical properties of the shell and core. Environmental conditions such as

hydrostatic pressure and dissolved gas saturation are also influencing factors. In general, low acoustic frequencies, high acoustic pressures, and smaller diameters increase the likelihood of microbubble destruction [105, 116].

The phenomenon of acoustic radiation force provides an additional method to increase theranostic utility of microbubbles. Primary radiation force displaces bubbles along the direction of acoustic wave propagation. This force can physically displace microbubbles from the center of flow of a vessel and concentrate them against the endothelium [117]. Secondary radiation force can cause groups of microbubbles to aggregate together and is most significant when microbubbles are in close proximity (several bubble diameters) of one another [118]. Radiation force has been shown to both enhance the *in vivo* retention of molecularly targeted contrast agents [79, 119, 120], as well as increase the local delivery of drug-carrying microbubble vehicles [121-123].

3.3.2 *In vivo* behaviour

During a contrast imaging exam, a solution of microbubbles is injected through a peripheral vein. Typically, circulation half-life is fairly short, and microbubbles remain in circulation on the order of several minutes [124]. Gamma scintigraphy of commercially available Quantison, Quadrant Healthcare Ltd, Nottingham, UK suggests the liver and spleen as the final destination of most microbubble shell components [125]. These observations have been corroborated more recently by PET imaging with lipid-shelled microbubbles [126]. Inert gases from defunct microbubbles are rapidly cleared through exhalation from the lungs.

3.4 Diagnostic applications

3.4.1 Contrast specific imaging methods

There are two primary categories of methods for detecting microbubbles that enable contrast-specific imaging. First, the oscillation of microbubbles in an acoustic field results in scattered broadband acoustic energy with a frequency range much greater than that produced by tissues. This signal is separated from tissue response via high- or low-pass filtering of the backscattered signal. Techniques include subharmonic imaging [127-129], the detection of microbubble signal at frequencies half of the imaging frequency; harmonic imaging [130, 131], the detection of microbubble signal at twice the imaging frequency; and superharmonic imaging [132, 133], the detection of higher harmonic multiples of the imaging frequency. A high-frequency contrast imaging technique called acoustic angiography is a subtype of superharmonic imaging which requires low-frequency excitation and high-frequency detection of the broadband response using specialty wide-bandwidth transducers [134-136]. The isolation of the microbubble-specific signal enables visualization of contrast agents without the high background signal from tissue which could otherwise contaminate the image. Acoustic angiography has an advantage of only needing a single pulse of ultrasound for each line of sight to create image data and therefore can operate at least twice the speed needed for multi-pulse imaging strategies. Multi-pulse imaging strategies detect nonlinear response from microbubble using consecutive acoustic pulses, as opposed to linear responses from tissue. In order to separate microbubbles from tissue echoes, these nonlinear imaging strategies excite microbubbles with two or more pulses of varying amplitude or phase and then combine the resulting response across multiple pulses [51, 137-139]. Nonlinear components of the received signal, such as those from the

echoes of microbubbles, will remain after the images are combined, while linear components such as echoes from most tissues, will ideally cancel each other out.

3.4.2 Perfusion imaging

Ultrasound contrast-enhanced imaging can be used to monitor tissue or organ perfusion rates by measuring the transit time of microbubbles into or out of tissue. This is accomplished through observation of a single contrast agent bolus, or by modulating contrast agent wash-in acoustically. The latter is achieved by sending a short, high intensity ultrasound pulse that fragments microbubbles in the field of view. After this clearance pulse, the returning microbubble signal wash-in rate is measured and can be correlated to microvascular flow. This method is typically performed under constant infusion of contrast agents, and imaging is performed using low intensity contrast-specific imaging in order to preserve the microbubble population during the measurement phase [140, 141]. This method, often referred to as ‘destruction-reperfusion’, ‘flash-replenishment’, or ‘clearance-refill’ imaging, can detect changes in very small flow rates below the tissue motion noise level that limits conventional color Doppler velocity estimates [142]. Use of perfusion imaging has been demonstrated to be effective in assessing blood flow in the kidneys [143-145] and capillary beds of tumors [146-150] among others.

The ability of contrast ultrasound perfusion imaging to detect small changes in blood flow conditions, such as those found in capillary beds, suggests substantial potential for assessing response to therapeutic approaches that affect tissue blood flow (such as antiangiogenic therapies, Figure 3.2) [149, 151-156]. Antiangiogenic treatment of tumors attempts to decrease tumor viability by inhibiting vascular function and development in order to curb tumor growth and cause eventual ischemic and necrotic conditions within the tumor [157]. Initial studies

focusing on antiangiogenic therapy response in tumors using perfusion imaging have reported ease of use, low cost, and high spatial resolution [149]. Similarly, contrast ultrasound perfusion imaging has been utilized as an immediate means to assess clinical response to high intensity focused ultrasound ablation [158, 159].

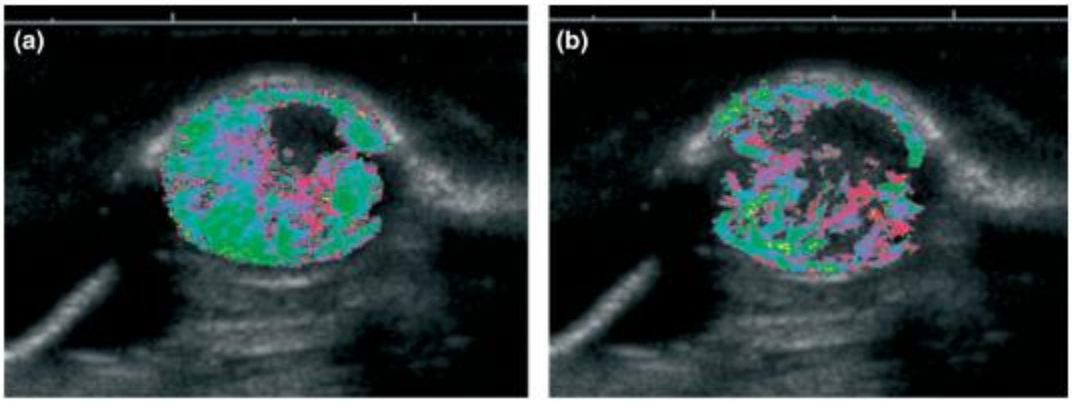

Figure 3.2: Example of contrast-enhanced destruction-reperfusion imaging in a rodent tumor xenograft model, (a) prior to and (b) 48 h post antiangiogenic administration, illustrating reduction in tumoral blood flow in response to therapy. Grayscale indicates anatomical orientation, the color map indicates blood flow, where red is slower flow and green is faster flow.

3.4.3 Molecular imaging

Molecular imaging enables contrast ultrasound to progress beyond anatomical imaging and provide information about changes in physiology on the molecular level [160-162]. Molecularly targeted contrast agents are formulated by incorporating targeting ligands, such as peptides, antibodies, or other adhesive molecules specific for disease biomarkers, into the contrast agent shell. Typical microbubble sizes are large enough to stay within the vascular lumen without extravasating to surrounding tissues, and thus are well equipped to target endothelial markers of disease. Upon injection, circulating targeted microbubbles adhere to endothelium presenting the appropriate receptor. After natural clearance of unbound circulating

microbubbles, retained molecularly targeted agents can be imaged using nondestructive microbubble imaging methods, providing information as to extent and degree of biomarker expression. Since ultrasound cannot directly assess molecular changes, the assumption that targeted microbubble retention on diseased endothelium is proportional to biomarker expression is a crucial tenet to this method. Commonly imaged biomarkers include the $\alpha_v\beta_3$ integrin, associated with angiogenesis, which can be targeted through cRGD peptides, as well as inflammatory markers such as ICAM-1 and VEGFR-2, often targeted directly with microbubbles bearing specific antibodies. Intriguing applications of ultrasound molecular imaging include but are not limited to assessment of atherosclerosis predisposition or progression [33], thrombus [163], ischemic damage [164, 165], inflammatory diseases [166], and tumor-related angiogenesis [167-169].

As any physical change in biological tissue is likely preceded by changes at the molecular level, the ability to assess molecular markers enables a method of predicting forthcoming biological response to treatment. Through the use of microbubbles targeted to angiogenesis markers, researchers have observed changes in biomarker expression in response to therapy (Figure 3.3) [170]. More recently, ultrasound molecular imaging has been shown to classify tumors as non-responder or responder earlier than standard tumor size measurement techniques [151, 171].

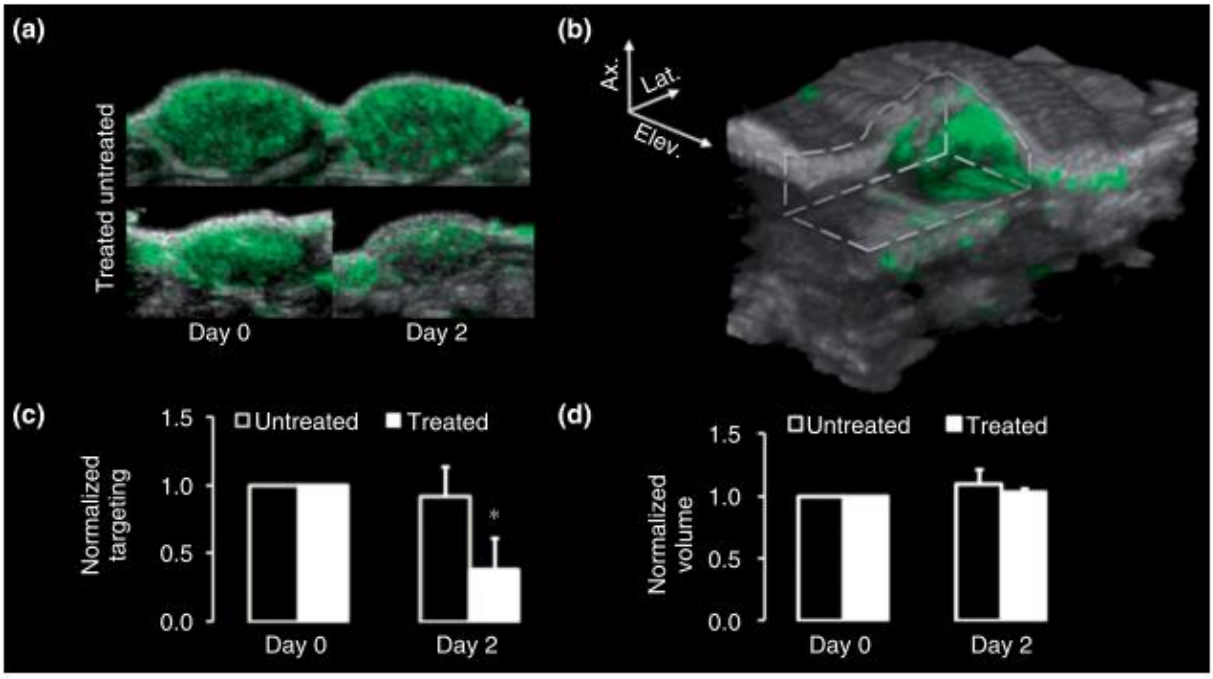

Figure 3.3: Ultrasound molecular imaging in a preclinical model. Data illustrate that molecular imaging indicates response to therapy prior to tumor size changes. (a) Ultrasound images of a representative treated and a representative untreated tumor, which were each acquired before and after treatment. The green color overlay illustrates contrast agent targeted to $\alpha_v\beta_3$, an angiogenic biomarker. The brightness of the green image overlay is assumed to be correlated with the degree of molecular marker expression. (b) Three-dimensional ultrasound rendering of a treated pancreatic adenocarcinoma tumor on day 0. The green overlay represents the contrast agent targeting to $\alpha_v\beta_3$. A section is removed to illustrate the spatial variability of contrast targeting to $\alpha_v\beta_3$ biomarker expression. (c) Percent increase or decrease in volumetric contrast targeting before and after therapy (untreated −N = 5, treated − N = 5). *$p < 0.05$ compared with untreated tumors on day 2. (d) Percent increase or decrease in volume as measured by regions of interest from brightness mode ultrasound images taken at known distances across the tumor (untreated − = 5, N treated − N= 5).

3.4.4 Acoustic angiography

When combined with an imaging mode that provides both high resolution and tissue signal rejection, microbubbles (inherently limited to the vascular space) can provide traces of detailed vascular structure (Figure 3.4). Several studies reported in the literature over the last decade have utilized contrast ultrasound as a means of assessing vascular architecture with the goal of either determining tumor presence or tumor malignancy. Contrast-enhanced acoustic

angiography has been demonstrated in multiple cancer types, including breast [172], liver [173, 174], and thyroid [175]. More recently, high-frequency acoustic angiography has enabled analysis of vessel tortuosity in a preclinical model that uses vessel morphology to distinguish between healthy and tumor tissue [6]. While various segmentation approaches have been implemented to extract and categorize vascular features from image data, the diagnostic utility of acoustic angiography is encouraging. Contrast-enhanced acoustic angiography could be utilized to assess vascular changes in response to therapy, based on the current understanding that vascular abnormalities re-normalize in response to treatment [176-178].

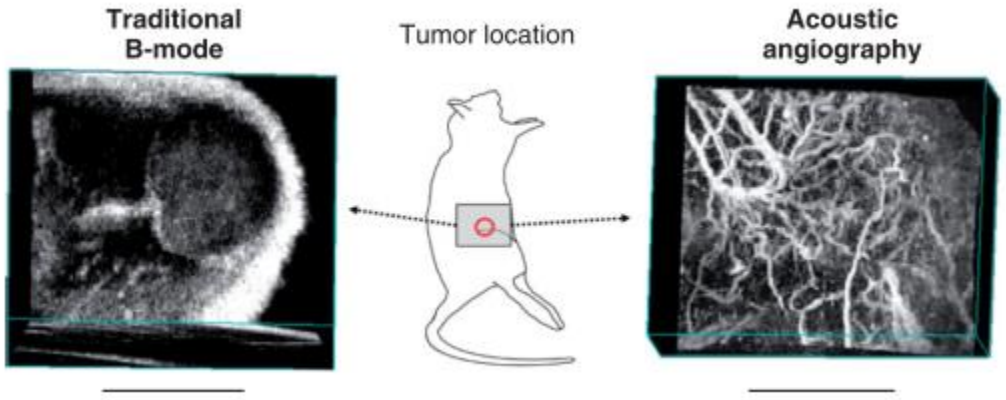

Figure 3.4: Comparison of B-mode and acoustic angiography. Two 3D images from the same sample volume acquired of a rat fibrosarcoma tumor model using traditional 30 MHz B-mode imaging (left) and contrast-enhanced acoustic angiography (right). Scale bars below the images indicate 1 cm. Cartoon in the center illustrates the approximate location of the tumor denoted by the red circle.

3.5 Therapeutic applications

The behavior of the oscillating bubble in an acoustic field lends itself not only to conventional imaging enhancement, but also to therapeutic applications which could be performed during the same sonography session. These applications range from slight physical modifications of the tissue itself—such as reversible changes in vascular or cellular

permeability—to more aggressive disruption, such as clot fragmentation. The mechanical action of oscillating microbubbles also enhances conversion from acoustic to thermal energy, resulting in tissue ablation at lower acoustic energy than that required for similar effect without microbubbles. Other applications involve secondary interactions such as the local delivery and/or release of a therapeutic compound mediated by acoustically driven microbubbles. Guidance can be provided by ultrasound imaging [179], MRI [180], or other modalities to help direct the treatment to the desired location, or to monitor the therapeutic effects of microbubble mediated therapies.

3.5.1 Modulation of vascular and cellular permeability

The mechanical oscillations of acoustically stimulated microbubbles have been shown to increase local vascular permeability [181, 182]. Effects range from mild transient changes in vascular permeability to gross vascular disruption and hemorrhage, depending on microbubble and acoustic parameters. Early *in vivo* studies demonstrated that insonified microbubbles were capable of small vessel rupture creating transcellular pathways for polymer microspheres ($\leq$ 503 nm) and red blood cells ($\sim$7 μm) to extravasate [183]. Extensive studies have shown that with appropriately chosen acoustic parameters, changes in vascular permeability due to insonified microbubbles can be mild and transient [184, 185]. Thus, there is a great interest for using this approach to locally enhance extraluminal bioavailability of therapeutic materials to surrounding tissues. Studies have illustrated substantial potential for the application of acoustically excited microbubbles to locally enhance delivery to the brain [186, 187], tumors [188], and other tissues [93, 189]. This is of particular interest in the brain, where the blood-brain barrier makes extravascular drug delivery challenging. There are several mechanisms hypothesized to be responsible for this permeability modulation, including disruption of the endothelium due to

mechanical stresses on the vessel wall [190, 191], endothelial disruption due to liquid jetting that occurs with bubble collapse [192], and increased cellular transport (Figure 3.5) [190, 193].

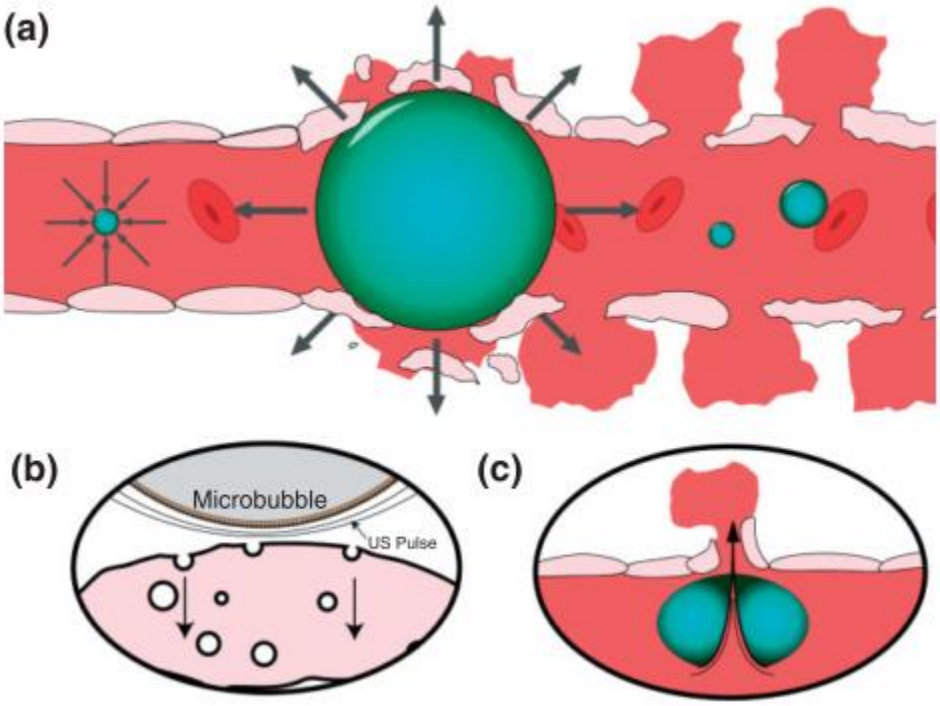

Figure 3.5: Illustration of MCA mediated enhanced cell permeability. (a) An ultrasound wave places a high pressure on the microbubble to compress it and is followed by low pressure that rapidly expands it creating several micro-hemorrhages due to mechanical stress. (b) An oscillating microbubble stimulates a cell to increase transcellular transport from the lumen of the vessel to the basal membrane. (c) A microbubble oscillates nonlinearly to the point of asymmetric collapse, producing a powerful micro-jet that breaches the endothelium.

Similar to the effect on vascular permeability, acoustically activated microbubbles have also been shown to enhance the permeability of individual cell membranes. This phenomenon, termed ‘‘sonoporation’’, can result in the internalization of compounds into a cell which otherwise would not cross the cellular membrane. The mechanisms causing sonoporation are still being studied; however, common mechanistic hypotheses include mechanical stresses, the formation of pores due to liquid jetting [194], or microstreaming [195, 196], as well as active

transport processes [197]. Sonoporation can be transient or irreversible, the latter often associated with cell death, depending on the acoustic parameters [184, 198, 199].

The magnitudes of changes in both vascular and endothelial permeability are related to ultrasound frequency, pressure, and microbubble parameters. In general, lower acoustic frequencies and increased pressures result in greater permeability. Identifying and characterizing which parameters can be used to modify vessel or cellular permeability, the mechanisms involved, and to what extent permeability can be modulated is an active area of study in microbubble acoustics [200].

3.5.2 Drug delivery

Many anti-cancer drugs suffer from a low therapeutic index, where the systemic dose becomes toxic at only slightly higher doses than may be effective in treating the disease. Thus, any means to significantly increase drug delivery at the disease site while reducing dose to healthy tissue is of great clinical interest. One approach is to spatially distribute the drug concentration unevenly such that the local dose to the disease site is elevated while the systematic dose remains low. Microbubbles can behave as a targeted delivery system by loading them with drugs and selectively lysing (fragmenting) them in regions where the drug delivery is desired [201-203].

Examples of drug loading techniques include the incorporation of therapeutic agents into the microbubble shell [204, 205], the formulation of multilayer vehicles containing drugs in a layer separate from the shell or gas core [206, 207], or conjugation of drug-loaded liposomes or nanoparticles directly to the microbubble surface (Figure 3.6) [122, 123]. Several drugs which have been evaluated for microbubble delivery to date include, but are not limited to, paclitaxel [208, 209], doxorubicin [206, 210], rapamycin [211], and 10-hydroxycamptothecin [212].

Although there is a broad range of drug loading methods and capacities, several studies have shown that certain types of drug carrier vehicles retain the capability for substantial acoustic response, indicating that these vehicles could be fully capable of both acting as imaging agents as well as therapeutic carriers [213, 214].

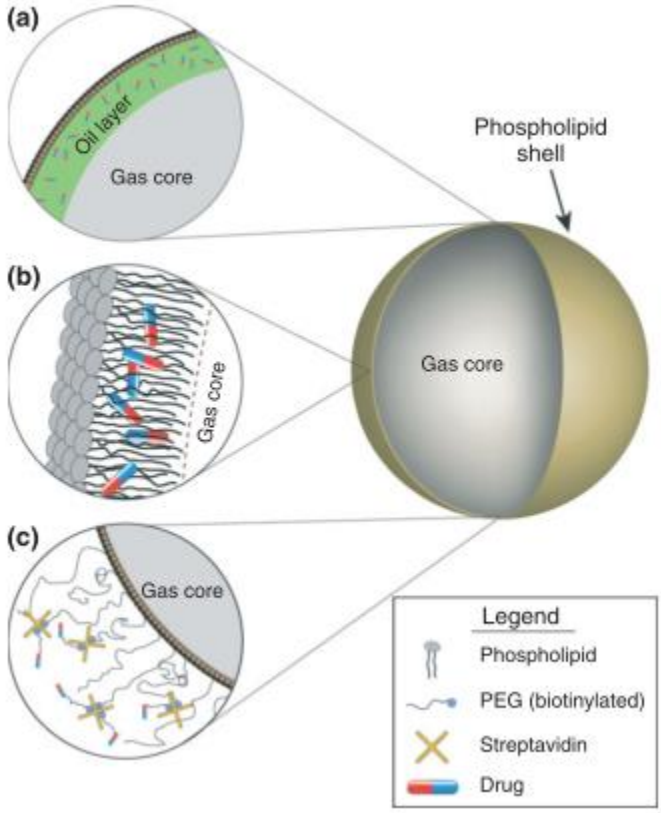

Figure 3.6: Schematic of commonly used drug attachment strategies in microbubble mediated drug delivery. (a) Drugs can be dissolved in a secondary oil layer using a multilayer microbubble construction. (b) Therapeutic agents can be seeded within the thin encapsulating shell. (c) Nanoparticles or other therapeutics can be attached to the outside of the shell, such as tethered to PEG chains.

3.5.3 Gene delivery

While the application of ultrasound alone has increased transfection rates compared to systemic delivery during gene therapy, the presence of acoustically-stimulated microbubbles

results in additional benefit. The results of several microbubble-mediated gene therapy studies indicate that gene transfection rates are highest when ultrasound, microbubbles, and genes are simultaneously delivered to the same target location [91, 189, 215, 216]. Although the mechanisms for enhanced transfection are still being assessed, permeability changes in cellular membranes due to the oscillating microbubbles (as described above) likely play a role [197]. Because of the strongly anionic backbone of plasmids and other gene transfection agents, cationic microbubbles can be used to electrostatically attach genetic material to microbubble shells in a similar manner first developed for liposomes [217]. Positively charged microbubbles bound with genetic material can use lower systemic concentration of plasmids because they have higher transfection efficiencies compared to neutral microbubbles [218]. Cationic binding of genetic materials likely increases transfection rates due to the increased proximity between genetic material and cell membranes which promotes intracellular flow of the genetic material [219]. Thicker-shelled microbubbles are an attractive option in targeted gene delivery since they are less likely to prematurely rupture, can load more genetic material, and can protect genetic material from nuclease activity if bound within the shell [220, 221].

3.5.4 Sonothrombolysis

Sonothrombolysis is the acoustically-mediated disruption of blood clots. The addition of microbubbles further enhances the thrombolytic effect [222], both with and without the combination of thrombolytic agents. The rate of clot dissolution increases and clots degrade more fully when treated directly with ultrasound and microbubbles in comparison to administration of thrombolytic agents alone [223, 224]. This technique has been explored for stroke [225], venous thrombosis [226], and myocardial infarction [227]. Ultrasound-assisted thrombolysis is one of the truly combinational theranostic procedures since real-time ultrasound

measurements of clot occlusion and therapeutic recanalization have been performed simultaneously with microbubbles and ultrasound [227].

3.5.5 Tissue ablation enhancement

Acoustic ablation involves focusing high intensity ultrasound to heat and destroy abnormal tissue. The conversion of acoustic energy into thermal energy causes a rapid rise in temperature at the target site resulting in localized tissue destruction and necrosis. One of the current challenges of high intensity focus ultrasound (HIFU) ablation is to heat only target tissue without damaging healthy tissues. HIFU ablation transmits wide beams of low acoustic energy through tissue which is then focused into a tighter beam of high acoustic energy to be delivered at depth to the target site. Microbubbles can be advantageous for HIFU ablation because they can enhance the conversion of acoustic energy to thermal energy, therefore making this approach more efficient and reducing the likelihood of thermal damage to healthy tissues [228-232]. Early *in vivo* studies examining the effect microbubbles have on ablation enhancement during HIFU was demonstrated in canines [233] and has been clinically evaluated in humans for uterine fibroid ablation [234].

3.6 Current challenges

Microbubbles are a unique platform that can unite established diagnostic ultrasound with relatively nascent therapeutic ultrasound. The largest challenges faced by microbubble technologies are government approval and physician acceptance. Microbubbles are still used clinically only for imaging applications. Even then, as an imaging agent—microbubbles are under-utilized. Although microbubbles are used for several clinical imaging applications in Europe and Asia, FDA approved microbubble use in the United States is still limited only to enhancement of the left ventricle during echocardiography and recently liver perfusion. A third

major challenge involves industrial interest and support and production of ultrasound systems optimized for use with microbubbles, as well as in design and manufacture of the microbubbles themselves. Largely due to the lack of clinical use, industry interest in supporting microbubble imaging and therapeutic approaches on commercial systems has been a low priority. Similarly, there are only a handful of companies involved in the development and sales of microbubble products, likely due to the same reason.

Nevertheless, an active push by both academia and industry is currently underway to extend the use of microbubbles for imaging outside the heart and liver as well as for therapeutic applications. Numerous studies, such as the ones discussed here, have demonstrated the potential uses of microbubbles beyond their current scope. Regulatory agency approval must be met both in the US and in other countries for both additional diagnostic applications, as well as any therapeutic applications of microbubbles, before their use will expand.

3.7 Conclusions

The microbubble platform is unique in that it presents a wide variety of strategies for ultrasound mediated diagnostics as well as therapeutics—thereby acting as a definitive theranostic agent. While there is extensive use of microbubbles in preclinical studies, clinical trials are still only in early stages for molecular imaging as well as for many therapeutic approaches. However, preclinical data are highly encouraging for the future use of microbubbles in theranostic medicine.

CHAPTER 4

DUAL-FREQUENCY TRANSDUCERS FOR CONTRAST ENHANCED ULTRASOUND

The primary aim of this dissertation is to explain and determine the steps required to translate acoustic angiography into the intravascular environment. This chapter discusses the specialized, broad-band transducers that can both elicit and detect the higher order harmonic responses generated by microbubble contrast agents necessary for microvascular detection using acoustic angiography. The methods of performing contrast specific imaging in commercial applications will be reviewed in the first section of this chapter with special attention given to the fabrication considerations of conventional transducers. In the following section, dual-frequency transducers will be introduced as an ideal tool for use in superharmonic contrast imaging as other applications.

4.1 Introduction

Fundamentally, ultrasound images are visual representations of the interaction between sound waves and the medium of wave propagation. However, at frequencies typically used in transthoracic and transabdominal ultrasound imaging, blood is a poor ultrasound scatterer which produces echoes approximately a factor of 300 times weaker than surrounding soft tissues [235],

---

KHM authored this paper with edits performed by BDL, JM, XJ, and PAD. Exceptions include portions of 4.1.3, which were authored by BDL and edited by KHM.

making the detection of blood flow in small vessels challenging. For this reason, microbubbles are used as injectable contrast agents which serve as strong scattering sources and thereby improve imaging of blood flow [82]. While contrast ultrasound is used primarily in cardiology in the United States, it is used more widely in Europe and Asia, and there are substantial ongoing research efforts aimed at evaluating microbubbles as a platform for additional diagnostic and therapeutic applications [87, 236]. This chapter will focus on development of dual-frequency piezoelectric transducers for imaging nonlinear harmonics produced by microbubbles under ultrasound excitation for the intended application of acoustic angiography.

4.1.1 Theory of operation

Microbubble contrast agents are micron-sized shelled gas bubbles that are injected into the vascular space in order to visualize blood flow. When excited by an external acoustic field, microbubbles oscillate non-linearly, producing waves with harmonic content in addition to the fundamental frequency. The degree of harmonic content produced by a single interaction between a microbubble and an acoustic wave increases as the amplitude of the acoustic wave increases, and also increases at frequencies near the resonance frequency of the microbubble [237-240]. Microbubble resonance frequency depends primarily on bubble diameter, though many other physical factors also play a role in determining resonance [103, 104]. While microbubbles are strong scatterers which are visible on standard B-mode imaging at the fundamental imaging frequency, the energy arising from microbubbles cannot be separated from that arising from the surrounding tissue. However, by isolating the harmonic signals resulting from microbubble nonlinear behavior it is possible to image microbubbles alone with high specificity – a fundamental requirement for contrast specific imaging in ultrasound.

An effective approach for minimizing tissue echoes in microbubble-specific imaging is to use higher order harmonics. An acoustic wave traveling through tissue generates harmonics due to nonlinear propagation effects, however, most of the energy received at the transducer remains confined to the transmitted frequency (f_c) and the second harmonic ($2f_c$) [241, 242]. Alternatively, microbubble echoes contain higher order harmonics (superharmonics) at frequencies 3-10 times the transmitted frequency [243-246]. In the following section, we describe transducer technology designed to transmit at low frequencies near microbubble resonance and receive only microbubble superharmonics at much higher frequencies, thus spectrally separating microbubble-scattered signals from tissue.

4.1.2 Summary of commercial contrast detection methods

Currently, commercial ultrasound systems form images of microbubbles using frequency content within the bandwidth of a single transducer, which is used for both transmitting and receiving. These systems typically reduce tissue echoes by transmitting multiple versions of similar pulses having varying phases and/or amplitudes, then summing received signals from these pulses. Using this process, linear signals principally originating from tissue cancel while nonlinear microbubble signals sum constructively. In the simplest of these techniques, pulse inversion, a pair of pulses are transmitted which are inverted replicas of one another (*i.e.* 180° out of phase) [51]. Linear scatterers produce two sets of similarly inverted signals, thus when the received signals from each of the two pulses are added together, the net sum due to linear scattering is zero assuming no motion has occurred. Because shelled microbubbles vibrate nonlinearly, waves scattered from the contrast agents contain components which do not sum to zero, producing an image of microbubbles alone. Various multi-pulse schemes exist in which the phases and amplitudes of transmitted pulses are altered in order to improve separation of

microbubble and tissue signals or to isolate a specific range of harmonics [247-250]. These algorithms are found on commercial ultrasound scanners under names such as Cadence Contrast Pulse Sequencing (CPS) (Siemens) or Power Pulse Inversion (Philips) [138]. The ratio of microbubble to tissue amplitude in an image is known as CTR and is often expressed in dB as a quantitative metric of the effectiveness of a contrast imaging technique. Multi-pulse approaches achieve high CTR at the cost of reduced frame rate and increased susceptibility to motion artifacts. Alternatively, dual-frequency transducers alleviate these problems because their large effective bandwidths allow high CTR imaging using a single pulse.

4.1.3 Design and fabrication of piezoelectric transducers in diagnostic ultrasound

4.1.3.1 Piezoceramic dimensions

While design theory of piezoelectric transducers is well-covered elsewhere [251, 252], basic principles will be reviewed briefly to elucidate challenges relating to dual-frequency transducer fabrication. Transducers used in medical ultrasound consist of a thickness mode resonator. Wave propagation velocity in PZT is approximately 4350 m/s [253], resulting in a nominal thickness ($\lambda/2$) of 435 μm at 5 MHz, for example, though other factors also affect transducer resonance [254]. In array transducers, grating lobes are avoided by maintaining inter-element separation less than or equal to $\lambda/2$. Element width-to-thickness ratio must also be considered, as element aspect ratios determine the acoustic resonance modes [255, 256]. Fabrication challenges tend to intensify as feature sizes decrease in all dimensions with increasing frequency. Tradeoffs between desired resonance frequency and element dimensions represent a primary challenge in array design

4.1.3.2 Element Boundary Condition Considerations

Matching and backing layers designed with desired acoustic properties are attached in series to the front and back faces of the piezoelectric material, respectively. By reducing the mismatch in acoustic impedance between the piezoelectric material (Z_{PZT}≈34 MRayl) and tissue (Z_{water}=1.5 MRayl), matching layers increase acoustic transmission into and from the tissue and act as quarter wave transformers. Backing layers improve bandwidth by damping acoustic vibrations at the rear boundary of the piezoelectric material. The loading provided by matching and backing layers also modulates the resonant frequency of the transducer [254]. The primary challenge in design of matching and backing layers is the tradeoff between high sensitivity and broad bandwidth.

4.1.3.3 Fabrication, Dicing, and Composites

For piezoelectric transducers operating in thickness mode, a "dice-and-fill" approach is commonly used in array fabrication. A wafer-dicing saw cuts and isolates sensing elements, and kerfs resulting from saw cuts are then backfilled to minimize acoustic crosstalk.

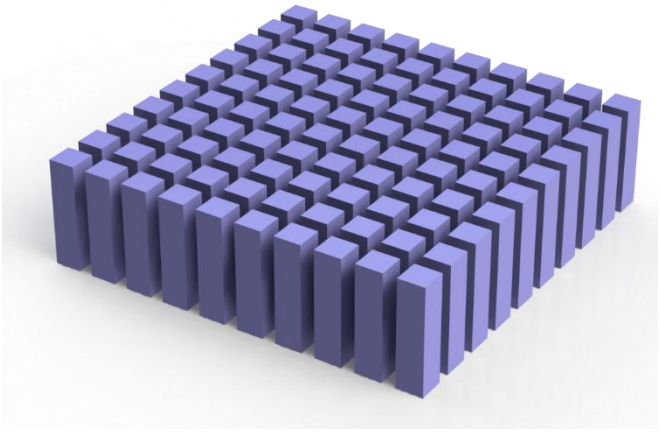

Figure 4.1: Example geometry resulting from a dice and fill method to create a composite material. The gaps are left open to illustrate the areas needing to be filled with polymer.

A dice-and-fill approach is also used to create low frequency composite materials [257-259] from plates of either piezoelectric ceramics [260] or an electrostrictive PMN-PT single crystals [261] by dicing the material and filling the gaps with a polymer [262], then further dicing into individual elements for fabrication of an array(Figure 4.1). Composite materials can produce better harmonic images than conventional materials because they yield transducers with broader fractional bandwidths (> 75%) and improved acoustic matching [263]. Fabrication challenges associated with physical dicing limit acoustic impedance matching in composites.

For harmonic imaging, it may be possible to design a transducer so that both transmission and receiving frequencies are within the bandwidth of a single composite transducer. These composites can be made with 1-3 connectivity, mechanically decoupling the thickness-mode vibration resonance from other undesirable resonances (lateral or elevational modes) [255]. Lateral modes are $\lambda/2$ resonances determined by the dimension of the transducer in the lateral direction, or the dimension of image formation. Designing with respect to lateral modes takes on added importance in environments such as IVUS in which strict limitations on device size imposed by lumen diameter can create severe aspect ratios (width-to-thickness) that are normally avoided to preserve forward looking directional sensitivity. As an alternative to dice-and-fill methods at higher frequencies, Jiang *et al.* have demonstrated fabrication of a 40 MHz, 1-3 composite transducer using a plasma etching-based micromachining technique [264]. A 60 MHz IVUS transducer using 1-3 composite has been fabricated and tested on a porcine animal model [263]. These high frequency broadband transducer materials are promising for imaging microbubble harmonics. The development of high frequency arrays was greatly facilitated by the introduction of laser micro-machining by Foster *et al.*, a process which has become a standard

for commercially-available high frequency imaging systems [265]. Providing individual electrical interconnects also poses a significant fabrication challenge in high frequency arrays.

While developments in materials and fabrication have led to diagnostic transducers having increased sensitivity and bandwidth, the use of two independent frequency bands having large separation (at least 3× to 5×) can maximize sensitivity while requiring lower transmit pressures for contrast specific imaging applications. In the following sections, we describe recent developments in dual-frequency transducer technology.

4.2 Dual-frequency transducers

The goal of dual-frequency imaging is to form images of only microbubble harmonics by transmitting acoustic waves at lower frequencies near microbubble resonance (approximately 1-6 MHz) and receiving only higher order harmonic vibrations produced by microbubbles (approximately 10-30 MHz). Researchers have recently demonstrated electrostatic transducers which are capable of encompassing both frequency ranges within a single, extremely broad bandwidth [266, 267]. Details of the operation and fabrication of these transducers, commonly referred to as capacitive micromachined ultrasound transducers (CMUTs) are discussed elsewhere [268-270]. CMUTs exhibit inherent nonlinear behavior which limits their ability to accurately distinguish nonlinear microbubble response, though ongoing investigations attempt to account for these nonlinearities so they may be used for contrast detection reliably [271]. Although CMUTs may eventually demonstrate superior performance to piezoceramics for contrast imaging, they have not yet been demonstrated for this use *in vivo.* While researchers continue to investigate ultra-wideband electrostatic transducers as well as approaches for increasing the bandwidth of piezoelectric transducers [263, 264, 272, 273], this chapter will

primarily focus on devices which use separate transducers for transmission and reception and thus allow for independent design of the two transducers to achieve desired characteristics.

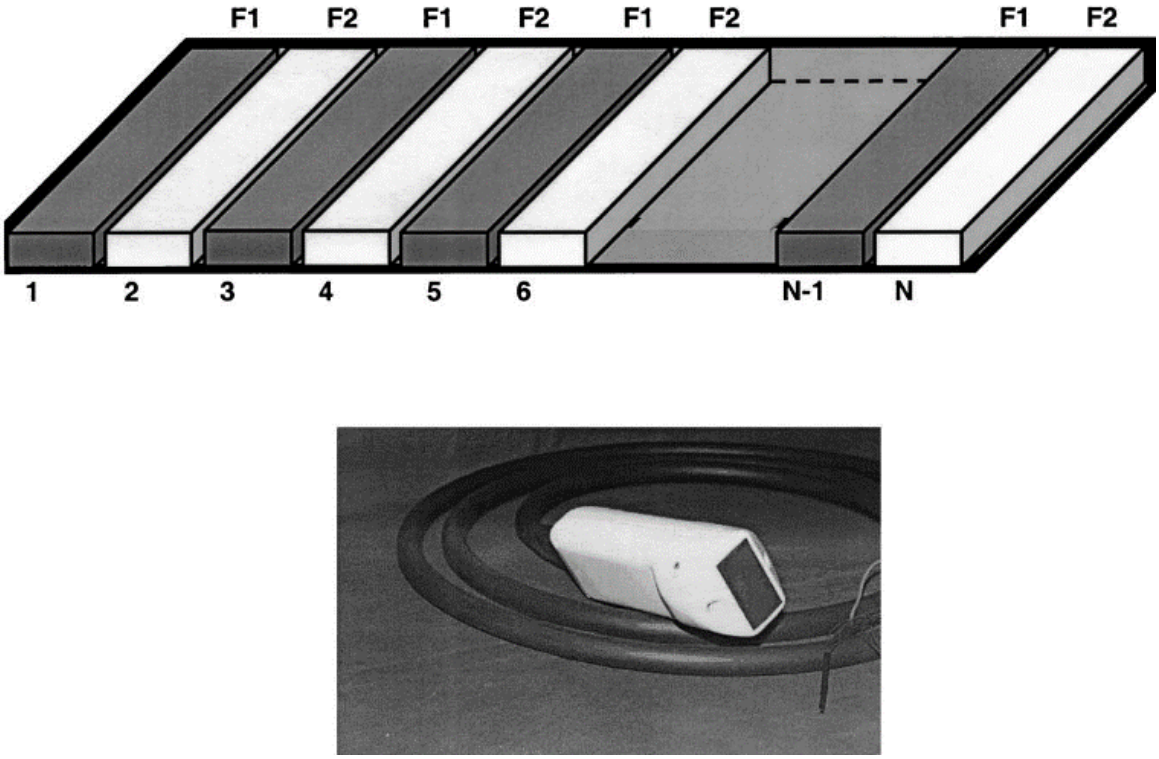

Figure 4.2: Schematic of the first design incorporating dual frequency transducers for the purpose of contrast detection (top). Odd numbered elements had a center frequency of 2.8 MHz with a fractional bandwidth of 80% while the even elements had a center frequency of 0.9 MHz with a fractional bandwidth of 50%. Odd numbered elements were used for imaging superharmonics generated by nonlinear vibrations of microbubbles excited with a low frequency pulse provided by the even elements. A photograph of the actual transducer is shown after the elevational lens has been added (bottom). Figure reprinted from [132] (Copyright © 2002 Elsevier)

4.2.1 Imaging microbubble contrast agents

Bouakaz *et al.* first reported imaging of third and fourth harmonics of microbubbles in 2002 in experiments which used a 96-element array with interleaved 0.9 MHz transmission elements (50% BW_f) and 2.8 MHz receiving elements (80% BW_f) [132, 274, 275]. Using this probe with a commercial imaging system, the authors demonstrated the ability to image

microbubbles while rejecting tissue signals *in vivo* [274] (Figure 4.2). While interleaving low and high frequency elements yields dual-frequency transducer arrays with smaller form factors relative to arrays stacked in the elevation direction, grating lobes were introduced due to an increase in inter-element separation, and signal-to-noise ratio (SNR) was diminished due to reduction in receiving area contributing to the beamformed signal.

In 2005, Kruse and Ferrara demonstrated the use of two piston transducers with a wide bandwidth separation for imaging microbubbles using a transmission frequency of 2.25 MHz (70% BW_f) and a receiving frequency of 15 MHz (66% BW_f) [134]. Wide separation between the two frequencies ensured high CTR due to the low amplitude of higher order tissue harmonics, while a high receiving frequency produced high resolution images. In more recent studies, Ferrara's group has designed transmit low/receive high (TLRH) arrays with two outer rows of 64 elements transmitting at 1.48 MHz, and a central row of 128 elements receiving at 5.24 MHz [276]. In addition to harmonic imaging of microbubbles, the high frequency row of this three-row array was used to deliver a long (100 cycle), low-amplitude (200 kPa peak negative pressure) "pushing" pulse for radiation-force enhanced adhesion of targeted microbubbles for molecular imaging [277, 278]. This work has recently been extended to 3D molecular imaging [279]. Subsequent generations of this array featured low frequency rows capable of delivering either broadband, high peak pressure waveforms for cavitation-mediated therapy or narrower band, high time-average power waveforms for thermal therapy [280, 281]. A similar three-row array with a central row of 128 elements operating at 1 MHz (90% BW_f) and elevationally-aligned outer rows of 128 elements operating at 10 MHz (90% BW_f) was constructed by Vermon (Tours, France) [282].

In 2010, van Neer *et al.* compared designs for interleaved and multi-row arrays [283, 284]. Designs with interleaved elements having high ratios of receive to transmit elements (*i.e.* at least three receive elements per transmit element) were capable of producing beams with reduced distortion artifacts and tighter -6 dB beam widths relative to two- or three-row arrays. By greatly increasing the number of receiving elements, grating lobes of interleaved designs were limited to -40 dB and high SNR was ensured. However, it should be noted that arrays with interleaved elements of different frequencies cannot be manufactured using standard dice-and-fill approaches from a single piezoelectric plate without significant alteration to manufacturing processes (see Section 4.1.3).

In spite of the promise shown by several of these dual-frequency arrays, transition towards transducers with higher receiving frequencies has been accompanied by several fabrication challenges. Because standard array production techniques faces difficulties scaling to higher frequencies [285], high frequency transducers can utilize mechanical steering of a single focused element in lieu of an array. Many of these focused single-element transducers have been possible due to the use of flexible piezoelectric composites rather than inflexible piezoelectric ceramics [286, 287]. An important advancement for high frequency arrays has been the development of composites with large triangular pillars to suppress lateral modes while maintaining high sensitivity [288, 289].

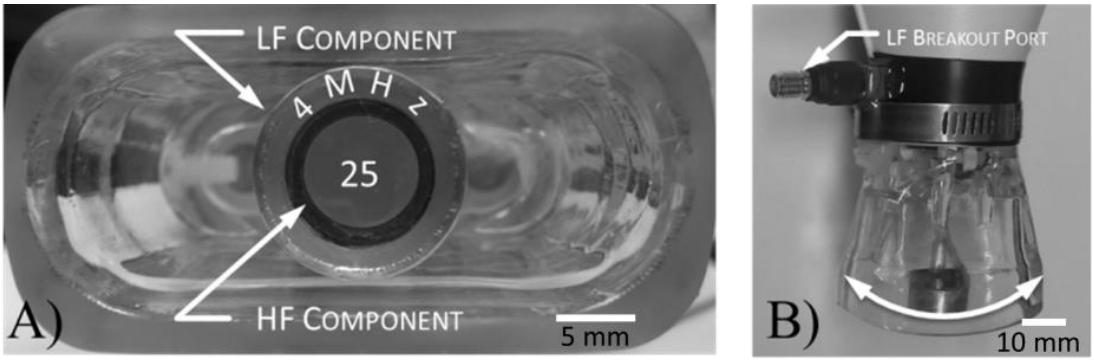

Figure 4.3: The mechanically steered dual-frequency transducer is composed of a central high frequency (25 MHz) spherically focused piston transducer inserted into an annular, confocally aligned low frequency transducer (4 MHz). (A, End-on view) Harmonic imaging is performed by mechanically sweeping the arm while transmitting on the outer element and receiving on the inner element. (B, Side view)

Using this technology, Foster's group working with Dayton has constructed several mechanically-steered transducers consisting of concentric low- (2.5-4 MHz) and high-frequency (25-30 MHz) elements [136, 290]. These probes have been integrated with a commercial small animal imaging system (VisualSonics, Toronto, ON, Canada) (Figure 4.3). Imaging with these dual-frequency transducers has provided a high-resolution (~200 μm), high CTR (~25 dB) imaging technique which the authors call "acoustic angiography" due to the resemblance between the vascular images acquired and those in x-ray or magnetic resonance angiography [291]. This approach has demonstrated sensitivity to vessels containing contrast agents at frequencies higher than previously published (as high as 10 times the transmission frequency) (Figure 4.4) [6]. As a result, acquired images can be segmented by computational algorithms to analyze vessel morphology based on quantitative metrics such as vessel density and tortuosity [6, 292, 293].

Several similar transducers have recently been reported. A mechanically-scanned transducer with two concentric elements operating at 4 MHz and 14 MHz was demonstrated by

Guiroy *et al.* [294]. Li *et al.* have alternatively demonstrated a micromachined PMN-PT 1-3 composite based dual-frequency (17.5/35 MHz) transducer (Figure 4.5) for harmonic imaging [295]. In this design, two active layers were mechanically bonded in series and poled in opposite directions. Composite piezoelectrics and electrostrictive materials such as PMN-PT have been increasingly utilized over traditional ceramics like PZT, which have limitations for use at higher frequencies due to manufacturing challenges and grain dimensions which become increasingly close to one wavelength as frequency increases [296].

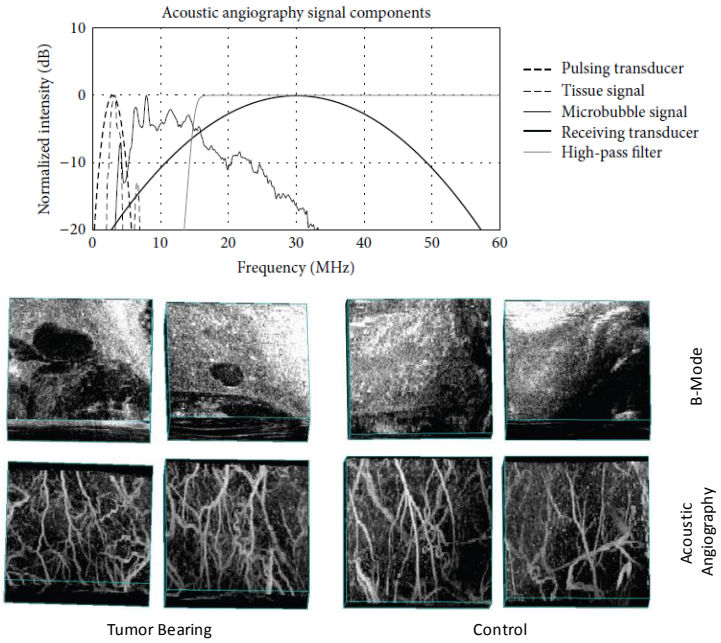

Figure 4.4: Acoustic angiography amplitude spectrum and example images. Wideband separation between tissue response and microbubble response produces images that are drastically different from conventional B-mode images and illustrate blood flow in the microvasculature with high resolution and high contrast to tissue ratio. Acoustic angiography images displayed using maximum intensity projections of volumetric scan volumes. Bounding boxes are approximately 0.75 x 1.25 x 1.5 cm (axial, lateral, and elevational). Figure adapted from [292] (Copyright © 2013 Hindawi Publishing Corp. under CCL).

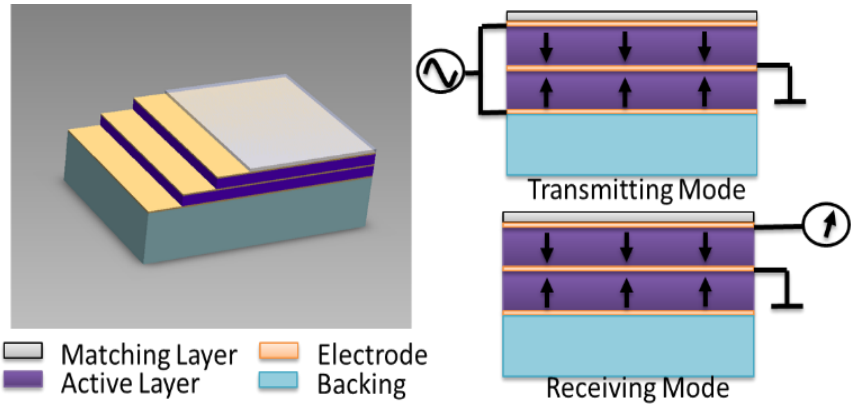

Figure 4.5: Schematic view of a dual layer, dual frequency transducer (left) and its operation for transmitting and receiving (right). When transmitting, both active layers are electrically connected in parallel and are excited by the same signal, effectively behaving as a single, active element at f_c. When receiving, the front layer records the majority of the signal with a resonance at twice the transmission frequency ($2f_c$) because the thickness of the active layer has effectively been halved. Figure reprinted with permission from [295]. (Copyright © 2013 IEEE)

Dual-frequency transducers may be used for intravascular ultrasound, in which a small catheter-based transducer is introduced into the body to perform minimally invasive imaging of occlusive plaques within the coronary arteries [297]. In particular, the detection of *vasa vasorum* (70 – 180 µm in diameter [298]) in plaques has been linked with decreased plaque stability and increased risk of future complications (see Chapter 2). Because superharmonic imaging of microbubbles could enable direct visualization of *vasa vasorum*, several researchers have pursued dual-frequency transducer designs for this application. In 2005, Vos *et al.* developed single element transducers for second harmonic imaging designed with dual resonance peaks at 20 and 40 MHz and a 1 mm outer diameter [54, 299]. This group has also used commercial IVUS catheters to demonstrate the benefits of pulse inversion detection methods for this application [56, 300]. It will be demonstrated in the remaining chapters of this dissertation how a dual-frequency IVUS transducer can be developed for imaging microvessels using superharmonic contrast detection strategies.

4.2.2 Other applications

Researchers have developed dual-frequency ultrasound arrays for applications other than contrast agent imaging which could provide useful insights into design or fabrication strategies. The earliest reported dual-frequency transducer was that of von Ramm and Smith in 1978, in which a phased array with adjacent rows of 1.5 and 2.5 MHz elements was designed to reduce off-axis contributions to the two-way point spread function by misaligning grating lobes from transmitting and receiving arrays [301]. In 1988, Bui *et al.* showed 1-3 composites can be designed to exhibit multiple frequency sensitivities by tailoring the dimensions for separate resonance modes [302]. De Fraguier *et al.* reported separate transducers for B-mode (4.6 MHz) and color Doppler mode (2.3 MHz) in order to improve Doppler sensitivity by reducing transmitted frequency and increasing pulse length [303]. Similarly, Saitoh *et al.* presented a transducer capable of operating at either 3.75 MHz or 7.5 MHz using two layers of PZT poled in opposite directions for increasing Doppler sensitivity [304].

In 2000, Hossack *et al.* reported a dual-frequency transducer to improve sensitivity for tissue harmonic imaging (THI) [305]. This transducer—based on earlier work by Hossack and Auld for increasing bandwidth [306]—used two piezoelectric layers having independent electrical contacts. The two layers were operated either in phase when transmitting at f_c, or 180° out of phase when receiving at $2f_c$. Several other authors developed similar transducers having two resonances at the fundamental and twice the fundamental [307, 308]. Dual-frequency transducer design in THI has been studied extensively in the past and has aided in the development of recent transducer design in contrast specific imaging. For example, confocal annular elements operating at large frequency separations (20 and 40 MHz) produced by Kirk

Shung's group were used in THI of excised porcine eyes before similar form factor transducers were used in acoustic angiography [309].

In addition, many other authors have demonstrated dual-frequency arrays for combined imaging and therapy applications. Recent imaging devices include a three-row array with 128 elements per row for use in prostate cancer imaging and treatment [310], a small-form factor 32-element system for guidance of high-intensity focused ultrasound (HIFU) [311], and a three-row array for thermal strain imaging performing heating at 1.5 MHz and imaging at 5.5 MHz [312]. While a comprehensive review of image guidance in therapeutic ultrasound is beyond the scope of this review, the interested reader is referred to recent reviews on image-guided therapy [313], HIFU [314, 315] and thermal strain imaging [316].

Several recent design developments within other applications are of particular interest for imaging microbubble harmonics. Azuma *et al.* have described the design and fabrication of a 0.5/2.0 MHz dual-frequency array for sonothrombolysis and transcranial ultrasound imaging [317]. This paper presented the first dual-frequency array to use a unique design in which the low frequency array is positioned directly below the high frequency array within the transducer housing. Low and high frequency arrays were isolated by a frequency selective isolation layer (FSIL), an important design achievement. Dual-frequency transducers could also provide distinct advantages over single frequency transducers in acoustic radiation force impulse (ARFI) imaging which visualizes mechanical properties of tissue using a low frequency pushing pulse and high frequency tracking pulses [318]. Finally, Yen *et al.* have described several dual-layer 2D array transducers capable of performing 3D rectilinear imaging at 5 and 7.5 MHz at a reduced cost relative to conventional 2D arrays with high channel counts [319, 320]. Linear and 2D bilaminar arrays with frequency-selective layers could enable imaging of microbubble harmonics over a

large field of view with greater image uniformity than that currently afforded by fixed-focus transducers.

4.3 Conclusions

This chapter has discussed how specialized, dual-frequency transducers can be used to preferentially image contrast and microvessels because of the larger bandwidth afforded by designing two separate, non-overlapping frequency elements within a single transducer. Additionally, we have explained how commercial systems rely on multi-pulse contrast specific imaging strategies which are prone to motion-invoked image artifacts and how a dual-frequency superharmonic approach can correct for these errors. Finally, we described a series of research efforts that target both diagnostic and therapeutic advantages that can be employed when using dual-frequency transducers compared to conventional transducers with a single, narrowband frequency response. In the following chapter, we will describe how a prototype IVUS transducer was designed along with the feasibility of performing acoustic angiography with such a transducer.

CHAPTER 5

PROTOTYPE TRANSDUCER AND PRELIMINARY EVALUATION

In this chapter, we outline the design, fabrication, and characterization of a small aperture, dual-frequency, IVUS transducer which provides sufficient bandwidth separation for high CTR, high-resolution contrast enhanced IVUS imaging through superharmonic imaging. This prototype is evaluated *in vitro* to describe and determine if acoustic angiography can be performed on a platform that is deployable to intravascular sites of interest such as the coronary and femoral arteries.

5.1 Introduction

The *vasa vasorum* is a network of microvessels which supports larger vessels such as the aorta, and increased density of the *vasa vasorum* has been associated with a plaque advancing from a stable state to a rupture prone state [4, 68]. Additionally, intraplaque hemorrhage occurring from thin-walled, immature microvessels has been present in plaques in many cases of sudden coronary death [321]. Evidence suggests that *vasa vasorum* proliferation and associated angiogenesis and inflammation is associated with plaque instability and rupture [321-324]. As our ability to predict the instability of atherosclerotic lesions remains a substantial challenge,

---

JM authored the work with edits provided by KHM, PAD, and XJ. JM conducted 5.2.1 and 5.3.1. KHM conducted 5.2.2, 5.2.4, 5.3.2, and 5.3.4. Both JM and KHM conducted 5.2.3 and 5.3.3.

there is an unmet need for new imaging methods to identify, detect, and differentiate these pathologies [325].

Acoustic angiography takes advantage of exciting microbubbles near resonance and detecting their high-frequency, broadband harmonics with sufficient bandwidth separation to achieve both high resolution and high contrast to noise ratio (CNR) [292]. Previous research has indicated that acoustic angiography enables detailed visualization and analysis of microvascular structure [6, 292], and will likely be applicable to *vasa vasorum* imaging. Thus in this chapter, we hypothesize that there is a role for acoustic angiography in detecting vulnerable atherosclerotic lesions in regions not accessible with transcutaneous contrast enhanced ultrasound.

Feinstein has illustrated the potential of contrast enhanced transcutaneous ultrasound imaging on the carotid artery [35], if the target is the deeper coronary arteries transcutaneous ultrasound would not be a viable option. This may present an opportunity for IVUS, although commercial IVUS systems lack contrast enhanced imaging capability. This absence of technology may be due to the fact that nonlinear detection strategies for contrast imaging are most effective near the resonant frequency of microbubble contrast agents, which is typically between 1-10 MHz [326]. Thus, conventional contrast imaging strategies are not very effective with high frequency ultrasound (35-50 MHz) that is typically used with IVUS. To overcome this challenge, Goertz and collaborators have been evaluating both subharmonic and harmonic contrast IVUS imaging, with the goal of *vasa vasorum* imaging [55, 300]. Their research showed a CTR of 28 dB in subharmonic imaging with a fundamental frequency of 30 MHz [55] and 25 dB in second harmonic imaging with a fundamental frequency of 20 MHz [300].

Despite the promising CTR and vessel imaging capability of this imaging approach, there is a substantial challenge for "ultra broadband" contrast enhanced intravascular ultrasound (CE-IVUS), which is likely why it is yet relatively undeveloped. The primary limitation is the large frequency span, which is outside of the current bandwidth of commercially available single frequency transducers. Such difficulty could be surmounted by using multiple confocal transducers as described by Gessner [136], however dual-frequency transducers of the necessary frequency range do not yet exist in a form factor required for IVUS.

5.2 Materials and methods

5.2.1 Transducer design and fabrication

The dual-frequency transducer was designed as a dual layer transduction structure, composed of a low frequency transmitting layer and a high frequency receiving layer (Figure 5.1) [327]. The transmission layer was placed behind the receiving layer (with respect to a forward traveling sound wave) since low frequency transmitted acoustic waves could propagate through the smaller, high frequency element. The placement of the receiving layer has little interference on the transmission because of its small thickness (65 μm) compared with the transmitting wavelength (616 μm). The selection of 6.5 MHz as the transmitting layer's center frequency was chosen since it was both close to the contrast agents' resonant frequency and since the piezoelectric material for this element was readily available. The high frequency receiving layer was positioned in the front of the transducer to minimize the interference from the transmitting layer. A frequency selective isolation layer with a quarter wavelength of 30 MHz [317] was placed between the two piezoelectric layers to allow the low frequency transmitting wave to pass through, but the high frequency receiving wave to be reflected at the isolation interface. Transducer dimensions were optimized using a KLM model [328] to validate

the thickness of layers, length, and width of each component for ideal thickness mode excitation. Material properties and final optimized parameters for modeling and fabrication are summarized in Table 5.1. The aperture of the high frequency receiving layer was designed to be similar to that of commercial IVUS transducers [60], and thus significantly smaller than that of the transmission layer. The relatively large aperture of the low frequency component was designed to obtain reasonably low electrical impedance at low frequencies for higher acoustic pressure transmission. The modeling of the 30 MHz element considered the existence of the 6.5 MHz element at Side B (back side) as backing according to the structure of the design in Figure 5.1.

The design of the transducer used lead magnesium niobate-lead titanate (PMN-PT) instead of polyvinylidene fluoride (PVDF) for the receiving layer since the sensitivity could be higher due to the following [296]: (1) Compared to PVDF, PMN-PT has a much higher piezoelectric and electromechanical coupling coefficient and (2) the dielectric constant of PMN-PT is 400 ~ 600 times higher than that of PVDF, making it easier to match the electrical impedance to the receiving system.

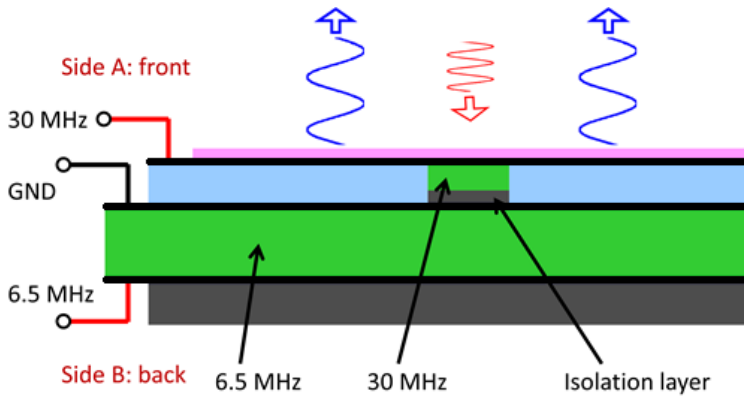

Figure 5.1: Design of the dual-frequency IVUS transducer.

Table 5.1: Fabrication parameters of the dual-frequency transducer.

Parameters	6.5 MHz layer	30 MHz layer
Active material	PMN-PT	PMN-PT
Thickness (μm)	300	65
Width (mm)	0.6	0.6
Length (mm)	3	0.5
Sound speed (m/s)	4004	4004
Impedance (MRayl)	32	32
Matching material	Al_2O_3/epoxy	Parylene
Thickness (μm)	80	15
Sound speed (m/s)	1600	2770
Impedance (MRayl)	4.32	3.16
Attenuation (dB/cm/MHz)	5.3	0.1
Backing material	Ag/epoxy	Ag/epoxy (isolation)
Thickness (μm)	200	15
Sound speed (m/s)	1900	1900
Impedance (MRayl)	5.15	5.15
Attenuation (dB/cm/MHz)	8	8

In the fabrication of the dual-frequency transducer, a 5 x 5 mm piezoelectric acoustic stack was first assembled and then diced into 0.6 mm wide slices as individual transducers. The assembly process started with a 5 x 5 mm PMN-PT plate which was lapped to 300 μm (f = 6.5 MHz) in thickness and then coated with Ti/Au (Ti: 10 nm and Au: 100 nm, E-Beam, Jefferson Hills, PA, USA) on both surfaces (Figure 5.2-1). A second piece of PMN-PT (0.5 x 5 x 0.3 mm) was then bonded on the first PMN-PT layer using conductive silver epoxy to form the high frequency receiving element and frequency selective isolation layer. Polystyrene microspheres (Polysciences Inc., Warrington, PA, USA) having a nominal diameter of 10 μm was added (about 1% in volume) to the silver epoxy so that the thickness of bonding layer was controlled to be 13 – 15 μm in order to function as a frequency selective isolation layer previously mentioned (Figure 5.2-2). After the silver epoxy cured, a composite layer of Al_2O_3 powder (1 μm grain size, Logitech Limited, Glasgow, UK) and Epo-tek 301 (Epoxy Technology Inc., Billerica, MA, USA) was mixed 1:1 by weight and centrifuged at 10000 RPM (5590 g) for 10 minutes (Microfuge Lite, Beckman Coulter Inc., Brea, CA, USA). The prepared composite was then cast

onto the front of the 5 x 5 mm PMN-PT layer beside the 0.5 mm width slice. A small margin (0.5 mm) at one edge was left as an electrical connection site for later wiring. After the Al_2O_3/epoxy composite cured, it was then lapped until the bonded composite layer was 80 µm thick, making the thickness of the top PMN-PT layer 65 µm (f_c = 30 MHz) on top of the 15 µm isolation layer (Figure 5.2-3). Another Ti/Au layer (Ti: 10 nm and Au: 100 nm) was then deposited onto the top surface to form the top electrodes. The final stack was then diced into 0.6 mm wide slices to form individual dual-frequency transducers (Figure 5.2-4). Each slice was bonded to the tip of a 20 gauge hypodermic needle (Fisher Scientific International Inc., Hampton, New Hampshire, USA) and then coated with a layer of parylene film (15 µm). The parylene film served two purposes: (1) to act as a matching layer of the 30 MHz element and (2) to provide electrical isolation in the form of a passivation layer for the entire transducer. Finally, the transducer was poled with a DC electrical field of 10 kV/cm for 15 minutes in silicone oil at room temperature.

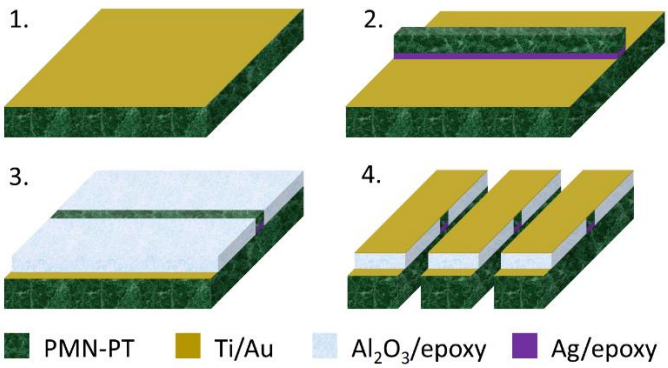

Figure 5.2: Fabrication process diagram of the dual-frequency transducer.

After the transducers were poled, electrical characteristics such as capacitance, loss, and input electrical impedance were characterized using an Agilent 4294A Precision Impedance Analyzer (Agilent Technologies, Inc., Santa Clara, CA, USA). Capacitance and loss were

measured at 1 kHz and the input electrical impedance was measured near the resonant frequency of each element, individually.

5.2.2 Acoustic characterization

The main design consideration for the low frequency (6.5 MHz) transmission element was to deliver adequate peak negative pressure (e.g. >1 MPa) in order to produce detectable nonlinear oscillations of microbubble contrast agents. The peak negative pressure of the small aperture transducer was measured using a calibrated needle hydrophone (HNA-0400, Onda Co., Sunnyvale, CA, USA) positioned axially at 3 mm away from the transducer. This distance was kept constant between pressure measurements and subsequent microbubble tests in order to estimate pressure levels applied to the contrast agents. The excitation pulse used was a sinusoidal burst (1-5 cycles) at 6.5 MHz generated by an arbitrary function generator (AFG3101, Tektronix Inc., Beaverton, OR, USA) and amplified by 55 dB with a radio frequency amplifier (Model 3200L, Electronic Navigation Industries Inc., Rochester, NY, USA). The amplitude of the transmission signal was adjusted from 50 to 350 mV_{pp} prior to amplification. Pressure output of the transducer was recorded using an in-house LabVIEW (National Instruments Co., Austin, TX, USA) data acquisition system.

While the main design criteria for transmission was pressure output, the receive element design optimized both reception sensitivity and bandwidth which is critical to detect the broadband, nonlinear microbubble signal. Pulse-echo tests were performed to measure the bandwidth of the transducer. A steel block with flat surface was positioned 3 mm in front of the transducer as the target. A pulser/receiver (5900PR, Panametrics Inc., Waltham, MA, USA) was used to interrogate the target in pulse echo mode with minimal energy. The reflected signal was high-pass filtered (f_{corner} = 3 MHz) by the pulser/receiver and then recorded using a digital

oscilloscope (DSO7104B, Agilent Technologies Inc., Santa Clara, CA, USA). Loop sensitivity was measured with a similar setup, but the excitation signal was replaced by a 10-cycle sinusoidal burst.

5.2.3 Contrast detection by the transducer

To validate the contrast response of the transducer, microbubbles were excited by the low frequency element and the nonlinear responses from microbubbles were detected using the high frequency element. Relative positions of the transducer and the tube were carefully adjusted in a water bath using a 3-axis precision rectilinear stage. In the alignment process, an acoustically transparent 200 µm diameter micro-tube was filled with air to provide a strong echo to indicate alignment in the lateral dimension of the 30 MHz element. Time of arrival of the echo was used to calculate the distance between the transducer and the tube in order to position it axially 3 mm away from the transducer. Polydisperse lipid shelled microbubbles (Figure 5.3) were formulated as described previously [97] and pumped through the aligned micro-tube at a concentration of 4.8×10^8 MBs/mL at a velocity between 1.8-4.4 cm/s to maximize the signal response. The tube was slightly angled (~10°) with respect to the front surface of the transducer to reduce specular reflections from the wall of the tube.

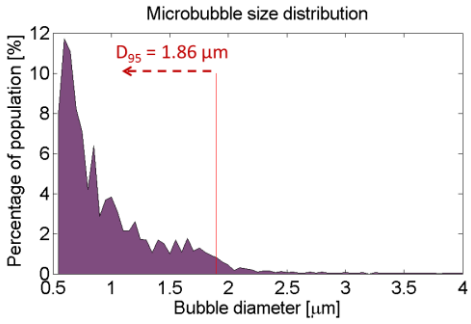

Figure 5.3: Microbubble number weighted size distribution measured between 0.5-10 µm.

Once the transducer was aligned and positioned for the contrast imaging, the excitation pulse sequence was adjusted for optimal imaging quality. A sinusoidal burst was used to excite the transmitting element with pulse lengths between 1 to 5 cycles and voltage variations from 50 to 350 mV_{pp} in 50 mV_{pp} increments. For each combination of testing parameters, 100 A-lines of microbubble echoes were received and recorded by the high frequency element for offline analysis. The contrast imaging data was evaluated using both time domain amplitude analysis and short-time Fourier transform.

5.2.4 Imaging with the transducer

Fundamental imaging at 30 MHz and dual-frequency super-harmonic contrast imaging were tested with the transducer in tissue-mimicking phantoms immersed in water (Figure 5.4). Typical phantoms had a speed-of-sound similar to tissue (1496 m/s), relatively high attenuation (0.9 dB/cm at 3 MHz), and had fully developed speckle. A hole was drilled through the phantom by a thin wall steel tube (5.5 mm OD, 0.4 mm wall thickness) to simulate a vessel. After drilling, the dual-frequency probe was placed in the center of the lumen and rotated to make an IVUS image. The rotation was controlled using a microcontroller that stepped the transducer at 0.9° angular increments for one revolution and provided a trigger for the excitation pulse. An acoustically transparent tube with 200 µm diameter was placed through the phantom, running parallel to the channel. Diluted microbubbles were pumped through the tube (4.4 cm/s) while imaging. A 0.6 mm diameter steel rod was placed in the phantom opposite of the microbubble tube to provide a strong reflection target for comparison. Both the microbubble tube and the steel rod were embedded at ~ 4 mm radially in the phantom to test if the system could detect contrast in a scattering and attenuating medium, which is typical of tissue.

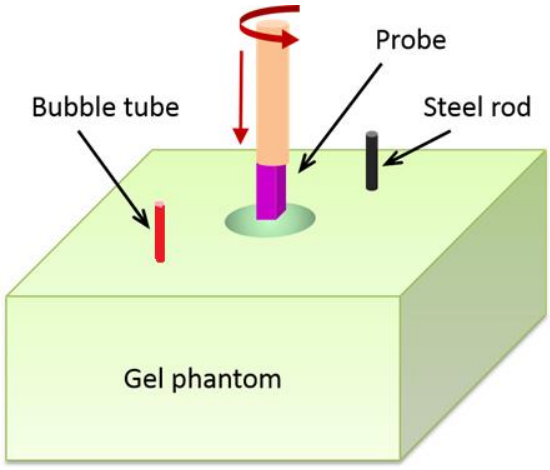

Figure 5.4: Experimental setup for imaging.

For fundamental imaging, both acoustic excitation and signal reception were performed using the 30 MHz element. A pulser/receiver supplied the transducer with a 1 µJ excitation pulse at every step and the reflected signal was recorded by the LabVIEW data acquisition system described previously. For super-harmonic imaging, a 2-cycle sinusoidal burst was amplified by the 3200L RF amplifier to excite the 6.5 MHz transducer while the 30 MHz element was used for receiving. The data was digitally band pass filtered with a frequency window of 25 MHz to 35 MHz corresponding to the receive element's bandwidth. The acquired A-lines were then envelope detected and scan converted to an IVUS image where the contrast to tissue ratio was measured by using regions of interest to calculate the mean signal strength.

5.3 Results and discussion

The dual-frequency transducer prototype was housed on the tip of a 20 gauge hypodermic needle (Figure 5.5). The back surface (Side B in Figure 5.1) of the transducer was bonded to the needle with conductive epoxy, allowing the needle to function as an electrical lead to the back side of the 6.5 MHz transducer. Co-axial wires (25 gauge) were attached to the top electrode and common electrode between the two PMN-PT layers and then threaded through the needle.

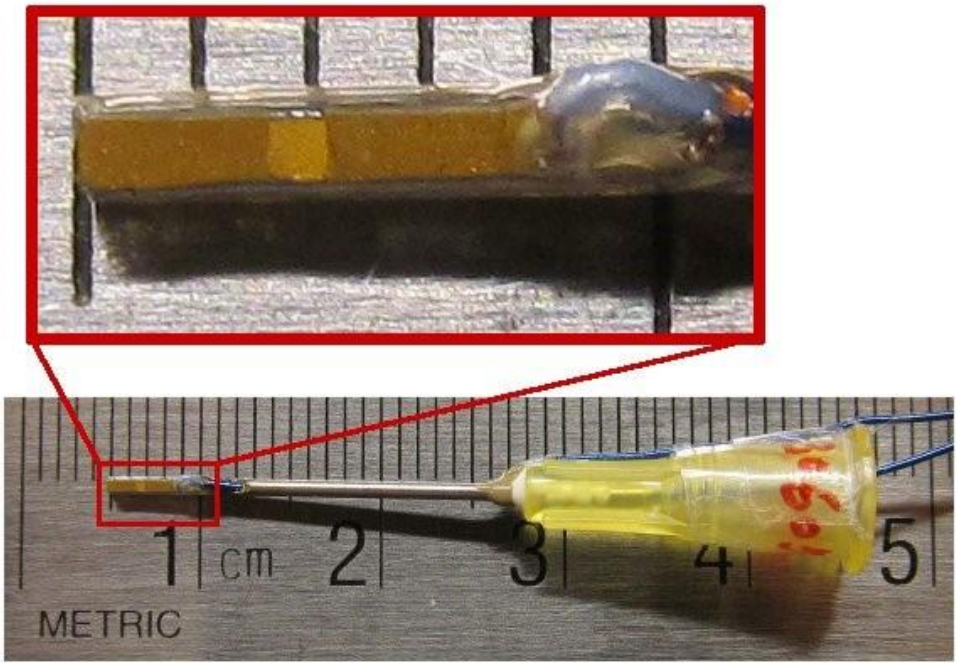

Figure 5.5: Prototype transducer housed on the tip of a 20 gauge hypodermic needle.

5.3.1 Electrical characterization

The capacitance and loss at 1 kHz (measured with an Agilent 4294A Precision Impedance Analyzer) showed good agreement to predicted values. Capacitance values of the transducers were 344 pF for the 6.5 MHz transmission element and 131 pF (including a 2 pF parasitic capacitance from Al_2O_3/epoxy layer) for the 30 MHz receiving element. This data was in agreement with theoretical calculations using a relative dielectric constant of 4000 (HC Materials, Inc.). Loss of the transducer was 1.1% for transmission and 2.7% for reception, similar to the properties of PMN-32%PT.

The measured input electrical impedance at the resonant frequency (Figure 5.6b, d) matched well with the results of the KLM modeling (Figure 5.6a, c). In order to obtain a strong resonance for high pressure output in the transmission element, the backing layer of the transmission element was designed with reasonable absorption for compromise of achieving

sufficient pressure output while minimizing ringing. In both the modeling and measured results, a strong resonance occurred at 6.5 MHz (Figure 5.6a, b). The center frequency of the receiving element was designed to be 30 MHz (Figure 5.6c, d) and the measured results agreed well with simulations.

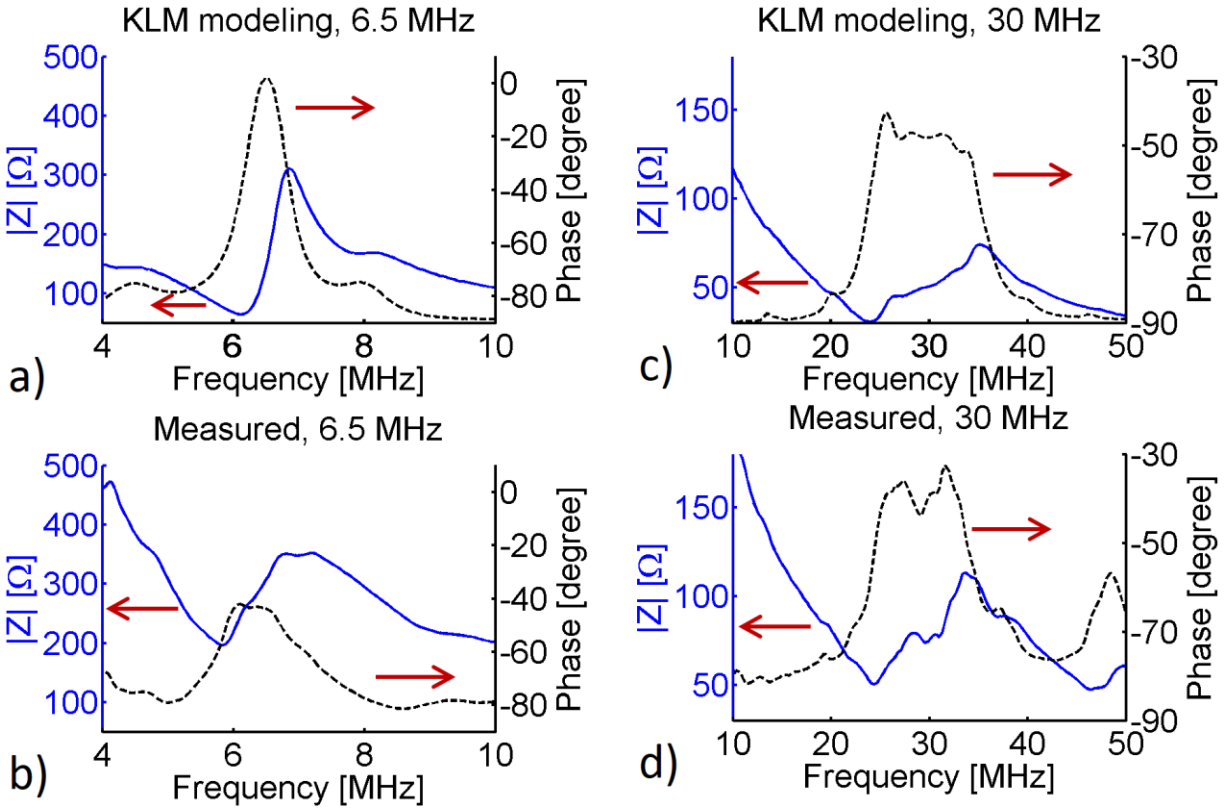

Figure 5.6: Electrical impedance measurements of prototype transducer. a), b) 6.5 MHz element and c), d) 30 MHz from a), c) KLM modeling and b), d) measurement from impedance analyzer.

5.3.2 Acoustic characterization

The peak negative pressure of the 6.5 MHz element was recorded with different excitation voltages. Measurements were recorded at the contrast imaging area in order to verify that this would be the pressure applied in the region of the microbubbles. As shown in Figure 5.7, the response of the low frequency transducer was nearly linear at excitation voltages lower

than 70 V, having an average transmitting sensitivity of 14.5 kPa/V. Nonlinearities showed up when the input was higher than 70 V. At about 100 V, more than 1.2 MPa rarefractional pressure (MI: 0.48) was generated, which was sufficient to produce a high-frequency, broadband response from microbubbles imaged in tissue in prior studies [6, 292].

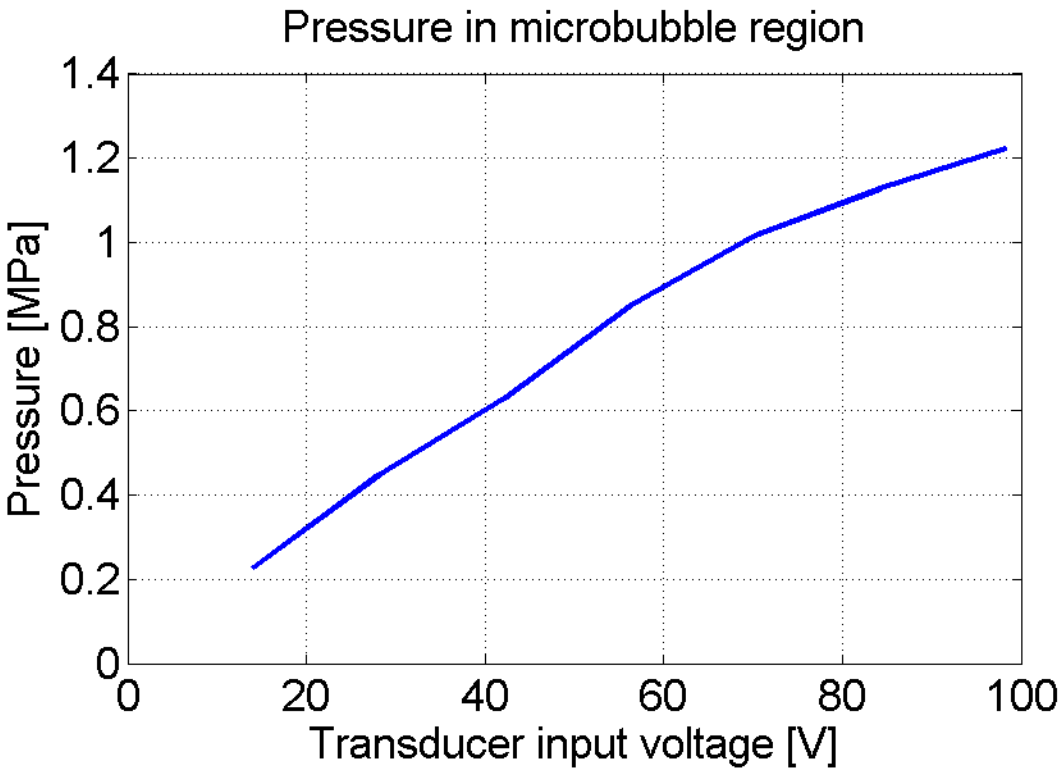

Figure 5.7: Peak rarefractional pressure by the transmission element. Pressure at the contrast imaging area, 3 mm away from the center of the transducer, using a 5-cycle burst excitation on the low frequency (6.5 MHz) element at varied voltages.

Pulse-echo experiments illustrated the broad bandwidth of the receiving element (Figure 5.8b). The pulse length of the echo signal was about 80 ns (at -20 dB), corresponding to an axial resolution of 60 μm in tissue, which means that the high frequency transducer can be used in pulse-echo mode for high resolution fundamental imaging. The -6 dB fractional bandwidth of the receiving element was measured to be 58.6%, covering a frequency span of 20 – 38 MHz,

providing good reception of the high-frequency, broadband microbubble response. Because of the frequency selective isolation layer, the high frequency element behaves as if there was little backing for it. As such, the bandwidth predicted by the modeling result was broad (Figure 5.8a) and is seen in the measured bandwidth (Figure 5.8b). Burst excitation showed that the loop sensitivity of the receiving element relative to the transmitting element was -38.3 dB.

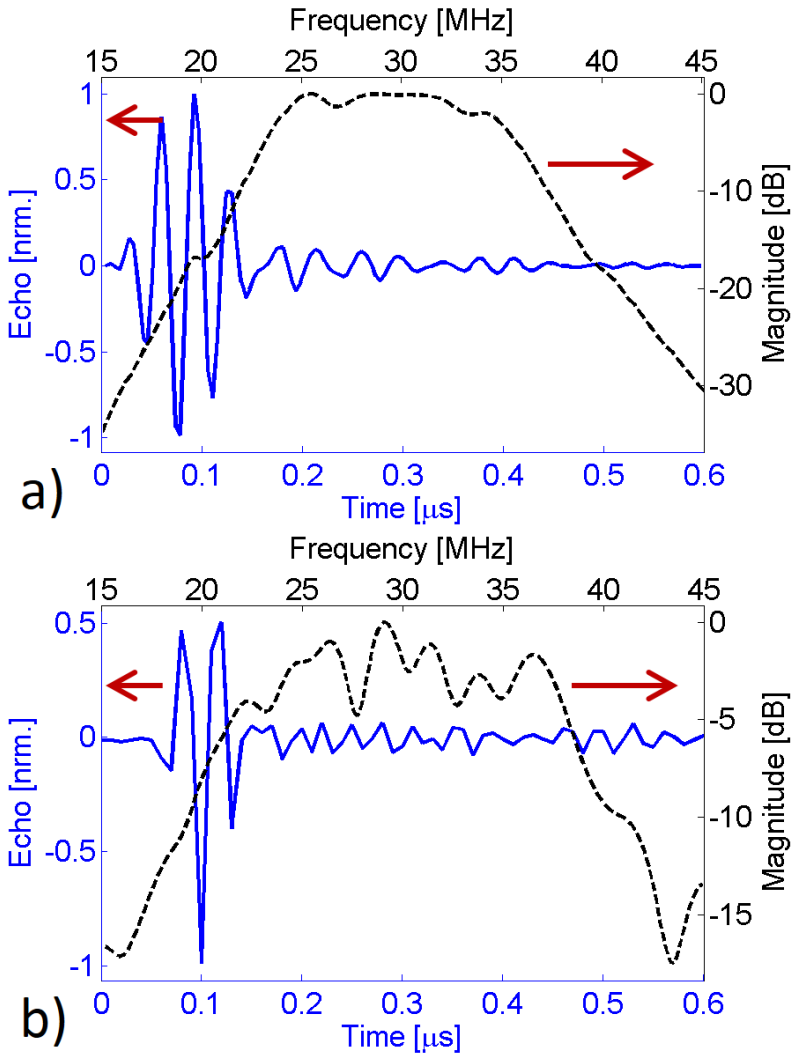

Figure 5.8: Pulse-echo response and its FFT spectrum of 30 MHz element in a) modeling and b) measurement.

The transmit frequency spectrum was measured by hydrophone using a 2-cycle burst excitation, and the receive bandwidth was measured from the pulse-echo experiment driven with a 1 µJ impulse. The -20 dB frequency response of the transmit element was 4.0 – 8.9 MHz. The frequency response of the transmitting and receiving elements were well separated (>5 MHz at -20 dB) (Figure 5.9), which is ideal for detecting microbubble broadband frequency content and achieving high contrast to tissue ratios.

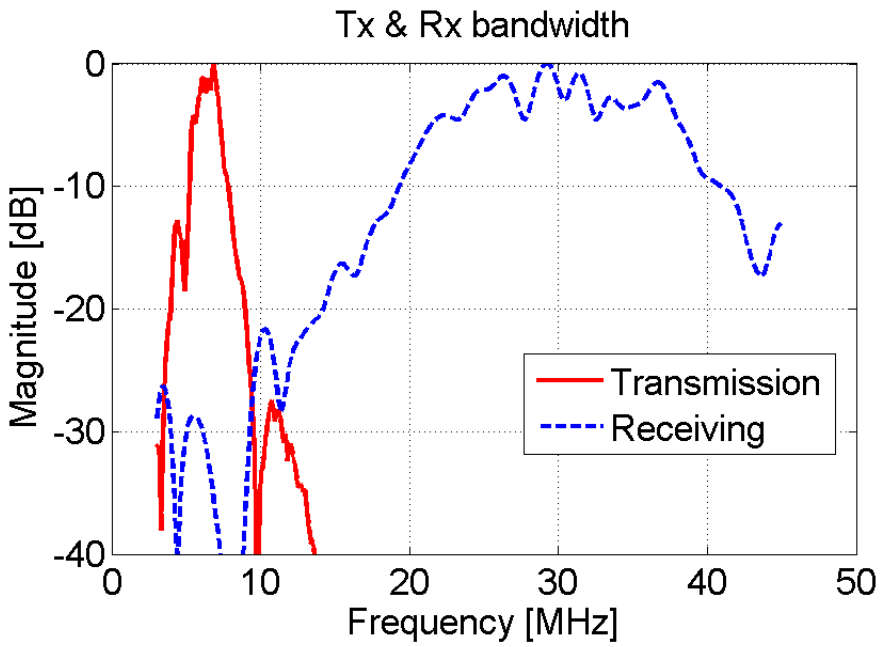

Figure 5.9: Transmission (2-cycle burst) and receiving (pulse-echo) bandwidth separation.

5.3.3 Contrast detection by the transducer

Microbubble response was clearly detected with the dual-frequency transducer. In the time domain amplitude analysis, a root-mean-square (RMS) value through the 100 lines of data was taken as the amplitude of the microbubble response. The received data was first high pass filtered at 10 MHz to thoroughly remove residual tissue/phantom responses at the fundamental or low harmonic frequencies. Residual stationary signals from the tube wall were filtered using a

clutter filter, leaving only the transient high frequency signal from microbubbles. RMS values of the microbubble response with different excitations were shown in Figure 5.10. As shown in the figure, the background noise was about 0.5 mV, the source of which primarily comes from the noise of the amplifier. With 1-cycle burst excitation, the peak negative pressure was low (PNP < 0.65 MPa) at all voltage inputs (14 V – 98 V), resulting in low (6 dB) SNR (Figure 5.10a). With 2 or more cycles in each burst, microbubble response could be more than 1.5 mV at 70 V excitation (PNP ≥ 0.8 MPa), and the SNR was larger than 10 dB (Figure 5.10b and c). Because of the small Q-factor of the receiving element, each negative peak of the transmission wave was clearly discernible temporally (Figure 5.10c). At 2 or more cycles in each burst, 42 V input excitation was high enough to excite the nonlinear microbubble response (however, at a low SNR of 4 dB), corresponding to a rarefractional pressure of 0.65 MPa. The microbubble response was just slightly higher at 98 V input compared to 70 V input, and we hypothesize that increasing the pressure too high may decrease the CTR due to increased nonlinear response in tissue. No signal was detected at low level voltage excitation (14 V) and the response was always within the noise. In summary, the SNR increased rapidly with increasing driving voltage and then leveled off (e.g. < 70 V). If the input voltage was higher than 70 V, the signal increase of the microbubble response was less significant. Gessner *et al.* also observed a similar plateau for nonlinear microbubble response as a function of pressure when excited at 2 MHz [136]. The excitation voltage may be further optimized for *in vivo* conditions.

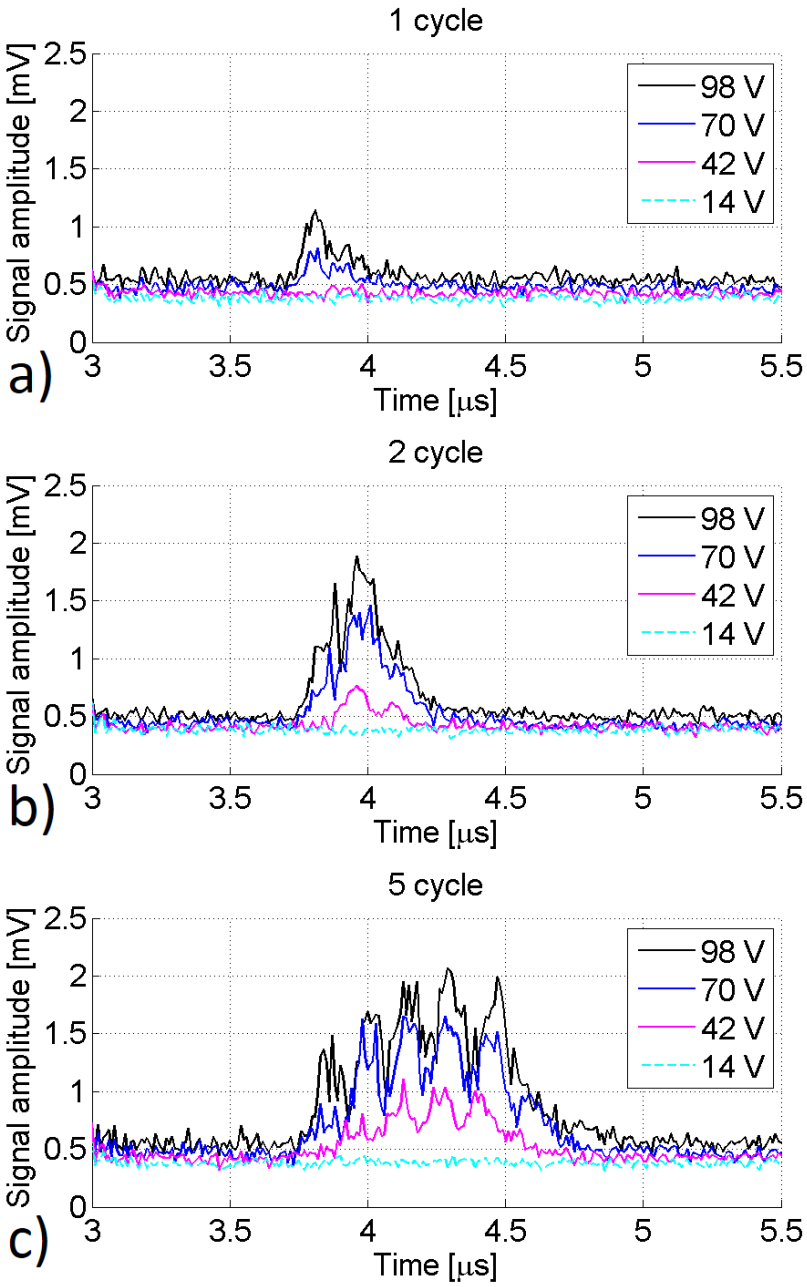

Figure 5.10: Amplitude of nonlinear microbubble response with sinusoidal bursts of a) 1-cycle, b) 2-cycle and c) 5-cycles at different voltage excitations.

The spectra of the received signals were analyzed to investigate the microbubble response in frequency space. Spectra of all the 100 measurements were calculated using the short-time Fourier transform and the spectrum for a given test condition was analyzed. As shown in Figure

5.11, frequencies lower than 20 MHz were intrinsically suppressed by the transducer's receiving sensitivity so low frequency harmonics of the fundamental do not greatly contribute to the image formation in dual-frequency imaging. Input voltage was kept at 70 V while number of cycles in the burst varied (Figure 5.11). Fewer number of cycles produced higher axial resolution, however, a 1-cycle burst suffered from low SNR because the peak negative pressure was too low to induce sufficient microbubble harmonics. With a 2-cycle burst at 70 V input, microbubble response was detected while minimizing loss of axial resolution (about 200 µm). The frequency content of the noise was less than -12 dB relative to the peak frequency content of the microbubble signal (Figure 5.11b).

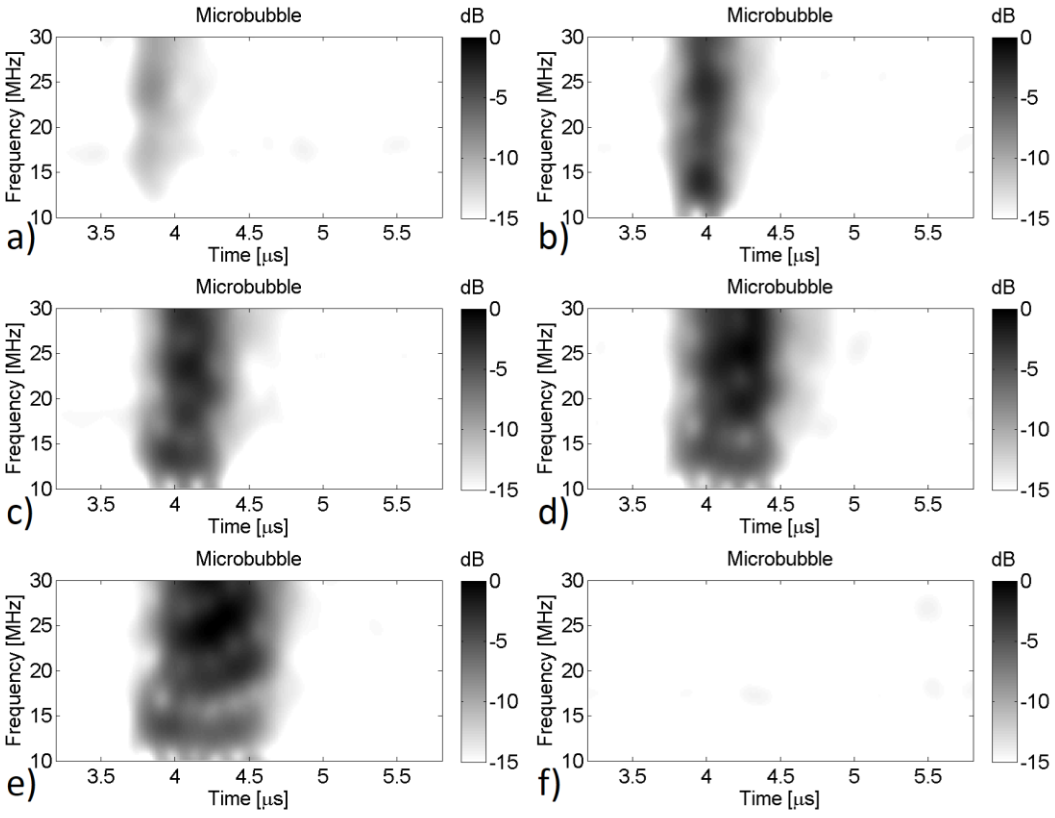

Figure 5.11: Spectrogram of microbubble responses at 70 V with a burst of a) 1-cycle, b) 2-cycles, c) 3-cycles, d) 4-cycles, e) 5-cycles. The spectrum of a water filled tube at 70 V with a burst of f) 5-cycles shown for comparison.

The presence of the microbubble signal was verified by rinsing the tube with pure water. The high frequency response observed when imaging microbubbles vanished when the microbubbles were cleared (Figure 5.11f).

5.3.4 Imaging with the transducer

5.3.4.1 Fundamental imaging at 30 MHz

Fundamental imaging mode was performed using the 30 MHz element in pulse-echo mode. An impulse with 1 µJ energy was used to produce acoustic waves and the reflected signal was recorded by a LabVIEW data acquisition system at 100 MHz sampling rate. The wave package was detected and the magnitude was scan converted to polar system as shown in Figure 5.12. In fundamental imaging mode, the reflection from the 0.6 mm steel rod was nearly 20 dB stronger than that from the 200 micron tube containing microbubbles.

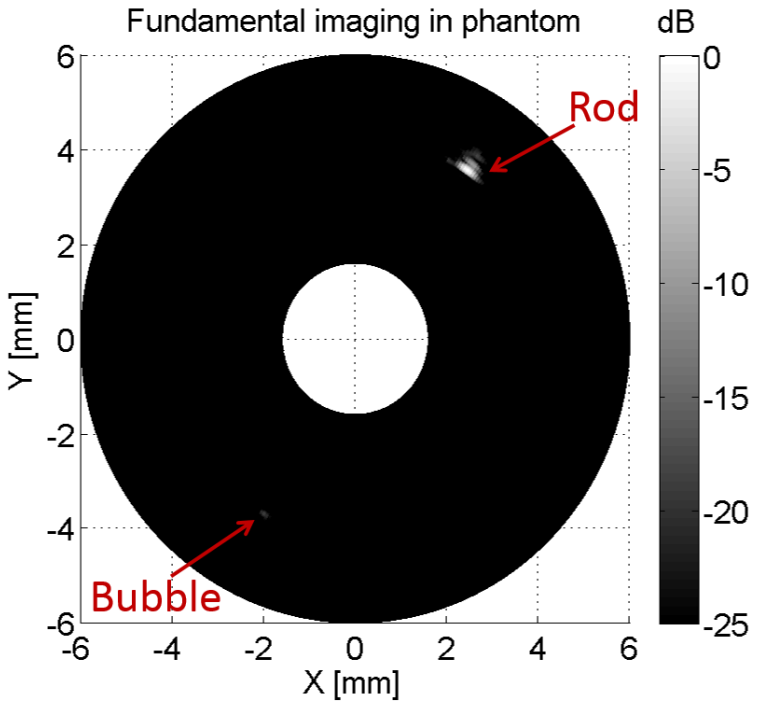

Figure 5.12: Fundamental imaging at 30 MHz.

5.3.4.2 Super-harmonic imaging

In the dual-frequency imaging mode, microbubbles were excited using the low frequency element and backscatter was received using the 30 MHz element. The transmission input was a 6.5 MHz 2-cycle sinusoidal burst at 84 V. The received signal was high pass filtered at 10 MHz before being digitized.

The data was filtered digitally and reconstructed to create an image offline in MATLAB. First, each line in the scan was band pass filtered with a 60^{th} order finite impulse response filter with corner frequencies of 25 and 35 MHz, which is also the sensitivity range of the transducer. The frequency content in this bandwidth covers the majority of the 4^{th} and 5^{th} harmonics of the transmission frequency. After filtering, the wave package was detected from the signal and the magnitude was scan converted to polar coordinate as shown in Figure 5.13.

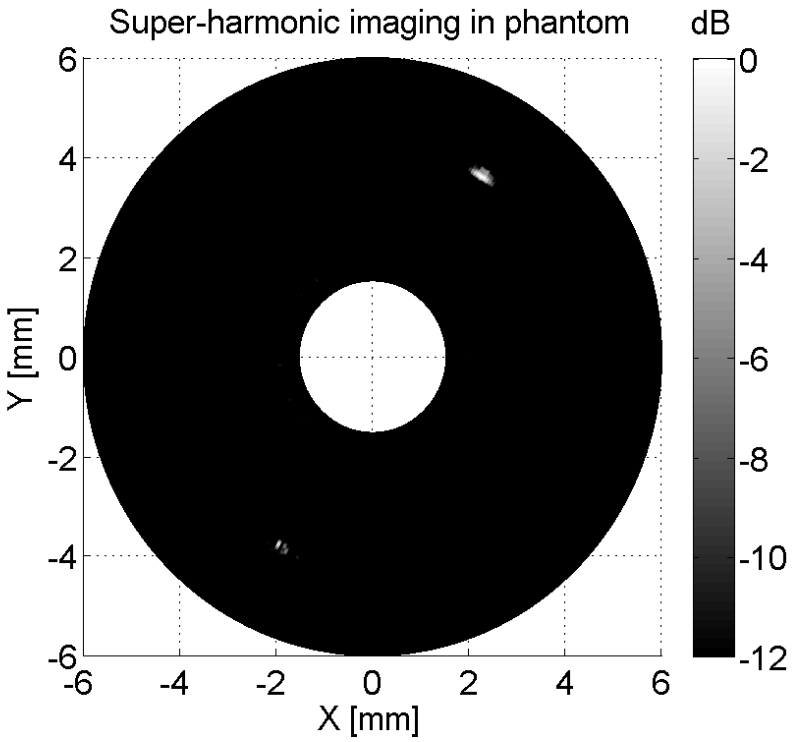

Figure 5.13: Super-harmonic imaging of the microbubble tube and a steel rod.

The microbubble filled tube was clearly detected and had a CTR of 12 dB. There was some nonlinear response on the rod signified by its presence in the image even after filtering, but the signal magnitude was strongly decreased in comparison to the fundamental mode image. In dual-frequency imaging, the microbubble response was almost the same magnitude as the reflection from the steel rod. Both axial and lateral resolutions were high enough to clearly resolve the 200 μm microbubble tube. The diameter of the steel rod can also be clearly visualized to be 0.6 mm in lateral direction but not easily seen in the axial direction. Because the sound speed in steel is about 4 times of that in water, the reflection from the back surface of the steel rod seems very close to the reflection from the front surface, introducing a high distortion in the axial resolution on the rod.

5.4 Conclusion

In this chapter, a dual-frequency IVUS transducer was designed, fabricated and characterized, and its contrast imaging and fundamental imaging capability were evaluated. The measured transducer performance matched the modeling results very well for both transmission and receiving components.

In the transducer design, two key features were proposed. First, the aperture of the receiving element was significantly smaller than the transmission element, enabling matched electrical impedance of both elements and matched acoustic impedance on transmit for increased acoustic deposition in the imaging field of view. Second, the isolation layer placed intermediately between the two active layers enabled the low frequency transmit wave to pass through the isolation interface, but the high frequency receive wave to be reflected which aided in decoupling signal content. Thickness control of the isolation layer was controlled by mixing a 1% microsphere (10 μm diameter) solution into the silver epoxy. The addition of the

microspheres had little effect on the acoustic or electrical properties of the silver epoxy. Finally, a layer of parylene coating acted both as shielding and as the matching layer of the high frequency receiver. Such design and fabrication processes were demonstrated successful in prototyping dual-frequency transducers for both fundamental mode imaging and CSI.

The feasibility of ultra-broadband contrast enhanced intravascular ultrasound imaging was evaluated *in vitro*, using a unique prototype dual-frequency small aperture transducer (T6.5/R30). Peak negative pressures higher than 1.2 MPa were generated at 3 mm away axially from the low frequency element (0.6 x 3 mm) of the transducer, which proved sufficient for contrast imaging. Sensitivity of the receiving element (0.6 x 0.5 mm) provided the capability to detect and record the broadband high-frequency response of microbubbles. Initial imaging of a 200 μm tube filled with microbubbles showed reasonably high SNR (> 12 dB). The small aperture dual-frequency transducer design presented demonstrates the first of its kind for contrast enhanced high-frequency ultra-broadband intravascular imaging.

Both fundamental mode and dual-frequency super-harmonic imaging were tested *in vitro* using a tissue mimicking gelatin based phantom. The 30 MHz pulse-echo fundamental imaging showed a very high SNR (>25 dB) with reasonable resolution (200 μm). While microbubble backscatter was very weak in the fundamental mode, dual-frequency super-harmonic imaging generated high CTR (12 dB) and good resolution (200 μm) in resolving the microbubble tube and the steel rod. The steel rod used in the experiments was an extremely exaggerated target with a reflection coefficient of 0.94 in water, thus the strength of the echo was large enough that weak high frequency components of transmission were detectable. Due to the viscoelastic behavior of tissue, we could not detect tissue harmonics in the high-frequency bandwidth at the transmission acoustic pressure levels (MI < 0.48 at 6.5 MHz) used in these experiments. Visualizing contrast

agents with high specificity is necessary for microbubble imaging strategies involved with both molecular imaging and *vasa vasorum* localization. Small aperture transducers with high CTR and high resolution capable of detecting contrast agents would promote the transition of advance contrast imaging methods to intravascular ultrasound applications.

While these results are promising, there are still improvements to be made in the near future. The noise level in the measurements was high (0.5 mV), resulting in a SNR lower than 20 dB in super-harmonic imaging. This noise may have come from several different sources such as the transducer, cabling, or the amplifier. It is anticipated that further isolating the power amplifier used in the transmission circuitry when receiving will likely decrease the noise level and improve the CTR and SNR. Digital signal processing methods, such as wavelet denoising, could also be employed to remove the broadband white noise from the amplifier efficiently. Additionally, it is believed that further improvement can be made by exploring other piezoelectric composites (PMN-PT 1-3) that have been considered previously for intravascular applications [329]. Due to its low acoustic impedance and high electromechanical coupling coefficient, PMN-PT 1-3 transducers generally have a broader frequency bandwidth and a higher receive sensitivity.

In conclusion, the small aperture dual-frequency IVUS transducer presented in this chapter can perform acoustic angiography in an IVUS form factor to detect microvascular flow in a phantom. Our next chapter will focus on hardware that may improve the noise characteristics of this system to improve the SNR from the higher order harmonics.

CHAPTER 6

APPLICATIONS AND EMBEDDED SYSTEM DESIGN

Intravascular ultrasound transducers use higher frequencies (20+ MHz) in commercial applications than transcutaneous transducers. Higher frequencies are desirable in IVUS because smaller wavelengths increase the image resolution and the ability to resolve fine features valuable to clinicians, such as the intima-media thickness. As a consequence to using higher frequencies, the hardware comprising the electrical connectivity, filtering, transmission, and acquisition circuits must adhere to a stricter tolerance in order to prevent noise from accumulating in the images. Furthermore, acoustic angiography requires a specialized transducer to detect superharmonics and these transducers should be operated using specialized hardware. High frequency ultrasound is sensitive to noise and requires the application of transmission line theory (impedance matching, shielding, and properly grounding your equipment among other requirements) in order to prevent noise from contaminating the imaging equipment.

As a result of our preliminary evaluation of our dual-frequency prototype IVUS transducer in Chapter 5, we were able to identify that the SNR could be improved further by

---

YL authored the work and was heavily edited by KHM and JM with additional edits by coauthors. YL designed and lead the PCB fabrication and characterization studies and additionally collected *ex vivo* data. JM provided the dual-frequency transducer and assisted with pulser characterization and imaging collection. KHM produced phantoms, provided MCAs, wrote background material, performed *in vitro* image collection, and wrote image processing code.

reducing system noise. Designing and fabricating the appropriate electrical driving and receiving equipment using a printed circuit board would not only reduce the noise, but would also facilitate the use of the device and reduce the amount of physical space needed to operate it. This chapter will present the results of using an embedded system design that is specifically tailored for use with wide-bandwidth, dual-frequency IVUS transducers and how this affects the image quality of the system.

6.1 Introduction

Contrast-enhanced ultrasound is a method of visualizing weakly scattering structures such as blood by perfusing the space with micron-sized contrast agents such as lipid encapsulated microbubbles [236]. By rejecting frequency bands occupied by tissue reflection, the backscatter from tissue can be largely suppressed while retaining the higher-order nonlinear superharmonics from MCAs (> 3rd order). Acoustic angiography using only superharmonics (> 3rd order) to form images has been studied using specialized transducers having widely separated center frequencies. It has been characterized with high sensitivity to contrast agents as well as great resolution of vasculature *in vivo*, and shows promise for *vasa vasorum* and other microvascular structure detection [292, 293].

Higher-order superharmonic CSI (for simplicity: referred to as superharmonic imaging) is only feasible with transducers designed to cover large bandwidths. Dual-element, dual-frequency transducers are uniquely qualified to satisfy this requirement and are used in this imaging approach, because of the difficulty in making a single transducer having a fractional bandwidth to accommodate 4th or higher-order harmonics ($f_{BW\text{-}6dB}$ = 120%) [330]. Previous IVUS transducers used a low-frequency (6 MHz) element for transmission and a high frequency (35 MHz) element for reception. In order to produce detectable nonlinear signals from MCAs,

adequate peak negative pressure needs to be delivered at the focus of the receiving element. Since the transmission efficiency between transducers will likely vary, a robust imaging system should be equipped with a transmit pulser capable of transmitting pulses with varying pulse length and voltage amplitude. In addition to supporting CSI, the proposed hardware should be able to collect traditional B-mode images using the high frequency element in order to provide anatomical reference. Previous experiments collected images using an external power amplifier and function generator for producing the excitatory signal, which adds to the cost and complexity of the approach [330]. Currently, there are no imaging systems capable of accommodating the unique design requirements imposed by this method of superharmonic imaging.

In order to facilitate translation of superharmonic imaging to pre-clinical and clinical applications, an integrated imaging system capable of operating these dual-frequency transducers would be greatly beneficial. A few research imaging systems have been developed for high frequency IVUS or dual-channel application [331-333], however, none of the lab-made or commercial imaging systems were designed to cater to superharmonic imaging and lack some system level design components that would greatly benefit this imaging approach. The development of a dual-channel transmit/receive system for superharmonic imaging is reported in this chapter. The system employs a field-programmable gate array (FPGA) as the central processing unit, making it reprogrammable in order to configure for multiple functions. The system is capable of doing user-defined pulse/burst generation, data acquisition, signal processing and PCIe signal communication. The layout of the imaging system is small and fits on a single 16 x 20 cm PCB, making it portable and convenient for pre-clinical studies.

6.2 Methodology

6.2.1 Design considerations

To obtain superharmonic and B-mode imaging, two identical and interchangeable transmit/receive channels were included for use with dual-frequency IVUS transducers. For superharmonic imaging, a low frequency element was used to transmit the excitation pulse while a high frequency element was used to receive the echoes. For B-mode imaging, only the high frequency channel was used for both transmit and receive.

On the receiving side, low distortion, low noise amplifiers were used to improve the dynamic range and suppress baseline noise with a target SNR of 50 dB. Variable gain was implemented since the amplitude of superharmonic signals can vary depending upon receive element sensitivity. The designed bandwidth of the receiving channel was from 1 to 60 MHz, which covered the fundamental (6 MHz) to the 10^{th} harmonic. The electrical impedance of the receiving channel was matched to 50 Ω at the transducer connection in order to efficiently operate the high frequency element of dual-frequency transducers based on their measured impedance spectra (Figure 5.6).

When operating in pulse-echo mode for B-mode imaging, the transmitter was designed to provide a broadband pulse with an adjustable center frequency (e.g. 35 MHz). However, when operating in superharmonic mode, the transmit pulser should also be able to generate a 1-2 cycle burst at a much lower center frequency in order properly excite the transmitting element for acoustic angiography [291]. Considering there will be variance among transducer transmission efficiencies, the pulser was designed to output high voltages that may be adjusted to control output acoustic pressures necessary to optimize superharmonic imaging.

The block diagram of the integrated dual-frequency dual-channel imaging system is shown in Figure 6.1A. The system was controlled by a FPGA. Bipolar pulses or single frequency bursts (aka, pulse trains) could be generated by the FPGA, which then could be passed to the pulser. A digital transmit/receive switch controlled the system to work in either DF-mode or B-mode for either acoustic angiography or anatomical imaging, respectively. After being amplified and filtered by the analog receiving circuit, the returned echo was digitized by a 12-bit 210 MHz ADC. Separate AC/DC power supplies were used to provide the analog and digital working voltages (1 V, 2.5 V, 3.3 V and 5 V), as well as the pulse generator voltage (up to 200 V_{pp}). General purpose I/O pins were include to provide timing control in order for external triggers to control synchronous activities such as firing at precise motor positions. The system communicated to the PC through a PCIe digital I/O card. A summary of the important device parameters are listed in Table 6.1.

Table 6.1: Devices used in the proposed system.

Function Block	Device	Parameters	Manufacture Specification
Pulse Generator	TC6320 MOSFET Pair	Max Voltage	200 Vpp
		Rise/Falling Time	15 ns
Amplifier	AD8331 Low-noise Amplifier	Gain	-4.5 to 55 dB
		-6dB Bandwidth	100 MHz
ADC	AD9230-210	Sampling	210 MHz
		Resolution	12 bits
		Input Range	1.25 V
FPGA	Virtex-6 XC6VLX75T	Number of I/Os	240
		Number of Logic Slices	11640
Data Transfer	PCIe Digital I/O Card PXIe6537B	Sampling Rate	50 MSPS
		Bus Width	40 bits/Sample
DC-DC Converter	LT3083, LT3633	Total Power	3 W,12 V

The system was fabricated on a small-form-factor 6-layer printed circuit board (16 x 20 cm, 400 g), depicted in Figure 6.1B. SMA connectors were used for transducer connectivity.

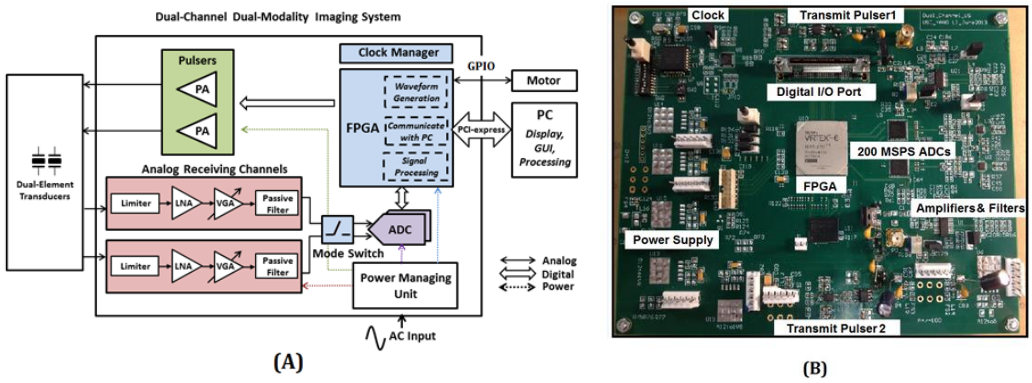

Figure 6.1: Embedded system flow chart and photograph. (A) Block diagram of the integrated dual-frequency superharmonic imaging system. Different color shows different power domain: blue: digital supply; green: high voltage for pulser; red, analog supply; purple, low-noise analog DC supply for ADCs. (B) Photograph of the system

6.2.2 Specific design consideration

6.2.2.1 FPGA logic

A Virtex-6 FPGA served as the central controller of the proposed system, working at 200 MHz clock rate. It received commands from the PC, controlled the pulse generator waveform and transmitted the data to the PC for display and further processing. The PC communicated to the FPGA through a PCIe 40-channel digital I/O card, with 50 MHz clock rate, which could be programmed using Labview software (National Instrument, Austin, TX).

The digital logic diagram of the FPGA is shown in Figure 6.2A. To collect one frame of data, an Acq_Start signal was sent to the FPGA from the PC through the digital I/O. Major user-defined control signals are summarized in Table 6.2.

Figure 6.2B shows the timing diagram of image acquisition. At the rising edge of signal Pulse_Trigger, digital pulse/pulse-train were sent out through one pair of differential signal pins

on the FPGA, which were then amplified by the pulse generator to get enough excitation voltage. We used single pulse excitation for B-mode imaging and multi-cycle burst for superharmonic imaging, which were generated inside FPGA in the form of a differential digital wave. The digital pulse was then given to the transmit pulser. After echo signal was received, optional processing such as finite impulse response filtering, envelope detection was implemented on-board. Raw/processed data was stored into a first-in-first-out (FIFO) buffer. Once full, a FULL bit was generated, acknowledged the digital I/O card for data transferring of a line of data. A Labview graphical user interface (GUI) was developed for control and data acquisition.

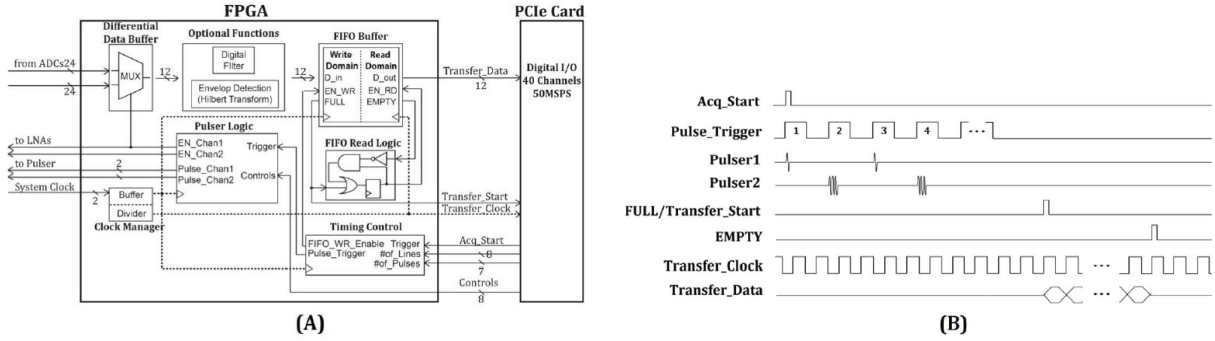

Figure 6.2: Programming block diagrams and timing charts. (A) FPGA logic block diagrams. The dashed lines show the clock signal. (B) Logic timing of one frame data acquisition. Pulse numbers 1 and 3 are bipolar pulses for B-mode imaging; Pulse numbers 2 and 4 are multi-cycle pulse-trains for superharmonics imaging.

6.2.2.2 Analog receiver design

The signal from each element was passed into an individual analog receiving channel. To protect the receiver circuit, the signal first went through a custom passive limiter, which shunted high amplitude transmit pulses to ground in order to prevent overvoltage [334]. To provide enough gain for the low-amplitude superharmonic signal, the received signals were then amplified by a low-noise variable-gain amplifier (AD8331), with overall adjustable gain of -4.5

dB to 54 dB. The -3 dB bandwidth of the amplifier spanned from 1 to 100 MHz when connected to a 50 Ω input impedance. The amplifier also converted the single-ended input to a differential output, which eliminated DC biasing. Signals were then LP filtered by a 3rd order Butterworth filter with -6 dB cut-off frequency at 60 MHz. The signal was digitized by a 12-bit ADC AD9230 at a sampling rate of 200 MHz. After conversion, the differential digital signals were routed to the FPGA.

Table 6.2: Major user defined parameters of the proposed system.

Parameter	Selection	Control Signal
Imaging Depth	2048/4096/8192 sample points/line	Pre-loaded in FPGA
Number of Lines in a Frame	N:1-10000	#of_Lines[0-7]
Repetition in Each Line	1-2000	#of_Pulses[0-6]
Transmit Pulse Polarity	0° or 180°	Control [0]
Transmit Pulse Frequency	Any Integer Division of the Clock Frequency	Control [1-7]
Stimulation Mode	Pulse Echo /Dual-frequency	Mode
Receiving Channel	Chan1/Chan2	Channel
Transfer Clock Speed	≤50 MHz	Pre-loaded in FPGA

6.2.2.3 Pulse generator

For superharmonic imaging, a Gaussian-weighted sinusoid driving signal would be the ideal choice, since this waveform has low spectral leakage in the frequency domain that could potentially contaminate the superharmonic signal derived from MCAs. An adjustable high voltage output was also necessary, considering the previously mentioned variation in transducer sensitivity. However, a high-frequency (30-40 MHz), high-voltage power amplifier and a high-speed D/A converter would have to be implemented in order for proper excitations with arbitrary waveforms such as the aforementioned Gaussian-weighted sinusoid. Additionally an impedance matching circuit would be required to get rid of the shape distortion at variable driving frequencies – both of which would increase the complexity and size of the circuit extensively.

Instead a bipolar high-voltage square wave generator provided by TC6320 (Supertex Inc.) was used which is considerably more affordable while still being acceptable as a driving circuit. A pair of high-speed MOSFETs controlled the output of the positive and negative voltage rails of the excitatory signal. The chip was able to provide a square wave between 40-50 MHz up to a maximum voltage of 200 V_{pp}. Two MOSFET drivers (ISL55110, Intersil Corp., Milpitas, CA) were used to amplify the digital pulses generated by the FPGA to 20 V_{pp} before entering the pulse generator. The transmitted waveforms were passed through two stages of expanders using PMDB7000 high-speed, high-breakdown voltage diode (NXP Semiconductors, Eindhoven, Netherlands) before being sent to the transducer.

The transmit pulse generator was able to produce high voltage, bipolar pulses for B-mode imaging, and burst (square wave trains) for superharmonic imaging. The center frequency of the pulses was controlled by the FPGA. Voltage output was adjusted by controlling the DC supply voltage to the MOSFET.

6.2.3 Transducer design

A photograph of the transducer is shown in Figure 6.3A. The transducer was designed as multiple layers with the high frequency layer in front of the low frequency layer, Figure 6.3B. The low frequency excitation wave was generated by the low frequency element and the wave could pass through the high frequency element to propagate into surrounding tissue. A summary of the fabrication information of this prototype transducer is the same as that shown in Table 5.1 except the center frequency of the receiving element was increased from 30 MHz to 35 MHz. Additionally, an acoustic filter layer was added and interleaved between the two piezoelectric layers. The acoustic filter layer functions as a matching layer for the low frequency wave and an anti-matching layer for the high frequency wave in order to prevent aliasing echoes from

accumulating in imaging data [335, 336]. The whole transducer (4 mm x 0.6 mm x 0.5 mm) was mounted on a 20 gauge hypodermic needle. A detailed fabrication procedure is given in Chapter 5.

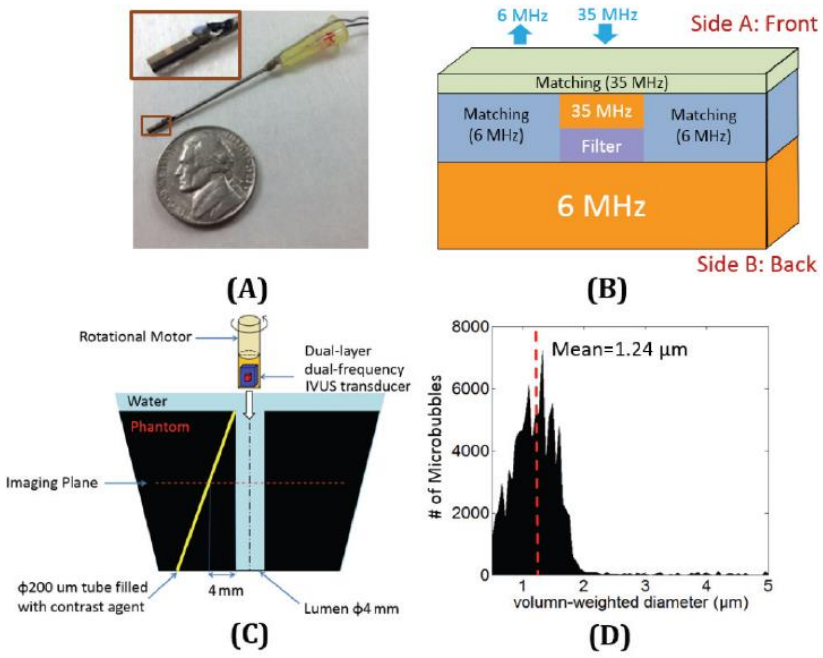

Figure 6.3: Embedded system experimental design and MCA population. (A) Photograph of the transducer. The inset shows the front look of the acoustic stack. (B) Acoustic stack of the dual-layer transducer. (C) Experiment setup for *vasa vasorum* phantom imaging. (D) Microbubble size distribution.

6.2.4 Imaging experimental setup

Ex vivo IVUS imaging of heathy rabbit aorta and *in vitro* phantom imaging was conducted to evaluate the imaging performance of the hardware and device. The artery samples were donated by Dr. Tzung Hsiai from the University of California, Los Angeles, after the rabbit was sacrificed for an unrelated study. A 15 mm long sample was removed from the animal. The first 5 mm of the sample was buried in a gelatin substrate for stabilization and the rest of sample was submerged in formalin. During the imaging experiment, the formalin was replaced by water

and the transducer was inserted into the vessel longitudinally and rotated using a stepper motor. The system was operated in B-mode using the 35 MHz element. The pulse generator provided a single cycle, bipolar pulse at 60 V_{pp} and 33 MHz center frequency. The experiment was repeated using two different dual-frequency transducers

For superharmonic *in vitro* imaging, both the high-frequency element and the low-frequency element were connected to the system. The transducer was attached to a motor and placed in a 4 mm diameter channel cut through a tissue mimicking phantom. The phantom was prepared using a 0.075 g/mL concentration of 275 bloom gelatin with a 0.032 g/mL concentration of graphite scatters. The speed-of-sound was measured to be 1532 m/s using a pulse transmission approach. The acoustic attenuation coefficient was expressed by the following equation:

$$\alpha = \alpha_0 f^n \qquad 6.1$$

with units of dB/cm for α_0 and MHz for f. In 4.5-7.5 MHz range, the phantom attenuation was $\alpha_0 = 1.399$, $n = 0.9439$ ($R^2 = 0.952$); in 15-30 MHz range, $\alpha_0 = 0.1228$ and $n = 1.4172$ ($R^2 = 0.982$). To mimic *vasa vasorum*, an acoustically transparent tube with a 200 μm inner diameter was inserted through the phantom. The tube was placed transversely to the imaging plane, as shown in Figure 6.3C. Additional details about the phantom formulation have been reported previously [337].

Polydisperse lipid-shelled microbubbles were formulated as described previously [103]. Lipid solutions were formulated using 1,2-distearoyl-sn-glycero-3-phosophocholine (DSPC-Powder, Avanti Polar Lipids, Alabster, AL) and 1,2-distearoyl-sn-glycero-3-phosphoethanolamine-N-methoxy (polyethylene-glycol)-2000 (DSPE-PEG-2000) in a 9 to 1 molar solution of propylene glycol, glycerol, and phosphate buffered saline (15%, 5%, and 80%,

respectively). Lipids were agitated in the presence of decafluorobutane in 3 mL sealed glass vials using a commercial agitator (VialMix Shaker, Bristol-Myers-Squibb, New York, NY). Concentrations and sizes of microbubbles were measured optically using an Accusizer 780A (Particle Sizing Systems, Santa Barbara, CA) to measure microbubbles within a range from 0.5 to 6.0 μm. Microbubbles were diluted to a concentration of $8x10^7$ MBs/mL and then were pumped through the tube at a mean velocity of 4.4 cm/s while imaging. The microbubble population had a mean volume-weighted diameter of 1.24 μm. For comparison with other relevant studies, the size distribution of this microbubble population would approximate that of Definity™ (Bristol-Myers Squibb Medical Imaging, North Billericia, MA) that has been decanted for 1 hour prior to use [338]. A microbubble population having a smaller mean diameter (<2 μm) has been reported to provide increased nonlinear response at frequencies relevant to this study (>10 MHz) [55, 339]. The microbubble size distribution is shown in Figure 6.3D. Raw RF data was acquired and data was post-processed in MATLAB (Mathworks, Natick, MA) using a 25-40 MHz 6^{th}-order band-pass Butterworth digital filter. Envelop detection was applied for image displaying using the Hilbert transform.

6.3 System calibration and imaging results

6.3.1 Analog receiver characterization

The impulse response of the system was measured using the following methods. A pulse generated by Panametrics 5900PR (Olympus Corporation, Tokyo, Japan) was delivered through the transducer SMA connection port after being attenuated by 40 dB. The pulse waveform and the received signal collected by the proposed system are shown in Figure 6.4.

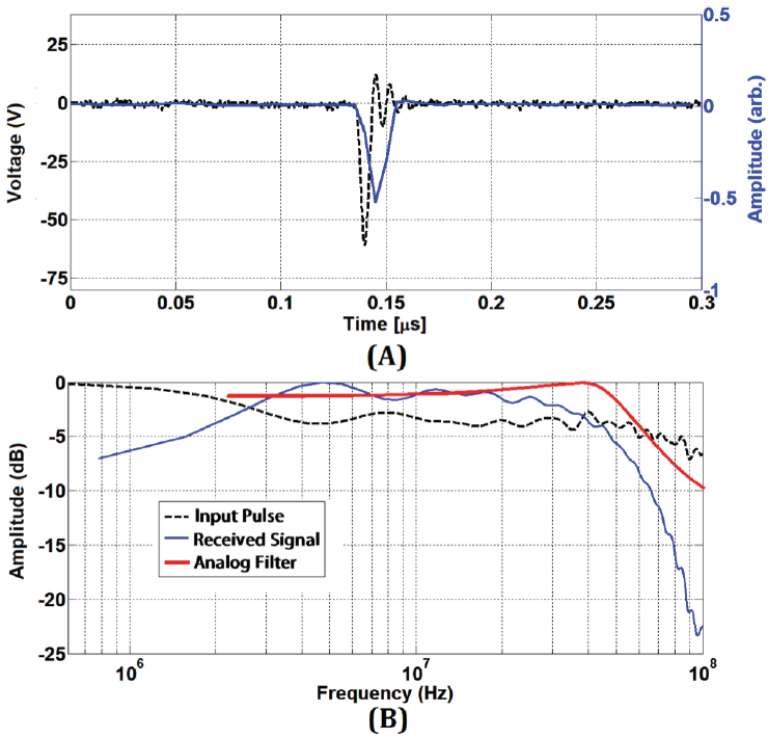

Figure 6.4: Impulse response of the receiver. (A) Input pulse voltage collected by the 2 GHz digital oscilloscope (dashed black) and the received signal (scaled to 1, blue) collected by the system. (B) The spectrum of the input pulse (dashed black), of the received signal (blue) and of analog filter simulation (red).

From the time domain waveform, it was evident that the baseline noise measured was removed by the analog receiving circuit. The frequency spectrum showed the analog receiver had a -6 dB cut-off frequency at 52 MHz, which was lower than the designed frequency of 60 MHz. The reason for the mismatch between the design and actual frequency was that a few passive components were not inserted at the input stage of the preamplifier in order to match the actual transducer impedance which changed the load seen by the filter versus the designed one.

The ADC SNR was 55.9 dB, calculated according to Equation 6.2:

$$SNR = 20dB\ log_{10}\left(\frac{A_{signal}}{A_{noise}}\right) \qquad 6.2$$

where A_{signal} was the dynamic range of the ADC (1.25 V) and A_{noise} was measured by powering the system without providing a signal input (open circuit) and recording. The noise level of the amplifier was tested by measuring the minimum detectable signal using a sine wave sent to the receiving channel of the system. At 35 MHz, the minimum detectable signal was 65 μV. The gain at 35 MHz was 42.9 dB.

6.3.2 Pulser characterization

The output of the transmit pulse generator was measured by a digital oscilloscope (TDS 5052, Tektronix, OR). Figure 6.5A and Figure 6.5C show the time and frequency domain of a pulse centered at 30 MHz along with the pulse-echo response of the 35 MHz element using the designed hardware. The pulser could generate a burst signal (square wave) for superharmonic imaging. As shown in Figure 6.5B, the spectrum of a 3-cycle square wave burst had strong odd harmonics, which were 10 dB weaker every 2 octaves. The acoustic output of the 6 MHz element driven by the burst was also measured, using a needle hydrophone (HNA-0400, Onda Corp., Sunnyvale, CA) placed axially 3 mm away from the transducer. Shown in Figure 6.5D, the odd harmonics present in the transmit pulse was suppressed by the convolution with the transducer impulse response, but there was still a 22 MHz frequency component in addition to the 6 MHz baseband. It was important that the excitation acoustic wave should have weak high frequency leakage, because tissue scattering of the high frequency would impair the distinction between signal originating from contrast versus tissue. To suppress the 22 MHz component, a HP filter (f_{corner} = 25 MHz) was applied during image post-processing.

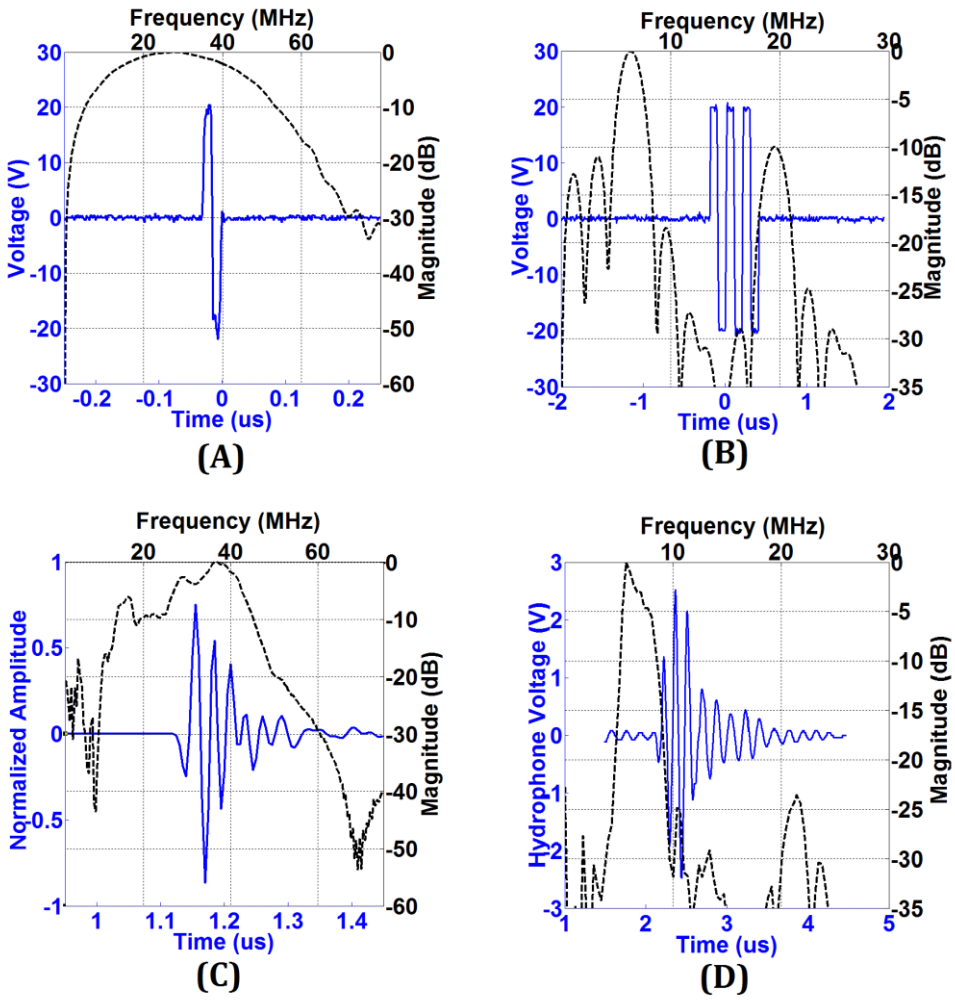

Figure 6.5: System excitatory pulse and corresponding transducer response. (A) Broad-band pulse and spectrum measured by oscilloscope. (B) 6 MHz pulse train and spectrum measured by oscilloscope. (C) Pulse echo signal of the 35 MHz element collected by the proposed system. (D) Acoustic pressure output of the 6 MHz element measured by the hydrophone, shown in hydrophone voltage

Figure 6.6 shows the relationship between the supply voltage and low-frequency element acoustic output. The slope was 19 kPa/V when using 2-cycles and 14 kPa/V for a single cycle pulse. Above 140 V_{pp}, both 1-cycle and 2-cycles could produce peak negative pressures over 1 MPa, which was sufficient to produce broadband transient responses from MCAs for acoustic

angiography [292]. In practice, we limit the driving voltage under 150 V_{pp} to extend the life of the transducer and prevent fatigue-based depoling.

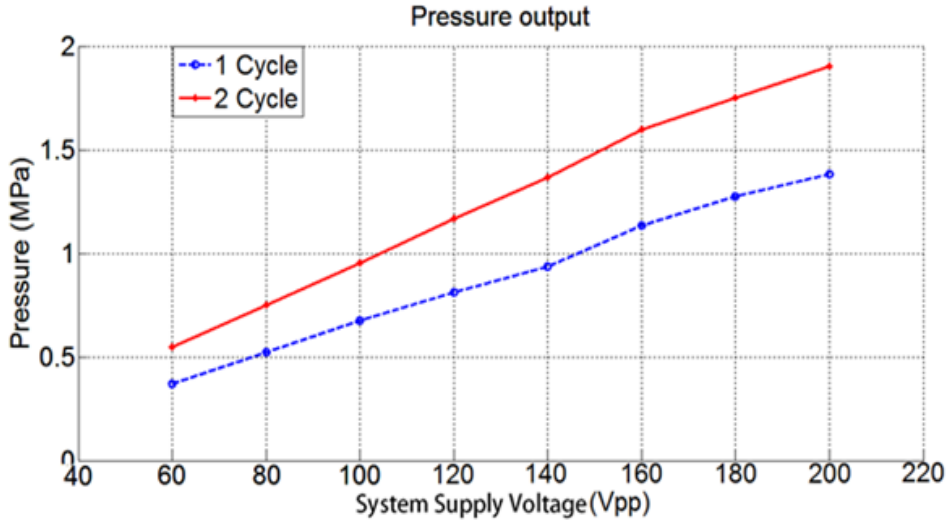

Figure 6.6: Acoustic pressure collected using a calibrated hydrophone. The transmitting element was excited using a 6 MHz 1-cycle or 2-cycle pulse

6.3.3 Imaging results

Figure 6.7 shows the B-mode image of the rabbit aorta collected using the high frequency (35 MHz) element of the IVUS transducer with the proposed system. A dynamic range of 45 dB was observed with the front and back layers of the artery remaining visible. The image was formed by acquiring 2000 lines for a single revolution. In addition to fast-time filtering, a clutter filter was applied to the dataset to reduce stationary echoes.

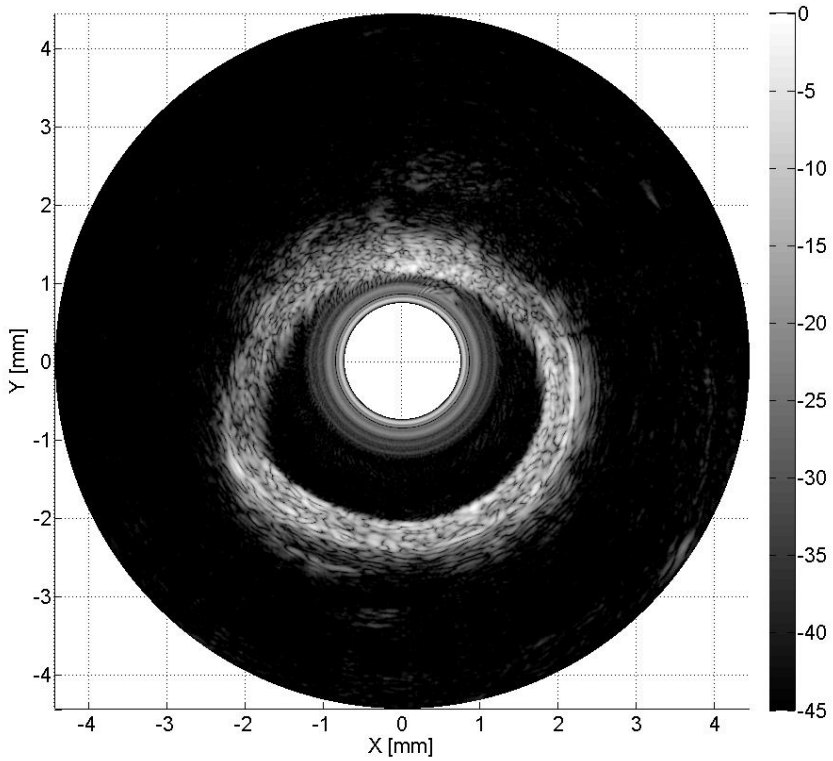

Figure 6.7: B-mode image of the rabbit aorta obtained by 35 MHz transducer element

Acoustic angiography acquisitions were performed in the tissue mimicking phantom. For B-mode, water or MCAs were injected continuously into the 200 μm diameter tube to simulate blood flow in a microvessel in a manner similar to *vasa vasorum*. The results of B-mode to acoustic angiography are compared in Figure 6.8. As intended, B-mode imaging methods cannot reliable locate microvascular contrast flow when surrounded by tissue. B-mode imaging with water injected was very similar to Figure 6.8A, (results not shown). Superharmonic images were acquired by transmitting a 3-cycle burst at 120 V_{pp} using the dedicated system. As shown in Figure 6.8B, the MCAs inside the tube were visualized, while the fundamental frequency containing mostly tissue mimicking phantom backscatter was successfully suppressed. A dynamic range of 30 dB was observed in phantom images, which was a 10 dB improvement over previously reported results (see Chapter 5). Stronger ring-down from the transmit wave can be

seen near the center of the image. The image was formed by acquiring 400 lines for a single revolution.

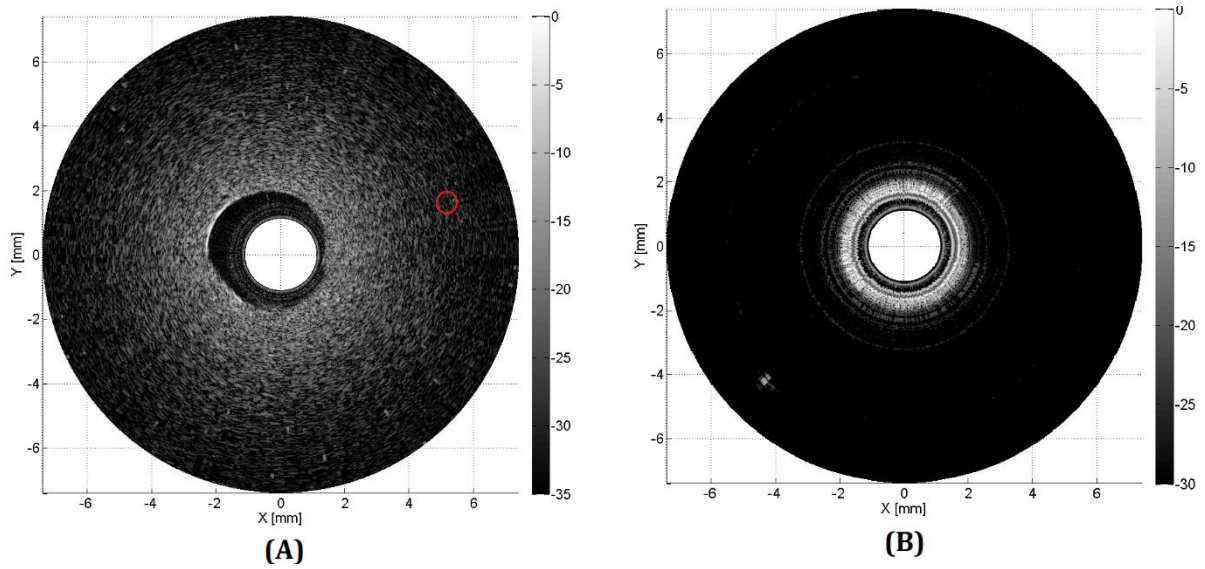

Figure 6.8: Phantom superharmonic imaging result. (A) B-mode image, when MCAs were injected into the micro tube. The approximated location of tube is circled with red. (B) Superharmonic image obtained when MCAs were injected continuously into the microtube located at the 8 o'clock position which is the only enhancement seen in the field outside of the ringdown effect.

Figure 6.9A shows a zoomed in view of MCAs inside the tube, re-drawn from Figure 6.8B. A scale bar (red) is drawn in the axial direction and has a length corresponding to 200 µm. The size of the tube in the image was approximately 300 µm from -6 dB measurements.

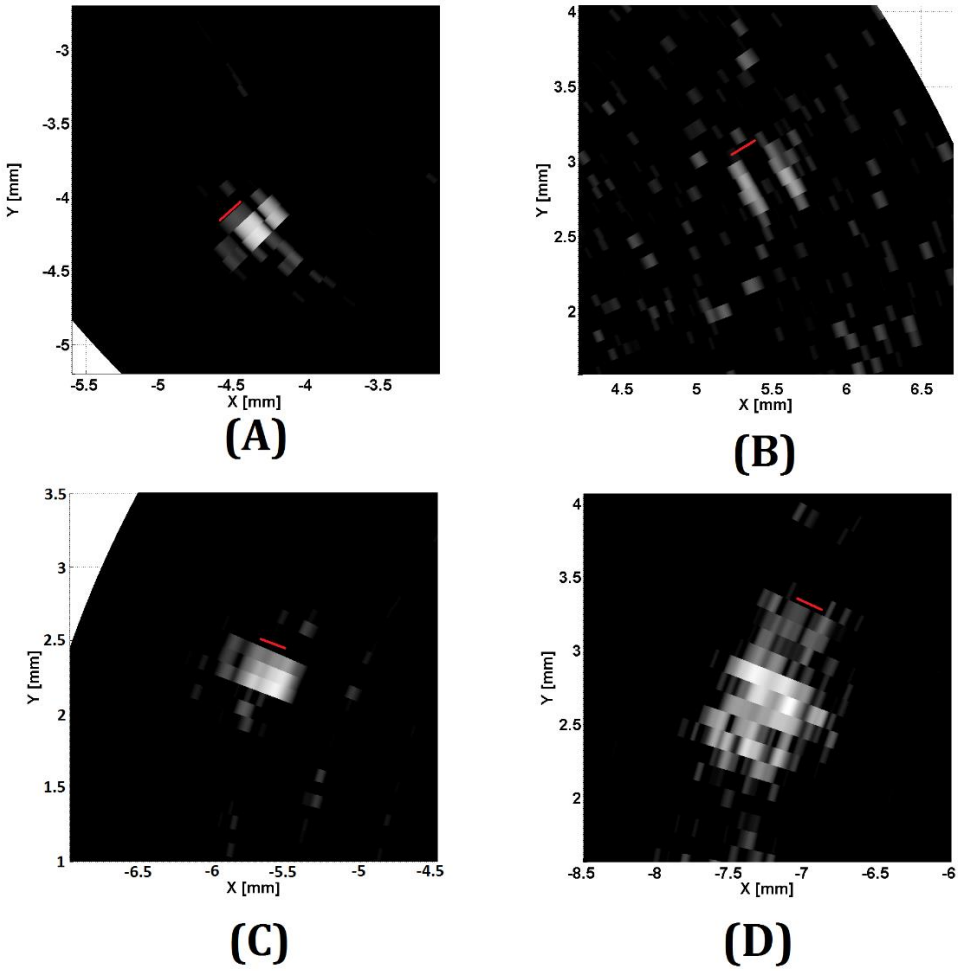

Figure 6.9: Expanded view of superharmonic image. (A) is redraw from Figure 6.8B. (B) is collected when water was injected into the vessel mimicking tube. (C) and (D) were collected using a different transducer with a narrower bandwidth. (D) was collected where the micro-tube ran parallel to the imaging plane. 200 µm along the axial direction is indicated by the red bars.

Figure 6.9B shows the superharmonic image when water instead of MCAs were injected into the vessel mimicking tube. The 200 µm lumen of the tube can be seen along with the front and back reflections from the tube wall.

Additional superharmonic images were collected using another dual-frequency transducer, whose 6 MHz element had a 20% BW_f (28% narrower than the one used for Figure 6.8). Figure 6.9C shows the cross-section view collected of the *vasa vasorum* mimicking tube,

where the front and back surface of the tube cannot be seen. In Figure 6.9D, another imaging plane was chosen, where the tube ran nearly parallel to the imaging plane, so the longitudinal cross section of the tube could be imaged. The sizes of micro-tube in these images were about 500 μm indicating that transmission fractional bandwidth can affect image resolution on a considerable level when performing acoustic angiography from an IVUS platform.

6.4 Discussion

The capability of the system for superharmonic contrast-enhanced imaging has been demonstrated. In the phantom *vasa vasorum* study, a dynamic range of 30 dB was achieved with 10 dB improvement of SNR. High frequency B-mode imaging was also acquired by the system. As shown in Figure 6.9, the size of the *vasa vasorum* mimicking tube in the image is larger than its actual size when the transmit transducer with narrower bandwidth was used, which might be explained by ringing in the excitation waveform. This implied that the superharmonic imaging resolution was related to both transmit and receive element resolutions.

Although imaging resolution can be improved by reducing the number of cycles in the transmit pulses, a threshold peak negative pressure has to be reached in order to produce detectable superharmonics. Under the current imaging conditions, we could not detect superharmonic responses using a 1-cyle 200 V_{pp} (maximum voltage) pulse. This can be explained by the damping introduced by the transducer when converting changes in electrical field to vibratory motion. As shown in Figure 6.5D, when driven by a multi-cycle pulse, the peak negative pressure ramped up after the first cycle. If the time constant of the transducer could be reduced, presumably a shorter pulse can be used to reach the transmit pressure threshold and thus resolution can be improved. However, this implies increasing the transducer bandwidth which normally presents a lower electromechanical coupling.

Other studies have reported that increasing the transmitted pressure used to excite microbubbles improves superharmonic signal returned until a threshold pressure is reached where it was likely that microbubble fragmentation occurs and limits further increases in SNR at higher pressures [136]. The loss of echogenicity from microbubbles fundamentally limits the maximum SNR obtainable at a given noise level.

6.5 Conclusion

An integrated, compact, dual-channel imaging system designed for performing acoustic angiography was developed. The system supported acquisition of high-frequency B-mode imaging, as well as superharmonic CSI. The images obtained using this system improved 10 dB in terms of SNR compared to previous setups. When connected to a dual-frequency (6 MHz, 35 MHz) intravascular transducer, the system was able to achieve 45 dB of dynamic range for *ex vivo* aorta B-mode imaging. A *vasa vasorum* mimicking vessel embedded in a gel phantom could be detected when operating in DF-mode but could not be seen in B-mode. This chapter has shown how hardware considerations can reduce noise levels and improve image quality in dual-frequency IVUS transducers *in vitro* conditions. Having demonstrated both *in vitro* detection of contrast-filled microvasculature, the next step in evaluating this device will be conducting experiments in both *ex vivo* and *in vivo* and to quantify image metrics in these scenarios.

CHAPTER 7

DF IVUS FOR 3D VISUALIZATION OF MICROVESSELS: *EX VIVO* AND *IN VIVO* IMAGE METRIC VARIATIONS WITH DEPTH

In Chapter 5, fabrication and initial analysis of the prototype transducer was described. It was shown that the transducer could produce both sufficient pressure to generate superharmonics from contrast agents and was sensitive enough to detect these superharmonics. In Chapter 6, improvements were made to the hardware that operates the dual-frequency IVUS probe which reduced noise and improved image quality in both B-mode and DF-mode operation. Additionally, an *in vitro* setup consisting of gelatin phantom was used to compare anatomical B-mode images to contrast specific DF-mode images. It was shown that using the appropriate hardware can aid the detection of microvascular flow when using a dual-frequency IVUS transducer. In this chapter, we seek to quantify and describe the depth dependency of SNR, CTR, and tissue suppression while operating in either B-mode or DF-mode. Quantification of image metrics will be performed in order of increasing difficulty using a gelatin phantom, an excised porcine artery, and finally *in vivo* using chicken embryos. Volumetric acquisitions will also be

---

KHM authored the work and was heavily edited by BDL and PAD with additional edits by coauthors. JM provided the transducers used for this study. BDL and KHM collected image data. KHM conducted acoustic field measurements, simulations, and prepared the phantoms and chick embryos. TCN provided the *ex vivo* sample. Image processing was performed by KHM.

presented in this chapter for direct 3D vessel visualization of vessel patterns and qualitatively compared to optical measurements of the same field of view.

7.1 Introduction

In healthy arterial walls, the outer layers are diffusion-limited and are supplied with nutrients and oxygen by a network of vessels known as the *vasa vasorum* arising in the adventitial layer. As atherosclerotic plaques develop, *vasa vasorum* extend through the media and intimal layers into the plaques themselves [340]. Prior to observable symptoms, plaque rupture and ensuing cardiac events occur infrequently and seemingly asymptomatically, further obscuring disease progression [341]. While IVUS is routinely used to image plaques, previous studies indicate that a diagnosis based solely on plaque morphology may lack the ability to discern between asymptomatic fibroatheroma and those prone to rupture [1, 342]. Additionally, histological data has confirmed that vulnerable plaques exhibit enhanced *vasa vasorum* proliferation, intraplaque neovascularizations, or intraplaque hemorrhages [7, 343, 344], potentially providing an alternative means for assessing plaque vulnerability through the detection of intraplaque blood flow.

Contrast agents have been imaged selectively using IVUS transducers by exploiting their nonlinear behavior through a variety of methods including, but not limited to, pulse inversion [57, 345], subharmonic imaging [55], chirp reversal [346, 347], and radial modulation [58]. While some techniques utilize the second harmonic signal, it has been noted that contrast imaging using the second harmonic can be nonspecific to MCAs since tissues also generate second harmonics through nonlinear wave propagation [52, 348, 349]. As a result, second harmonic imaging of MCAs can result in loss of specificity in contrast images if measures are not taken to suppress tissue-derived harmonics.

Alternatively, higher order superharmonic imaging of MCAs provides high resolution and high contrast signal to noise in acquired images. In this chapter, we present contrast specific *in vivo* superharmonic imaging using custom DF-IVUS transducers. The described experiments evaluate and measure the spatial resolution, sensitivity, and specificity of this intravascular approach for imaging microvessels, in order to establish the feasibility of DF-IVUS superharmonic imaging of intraplaque v*asa vasorum*.

7.2 Methods

7.2.1 The dual-frequency probe and imaging system

Contrast imaging at higher harmonics requires transducers with even broader bandwidths. For example, performing 5^{th} harmonic imaging using single element transducers would require a -6 dB fractional bandwidth of at least 133% which is difficult to achieve with piezoelectric materials. However, using multiple elements with separate frequencies allows the transducer to cover a broad range of frequencies to make higher order superharmonic imaging feasible [350]. The dual-frequency IVUS prototypes used in this study had both elements composed of PMN-PT single crystal with different aperture dimensions oriented in a stacked configuration such that the low frequency element is placed behind the high frequency element.

The unfocused low frequency element (f_c = 5.5 MHz, BW_f = 50.0%, 0.6 mm laterally by 3 mm elevationally) would emit the excitatory pulses for generating nonlinear echoes from MCAs while the high frequency element (f_c = 37.2 MHz, BW_f = 28.5%, 0.6 mm laterally by 0.5 mm elevationally) would detect only the superharmonics produced by microbubbles. Thus, images formed by operating the transducer in DF-mode will preferentially image nonlinear targets that produce superharmonics such as MCAs. The two elements are acoustically isolated to prevent undesirable coupling using a frequency selective isolation layer [317, 335].

Conventional B-mode IVUS imaging was performed for comparison by using the high frequency element in pulse-echo operation.

Signals were acquired from the dual-frequency probe using a custom imaging system capable of volumetric acquisitions (Figure 7.1). A programmable microcontroller was used to mechanically rotate the probe using a stepper motor having 400 discrete angular positions per revolution (angular step size, $\Delta\theta = 0.9°$) and images were acquired at a pulse repetition rate of 100 Hz. The motor and transducer assembly were mounted to a three-axis computer controlled motion stage (Newport XPS, Irvine, CA, USA) which controlled transducer pullback in order to collect images of the entire volume for 3D rendering. The transducer was operated in either DF-mode for contrast detection or B-mode for conventional pulse-echo IVUS imaging.

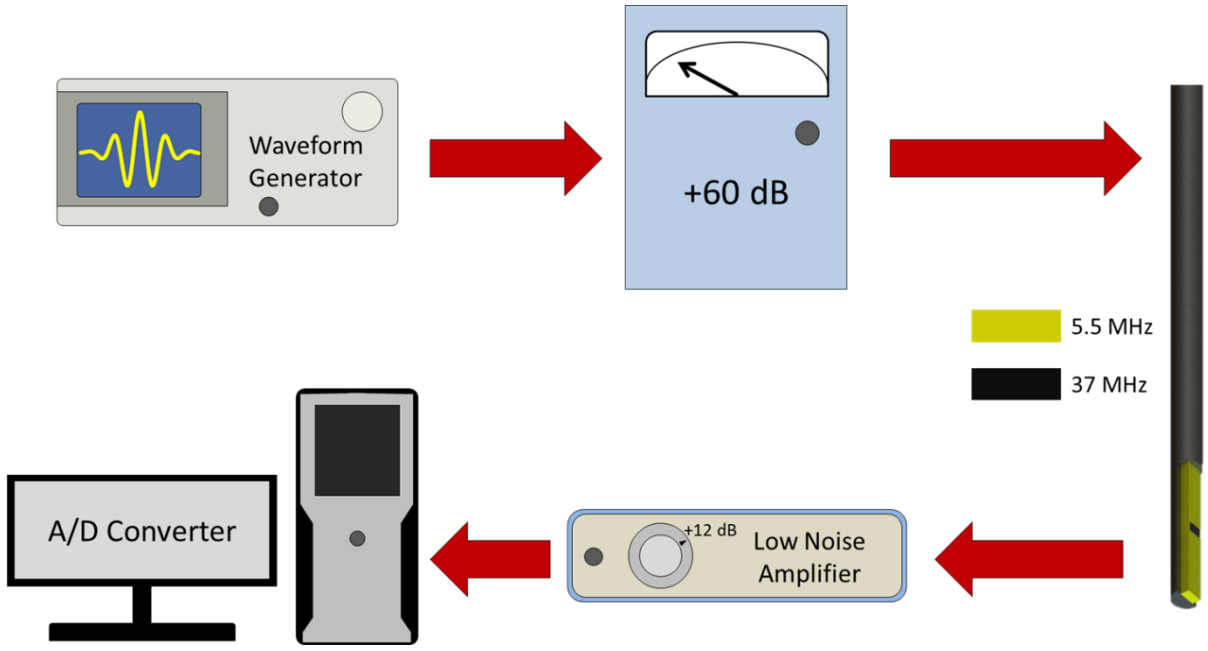

Figure 7.1: Data and control signal flow for acquiring superharmonic signals using the dual-frequency transducer.

In DF-mode, the low frequency element was excited using a 5.5 MHz, 50% bandwidth Gaussian enveloped pulse from an arbitrary function generator (AFG3101, Tektronix, Inc.,

Beaverton, OR, USA). The pulse was amplified to 275 V_{pp} using a 60 dB radiofrequency amplifier (A-500, Electronic Navigation Industries, Rochester, NY, USA) in order to generate 1.2 MPa of peak rarefractional pressure at a depth of 2 mm in water, which was measured using a needle hydrophone (HNA-0400, Onda Corp., Sunnyvale, CA, USA) (Figure 7.2). The transmission pressure was selected in order to produce detectable nonlinear responses above the 4th harmonic using the high frequency element, similar to reported observations in earlier prototypes (see Chapter 5). A beam map of the peak rarefractional pressure from the transmit element was performed by scanning the hydrophone in a water bath using an automated script (Labview, National Instruments, Austin, TX, USA).

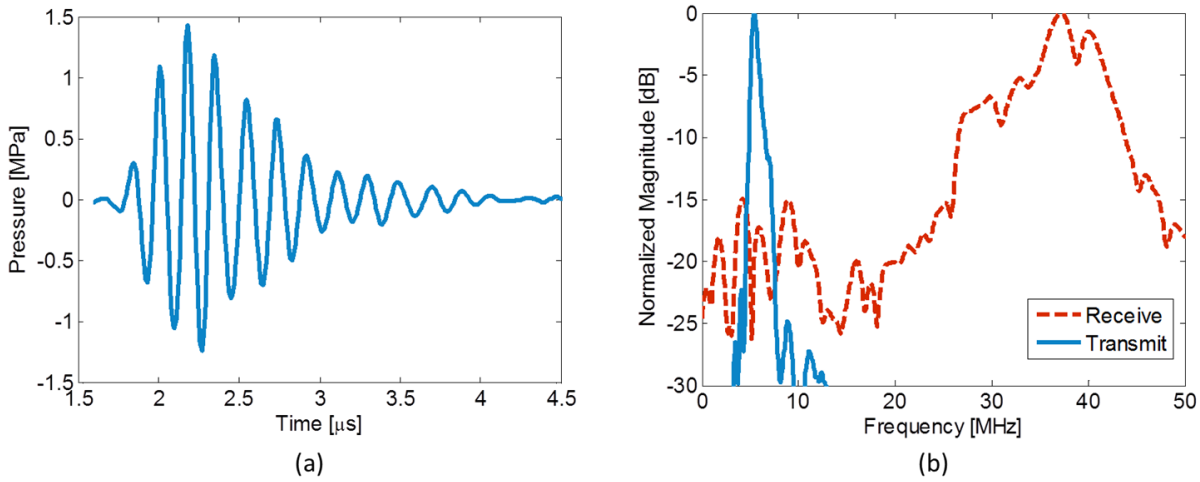

Figure 7.2: Transmission and reception characteristics of the dual-frequency IVUS probe. (a) The time-varying pressure produced by the 5.5 MHz element that was used when the transducer was operated in DF-mode. The pressure response was recorded using a calibrated hydrophone in water at a depth of 2 mm. (b) The normalized power spectra of the transmitted pulse and the receiving element impulse response. There is little overlap between transmission and reception spectra, indicating that received signals will primarily consist of nonlinear harmonics.

The received high frequency signal was amplified by 12 dB using a low noise amplifier (BR-640A, Ritec, Warwick, RI, USA) before being digitized at a sampling rate of 100 MHz

(PDA14, Signatec, Lockport, IL, USA) for offline post-processing. B-mode imaging was performed using a commercial pulser-receiver (5900PR, Panametrics Inc., Waltham, MA, USA) operating in pulse-echo mode on the high frequency element in order to provide a comparison of imaging modes. Raw signals were first filtered using a zero-phase 8^{th} order Butterworth bandpass filter (33-41 MHz) before being envelope-detected and scan-converted to polar coordinates for display. After image processing each individual slice in the volume (Matlab, The Mathworks, Natick, MA, USA), three-dimensional filtering with a Gaussian kernel (0.59 mm isotropic variance) was applied to smooth the dataset. Finally, the entire volume was then exported to ImageJ (National Institute of Health, Bethesda, MD, USA) where maximum intensity projections were performed to visualize the 3D volume. Statistical significance between computed image metrics were determined with two-sided *t*-tests at a significance level of $p < 0.05$.

7.2.2 Microbubble formulation and preparation

Phospholipid shelled microbubble suspensions were formulated as previously described (Section 6.2.4) and aliquoted into 3 mL glass vials sealed with a butyl rubber stopper. A needle was inserted into the headspace of the vial and the gas was exchanged with an inert perfluorocarbon (decafluorobutane, Fluoromed, Round Rock, TX, USA) to form the gaseous core of the MCA. Mechanical agitation using a commercial vial agitator (VialMix, Lantheus Medical Imaging, North Billerica, MA, USA) was performed for 45 s to encapsulate the perfluorocarbon, producing a polydisperse microbubble population. The microbubble population concentration and diameters were measured using a light obscuration and scattering method (AccuSizer 780, Particle Sizing Systems, Santa Barbara, CA, USA). Prepared microbubble populations had a number-weighted mean diameter of 1.08 μm measured between 0.5 to 20 μm

with 95% of the measured population having a diameter below 1.97 µm. *In vitro* and *ex vivo* contrast experiments were conducted after diluting the stock concentration of microbubbles with distilled water to 10^{8} $^{MCA}/_{mL}$, while *in vivo* experiments used undiluted concentrations of 10^{10} $^{MCA}/_{mL}$.

7.2.3 *Vasa vasorum* phantom

In vitro phantom experiments were conducted in order to quantify differences between conventional B-mode and contrast specific dual-frequency images of MCAs as a function of depth in an attenuating medium. A gelatin tissue-mimicking phantom using graphite scatterers was made to simulate arterial tissue. The phantom formulation was adapted from a previously described method reported elsewhere (Section 6.2.4). Amorphous graphite sized between 0.75-5 µm (Superior Graphite, Chicago, IL, USA) was used to simulate backscattering from tissue and was added at a concentration of 32 $^{mg}/_{mL}$ for attenuation control. Attenuation of the phantom material at applicable frequencies was measured by comparing pressure reduction after inserting phantom material between a piston transducer and a hydrophone. Cellulose tubes with an inner diameter of 200 µm were fixed in the phantom material to simulate larger vessels of the *vasa vasorum*. The *vasa vasorum* of human carotid plaques range from 1.6-199.7 µm, with a mean diameter of ~40 µm , while the diameter reported for porcine coronary *vasa vasorum* ranges between 70-160 µm [298, 351]. In order to determine the image metrics as a function of depth, the microcellulose tube was angled relative to the central axis of the vessel lumen so that the amount of phantom material between the contrast-filled vessel and the transducer varied during a volumetric scan (Figure 7.3). Additional phantoms containing tube networks were fabricated in order to evaluate 3D imaging performance in a more complex environment similar to that encountered *in vivo*. Diluted MCAs were injected into the phantom at a mean velocity of 17.7

$^{mm}/_{s}$ using a calibrated syringe pump (PHD2000, Harvard Apparatus, Holliston, MA, USA). At this rate, the volumetric flow approximates human *in vivo* conditions of an arterial vessel of approximately the same diameter [352]. The central lumen containing the transducer was 4.5 mm in diameter and filled with distilled water during imaging. This simulates clinical procedures in which a bolus of saline is injected to clear the lumen during the time of imaging to avoid shadowing from microbubble attenuation within the parent artery. The approach is analogous to that described for optical coherence tomography where saline boluses are used during percutaneous interventions to clear red blood cells so that the vessel endothelium may be imaged [353-355].

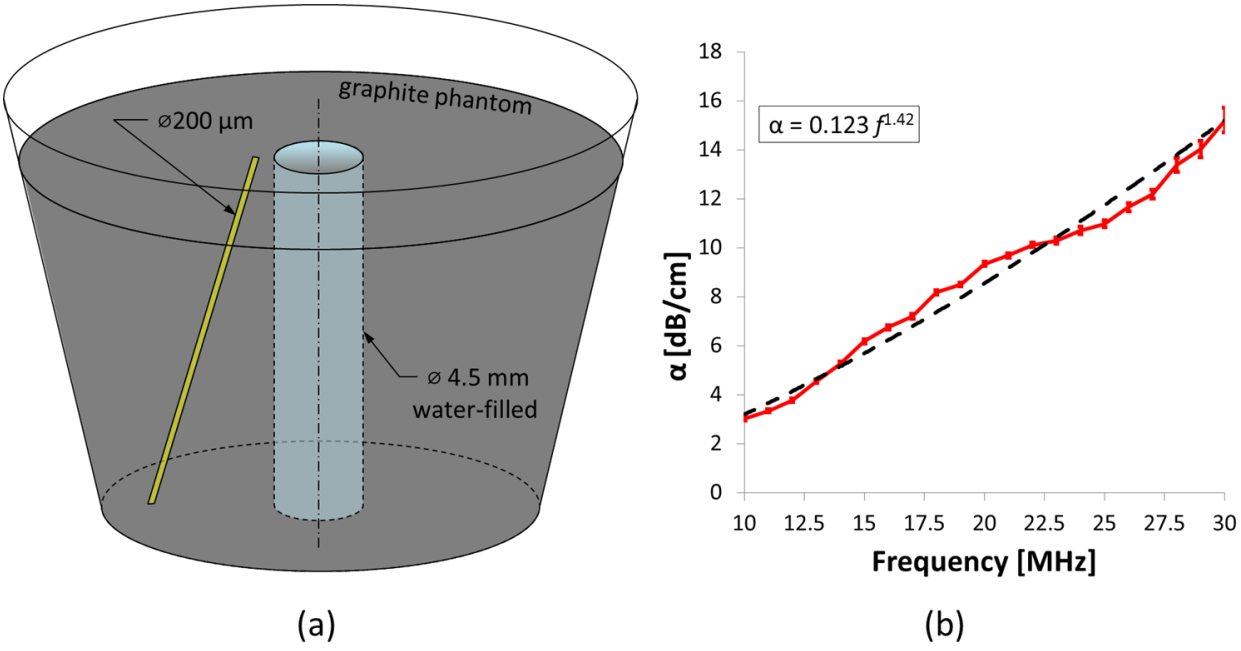

Figure 7.3: Overview of the *in vitro* methods. (a) Schematic of the microvascular phantom used to simulate *vasa vasorum* embedded in tissue. A 200 µm diameter cellulose tube was used to simulate a microvascular channel of the *vasa vasorum* within the tissue. (b) Frequency-dependent attenuation of the graphite phantom. The speed-of-sound measured to be 1548 ± 44 m/s at 22°C.

7.2.4 *Ex vivo* porcine vessel imaging

While phantoms provide a useful tool for quantifying DF imaging performance under highly controlled conditions, imaging using an *ex vivo* model can be used to test the feasibility of the approach when imaging through actual arterial tissue. Mesenteric arteries from Rapacz familial hypercholesterolemic pigs (RFH) were used as a surrogate for human arteries, and were donated by the Francis Owens Blood Research Lab (FOBRL, Chapel Hill, NC, USA). RFH pigs are genetically predisposed to develop atheromata at a younger age and these atherosclerotic lesions closely mimic the pathology found in humans. The mutation that results in familial hypercholesterolemia is a missense mutation ($C_{253} \rightarrow T_{253}$) resulting in a transcription substitution ($R_{94} \rightarrow C_{94}$) of a region of the low density lipoprotein receptor that is analogous to exon 4 in the human ligand binding domain [356-358]. RFH pigs have been used previously to evaluate contrast enhancement methods for detecting *vasa vasorum* during the progression of atherosclerosis [344]. All arteries were collected within 1 hour after euthanasia and stored immediately in phosphate buffered saline (PBS) solutions at -20°C until the time of the experiment. Previous work involving human coronary arteries have noted that fixing tissue in formalin significantly alters the acoustic properties of specimens, but freezing and thawing have not produced significant changes in acoustic properties [359, 360]. Specimens were thawed, sutured, and attached to a custom fixture to allow the vessel to be stretched to approximately 1.5 times the resected length to approximate *in vivo* conditions (Figure 7.4) [361].

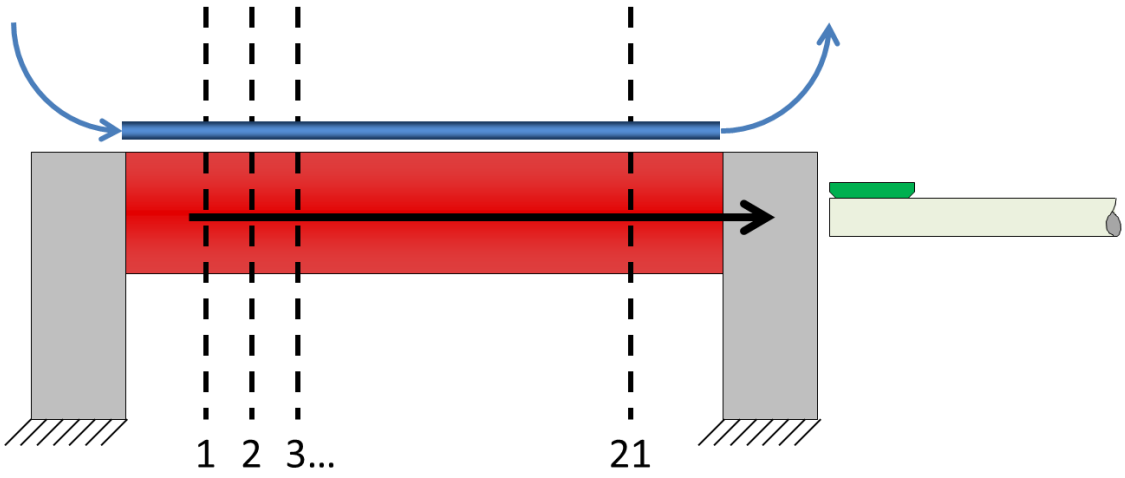

Figure 7.4: Illustration of the *ex vivo* imaging setup. The porcine artery is sutured and attached to a custom fixture on either side that immobilizes the tissue during the imaging process. A 200 µm diameter microcellulose tube is placed outside of the artery to simulate a deep *vasa vasorum* vessel and contrast agents are flowed through the vessel at a fixed concentration. The transducer is placed within the lumen of the vessel and images are acquired in 21 different planes (dashed lines) separated by 200 µm under automated pullback. At each imaging plane, the transducer is rotated for one revolution to acquire an image before advancement to the next imaging plane.

A 200 µm diameter tube was placed outside the artery to simulate a deep *vasa vasorum* vessel and contrast agents were pumped through the vessel at the same rate used in the phantom study using the same equipment. The artery was submerged in a tank filled with PBS, and both B-mode and DF-mode pullbacks were acquired. Arteries collected from 3 different animals were used in this study. All pigs were handled in strict accordance with the USDA regulations and the standards described in the 2011 Guide for the Care and Use of Laboratory Animals [362]. All procedures and protocols were in accordance with institutional guidelines and approved by the University of North Carolina Institutional Animal Care and Use Committee (IACUC).

7.2.5 Chorioallantoic membrane *in vivo* model

In vivo validations of the approach to selectively image MCAs were performed in developing chicken embryos as a surrogate for *vasa vasorum*. The chorioallantoic membrane

(CAM) of developing chicken embryos is composed of a dense capillary network cradled in a sheet of connective tissue and is the primary site for cellular exchange of respiratory gases and metabolic wastes. Due to the low optical scattering of the albumen and the direct visualization of the exposed vasculature, the embryo's developing circulatory system can be imaged and studied optically after removal of the shell. Vessels diameters within the CAM are similar to sizes of human *vasa vasorum* lumens reported previously (43.4 ± 47.4 μm diameters, mean ± s.d.), making it a good model for evaluating the sensitivity of the imaging system to detect small vasculature [351].

Fertilized chicken eggs (broiler line, Ross 708) were collected from a local poultry farm (North Carolina State Chicken Educational Unit, Raleigh, NC, USA) and refrigerated at 6°C upon arrival for 3-7 days until incubation. Eggs were first incubated *in ovo* at 37.5°C with 70% relative humidity for 3 days, turning every 4 hours using an automated egg rocker (Model 4200/3200, Farm Innovators, Plymouth, IN, USA). Eggs were then cracked and explanted into disposable holders as described by Schomann, *et al.* [363], and incubated for 14 days in a humidified incubator at 37.5°C, 70% humidity, and 2.0% CO_2 (NAPCO 8000 Series, Thermo Scientific, Waltham, MA, USA). Chicken embryo morphology was classified at the time of imaging according to the Hamburger and Hamilton criteria, with the majority of embryos being classified as HH39-40. The vitelline vein was cannulated to allow the injection of MCAs at a concentration of $10^{10}\ ^{MCA}/_{mL}$ at a flow rate of 1.0 mL/hr using a syringe pump. A continuous infusion of contrast agents was administered during the entire imaging session. The CAM was prepared for imaging by coupling the transducer to the structure with 37°C phosphate buffered saline.

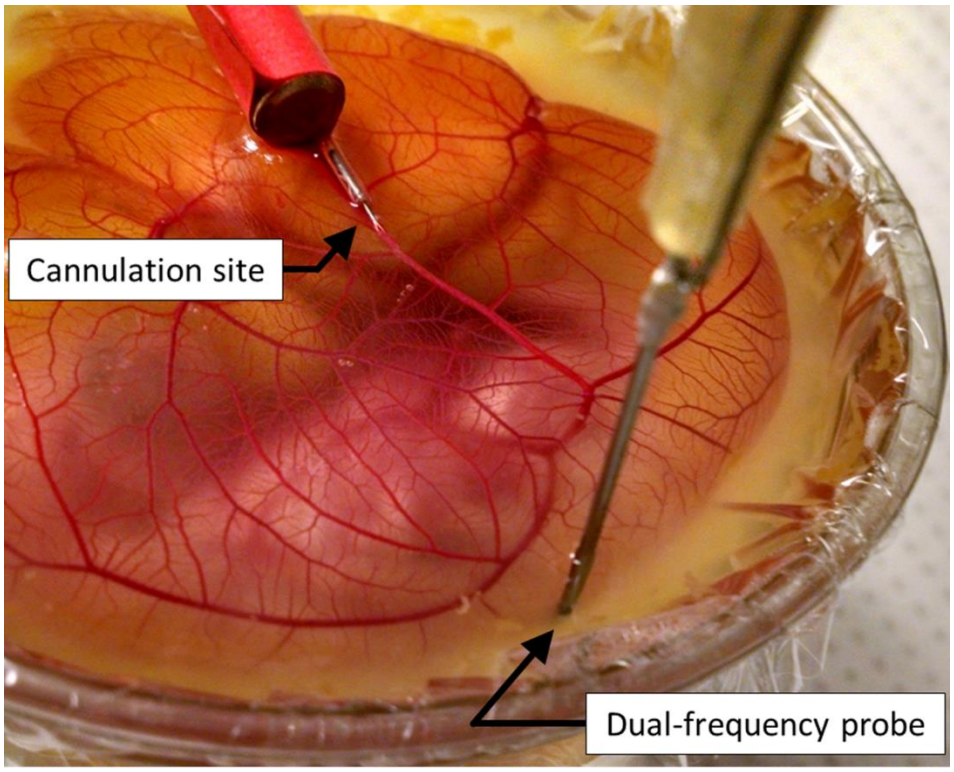

Figure 7.5: Photograph of CAM illustrating the position used to acquire images during the *in vivo* experiments.

The intravascular ultrasound probe was positioned adjacent to the CAM and a volumetric acquisition was performed 2 minutes after starting the flow of contrast (Figure 7.5). Image slices orthogonal to the direction of transducer pullback were acquired at 200 µm intervals while operating in DF-mode for contrast specific imaging. Conventional B-mode and DF-mode volumetric scans were acquired both before and after administration of MCAs for comparison. Additionally, contrast infusion was monitored by acquiring volume scans in DF-mode at 2 minute intervals for a total 12 minutes. Photographs of the CAM corresponding to the region that was scanned were taken to provide an optical reference to measure vessel diameters. Eleven embryos were imaged. Photographs were analyzed in ImageJ to measure the width of the vessels within the imaging region.

7.3 Results

7.3.1 Field profile during transmission and received spectra from MCA

The transmission profile of the low frequency element was recorded using a needle hydrophone positioned in a water bath in order to determine spatial variation of the excitatory signal for the custom IVUS transducer. The 5.5 MHz element was capable of producing 1.2 MPa on-axis at a range of 2 mm from the surface of the transducer (Figure 7.6). Hydrophone measurements indicate that the beam remained collimated at a depth of 7.4 mm where the pressure dropped -6 dB relative to the peak (600 kPa). Field II [364, 365] was used to simulate the pressure field produced by the low frequency element to compare the measured field to ideal results (Figure 7.6b). While simulated and measured results show good agreement, some off-axis energy deposition occurs that was not predicted by the simulation. However, these off-axis energy levels are located at angles where the receive element is highly insensitive making undesirable effects, such as clutter, less of an issue when operating in DF-mode. For reference, a contour is drawn in Figure 7.6 to approximate the region of highest microbubble destruction and loss of echogenicity where the transmitted waveform exceeds a mechanical index (MI) of 0.20. This MI corresponds to the microbubble fragmentation threshold for the type of microbubbles used in this study [366].

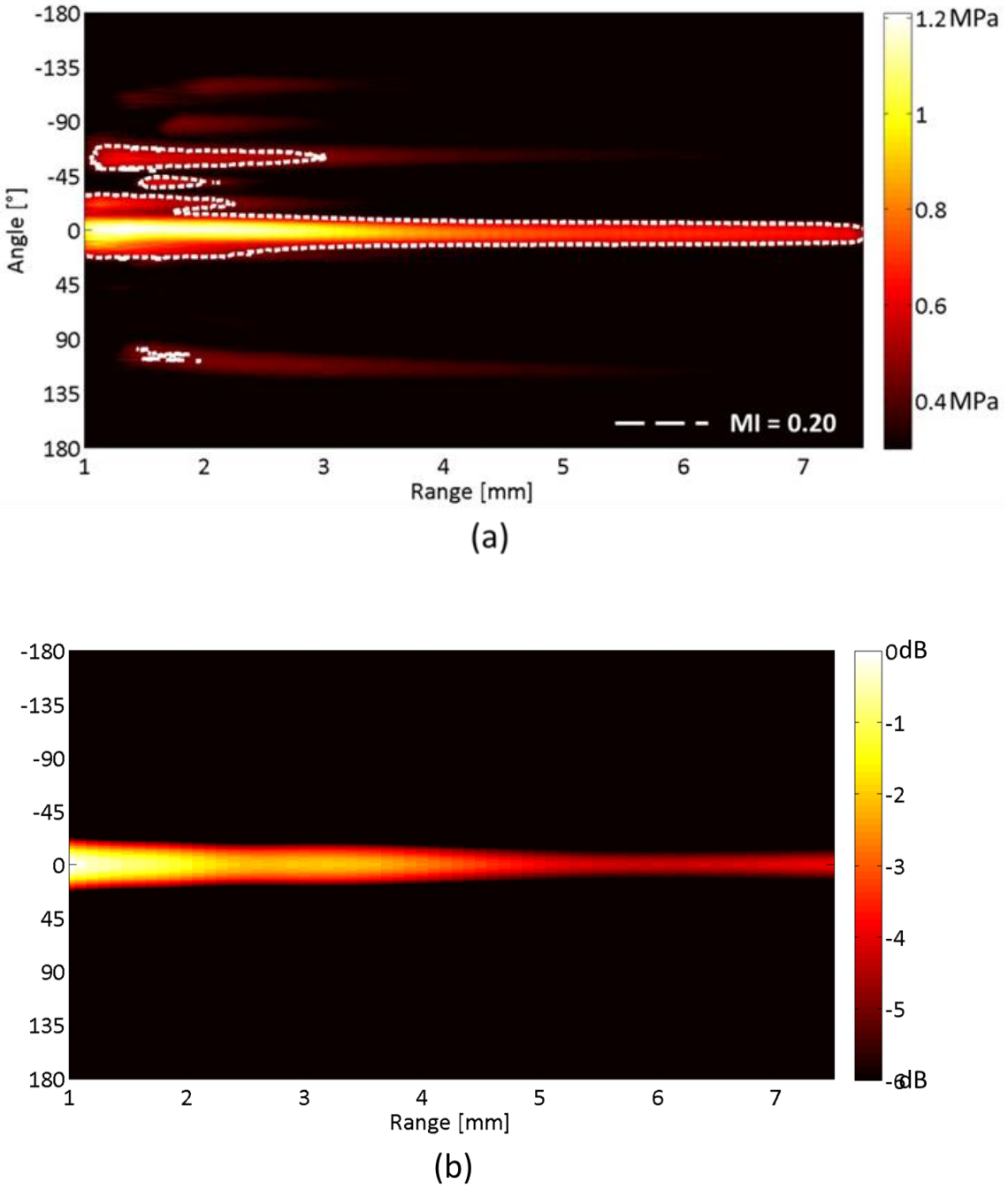

Figure 7.6: Measure vs simulation of transmission field profile. (a) The measured pressure field distribution obtained by exciting the low frequency element with a Gaussian enveloped pulse and recording with a needle hydrophone. A dashed contour is overlaid on the field to identify the region having a mechanical index of 0.20 or higher which is the region containing the most nonlinear activity. (b) The simulated transmit pressure field using the impulse response from the low frequency element.

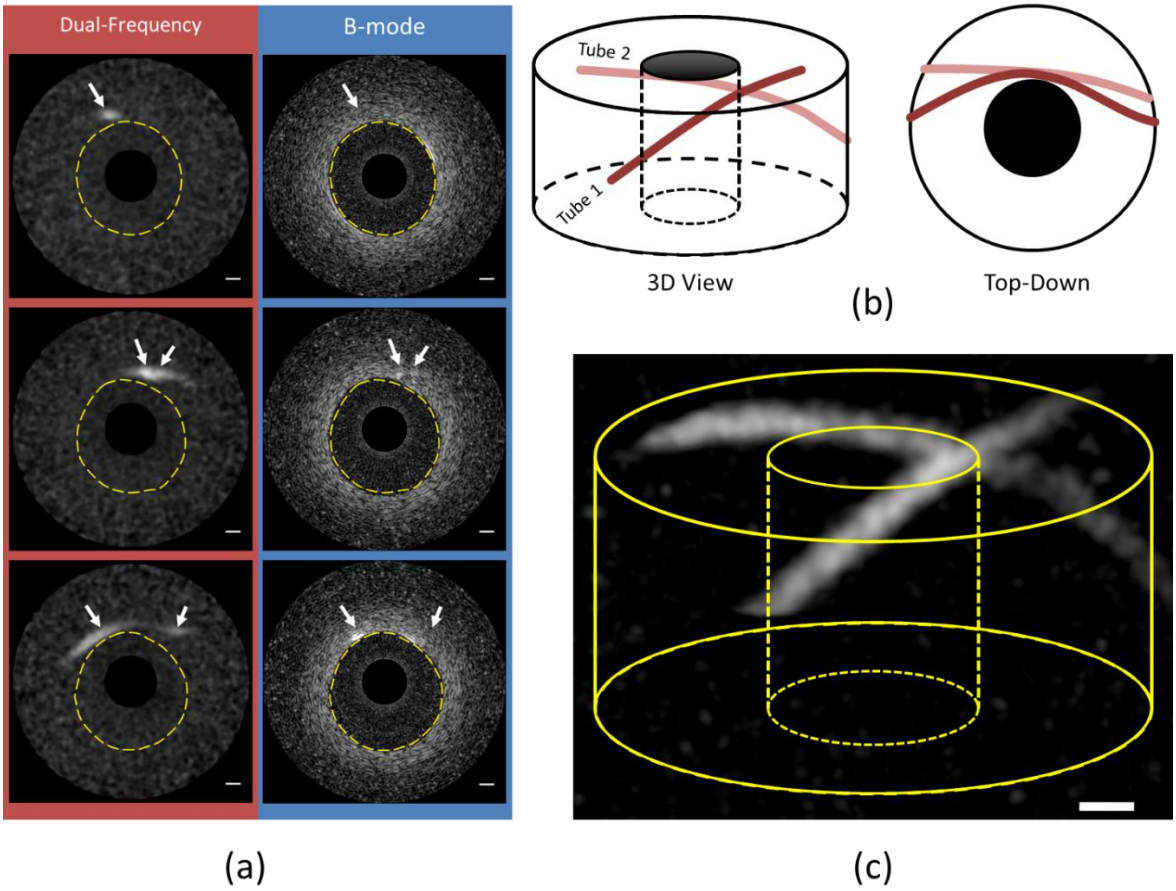

Figure 7.7: Image summary of DF-mode IVUS transducer. (a) Cross sectional images of dual-frequency mode (left pane) and B-mode (right pane) show the presence of contrast agent (arrows) in a tissue mimicking phantom. The phantom lumen is outlined in both imaging modes for reference. (b) Cartoon illustrating the relative orientation of the contrast filled tubes embedded in the graphite phantom. (c) Three-dimensional rendering of DF contrast specific imaging highlight the location of contrast filled tubes embedded within the phantom. Scale bars correspond to 1 mm in all figures while DF images are displayed with a 10 dB dynamic range and 40 dB for B-mode.

7.3.2 Three dimensional renderings of microvascular phantoms

Three dimensional imaging was performed on several phantoms in order to compare B-mode with DF-mode contrast imaging (Figure 7.7). Conventional B-mode images were unable to differentiate contrast-enhanced microvessels from surrounding phantom tissue. In comparison, DF images were highly selective to detecting signal only from regions containing contrast

agents. In light of these results, quantitative image analysis was performed as a function of depth into tissue for both B-mode and DF-mode operation of this transducer.

IVUS pullbacks were performed using a 200 μm diameter tube embedded in a graphite phantom at varying depths. Prior to contrast administration, baseline scans of both imaging modes were performed to provide a reference point for imaging improvement after MCAs were added. CNR, CTR, and tissue-to-noise ratios (TNR) were calculated from images by segmenting regions of interest (ROI) corresponding to MCAs for contrast measurements, water for noise measurements, or phantom material for tissue measurements [55]. Power estimates from these regions were calculated from the square of the RF lines. Because of the radial symmetry of our phantoms, ROIs were rotated about the transducer to ensure the compared locations were calculated at the same depths using the same number of pixels to calculate the average (Figure 7.8). Centroids of the ROIs were calculated and used to determine the radial distance from the aperture of the transducer. Results of the analysis were grouped according to distance with bin sizes of 1.5 mm ranging from 2.5 to 10 mm. Student's *t*-tests ($\alpha = 0.05$) show that CNR was non-zero for both imaging modes at depths below 7.0 mm. Paired testing between the imaging modes indicate that B-mode images had a statistically higher CNR (7.36 vs 2.35 dB at 3.25 mm), however, CTR and TNR calculations suggest that this enhancement is not specific to MCAs alone. At all tested depths, B-mode CTR was statistically zero while DF images had non-zero CTRs of 1.00 dB at 6.25 mm and up to 1.75 dB at 4.75 mm. CTR values using DF images were fundamentally limited by low CNR of the imaging system in that received contrast signal was very close to the noise floor, diminishing the potential for higher values of CTR. Lower values of CTR are accompanied by higher specificity to contrast signal in images which can be observed when evaluating the differences in TNR. The TNR of B-mode images at depths below 7.0 mm

were non-zero and statistically higher than DF images which averaged 0.47 dB through depth. As a result, DF images using higher order superharmonics produce images with excellent tissue suppression within physiologically relevant depths for IVUS imaging. The axial and lateral size of the 200 μm diameter tube was measured from processed DF-mode images after administration of contrast agents. Tube measurements were calculated as the full-width half maximum of the tube region relative to the background noise level in a phantom. Using this method, the axial measurement of the tube was 704.0 ± 24.6 μm (mean ± s.e) while the lateral measurement was 510.5 ± 19.4 μm at an average depth of 4 mm in tissue.

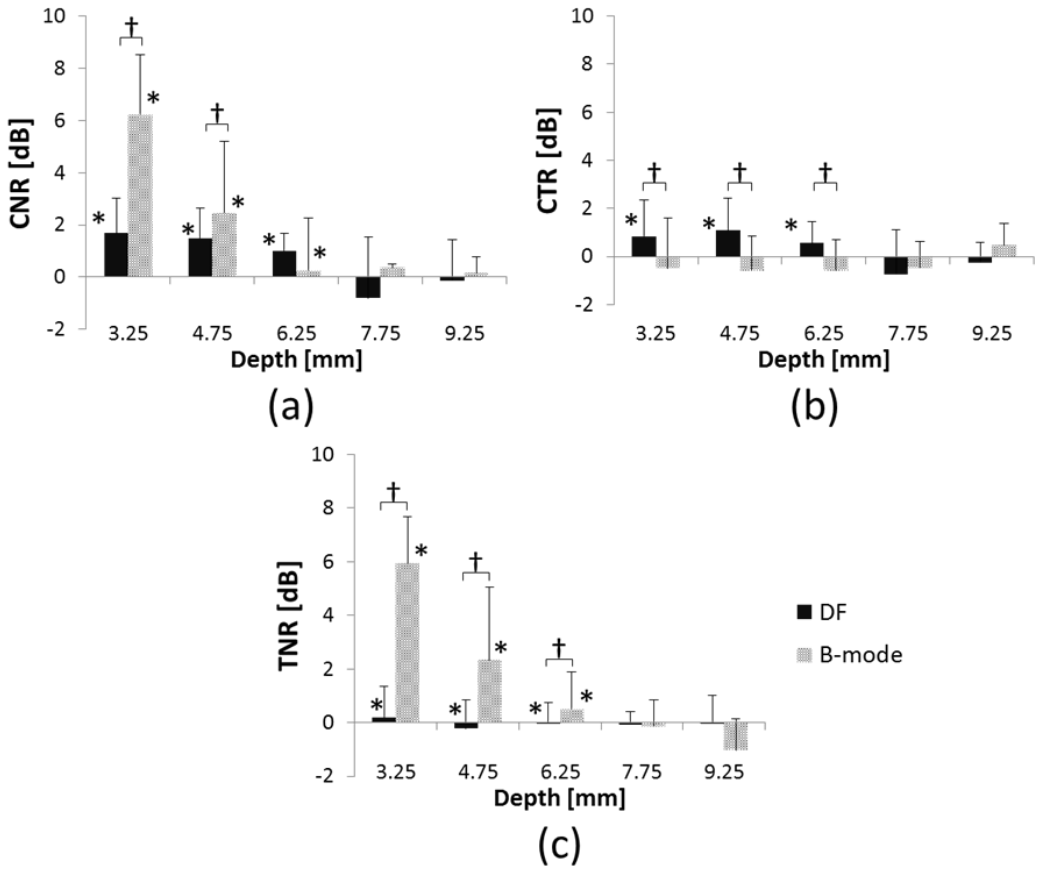

Figure 7.8: *In vitro* comparison of image metrics as a function of depth for both B-mode and dual-frequency mode contrast imaging. (a) Contrast-to-noise ratios using B-mode exceed those provided by DF-mode, and at depths beyond 7 mm, the signal quality of both imaging modes fall below the noise floor giving CNR equal to zero. (b) Contrast-to-tissue ratios provide a measure of specificity of preferentially enhancing regions of contrast agents relative to surrounding tissue. DF-mode images were non-zero and statistically higher than corresponding B-mode images. (c) The TNR of DF images were much lower than those found in B-mode, indicating that DF-mode images are largely devoid of tissue backscatter. Asterisks (*) indicate that the mean is non-zero while daggers (†) show the means between groups are statistically different.

7.3.3 *Ex vivo* contrast detection in arteries from RFH pigs

Preliminary results indicate that imaging through the arterial wall can be accomplished in mesenteric arteries. Coregistered B-mode and DF-mode contrast specific images of an example specimen are given in Figure 7.9 along with CTR. Contrast to tissue ratios were calculated using the ROI approach described previously with tissue ROIs enclosing the B-mode vessel structure

through all slices in the volumetric set. Prior to injection of contrast agents, a B-mode scan was gathered and used to locate the front and back boundaries of the cellulose tube to accurately define contrast signal ROIs for subsequent scans (Figure 7.9a). In DF-mode, the microcellulose tube could be clearly located with excellent tissue suppression (Figure 7.9b).

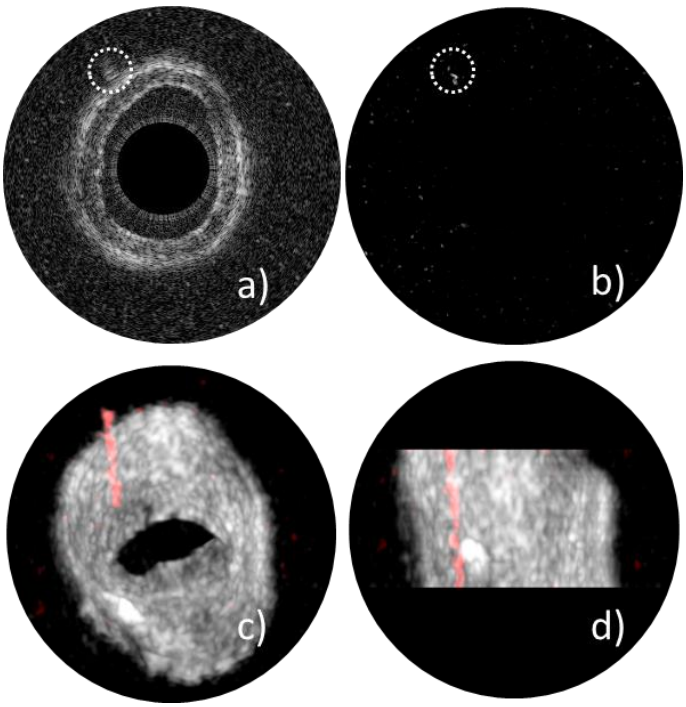

Figure 7.9: *Ex vivo* imaging experiments through a porcine vessel using B-mode and dual-frequency contrast imaging show significant tissue reduction when operating in dual-frequency mode. (a) The B-mode image is acquired by placing the transducer within a suspended porcine coronary artery. The mean diameter of the lumen was measured to be 8.1 mm with a wall thickness of 1.42 mm. The dotted white circle indicates the location of the microcellulose tube placed external to the vessel. (b) A DF-mode contrast image. Backscatter from tissue is largely suppressed while microbubble signal is still retained (dashed circle). (c) Orthotropic view and (d) side views of a 3D volume rendering of the vessel. Contrast signal (depicted in red) was detected through the vessel and has been overlaid on traditional B-mode images (gray), showing the capability of the system to clearly identify the location of the 200 micron artificial microvessel.

Acoustic backscattering intensity from tissue was higher than that from microbubbles at the fundamental frequency (37 MHz), resulting in negative *ex vivo* B-mode CTR while DF-mode CTR remained positive. Combining the DF and B-mode images provides both morphology of the

vessel typically found in IVUS with contrast detection of microvascular flow (Figure 7.9c-d). These *ex vivo* studies demonstrate that higher order superharmonic signals from contrast agents can be generated using a low frequency element and detected using a high frequency receiving element through excised porcine arteries, suggesting that penetration through similar tissues should also be feasible *in vivo*.

7.3.4 *In vivo* contrast detection of microvascular flow

Translation of this technique into the *in vivo* environment was performed after establishing feasibility from *in vitro* experiments. Photographs were taken of the chicken embryo to provide optical verification of vascular structures after embryos were cannulated for vascular perfusion of contrast agents (Figure 7.10a). Three-dimensional renderings of vessel networks were visualized by performing maximum intensity projections on volumetric datasets (Figure 7.10b). Contrast flow was monitored over time as a continuous infusion of contrast agents was administered while acquiring DF volumetric pullbacks. Contrast enhancement (CE), defined as the signal increase from pre-injection values, was calculated and used as a surrogate for CTR while CNR was computed as described previously. Since tissue devoid of contrast agents was not realizable in this animal model, the method of calculating the TNR *in vivo* was estimated by taking the ratio of CNR to CE. This method of calculation relies on the assumption that CE behaves similarly to CTR since TNR can be computed from the ratio of CNR to CTR. Image metrics were calculated and plotted over time for comparison (Figure 7.10c-d).

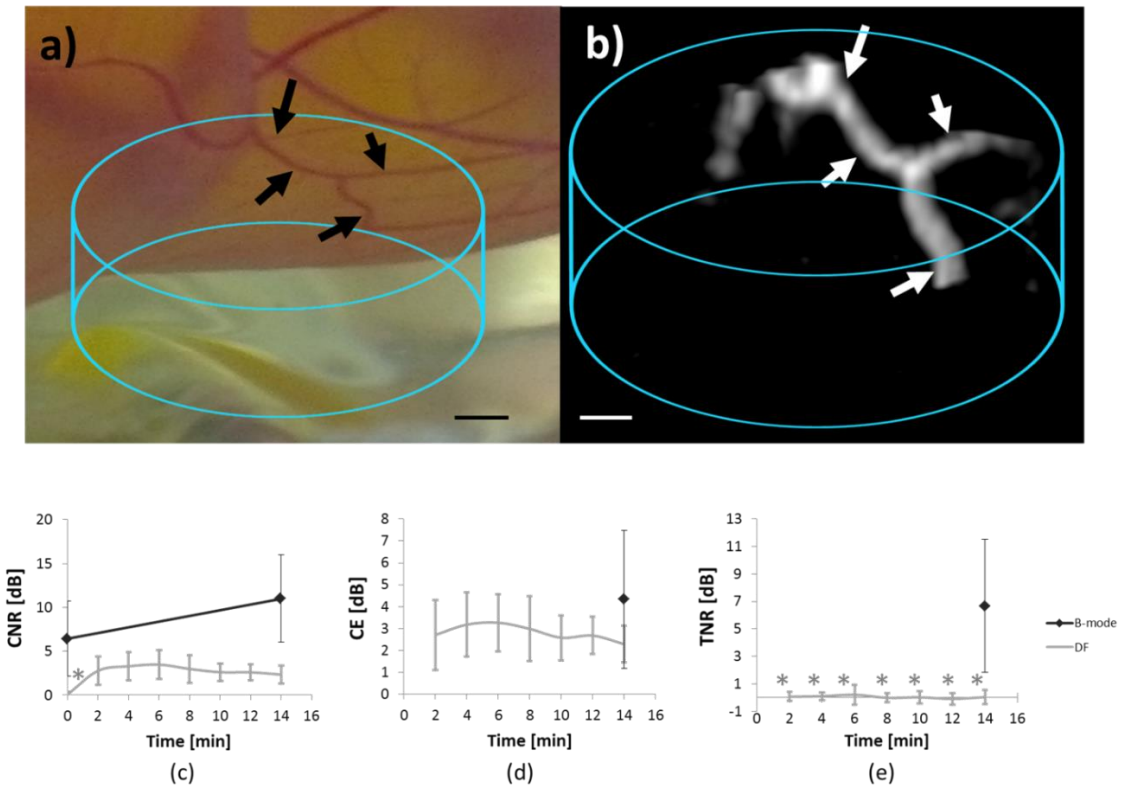

Figure 7.10: Example *in vivo* images and image metrics. (a) Photograph taken of the chorioallantoic membrane at 14 days showing microvasculature. The IVUS transducer was positioned relative to the vessels of interest (arrows) where a 4 mm pullback was performed (cylindrical outline). (b) Three dimensional contrast specific rendering of the same region photographed using the dual-frequency IVUS transducer. Fiduciary marks (arrows) are used to aid the reader in coregistration of the optical and ultrasound images. Scale bars correspond to 1 mm distance. (c) Contrast-to-noise ratios improved for either imaging mode after injection of MCAs, with B-mode images having larger CNRs compared to DF-modes. (d) Contrast enhancement after 14 minutes of infusion was not statistically different between the imaging modes (p = 0.07). (e) Tissue-to-noise ratios at all time points were statistically zero for DF images, indicating this imaging mode is capable of suppressing tissue harmonics effectively. B-mode images had a mean tissue to noise ratio of 6.67 dB after contrast injection.

As seen in the phantom case, B-mode images had a non-zero CNR prior to contrast administration (6.42 dB) resulting from tissue backscatter from vessel walls. Dual-frequency mode images started with a statistically zero CNR (p = 0.28) but improved to a maximum value of 3.49 dB after 6 minutes of infusion. The slightly negative slope over time observed in DF-mode CNR is likely to be a result of decreased cardiac function of the embryo. Contrast

enhancement for B-mode was greater than DF-mode (4.34 vs 2.30 dB) at the end time point, however, the difference was not statistically significant ($p = 0.071$). Tissue-to-noise ratio was computed to determine the ability of the imaging mode to be specific to contrast agents. The TNR for DF images was statistically zero for all time points recorded while B-mode images had a mean TNR of 6.66 dB.

Axial and lateral resolution was computed in optical and DF contrast images of the CAM vasculature. Optical measurements of vessels were taken such that they would correspond to lateral measurements in DF images and it was assumed that the diameter of the vessel in this plane would also be the diameter in the axial direction. The smallest vessel detected *in vivo* was measured to have a diameter of 140 ± 8.1 μm (mean ± s.e.) optically while the DF image measured 626.5 ± 16.9 μm axially and 603.2 ± 22.6 μm laterally.

7.4 Discussion

Our study has demonstrated that imaging using an IVUS transducer with an exceptionally large bandwidth achieved through multiple elements of different frequency ranges produces images with sensitivity to contrast in the microvasculature and tissue suppression not possible with standard single frequency IVUS probes. Superharmonic contrast images have reduced tissue contamination because the amplitude of the signal emitted by MCAs is much higher than that produced by tissue at frequencies 3 to 5 times higher than the transmitted frequency [367]. While increasing tissue suppression in contrast images is beneficial, the contrast signal-to-noise ratio using higher order harmonics is reduced compared to using lower harmonics such as the 2nd or 3rd harmonics and provides a significant challenge to this approach using single element transducers. The peak CTR from the phantom study (1.75 dB) was approximately the same as the measured CNR, implying that contrast images were specific to MCAs alone. However, other

studies of contrast-enhanced IVUS have reported higher values for CNR (approximately 30 dB, 20 dB, and 20 dB for sub-, ultra-, and superharmonic, respectively) than those presented here, though it is difficult to draw a direct comparison since imaging depths, vessel diameter, and type of contrast agents used are not the same [55, 57, 345]. This imaging approach would likely benefit from translation to circular arrays where post-processing approaches such as beamforming on either transmit or receive would help improve the CNR over what can be obtained using only a single element.

The moderate mechanical indices used for causing broadband excitation of contrast agents disrupts the shell of the microbubbles and can lower the echogenicity of contrast agents upon further insonation [116, 366]. Replenishment of the contrast agents with blood flow allows echogenicity to recover over time making this issue less prevalent in larger diameter vessels which have higher volumetric flow rates, but may impact how well smaller vessels are resolved. *In vivo* measurements have indicated that vessels of 140 μm in diameter may be the limit of detection with the current imaging system, but it is unclear whether this limit is imposed by reduced cross-sectional backscatter or by contrast destruction and replenishment rates.

While off-axis energy deposition is normally avoided in ultrasound imaging to reduce clutter [368], an added consequence when imaging contrast agents is to prevent the destruction of contrast agents. In Figure 7.6, the measured transmit pressure field of our transducer exhibited some off-axis energy deposition in the near field, which could potentially destroy contrast agents before being imaged by the receiving element, thus reducing CNR. However, this effect was not significant enough to prevent full 3D reconstructions of vascular phantoms. A 200 μm diameter vessel could be resolved in a tissue mimicking phantom at depths up to 7 mm deep without the aid of signal averaging or use of multiple pulses.

Traditional B-mode IVUS images typically have greater axial resolution rather than lateral resolution since they use higher frequencies with small aperture transducers on both transmission and reception. However, axial resolution in contrast specific images using the described dual-frequency transducer was on average lower than the lateral resolution even though B-mode images using the high frequency element were able to resolve structures smaller than 200 μm axially. These observations provide growing support that axial resolution is degraded in DF operation primarily due to the increased pulse length used on transmission as observed previously(Chapters 5 and 6), while lateral resolution was primarily dependent upon wave diffraction of the receiving element, but further analysis would be required to determine the validity of this hypothesis.

The *ex vivo* studies demonstrated that DF contrast specific imaging could detect the presence of a 200 μm diameter tube located outside of an excised porcine artery. Detection of microvascular flow external to the adventitial layer of the vessel is important since most *vasa vasorum* are externally derived and this location would be more difficult to detect due increased depth and attenuation. DF-mode CTR increases at shallower depths suggesting that if vascular flow external to the vessel can be detected, the neovascularizations occurring in fatty plaques at reduced depths would likely be detectable as well. The low number of animals used in this study prevents statistical analysis.

At frequencies relevant for IVUS imaging, blood scattering effects become significant and attenuation becomes more severe [359]. Additionally, the presence of MCAs in the lumen of the vessel where the IVUS catheter is placed results in attenuation and nonlinear propagation effects, which can produce pseudoenhancement artifacts, or contrast signal where no MCAs are present [369, 370]. This artifact may mask the presence of true contrast in IVUS if vessels

supplying the lesion lie close to the lumen of the parent artery. The experiments presented in this work represent a scenario in which the majority of microbubbles have been cleared by either temporary balloon occlusion or a saline flush to clear blood flow in the main artery while collecting an image [355]. The studies presented reflect the saline flush case; it should be noted that the results would be subject to more severe attenuation if red blood cells and MCAs fill the vessel lumen during imaging.

Microvascular networks of the galline chorioallantoic membrane were imaged and rendered. Dual-frequency contrast images were highly selective to imaging only contrast signal and had a TNR of zero for all time points. Contrast signal-to-noise ratios were higher in B-mode images compared to DF images in both *in vitro* and *in vivo* trials, but B-mode images had a CNR that was non-zero even though contrast agents had not yet been injected (Figure 7.10c) indicating that this signal was not from contrast agents but rather vascular tissue within the region of interest. Fundamentally, the CNR of the imaging system limits the CTR that can be acquired, producing CTR values that were nearly equivalent to CNR when operating in DF-mode.

7.5 Conclusions

A new intravascular ultrasound method for visualizing microbubble contrast agents using higher order superharmonics has been described and demonstrated to detect microvascular blood vessels *in vivo*. Dual-frequency images effectively suppress tissue signal, but have lower signal-to-noise ratios than other contrast specific imaging methods. However, contrast images obtained using this method reject tissue well, making it suitable for producing 3D renderings of vessels. This technique has demonstrated its ability to detect contrast in 200 µm vessels *ex vivo* using porcine arteries and vessels smaller than 200 µm in diameter *in vivo* without using multiple

pulses. Additionally, phantom studies have demonstrated the feasibility of a dual-frequency approach to detect *vasa vasorum*-sized vessels at depths up to 7 mm.

CHAPTER 8

SIGNAL PROCESSING TO IMPROVE VASCULAR IMAGES

Previous analyses on the use of a dual-frequency transducer for the superharmonic detection of microbubble contrast signal has shown trends of growing selection to imaging only the contrast agents at the cost of reducing the signal content nearing the noise floor. It has also been shown in other works that the concept of diminishing returns applies in this imaging method, namely that increasing pressure during transmission cannot indefinitely increase the SNR using this approach [136, 371]. A requirement to practically use acoustic angiography for microvascular imaging is post-processing the signal effectively since the SNR is natively lower than other forms of imaging in medical ultrasound. While the data presented previously has included various forms of signal processing in order to construct the images displayed in preceding chapters, the signal processing is basic and limited to causal filtering, enveloping, log compressing and scan conversion – all processes that are integral but not noteworthy. In this chapter, we present some advanced signal processing for acoustically detected medical imaging and provide quantification of improvement in terms of image quality metrics and resolution. In Chapter 8.1, we compare unsummed images to delay and sum beamforming, adaptive windowing, and phase coherence approaches on DF-mode IVUS datasets to show how additional post processing can improve resolution and CTR at the cost of computational time. Chapter 8.2 shows the derivation and application of an autofocusing algorithm that operates on 2D or 3D datasets to correct for speed of sound errors that manifest in acoustic beamforming of

heterogeneous tissue. Accurate beamforming approaches are an invaluable tool that can be modified and tailored to acoustic angiography to improve image quality on low SNR signals seen when using a small aperture, prototype dual-frequency IVUS transducer.

8.1 Beamforming methods applied to vascular images

In this chapter, we describe signal processing approaches based on minimum variance (MV) beamforming and the phase coherence factor (PCF) for improving the spatial resolution and CTR in IVUS imaging. These approaches are examined through phantom studies, *ex vivo* studies in porcine arteries, and *in vivo* studies in chicken embryos. In phantom studies, PCF processing improved CTR by a mean of 4.2 dB, while combined MV and PCF processing improved spatial resolution by 41.7%. Improvements of 2.2 dB in CTR and 37.2% in resolution were observed *in vivo*. Applying these processing strategies can enhance image quality in conventional B-mode IVUS or in contrast-enhanced IVUS, where SNR is relatively low and resolution is at a premium.

8.1.1 Introduction

Conventional grayscale (B-mode) IVUS imaging is useful for determining plaque extent and morphology [372], for guiding percutaneous coronary interventions (PCI), and for assessment of stent placement in follow-up imaging [373]. However, grayscale IVUS cannot reliably identify vulnerable plaques which are likely to rupture and produce ensuing ischemic cardiac events such as myocardial infarction [374, 375].

BDL authored the above work and was edited by coauthors. Comparisons of signal processing approaches were written and conducted by BDL. KHM conducted all imaging acquisitions while JM provided the transducers.

Despite the demonstrated promise of contrast-enhanced IVUS, there are several technical challenges which have prevented this imaging approach from realizing its full clinical potential. First, the resonance frequencies of commercial microbubble contrast agents are typically <10 MHz [376], while transducers used in coronary IVUS typically operate at frequencies >20 MHz, making them poor excitation sources for microbubbles. Bandwidth limitations in commercial IVUS transducers generally result in reductions in either transmit pressure, receive sensitivity, or both. In small vessels containing relatively few microbubbles, sensitivity is also at a premium, accentuating losses due to operating off-resonance when transmitting or receiving.

Beamforming approaches in ultrasound offer an attractive solution to increasing the SNR of images which would be ideal for situations in which the signal amplitude is weak compared to the noise. The basic principle of beamforming is to form an image by aligning acquired RF signals in phase and then summing these signals together. Portions of the RF signal that derive from reflections and scattered sources will sum together coherently while those pertaining to noise will sum destructively. This method of beamforming is often referred to as delay and sum since phase alignment is performed by delaying RF signals by assuming a constant speed of sound and calculating the time of arrive based on the depth of the image being formed.

In recent years, the application of Capon (minimum variance) beamforming to ultrasound imaging has received great attention due to its ability to offer improved resolution by adaptively steering toward on-axis scatterers [377-379]. More recently, several groups have reported improvements to classical minimum variance beamforming when applied to ultrasound imaging by reducing computational complexity or improving robustness [380, 381], applying coherence factor weightings [382], or implementing in the frequency domain [383]. In general, these

authors report increased spatial resolution, increased contrast, and decreased CNR in B-mode ultrasound images as a result of applying minimum variance beamforming techniques [377-383].

An alternative adaptive approach for the improvement of spatial resolution and image contrast is the application of the PCF, which is computed using channel data but applied after beamforming. Camacho *et al*. first presented the phase coherence factor as an approach for decreasing sidelobe contributions in ultrasound images, with concomitant improvements in lateral resolution and beamsummed SNR [384]. More recently, Hasegawa and Kanai demonstrated the application of the phase coherence factor to increase resolution in echocardiography while using sub-aperture beamforming to reduce suppression of echoes from diffuse, speckle-producing targets, such as those in the cardiac wall which are essential for diagnosis [385].

Adaptive beamforming and adaptive imaging remain unexplored in the context of contrast-enhanced ultrasound imaging, despite the fact that microbubbles represent an ideal target for a beamformer having high point target resolution. Additionally, when a dual-frequency contrast imaging approach is used, echoes originating from tissue scatterers will be minimized due to the low energy generated by tissue relative to microbubbles at high frequencies [291]. This may mitigate the reduced performance of minimum variance ultrasound imaging that occurs when there is a high degree of correlation between signals acquired on neighboring elements.

In this work, we investigate approaches for improving the CTR and spatial resolution in contrast-enhanced intravascular ultrasound imaging using both MV beamforming and the PCF. These techniques are applied to prototype dual-frequency IVUS ultrasound transducers [330], which provide high-contrast, high-resolution images in an 8 French form factor. It should be noted that the experiments presented in this work represent a scenario in which the majority of

microbubbles in the main artery have been cleared by saline flush in order to image microbubbles in the *vasa vasorum*, an approach which is analogous to that described for intravascular optical coherence tomography where saline boluses are commonly used during percutaneous interventions to clear red blood cells for imaging vessel endothelium [354]. To our knowledge, this is the first application of adaptive beamforming to either contrast-enhanced ultrasound or intravascular ultrasound imaging.

8.1.2 Background

8.1.2.1 Imaging system

The transducer used in this work has previously been described (Chapter 5); its characteristics are given in Table 8.1. This transducer was mounted on the end of a hypodermic needle and the needle hub was attached to the drive shaft of a stepper motor. Motor rotation and data acquisition were controlled through LabVIEW (National Instruments, Austin, TX) via a microcontroller (Arduino UNO, Torino, Italy) running a custom program. The stepper motor and its electronics were mounted on a computer-controlled three-axis motion stage (Newport, Irvine, CA) to allow automated pullback for acquisition of 3D imaging data. At each step along the pullback direction, the transducer was rotated through 360° for a total of 400 acquisitions (0.9° step size). For this prototype system, approximately 2 seconds were required to acquire each image slice (a full 360° rotation).

Table 8.1: Characteristics of the prototype transducer used in this work.

Parameter	Transmit element	Receive element
Center frequency (MHz)	6.5	30
-6 dB bandwidth	20%	59%
Thickness (μm)	300	65
Width (mm)	0.6	0.6
Length (mm)	3	0.5

8.1.2.2 Minimum variance beamforming

Ultrasound beamforming consists of applying complex weights to an acoustic wave field which has been spatially sampled in the lateral direction by a discrete number of transducer elements and in the axial direction by a discrete number of samples. In conventional (delay-and-sum) beamforming, spatiotemporal filtering is achieved by applying a data-independent amplitude weighting or apodization (for example, a rectangular or Gaussian window) to acquired data in the lateral direction, with delays providing focusing to individual points in the field. Alternatively, amplitude weightings may be computed which depend on the acquired sampled data, thus adaptively forming a beamsum.

While adaptive processing techniques are typically utilized for array configurations, transmitting and receiving from the same element at successive locations produces received signals containing the same information when a small step size is maintained and focusing delays are applied. For the parameters used in this study, from one step to the next, the percent overlap is 97% for the low frequency beam and 62% for the high frequency beam for a step size of 0.9° at a depth of 0.5 mm using one-way beams simulated in Field II. While this overlap is relatively high for B-mode IVUS imaging, due to microbubble motion, differences in microbubble size, and because superharmonic imaging of microbubble contrast agents is at least partially destructive in nature, populations of microbubbles are likely to produce different signals from one pulse to the next, which would be expected to yield significantly reduced correlation in dual-frequency IVUS relative to B-mode IVUS. However, previous studies indicate that 1) lower amplitude superharmonic signals may be produced without microbubble destruction [366], and 2) superharmonic signals produced by microbubbles exhibit partial correlation across short spatial distances [291]. Thus while the performance of the signal processing techniques

presented here would be expected to exhibit less improvement and greater variation for superharmonic imaging of microbubbles than for B-mode IVUS, some improvement can still be expected due to this microbubble partial coherence, which has also been reported by others [386].

In the case of mechanically-rotated IVUS, the received data matrix **X** is an [m × n] matrix containing n axial samples at each of m acquisition angles. In minimum variance beamforming, the [m × 1] weight vector $\boldsymbol{w}$ is defined as:

$$\boldsymbol{w} = \underset{\boldsymbol{w}}{arg\,min}\, \boldsymbol{w}^T \boldsymbol{R} \boldsymbol{w} \tag{8.1}$$

$$\text{subject to } \boldsymbol{w}^T \boldsymbol{a} = 1 \tag{8.2}$$

where $\boldsymbol{a}$ is the steering vector, in this case an $m \times 1$ vector of ones because the data has already been delayed. Receive beamforming delays are computed according to the equation:

$$\tau_m(r_p) = \frac{\|r_{Tx} - r_p\| + \|r_{Rx} - r_p\|}{c} \tag{8.3}$$

where r_p is the point in the field (x_p, z_p), r_{Tx} and r_{Rx} are the coordinates of the transmit and receiving elements, and c is the speed-of-sound. In this work, sampling frequency f_s = 100 MHz, yielding a delay resolution of 10 ns. The turning radius is 0.45 mm.

The solution to the constrained optimization problem posed by Equations 8.1 and 8.2 is [387]:

$$\boldsymbol{w} = \frac{\boldsymbol{R}^{-1}\boldsymbol{a}}{\boldsymbol{a}^T\boldsymbol{R}^{-1}\boldsymbol{a}} \quad 8.4$$

where **R** is the [$m \times m$] sample covariance matrix:

$$\boldsymbol{R} = \boldsymbol{X}\boldsymbol{X}^T \quad 8.5$$

and $\boldsymbol{a}$ is the steering vector. In this work, delays were applied prior to computation and application of the weight vector $\boldsymbol{w}$, as is customary in ultrasound adaptive beamforming [377-383]. Delays were updated every 60 samples (0.46 mm) and for every angular step (0.9°).

In the approach implemented in this work, $\boldsymbol{w}$ is computed only for sub-apertures of size m = 7 with an angular spacing of 0.9° and a rectangular sliding window. The total acquired depth was subdivided into non-overlapping axial segments of n = 60 samples (0.46 mm) to compute adaptive weightings that vary through depth. After computation of **R** from acquired data, the windowed sum for a given sub-aperture and axial segment can be computed directly using

$$\boldsymbol{Y}[n] = \boldsymbol{X}^T w \quad 8.6$$

Because power minimization techniques are heavily dependent on SNR, diagonal loading is often performed by adding a constant to the diagonal of the covariance matrix (*i.e.* uncorrelated noise), in order to improve robustness to noise:

$$\boldsymbol{R} = \boldsymbol{X}\boldsymbol{X}^T + \tau\boldsymbol{I} \quad 8.7$$

where $\boldsymbol{I}$ is an [$m \times m$] identity matrix and τ is the degree of diagonal loading. Synnevåg *et al.* reported diagonal loading with τ proportional to the trace of **R** [379], while Vignon and Burcher selected τ based on the eigenvalues of **R** [378]. Adjusting the degree of diagonal loading allows tuning between robustness to electronic noise and rejection of off-axis energy. That is, for heavy

diagonal loading, $\boldsymbol{w}$ defaults to conventional beamforming, while for low-level diagonal loading, Equation 8.4 is more susceptible to electronic noise. In this work, we selected $\tau = 0.01 \times tr\{\mathbf{X}\mathbf{X}^T\}$, where $tr\{.\}$ is the trace operator, as preliminary simulations indicated that this value of τ ensured robustness while maintaining approximately the same resolution as lighter levels of loading.

8.1.2.3 Phase coherence factor processing

In order to increase the CTR in mechanically-steered contrast-enhanced IVUS imaging, signals arising from subsequent acquisitions over several closely-spaced angular positions can be treated as a sub-aperture. This sub-aperture beamsum is $\mathbf{Y}[n]$ as defined in Equation 8.6. While minimum variance and related beamformers have demonstrated improved resolution, they also require increased computation and produce images with increased speckle variance relative to the conventional delay-and-sum beamformer [377-383]. An alternative approach to adaptive imaging for the improvement of spatial resolution and contrast is the application of the PCF, which operates on beamformed data **Y** rather than on channel data **X**.

The PCF was computed using the phase of delayed RF data as previously described [384, 385]. Delays were applied identically to the other processing cases according to Equation 8.3. Briefly, for every i^{th} depth sample in the axial direction, the phase ϕ_i was obtained via the analytical signal as described by Camacho *et al*. [384], as well as the auxiliary phase ϕ_i^A , in which π was added to ϕ_i if $\phi_i < 0$ and $-\pi$ was added to ϕ_i if $\phi_i > 0$ to avoid phase discontinuities at $\pm \pi$ [385]. The standard deviation of the phase across all received lines in a sub-aperture (in this work, $m = 7$ angular positions) were computed for both ϕ_i and ϕ_i^A, where the standard deviation of ϕ_i is denoted as σ_i and that of ϕ_i^A, is denoted as σ_i^A. The minimum of σ_i and σ_i^A, denoted σ_{min}, was used in the computation of the phase coherence factor as follows:

$$PCF[n] = 1 - \frac{\sigma_{min}}{\sigma_0} \tag{8.8}$$

where $\sigma_0 = \pi/\sqrt{3}$, the nominal standard deviation for a uniform distribution of phases between -π and +π. In order to allow for tuning of the phase coherence factor, the modified version of PCF was used [384]:

$$PCF^{\gamma}[n] = 1 - \gamma\frac{\sigma_{min}}{\sigma_0} \tag{8.9}$$

where γ = 1 yields increased sidelobe suppression and γ = 0 is the non-adaptive case (no PCF weighting).

The phase coherence factor is then applied by using the value of the PCF^{γ} to weight the output of the sub-aperture beamsummed data at each depth:

$$\boldsymbol{Y}_{PCF}[n] = PCF^{\gamma}[n] \cdot \boldsymbol{Y}[n] \tag{8.10}$$

8.1.3 Methods

8.1.3.1 Phantom imaging

Imaging performance was assessed using a custom tissue-mimicking phantom having an attenuation of 0.44 dB/cm/MHz [337]. This phantom was characterized up to 25 MHz after fabrication to measure attenuation and verify the presence of fully-developed speckle at the transmit frequency. The phantom had three straight channels comprised of 200 µm-inner diameter cellulose tubing at depths of 4.0 mm, 4.5 mm, and 7.1 mm. A depiction of the phantom is given in Figure 8.1 and the schematics are given in Appendix B.1.

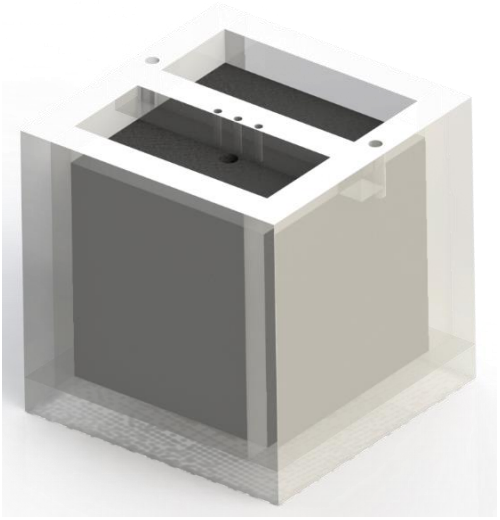

Figure 8.1: Illustration of the 3-channel microvascular phantom used for this experiment.

For phantom experiments, lipid-shelled microbubble contrast agents (10^{8} $^{\mathrm{MCAs}}/_{\mathrm{mL}}$) were infused through the flow channels at a mean velocity of 17.7 mm/s using a calibrated syringe pump (PHD2000, Harvard Apparatus, Holliston, MA, USA). Radiofrequency data was acquired as the IVUS transducer was pulled through the center of the phantom along a distance of 15.0 mm with step size of 200 μm. Acquired RF data were digitized at 100 MHz (Signatec PDA14, Corona, CA) and filtered using a 7$^{\mathrm{th}}$-order Butterworth bandpass filter (-6 dB pass band 24.75-30.25 MHz) in Matlab (The Mathworks, Natick, MA). The processing cases examined were: no summation, rectangular windowing, minimum variance windowing, rectangular windowing with application of the phase coherence factor after beam summation, and minimum variance windowing with application of the phase coherence factor after beam summation. The PCF tuning parameter was $\gamma = 0.25$ and the diagonal loading parameter was $\tau = 0.01 \times tr\{\mathbf{R}\}$ and were applied to PCF and MV weightings, respectively, on phantom data. Final images were displayed in Matlab with 30 dB dynamic range to assess tube diameter.

Manual target identification was required for phantom data. Manual regions of interest (ROIs) were drawn in each slice using ImageJ (NIH, Bethesda, MD) to assess CTR for each type of processing. In order to measure tube diameter, the image was loaded into ImageJ and the tube diameter was determined by drawing a straight line across the target in the lateral (circumferential) direction while displaying only the brightest 6 dB in an image. The observer was not blinded to the data. CTR was computed for each experimentally acquired image using the following equation:

$$CTR = 20\,log_{10}\left(\frac{C}{T}\right) \tag{8.11}$$

where *C* and *T* are the mean pressure signals from regions microbubble contrast agent and tissue, respectively, at equivalent depths and after envelope detection. Improvements in lateral resolution due to applying adaptive windows were evaluated using paired *t*-tests.

8.1.3.2 Ex vivo *and* in vivo *imaging*

In order to assess the performance of these techniques for imaging *vasa vasorum*, both *ex vivo* and *in vivo* models were utilized. The same RFH data collected in Chapter 7 was re-processed with beamforming applications. The chorioallantoic membrane (CAM) of the chicken embryos imaged in this previous study were also used to describe beamforming effects on *in vivo* data. *In vivo* and *ex vivo* data were acquired and processed in the same manner as in the phantom imaging study. Final images were displayed in ImageJ with 30 dB dynamic range.

8.1.4 Results

8.1.4.1 *Phantom imaging*

Illustrative slices through the phantom volume containing the three tubes with microbubble contrast agent are shown in Figure 8.2. The full view of the acquired IVUS image

(with conventional processing, no summation) is displayed in Figure 8.2A, while magnified views of the central tube for each processing type are displayed in Figure 8.2B-F.

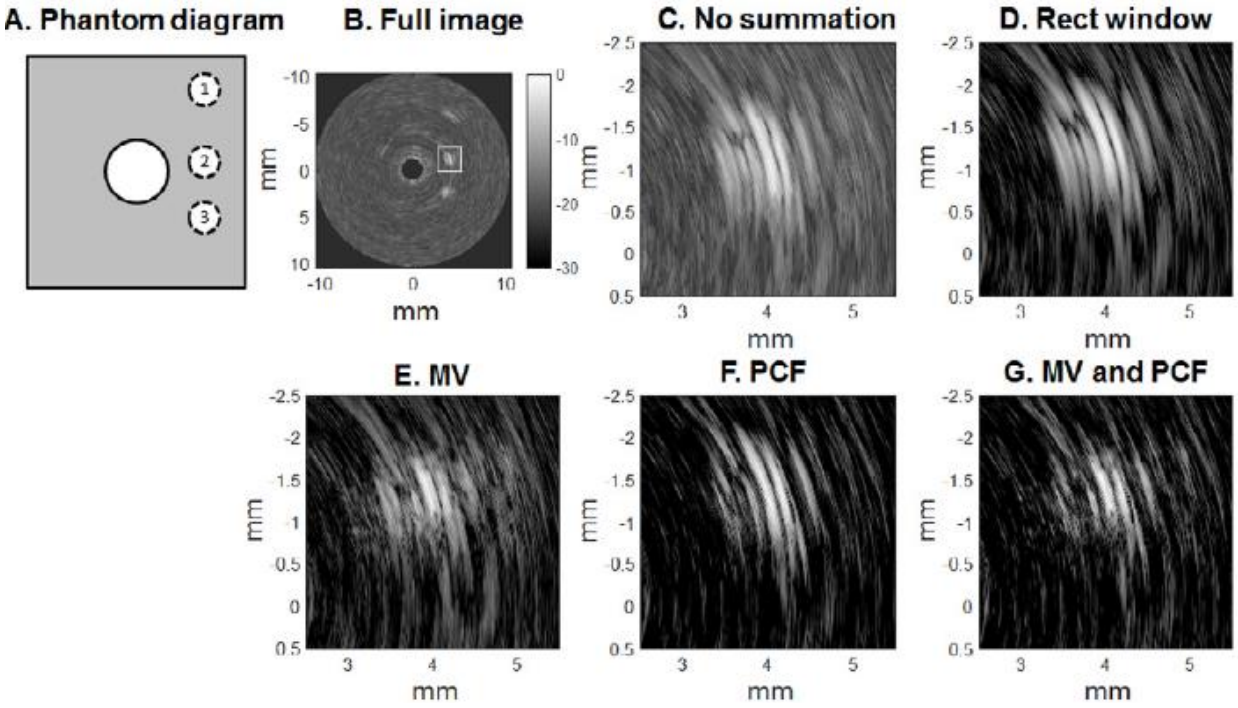

Figure 8.2: Image summary of phantom processing reuslts. Illustrative slices through the center of the tissue-mimicking phantom (A) with three parallel tubes filled with microbubble contrast agent at distances of (1) 7.1 mm, (2) 4.5 mm, and (3) 4.1 mm. (B) Full image view (no summation) indicating the region of interest, and magnified views of the center tube with (C) no summation, (D) summation with a rectangular window, (E) MV window, (F) rectangular window with PCF, and (G) MV window with PCF.

CTR and measured tube diameter for every slice in the 15 mm pullback in are summarized Figure 8.3. While summation with a rectangular window was expected to produce inferior lateral resolution to the no summation case, we found similar resolutions at the -6 dB level for these two processing types in phantom testing. This may be due to the reduced contrast in the “no summation” images, as noisy pixels in final “no summation” images may have been included when measuring the target lateral extent. Minimum variance weighting improved resolution by 41.7% at the cost of only a slight decrease in CTR (0.34 dB relative to the

rectangular window case). Applying the phase coherence factor alone yields an increase in CTR of 4.2 dB but only a slight improvement in resolution (21.8% relative to the no summation case). Applying both MV and PCF produces improvements in both CTR (4.1 dB) and resolution (41.7%). All improvements in resolution due to application of MV, PCF, or MV and PCF weighting are statistically significant relative to the rectangular window case ($p < 0.01$, all cases).

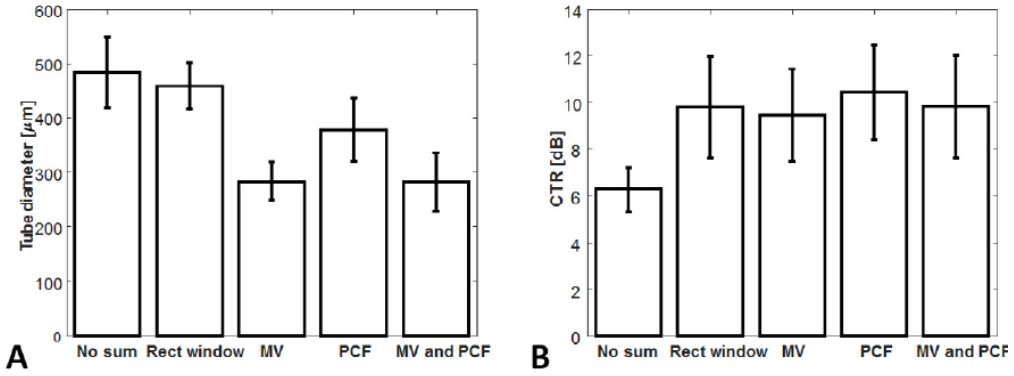

Figure 8.3: Summary of phantom imaging metrics. (A) Mean vessel diameter in a tissue mimicking phantom (Figure 8.2) as a function of processing type across all slices in the acquired 3D phantom pullback. Improvements in resolution due to application of MV, PCF, and MV + PCF weighting are statistically significant relative to the rectangular window case ($p < 0.01$ in all cases). (B) Contrast-to-tissue ratio as a function of processing type across all slices in the acquired 3D phantom pullback.

8.1.4.2 In vivo *imaging*

Single slice IVUS images acquired in a 15-day-old chicken embryo are shown for the various types of processing in Figure 8.4. Vessel diameter and CTR are reported in Table 8.2 for the two embryos. CTR was computed by measuring the mean pixel brightness in the central vessel (Figure 8.4 and Figure 8.5) and also in a region outside the vessel at the same depth. Vessel diameter was measured manually in the same central vessel in ImageJ at the -6 dB level as described in Section 8.1.3.1. Both CTR and vessel diameter were measured for every slice

which contained the vessel. Measurements were averaged across these slices for each animal. The characteristics observed in simulation and phantom studies persist: any form of summation improves CTR by increasing SNR, while MV windowing improves spatial resolution over non-adaptive windowing at the expense of CTR.

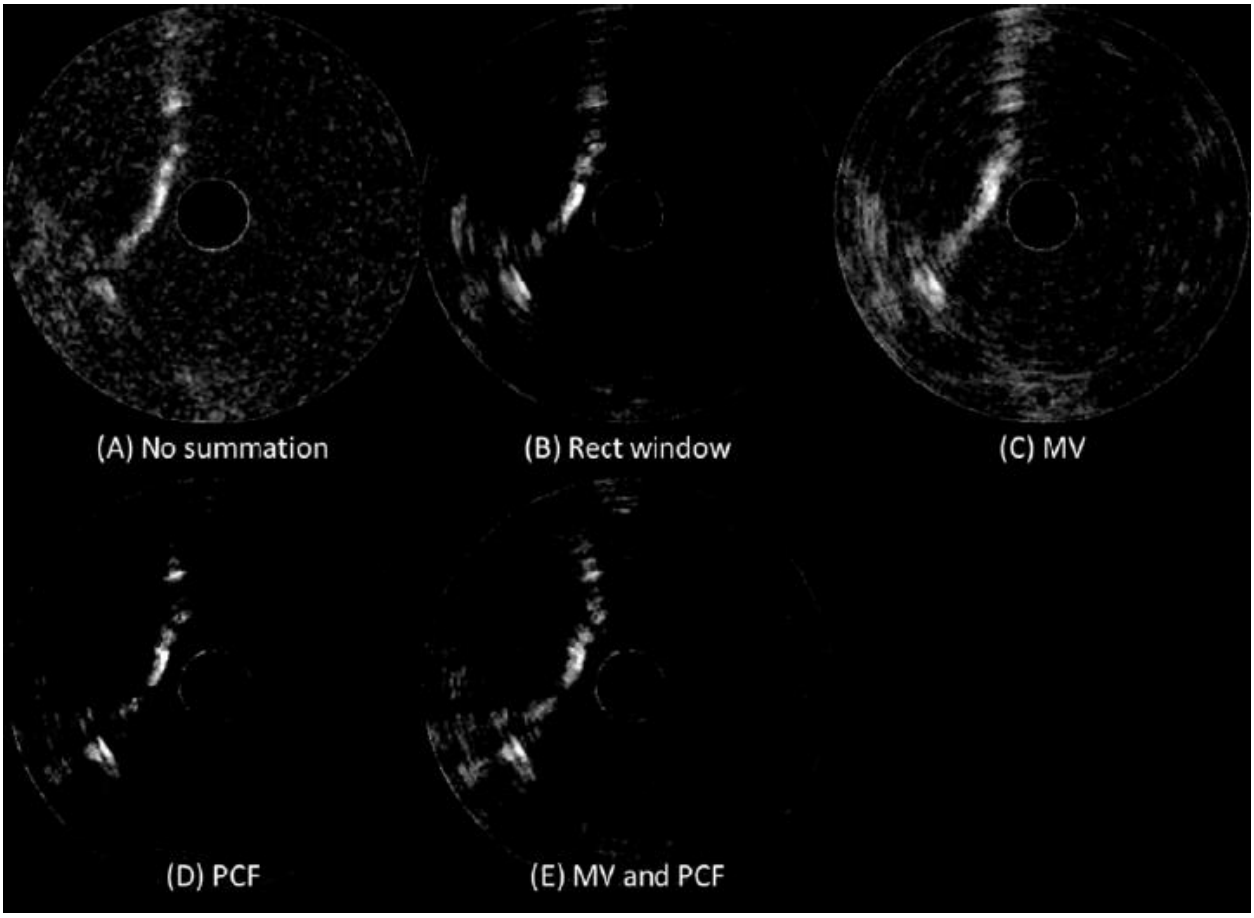

Figure 8.4: Chorioallantoic membrane images with adaptive processing methods. *In vivo* slices through vessels of the chorioallantoic membrane in a 15-day-old chicken embryo with (A) no summation, (B) rectangular window, (C) minimum variance window, (D) rectangular window and phase coherence factor, and (E) minimum variance window and phase coherence factor. Total scan depth is 1 cm.

Summation with a rectangular window yields a mean increase in CTR of 3.20 dB relative to no summation, while summation with a rectangular window and PCF produces a nearly

identical improvement in CTR of 3.19 dB. While CTR is relatively similar for summation with a rectangular window, rectangular window with PCF, or MV window with PCF, measured vessel diameter decreases with the adaptive processing as the PSF decreases in width. MV windowing, PCF with rectangular windowing, and MV windowing with PCF yielded mean decreases in vessel diameter (*i.e.* improvement in resolution) of 28.0%, 30.7%, and 37.2%, respectively (Table 8.2).

Table 8.2: CTR and vessel diameter measured across all relevant slices in two 15-day old chicken embryos.

	CTR [dB]			Vessel Diameter [μm]		
	Embryo 1	Embryo 2	Mean change	Embryo 1	Embryo 2	Mean change
No summation	10.84 ± 2.35	11.99 ± 1.51	-	430.90 ± 102.24	484.88 ± 62.24	-
Rect window	13.91 ± 2.78	15.32 ± 1.03	+3.20 dB	394.54 ± 104.10	353.75 ± 55.56	-17.74%
MV window	10.98 ± 2.79	12.48 ± 1.12	+0.32 dB	363.86 ± 71.58	288.57 ± 77.17	-28.03%
PCF	13.48 ± 2.74	15.72 ± 0.76	+3.19 dB	372.62 ± 109.13	253.20 ± 32.98	-30.65%
MV and PCF	11.65 ± 2.74	15.53 ± 0.75	+2.18 dB	323.58± 115.21	244.58 ± 32.53	-37.23%

8.1.4.3 Ex vivo *imaging*

The results of 3D pullback imaging in the porcine artery are shown in cross sections in Figure 8.5 and in volume renderings in Figure 8.6. This image provides a view of the type of data that might be provided by utilizing this imaging approach clinically: B-mode (grayscale) IVUS imaging data providing vessel anatomy (transmit and receive at 30 MHz) is combined with dual-frequency imaging data (transmit 6.5 MHz, receive 30 MHz, shown in red) providing visualization of the microtube simulating the *vasa vasorum* along the larger excised porcine vessel. The described processing techniques were applied to both the B-mode and dual-frequency data. Summation across m = 7 elements visibly enhances the ability to visualize the contrast agent in the 200 μm tube. Images similar to these could prove diagnostically valuable for assessing plaque vulnerability, planning interventional procedures, or for post-procedural monitoring.

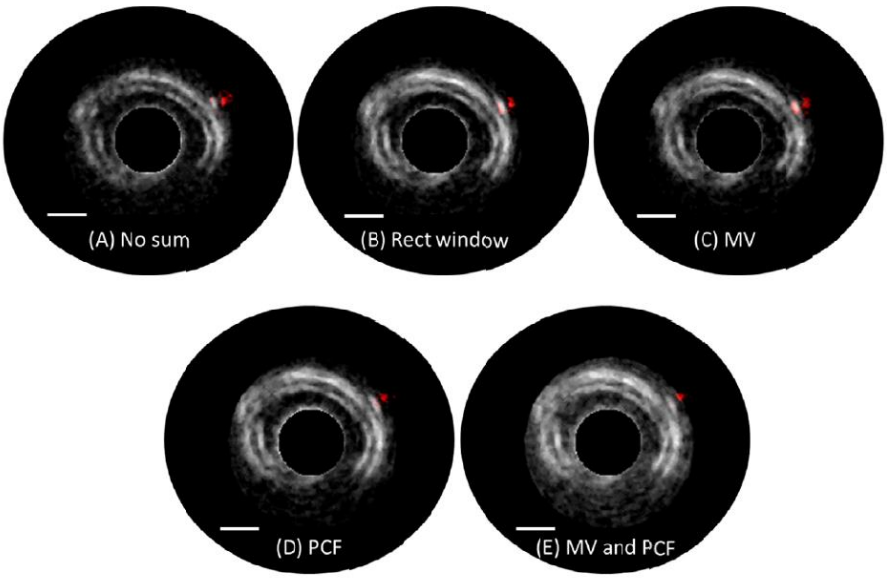

Figure 8.5: Adaptive beamforming methods applied to *ex vivo* porcine vessels. Cross-section views of *ex vivo* porcine arteries (grayscale) and an adjacent tube filled with microbubble contrast agent (red) positioned outside of the vessel to mimic *vasa vasorum*. Scale bar indicates 1mm.

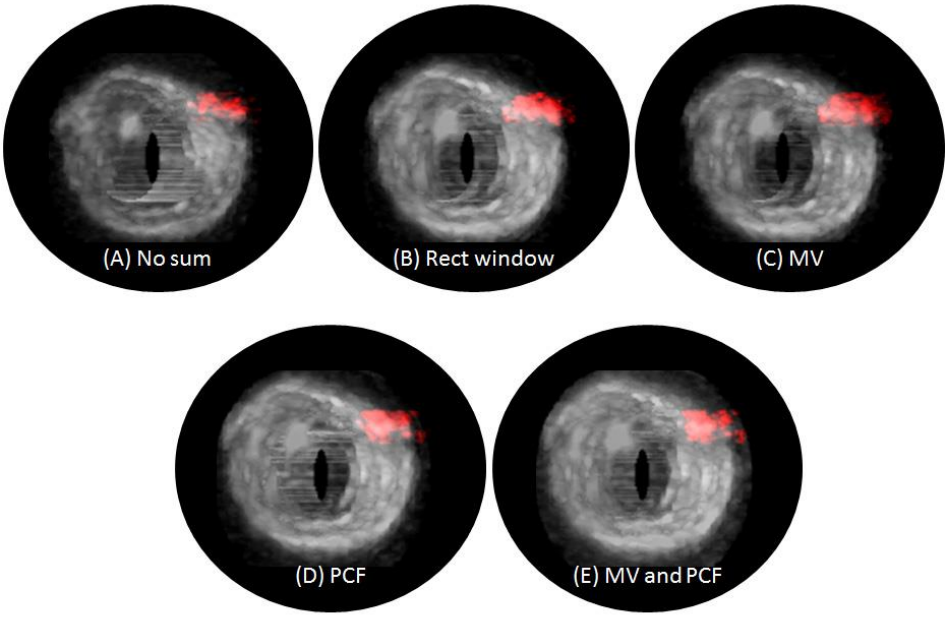

Figure 8.6: 3D renderings acquired via motorized pullback in a porcine artery with a tube filled with microbubble contrast agent positioned outside of the vessel to mimic *vasa vasorum*.

8.1.5 Discussion

8.1.5.1 Phantom and in vivo *imaging experiments*

In phantom studies, application of MV weights and the PCF both produced improvements in resolution (Figure 8.3A), with all summed cases exhibiting similar CTR (Figure 8.3B). This behavior was also observed *in vivo* in the vessels of the chorioallantoic membrane of the two chicken embryos (Table 8.2), with a 37% improvement in resolution and 2.2 dB improvement in CTR when both MV weighting and PCF were applied. Given the relatively low SNR *in vivo* in [330] the no summation case (14 dB) , it is possible that diameter estimation in this case is limited by the SNR, leading to underestimation.

High variances in measurements of CTR in phantom and *in vivo* experiments when either MV or PCF were applied are indicative of the dependence of these processing techniques on SNR, which is consistent previous work investigating adaptive beamforming techniques [377-383]. However, the PCF, which was applied only at low levels in this work ($\gamma = 0.25$), appears to be more robust than adaptive beamforming such as MV in a low-SNR environment. The unique nature of this data, in which echoes originate only from microbubbles with very low-amplitude tissue echoes, must also be considered, as it is quite different from B-mode ultrasound data to which MV and PCF have previously been applied. Specifically, the fully-developed speckle present in B-mode ultrasound images is not expected to be present in these dual-frequency contrast-specific images, though this has not been examined in detail. Acquired *in vivo* images of the fine vasculature in the CAM demonstrate an additional challenge in that some echoes arise from microbubbles in sub-resolution vessels, making these regions appear noisy when they are actually filled with microbubbles in vessels that are still too small to resolve in spite of the described improvements.

In quantifying observed improvements in the phantom images presented in this article, (Figure 8.3), we are able to measure vessel diameters closer to 200 μm when using adaptive processing techniques (*i.e.* 282 μm for 200 μm tubes, Figure 8.3B). We have also observed modest improvements to both CTR and the ability to measure vessel diameters *in vivo* in a chicken embryo model (Figure 8.4, Table 8.2), which is encouraging for high resolution IVUS imaging in an *in vivo* environment such as for *vasa vasorum* imaging.

8.1.5.2 Considerations for implementation and implications for vasa vasorum *imaging*

In this chapter, we have demonstrated the potential benefits to both image contrast and spatial resolution due to applying two adaptive processing techniques to contrast-enhanced IVUS imaging. These benefits occur with the same hardware and acquisition parameters that we have previously used with this prototype system. However, as all processing presented in this work was performed offline, a potential challenge exists in implementing these techniques in real-time. In the initial paper describing the application of the phase coherence factor in ultrasound, Camacho *et al*. discuss in detail the efficient implementation of this technique [384], suggesting that PCF may be able to be implemented in a commercial IVUS system. Implementing adaptive beamforming may be more difficult and costly, though several near-real time implementations of adaptive beamformers with large array-based systems have recently been demonstrated [388-391]. Another consideration for this particular technique, which utilizes superharmonic echoes from partial destruction of microbubbles [366], is the frame rate, which needs to be kept sufficiently low to allow microbubble reperfusion. While IVUS imaging in general strives to maintain higher rotation rates to allow for averaging and high frame rates, decreased rotation rates which are necessary to allow for microbubble reperfusion also provide increased computation time. For reduced rotation rate IVUS such as for superharmonic microbubble

imaging, sub-aperture beamforming could provide an alternative means of improving SNR and contrast given that averaging across multiple revolutions may be impractical due to the influence of motion artifacts at these lower rates. For IVUS in general, the techniques presented in this chapter could be applied by saving RF data (*i.e.* during a single pullback) and reconstructing afterwards to yield a higher resolution image. For B-mode IVUS, averaging signals acquired from the same angular positions could be used to improve SNR while maintaining constant resolution.

In this chapter, we have described signal processing approaches which allow formation of images in which a 200 µm tube measures 282 µm using a prototype dual-frequency IVUS transducer. We have also demonstrated the ability to image 200-300 µm vessels in an animal model, with the proposed processing yielding a mean decrease in vessel diameter of 37.2%. Further improvements in resolution may be realized by the development of new transducer prototypes. The reported improvements in resolution may also be helpful in other applications of intravascular ultrasound such as peripheral vascular disease or in endoscopic ultrasound.

8.1.6 Conclusion

In conclusion, we have applied sub-aperture beamforming to data acquired using a prototype mechanically-steered IVUS transducer at adjacent angular locations. Specifically, conventional and minimum variance beamforming were applied to sub-apertures of seven elements, and the phase coherence factor was applied after summation. These approaches were demonstrated in tissue-mimicking phantoms, an *ex vivo* porcine artery, and *in vivo* using a chicken embryo model. In phantom studies, PCF processing improved CTR by a mean of 4.2 dB, while combining PCF and MV processing decreased spatial resolution by 41.7%. Combining both techniques demonstrated preservation of both benefits, with mean improvements of 2.2 dB

in contrast and 37.2% in resolution observed *in vivo*. Additional gains may potentially be realized in the future by optimizing selection of tuning parameters for these adaptive techniques to better match the SNR. Applying these processing strategies can enhance image quality in IVUS, a low-SNR imaging technique where resolution is at a premium.

8.2 Automated, multi-dimensional speed-of-sound estimators for vascular enhancement

Vascular images can be obtained in a variety of acoustic methods. Until this point, the discussion has been limited to those obtained using superharmonic detection of nonlinear microbubble responses in IVUS. However, other acoustic methods of obtaining vascular images can benefit from the equivalent post processing approaches to enhance image quality. Photoacoustics is a method of obtaining images from endogenous contrast in tissue as a product of light-induced thermal expansions and passive acoustic array detection. Images volumes can be reconstructed using an acoustic array and beamforming algorithms. Images from this acoustic modality have a common assumption shared with those produced in superharmonic contrast imaging or even B-mode imaging. In the process of creating or reconstructing these images, one assumes a wave speed-of-sound based on the medium that the acoustic signal is expected to

travel through and this assumption is frequently violated *in vivo*. In the remainder of this chapter, we discuss an automated algorithm for determining and correcting for these sound speed errors as well as demonstrate the effect on image quality when these errors are not taken into account. This approach is based on the use of focusing metrics to spatially determine the correct

---

Chapter 8.2: K. H. Martin, R. B. Lam, C. M. Kuzmiak, P. A. Dayton, S. P. del Rio, D. R. Reinecke, and R. A. Kruger, "Spatially adaptive speed of sound selection for photoacoustic tomography using multi-dimensional autofocusing." *Journal of Biomedical Optics*. 2016. Submitted.

KHM authored the above work with edits provided by RBL, PAD and RAK. SPR, DRR, RBL and RAK designed the photoacoustic system and collected *in vitro* data. CMK collected *in vivo* data. KHM performed numerical studies, designed the algorithm, evaluated their performances.

speed used to reconstruct individual voxels within a vascular image dataset obtained using photoacoustics, however, it is fully extendable to any image that makes a speed-of-sound assumption, such as superharmonic IVUS imaging.

8.2.1 Introduction

Photoacoustic tomography (PAT) relies on accurately knowing the speed at which sound propagates through the medium in order to reach the transducer. Most often, a single speed-of-sound (SOS) is assumed to apply to the whole volume of the reconstruction in order to make an image [392]. However, propagation speed in tissue can vary widely depending on its composition, ranging from 1.450 mm/μs in fat to 1.615 mm/μs in skin (10.7% change) [393]. When the SOS used for reconstruction is different from the actual SOS, the signals are not properly aligned prior to summation in conventional beamforming or back-projection, reducing the resolution and the SNR of the resulting image. When reconstructing locations at increasing distance from the transducer array, SOS errors as small as 0.3% can double the resolution size and drastically lower the SNR (Figure 8.7). Common practice for precision acoustic imaging systems, which are sensitive to SOS variations, includes manually adjusting the reconstruction SOS through trial and error until a "best" image is achieved for a region of interest. The SOS optimally focusing in one location is oftentimes not appropriate for a different part of the image as tissue sound speed is heterogeneous.

Compensating for variations in SOS in PAT has been studied previously using a variety of methods. Iterative reconstruction approaches using ultrasound transmission tomography have been shown to produce SOS distributions by utilizing wavefront propagation models [394, 395]. Operating the receiving array in transmission mode has aided other photoacoustic based

techniques, but ultrasound transmission cannot be applied to all photoacoustic setups and often requires additional hardware [396], or may rely on exogenous absorbers for generating an ultrasound pulse using optical excitation [397, 398]. Time reversal reconstructions can provide speed-of-sound information within conditionally stable scenarios, although it is computationally expensive [399]. Additionally, three dimensional reconstructions using finite element approaches have been demonstrated to provide not only volumetric images but also 3D SOS variations through simulation [400]. Seemingly disjoint SOS variations found at tissue interfaces, such as bone and tissue or air and tissue, can be detected immediately and corrected for using statistical analysis in an automated approach [401].

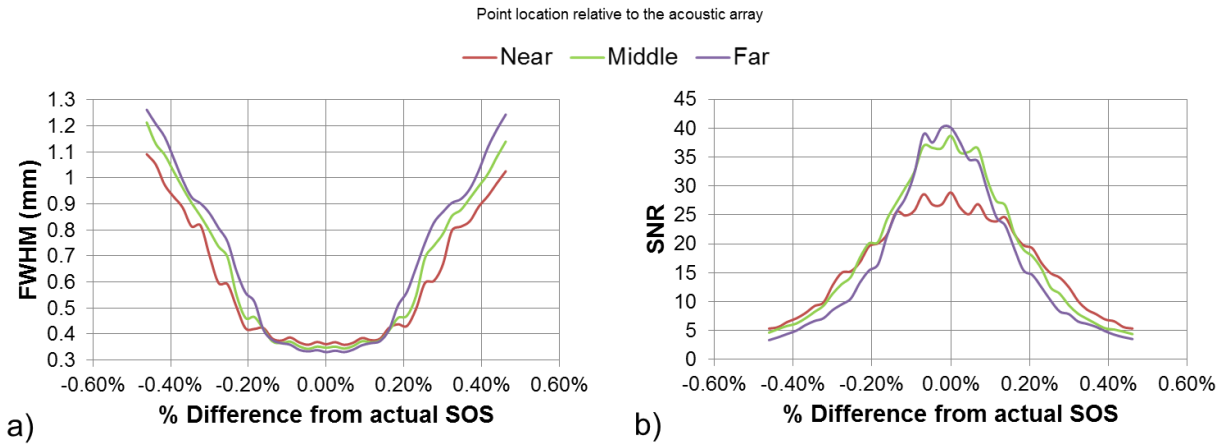

Figure 8.7: A single point target is simulated and then reconstructed with varying SOS. The distance of the point from the array is adjusted to be 11.7 cm (near), 12.7 cm (middle), or 13.7 cm (far) from the reception array. a) The full-width, half-maximum (FWHM) of the target increases rapidly when small errors in SOS are present. b) The signal to noise ratio (SNR) of the same target is reduced as a consequence of performing reconstructions with SOS errors.

When the object being imaged has highly delineated edges, such as when imaging vasculature, sharpness metrics have been used to determine when images are maximally focused with respect to varying SOS. Treeby *et al*. showed that focusing metrics in photoacoustic

imaging of murine vasculature can determine the optimal SOS applied to a whole image using a variety of sharpness metrics [402]. The approach presented in this paper extrapolates from Treeby by extending it to 2D and 3D, creating spatially varying SOS maps (referred to as CMAPs) by comparing image focus on a voxel by voxel basis. The methods to produce spatially adaptive SOS reconstructions are outlined and the results are compared to conventional, single SOS images.

8.2.2 Materials and methods

8.2.2.1 Imaging system description

The spatially adaptive speed-of-sound selection algorithm was designed and tested using a dedicated photoacoustic imaging system for breast mammography that has been described previously [403]. Briefly, the photoacoustic mammography (PAM) system consists of an Alexandrite tunable laser combined with a hemispherical passive array of 512 transducer elements coupled with water to the imaging space. The radius of the hemispherical array was 127 mm. The transducers were composed of a 1-3 composite piezoelectric material with an aperture of 3 mm in diameter. The transducers operate at a center frequency of 2 MHz with a -6 dB BW_f of 70%. Optical exposures were performed at 756 nm for 75 ns (~300 mJ/pulse) after passing the laser beam through a diverging lens to conically spread the beam to approximately 60 mm in diameter at the breast skin surface. Peak light fluence was measured to be well below maximum permissible exposure (MPE) limits sanctioned by the American National Standards Institute [404]. Images of phantoms and patients were acquired by firing the laser at a pulse repetition frequency of 10 or 20 Hz while synchronous motors were used to scan both the laser source and acoustic detecting array from beneath the imaging space. Transducer signals were pre-amplified, then digitized in parallel at a sampling rate of 20 MHz, and saved for offline reconstruction.

Image volumes were reconstructed using a modified approach to previously described filtered back-projection algorithms [403, 405, 406]. The reconstruction algorithms were modified to accept SOS distributions that vary as a function of voxel position. Deconvolution of the transducer impulse response and application of a ramp filter was performed digitally before back-projecting the data to iso-surfaces determined from times of flight using the pre-computed CMAP which contained the SOS value per voxel. Reconstruction time was dependent on the number of positions collected during acquisition as well as the number of voxels chosen to represent the image space. Reconstruction was performed using a single NVIDIA Tesla C1050 GPU (CUDA compute capability of 1.3) at a rate of approximately 6.25e6 (vx*positions)/s. Single SOS reconstructions were performed by supplying a repeating scalar as an input to the modified reconstruction algorithm for direct comparison of image volumes.

8.2.2.2 Automated speed-of-sound selection

Autofocusing methods in photoacoustics using quality metrics such as image sharpness have been explored previously for selecting an optimal speed-of-sound for an entire reconstruction volume [402]. Treeby *et al*. reported comparisons of three different focus functions applied to PAT, and evaluated them on either 2D maximum intensity projections (MIP) of image volumes or upon the 3D image volumes themselves. Of the focusing metrics tested, the Brenner gradient performed the best as indicated by having a narrow, unimodal focus function that was maximum when at the correct SOS. Internal review with preliminary data confirmed these observations and thus was selected as the focus metric for this study. The Brenner gradient was modified to allow local variations in image sharpness, yielding Eq. 8.12.

$$F_N = \sum_{i=1}^{N} (\boldsymbol{r}[x_i + 2] - \boldsymbol{r}[x_i])^2 \qquad 8.12$$

where N represents the dimensionality of the discrete imaging space, $\boldsymbol{r}$ is the image intensity across dimensions $x_1, x_2, \ldots, x_N$, and F_N is the N-dimensional modified Brenner gradient. Application of a kernel over the Brenner gradient then can provide a metric to identify regions that are in focus by summing components of local sharpness to evaluate the relative focus at the voxel where the kernel is centered. Multiple kernel types were internally reviewed, but for the purpose of reporting this approach, only the results from a Hamming window kernel are given. The size of the kernel (the width of the Hamming window) was varied from 0.25 mm to 10 mm at non-uniform increments (0.25, 0.5, 1, 5, 10 mm) to understand the behavior of this approach with respect to kernel size.

Multiple single SOS reconstructions were initially solved to produce a reference library to quantify image focus, using either 2D or 3D variants of the modified Brenner gradient. Unless specified otherwise, single SOS reconstructions were performed within the range of 1400 – 1550 m/s at a step size of 2.5 m/s. The selected range corresponds to limits of reconstruction that are typically seen in physiological data acquired using this system, and this range can be changed as required for other PAT systems. After the reference reconstructions using constant SOS were solved, the local sharpness was quantified using the N-dimensional Brenner gradient for every image. An N-dimensional summing kernel of varying size would then be convolved with the sharpness metric to identify regions of high focus, $S(k_N)$ (Eq. 8.13).

$$S(k_1, k_2, \dots, k_N) = \sum_{m_1=a_1}^{b_1} \sum_{m_2=a_2}^{b_2} \dots \sum_{m_N=a_N}^{b_N} F_N(m_1, m_2, \dots, m_N) \times w(k_1 - m_1, k_2 - m_2, \dots, k_N - m_N) \quad 8.13$$

where N represents the dimensionality of the discrete imaging space, w is the N-dimensional summing window of length L_N, F_N is the Brenner gradient with length M_N, $a_N = \left\lceil \frac{L_N - 1}{2} \right\rceil + 1$, and $b_N = a_N + M_N - 1$.

After applying a kernel to the Brenner gradient, image sharpness was compared on a voxel-by-voxel basis by iterating through each constant SOS reconstruction to create an N-dimensional lookup table storing the SOS that produced the maximum sharpness for each voxel. While the entire image volume was used for the 3D Brenner gradient, the 2D Brenner gradient was applied to the MIP of the image volume. The orientation of the projection vector in which the MIP was processed was varied, and it was found from initial testing that SOS estimates were more accurate when the vector was selected to be parallel to the direction of laser illumination.

In the case of the 2D Brenner gradient, 3D CMAPs were generated by generating a 2D SOS lookup table and then repeating that matrix in the direction originally used to generate the MIPs. The 3D CMAPs are then used as an input to the reconstructor to form the final, adaptive image volume. A graphical depiction of the approach is summarized in Figure 8.8.

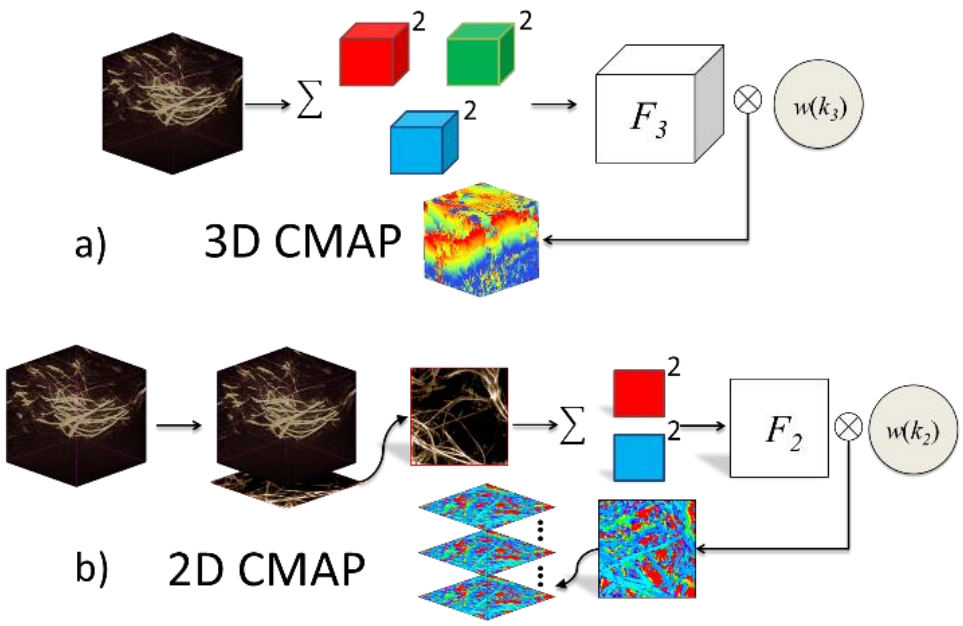

Figure 8.8: Processing chart describing the steps used to create spatially varying speed-of-sound maps using automated selection in either a) 3D or b) 2D. Portions of this figure were created using 3D slicer (www.slicer.org) [407].

8.2.2.3 Numerical phantoms

We evaluated this approach with numerical studies, a breast phantom, and on clinical trial patient data. To accurately determine the behavior of the algorithm, we performed numerical studies by simulating acquired data in phantoms with a known SOS. The numerical phantoms modeled a pattern of point targets embedded in a non-dispersive, non-attenuating medium, with each point target having a known SOS that would optimally reconstruct it. For this study, two numerical phantoms were developed to test algorithm performance in conditions where the photoacoustic signal sources would be distributed either sparsely or closely packed. In either case, radiofrequency data was simulated per transducer channel by calculating the transit time between the target and the transducer array using a single SOS for each target provided by the user. It is important to note that the numerical phantoms do not attempt to simulate the physics of sound wave travel through anisotropic mediums with varying speeds, but instead seek to provide

a unique distribution of point targets that would be reconstructed optimally with a known speed-of-sound to test the effectiveness of the algorithm.

The first phantom was designed to model the condition where signals arising from targets are sparsely distributed, a case that may arise in PAM where detectible blood vessels may be absent from a portion of the breast. The point targets of this numerical phantom were arranged in a uniform grid pattern with an inter-point spacing of 40 mm. The grid was located in a direction normal to optical illumination with a distance to the laser source modulated by a Gaussian function (σ = 15 mm) within ±40 mm of the hemispherical bowl's focus. The SOS for these points ranged from 1.400–1.550 mm/μs and were distributed according to another Gaussian function (σ = 15 mm). The outer dimensions of the grid were 240 x 240 x 80 mm which represents a full volume scan of this system, similar to the size used when imaging a breast. The positions of the point targets of the grid phantom as well as the distribution of SOS for each point are depicted in Figure 8.9a. Images were reconstructed using 256 x 256 x 100 voxels with a voxel spacing of 1 mm/vx. Reconstructing a single image took approximately 8 seconds using our previously mentioned hardware.

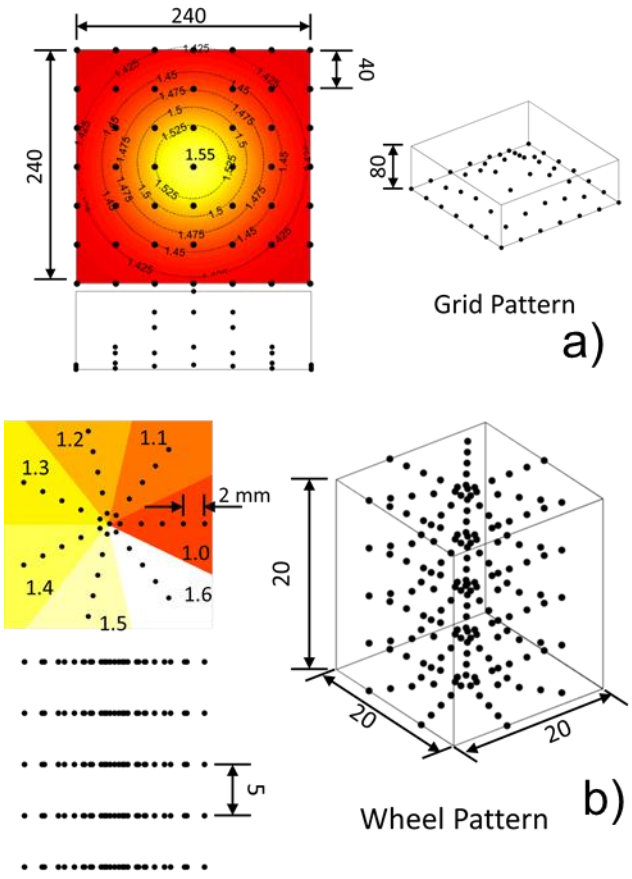

Figure 8.9: An illustration of the numerical phantoms. a) The grid phantom is designed for evaluating performance when using a large field of view with large voxel sizes. The SOS is listed in isocontours on the grid pattern overlay. b) A wheel phantom consisting of several rays of point targets spaced regularly. Each ray should be reconstructed with a single speed-of-sound depicted by the number located outside the ray. The point in the center of the phantom has a SOS of 1.490 mm/µs. All reported distances are in mm.

The second numerical phantom consisted of a closely packed set of point targets arranged in a spoke and wheel arrangement – this simulates different SOS tissues in close proximity. Each spoke of the wheel phantom contained a set of points radially placed between 1 and 9 mm with 2 mm spacing (Figure 8.9b). All points within a spoke had a single speed-of-sound that increased from 1.0 to 1.6 mm/µs tangentially. The wheel pattern of points were repeated at differing imaging planes normal to the laser source and occupied a region within ±10 mm from the focus

of the spherical array. Images were reconstructed using 256 x 256 x 256 voxels with a spacing of 0.125 mm/vx and it took approximately 80 seconds to reconstruct a single image volume.

The number of positions acquired using the system affects image quality as well as the time it takes to collect data and reconstruct the image. Generally, using more positions improves the image quality (higher SNR and possibly smaller FWHM) but takes more time to process and thus is important to consider when making a phantom used to quantify performance. The positioning of the scanner bed in the numerical phantoms was arranged as a planar grid of uniformly spaced points matching the outer dimensions of the phantom when observing the phantom in the top-down direction seen in the SOS variations of Figure 8.9. The spacing between positions was 40 mm for the grid phantom and 4 mm for the wheel phantom. The number of positions used was 49 and 36 for the grid and wheel phantoms, respectively. Both phantoms were evaluated with 2D and 3D versions of the automated sound speed selection algorithm and the image metrics were summarized.

8.2.2.4 Graphite phantom

The behavior of the autofocusing algorithm using acquired data in a controlled environment was evaluated in a graphite fiber phantom to simulate fine vasculature within a breast. The graphite fibers had a diameter of 6 μm and were embedded in an agar mold and placed in the breast cup for imaging as described previously [403]. A MIP of the graphite phantom is shown in Figure 8.10 using a single speed-of-sound at 1.4925 mm/μs to illustrate how the phantom appears in photoacoustic images. Imaging the phantom took approximately 50 seconds to scan 480 locations arranged in a spiral pattern with an outer radius of 48 mm. Image volumes were reconstructed using 256 x 256 x 256 voxels with each voxel representing 0.125 mm to give a field of view of 32 mm in each direction, and this took approximately 60 seconds

to reconstruct. The adaptive images were compared against single SOS images in order to compare the effects of accounting for SOS heterogeneities.

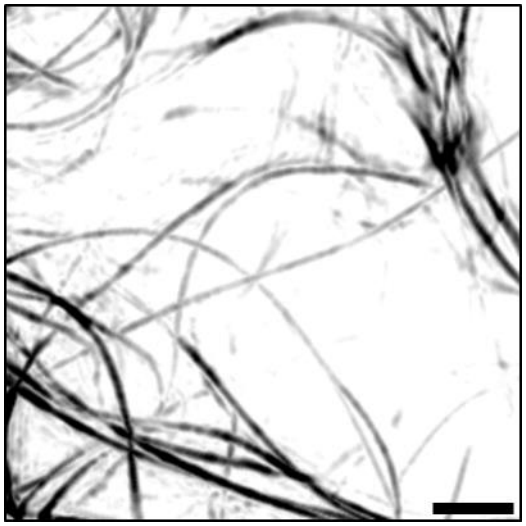

Figure 8.10: Reconstruction using a single speed-of-sound of the graphite fiber phantom. Scale bar in the lower right corresponds to 5 mm.

8.2.2.5 Photoacoustic mammography data

Automated SOS selection was performed on breast mammography collected previously from a volunteer. The patient was instructed to lay prone on the imaging table, with her breast placed into the scanning region of the hemispherical array. Clean water was used to couple the breast to the imaging array and the patient was instructed to breath normally during the scan. A trained research technologist positioned the patient with her opposite arm above her head of the breast being scanned. The scan was completed using 2048 positions along a 96 mm spiral which took less than 3.5 minutes to complete. Patient data was de-identified and offloaded from the system for later analysis. Image volumes were reconstructed using 800 x 800 x 256 voxels with a spacing of 0.25 mm/vx, requiring approximately 70 minutes to reconstruct a 3D image. Patient protocols were approved by the Institutional Review Board of North Carolina University.

Constant SOS reconstructions were performed on an interval of 1.4650 – 1.5300 mm/μs at 0.0025 mm/μs spacing.

8.2.3 Results

8.2.3.1 Numerical phantoms

Image quality of numerical phantoms were quantified using SNR and by measuring the FWHM of point targets using an automated method. The local SNR was measured by cropping a cube of the total image volume (side lengths of 35 mm for the grid phantom, and 1 mm for the wheel phantom) centered on the point target. Signal regions were considered lying within a fixed radius of 2 mm (grid) or 0.5 mm (wheel) from the center of the cropped image sub-volumes while noise regions were considered lying outside of this radius. SNR was computed by subtracting the maximum voxel value of the signal region from the noise region and dividing the result by the standard deviation of the noise. The FWHM of the point targets was measured using two orthogonal directions from MIPs of each target. Profiles having a single pixel width were pulled from image volumes at coordinates where point targets would reside when perfectly reconstructed. The two orthogonal profiles were up-sampled by a factor of 8 using cubic interpolation in MATLAB (The Mathworks, Natick, MA, USA) before measuring and averaging the two FWHM of each point. The number of point targets that were reconstructed for each trial was also monitored. Point targets having a negative SNR or lacking a single peak in both directions were classified as being improperly reconstructed. Image metrics of the targets considered improperly reconstructed are excluded from the summary of data seen in Figure 8.11, but the number of point targets that failed to be reconstructed were tracked and summarized separately to the image metrics provided.

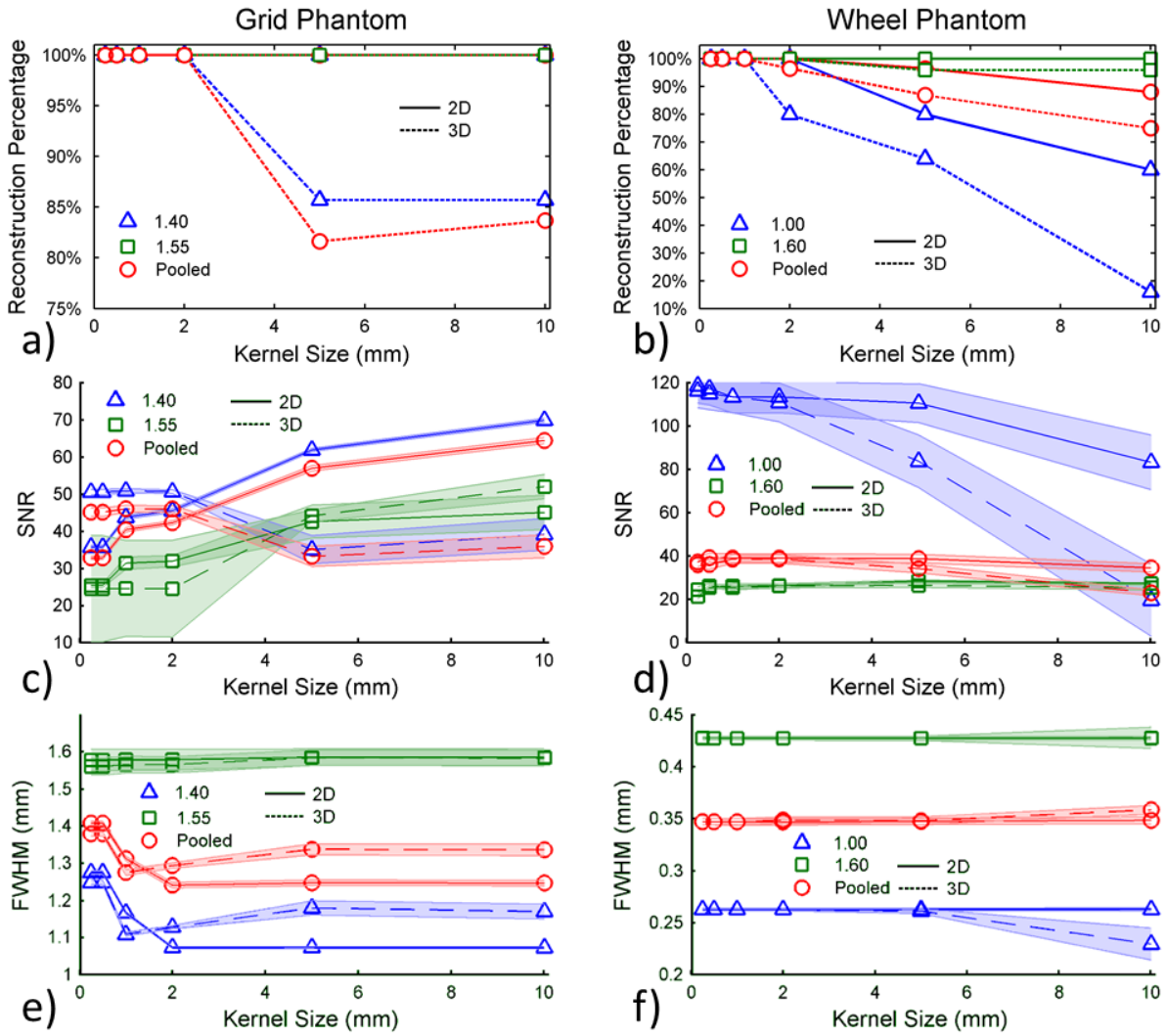

Figure 8.11: Summary of image metrics for both numerical phantoms. The grid phantom (left column) and wheel phantom (right column) metrics are computed on adaptive images. Point targets at different SOS were considered both separately according to the SOS listed in the legend as well as combined (pooled). Either 2D (solid line) or 3D (dashed line) summing kernels were used to generate CMAPs as the kernel size was varied. Shading about the line represents the standard error of the mean (sem).

The frequency content of the RF signals used to simulate the point targets was created using a single, representative impulse response of the transducer array. While the frequency content was maintained across all points, the SOS used to reconstruct the point targets was changed. This caused the wavelengths of the simulated targets to vary directly with their SOS

and introduces variability in terms of the image metrics. Point targets having a higher SOS have a longer wavelength and correspondingly larger FWHM. To monitor the effectiveness of this algorithm on point targets with varying sound speeds, image metrics were either pooled across all SOS or by binning them into a small range (Figure 8.11a, c, e). The lower SOS bin selected for the grid phantom was 1.400 – 1.425 mm/μs (labeled 1.40) while the upper SOS bin was 1.525 – 1.550 mm/μs (labeled 1.55). Binning was performed on the grid phantom since the SOS distribution was a sampled continuous function, but binning did not have to be performed on the wheel phantom since only 8 discrete SOS were assigned within the whole phantom.

The point targets having the highest speed-of-sound for each phantom had larger FWHM (Figure 8.11e-f) and were reconstructed with higher success rates (Figure 8.11a-b) than their slower counterparts, but generally with lower SNR (Figure 8.11c-d). This trade-off may have been impacted by the way the numerical phantoms were simulated, as the same amount of energy was used to simulate a larger target (a target with a larger wavelength) as it was to simulate a smaller target (a target with a smaller wavelength). The signal magnitude would likely vary between these two since the volume in which the energy is deposited is largely influenced by simulated wavelength. Image metric results between the two phantoms illustrate the behavior of the phantom based on the proximity of point targets. In the grid phantom, the targets sparsely populate the field of view, so the image quality becomes better (higher SNR and lower FWHM) when using larger kernel sizes. Likewise, the reverse is true for the wheel phantom, which has multiple targets located within a small region. The reconstruction percentage, SNR, and FWHM of the wheel phantom were worse when using a larger kernel size. These results suggest that the kernel size should be selected based upon the imaging environment in order for the approach to work optimally.

Figure 8.12 shows a comparison of reconstructing the numerical phantoms using a single SOS applied to the image space versus when using either a 2D or 3D version of the adaptive reconstruction with spatially varying SOS. Performing a single SOS reconstruction for either of these phantoms is not appropriate as the large majority of the targets have a considerably different SOS, causing many point targets not to appear in the image (Figure 8.12, a-d). Conversely, both the 2D and 3D adaptive SOS images (Figure 8.12, e-h) display nearly all the point targets. The performance of the 2D adaptive approach for estimating the SOS generally produced images of better quality than the 3D version of the algorithm. This observation has been cited previously when using autofocusing metrics to select for SOS [402], where it was suggested that the MIP operation used when performing the 2D approach reduces the overall noise to aid in accurate SOS estimation.

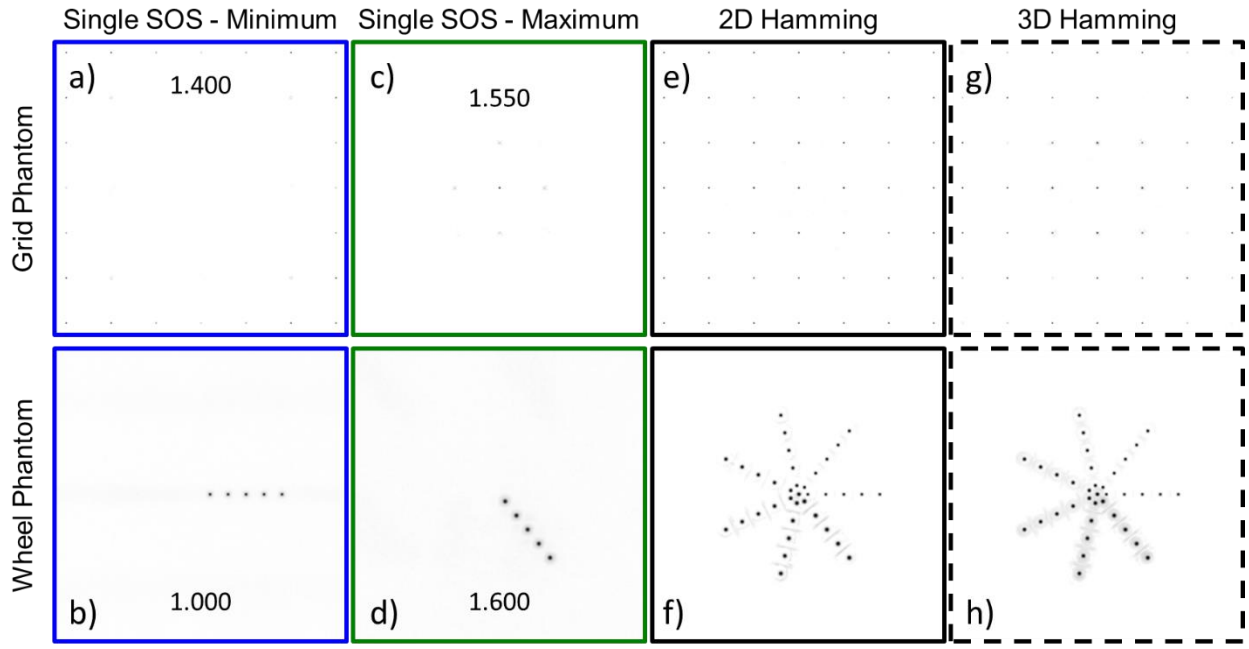

Figure 8.12: MIPs of image volumes of the numerical phantoms using either single SOS reconstructions or a spatially adaptive approach. When using an adaptive approach, SOS errors are minimized across the entire field of view making more point targets visible. The presented adaptive approaches have a Hamming window width of 10 mm for the grid phantom and 0.5 mm for the wheel phantom.

The SOS error of the algorithm was quantified by comparing the calculated CMAP output to the input SOS variations used to construct the numerical phantoms. The percent error was averaged in sub-volumes by cropping around point targets in a similar manner already reported for the SNR calculation. The means of the volume-average percent error across all points are provided (Figure 8.13a-b). The volume-weighted percent error reported is higher than what has been observed to cause drastic image degradation (0.2-0.3% error), however image metrics do not reflect poor performance of the adaptive algorithm. It should be noted that the volume-weighted percent error includes values of point targets not successfully reconstructed, so the mean across points of the volume-weighted percent error includes several outliers that shift the mean substantially. In addition to reporting the mean across points, the median of the volume-weighted percent error is also reported (Figure 8.13c-d), showing that a large portion of

the population has little or no error, a finding that agrees with the image metric summary reported in Figure 8.11.

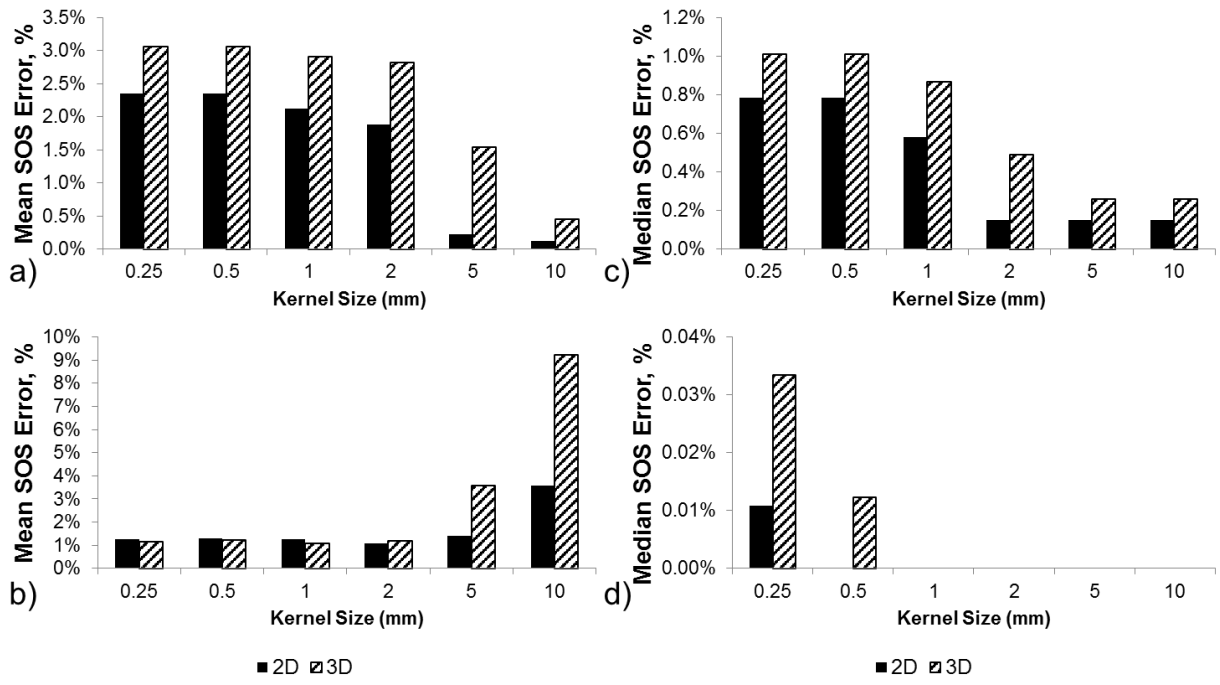

Figure 8.13: Cumulative SOS percent error calculated by comparing the CMAPs produced using the spatially adaptive approach to the input SOS variation of the numerical phantoms. The mean across all points of the volume-weighted percent error is given for a) the grid and b) the wheel phantoms. Since the mean of the volume-weighted percent error is sensitive to outliers, the median of the volume-weighted percent error is also reported in c) and d) for the grid and wheel phantoms, respectively.

8.2.3.2 Graphite phantom

In a similar manner to the numerical phantoms, the image quality of the graphite phantom was assessed by measuring SNR and FWHM of targets throughout the field of view. However, since the SOS is not known *a priori*, image metrics were compared to individual single SOS images to evaluate the performance of the spatially adaptive approach. The FWHM was measured by loading a good quality single SOS reconstruction (1.4925 mm/μs), performing a MIP on the volume, and then drawing ROIs in an interactive graphical user interface. A total of

30 line profiles were hand drawn across single fibers throughout the entire image and the coordinates of these profiles were stored and applied to all images for comparing the FWHM between different reconstructions. Similarly, the SNR was measured locally by drawing 50 elliptical ROIs to sample regions of the entire image. The mean pixel value of a good quality single SOS MIP (1.4925 mm/μs) was used as a threshold to generate a mask that was used to distinguish signal regions from noise regions for SNR calculations. In addition to SNR and FWHM, the reconstruction percentage was tracked. The reconstruction percentage is the percentage of targets that had both a positive SNR and a single peak when measuring the FWHM across the graphite fibers. A summary of these results are reported in Figure 8.14.

The 2D adaptive SOS approach performed better than the 3D version for a given kernel size. When the 2D kernel size was increased to the maximum tested value of 10 mm, the SNR across the image was increased to 19.6 ± 1.8 (sem) which was better than the best single SOS reconstruction which was 16.7 ± 1.5 at 1.4925 mm/μs. Additionally, the mean FWHM of the line targets was reduced when using the 2D adaptive approach, indicating reduced blurring and better image resolution when compared to using a single SOS. The lowest mean FWHM when using a constant SOS distribution was 0.539 ± 0.016 mm at 1.4925 mm/μs, while the lowest 2D adaptive approach had a mean FWHM of 0.536 ± 0.015 mm at a kernel size of 10 mm, although a two-sample *t*-test shows no significant difference between means ($p = 0.92$). The 3D spatially adaptive approach in terms of both SNR and FWHM did not outperform the best single SOS reconstruction. The best metrics were achieved at the largest tested kernel size and were 10.5 ± 1.1 for SNR and 0.605 ± 0.025 mm for FWHM (Figure 8.14b).

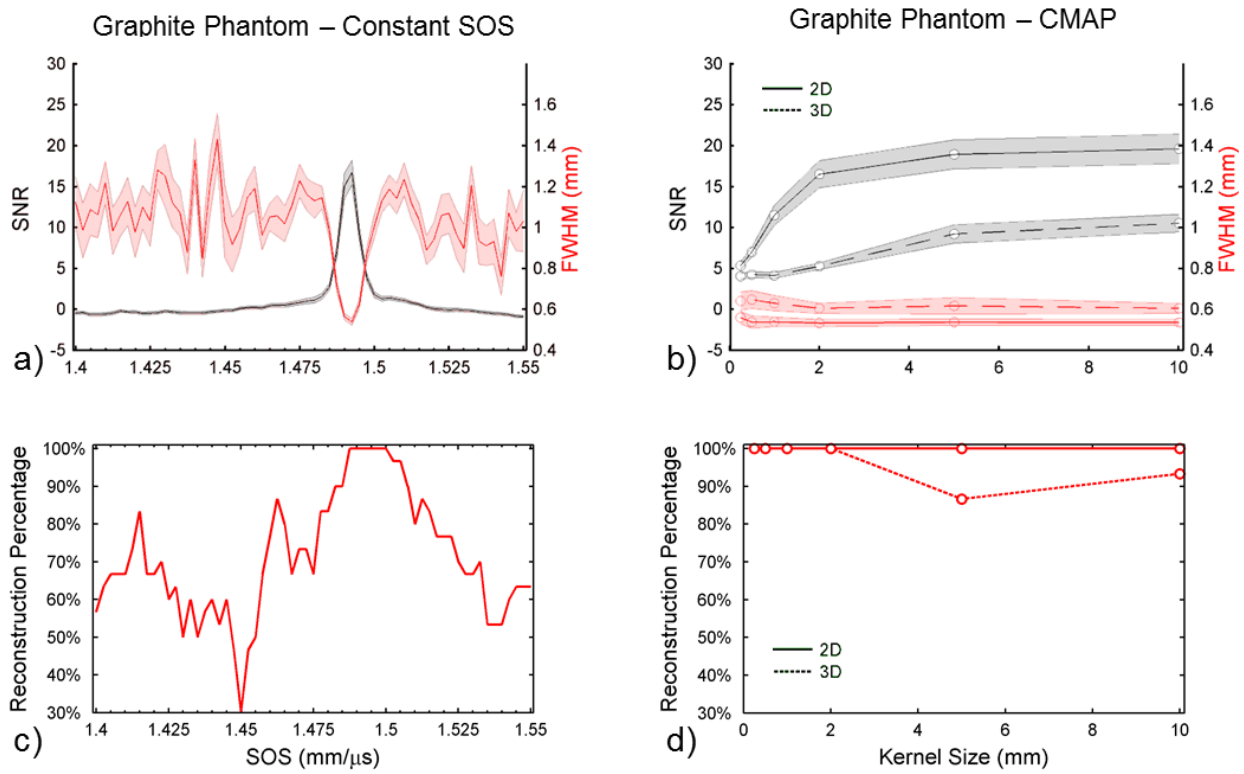

Figure 8.14: Comparison of image metrics obtained from the graphite phantom for both the single SOS reconstructions (a and c) and spatially varying CMAP reconstructions (b and d). a) and b) plot the SNR (black) and the FWHM (red) of image reconstructions while c) and d) plot the reconstruction percentages. The 2D algorithm results are plotted in solid lines and the 3D results are plotted using dashed line (b and d). The shading about the lines corresponds to the standard error of the mean (a and b).

When nearing the speed-of-sound that produced the best image in the graphite phantom, the reconstruction percentage of all the targets reached 100% (Figure 8.14c). While the single SOS reconstruction at 1.500 mm/μs reports 100% reconstruction success, it is important to note that at this speed the FWHM was 1.00 ± 0.056 mm and the SNR was 1.80 ± 0.35, which is considerably worse than the best SOS despite only being 0.5% different in terms of SOS. Regardless of the size of the kernels tested, the 2D spatially adaptive approach had 100% reconstruction success. The 3D approach was less robust and showed a drop in reconstruction

percentage at larger kernel sizes, dropping to a minimum of 87% at a kernel size of 5 mm (Figure 8.14d).

8.2.3.3 Photoacoustic mammography

Images created using the adaptive SOS approach followed similar trends that have already been presented for other data sets. A set of select regions of the breast vasculature are given for comparison in Figure 8.15, highlighting some areas of improvement when using a spatially adaptive approach to account for SOS differences encountered in breast tissue. The 3D adaptive approach did not produce images of similar or better quality compared to using an ideal single SOS for the entire image; however, the same cannot be said regarding the 2D approach.

As evident in Figure 8.15, the 2D spatially adaptive approach could identify vasculature that was not visible when using the single best SOS throughout the entire image. Image metrics were quantified using the same principle as described for the graphite phantom and CMAP images were compared to single SOS images. One key difference in this data set compared to the graphite dataset was using 243 profiles to report metrics of FWHM. The additional profiles were required to provide a similar sampling density as the graphite phantom, as the field of view for the patient data was substantially larger. SNR was calculated using 50 regions, however, the area of these regions were increased rather than increasing the number of regions to account for the larger image area. A summary of these metrics are provided in Figure 8.16.

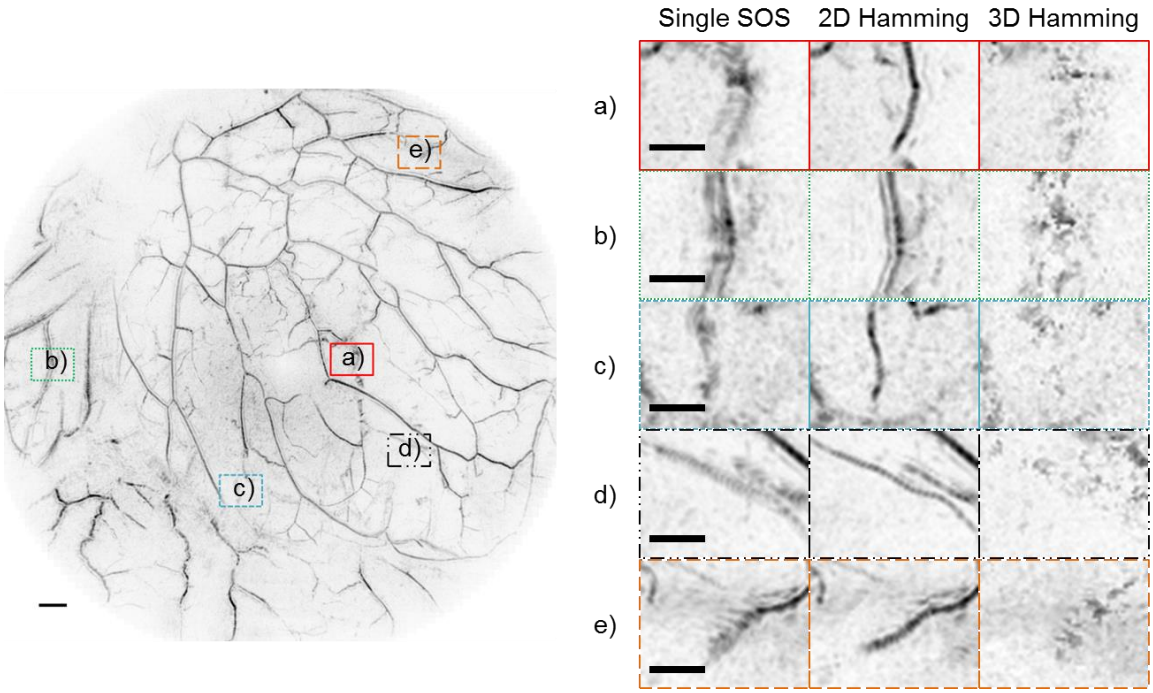

Figure 8.15: A maximum intensity projection viewing the vasculature of a whole breast using 2D adaptive SOS selection (left panel). The lettered boxes correspond to regions of interest for qualitative comparison of reconstruction techniques. The right panel is populated with enhanced regions reconstructed with either the best single SOS (left column, 1.505 mm/μs) or with a spatially varying SOS estimated from a 2D (middle column) or 3D (right column) autofocusing approach.. The black scale bar in the left image corresponds to 10 mm while the right panels correspond to 5 mm. The size of the Hamming summing kernel used to estimate the SOS was 5 mm for 2D and 0.5 mm for 3D.

The image metrics of the PAM dataset showed similar trends to what was seen in the graphite fiber phantom (Figure 8.16a-b). The best 2D CMAP images had the highest SNR (39.8 ± 2.1 at a kernel size of 5 mm) and the smallest FWHM (0.789 ± 0.017 mm at a kernel size of 10 mm), which exceeded the best single SOS reconstruction SNR (28.3 ± 2.1 at 1.5050 mm/μs, $p <$ 0.01) and FWHM (0.855 ± 0.024 mm at 1.5050 mm/μs, $p = 0.027$). The 3D CMAP approach did not perform as well at the tested kernel sizes, producing a maximum SNR of 8.0 ± 0.6 at a kernel size of 0.5 mm and a minimum FWHM of 1.406 ± 0.0714 mm at a kernel size of 0.5 mm. The FWHM minima for the 3D approach appearing at the smaller kernel sizes was primarily due to incomplete reconstruction of single vessels throughout the image due to incorrect SOS estimates,

causing half of the vessel to be severely defocused and making it seem like a smaller vessel. The FWHM at the larger kernel size of 10 mm for the 3D approach did not have partial vessel reconstruction and the mean FWHM is likely a better indicator of the algorithm performance without the presence of partial reconstruction bias.

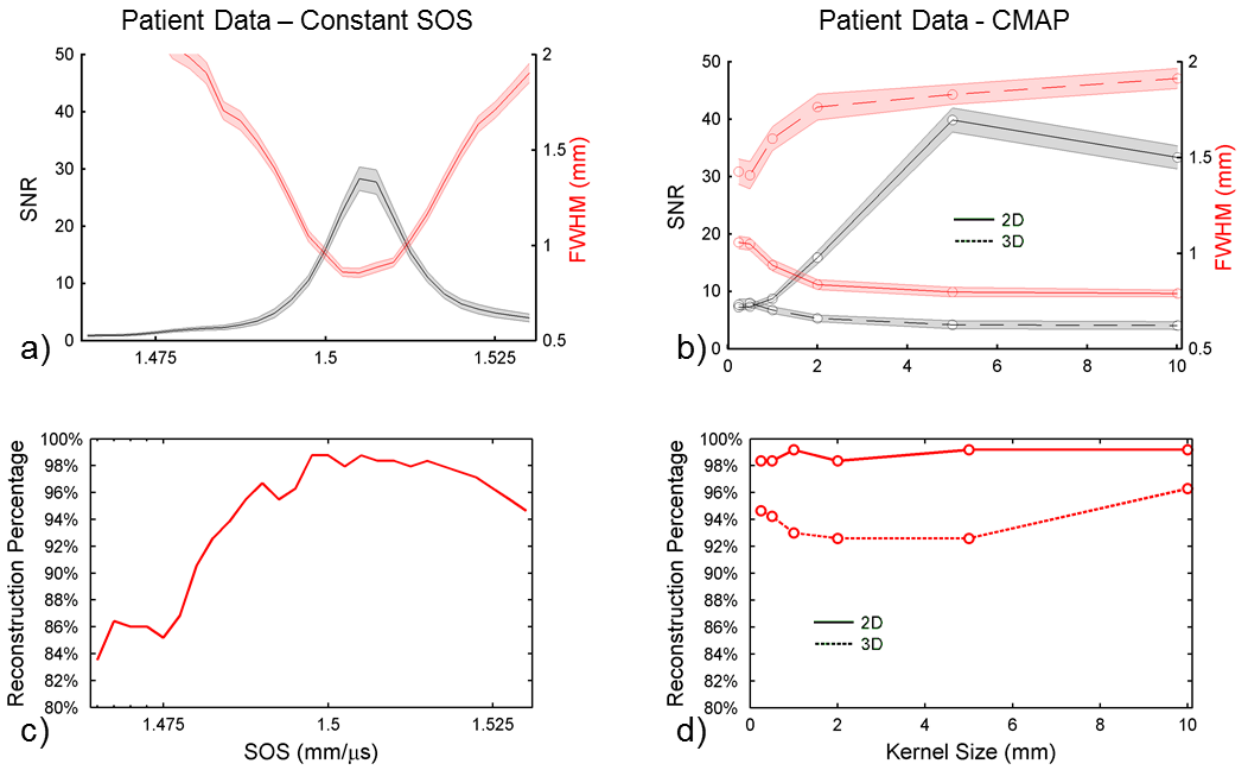

Figure 8.16: Comparison of image metrics when applied to data obtained from a patient's breast. SNR and FWHM are summarized in a) and b) for constant SOS and spatially varying CMAP reconstructions, respectively. Figures c) and d) plot the reconstruction success across the entire image for either varying SOS or kernel size. The shading about the lines corresponds to the standard error of the mean.

8.2.4 Discussion

The outlined procedure for estimating the SOS distribution within beamformed photoacoustic data leverages the previous success of autofocusing metrics to determine the optimal SOS for a whole imaging space. This approach was first extended into 2D to allow for

spatial variations corresponding to the dimensions of a MIP and then further extended into 3D to create a full volume estimate of the SOS useful for reconstructing a focused image. Our results showed that, in most cases, the 2D spatially adaptive approach performed better than the 3D approach. As previously explained by Treeby *et al.* and further observed in our studies, utilizing a MIP operation on a volume dataset has the effect of silencing large portions of the imaging space which contain little or no signal contributing to the SOS estimate, while only retaining portions of the image volume that contain strong photoacoustic signal sources [402].

While previous works used iterative search algorithms to predict the optimal SOS, this approach built a set of reference images to iteratively compare *post hoc* to make the SOS estimate in 2D and 3D. Algorithms that function by comparing a set of results rather than predicting future behavior require more computational time to come to a solution and this is an area that can be improved in this approach. In this work, approximately 60 reference reconstructions were completed prior to determining SOS distributions. These 60 reconstructions covered a broad range of SOS with a fine interval between tested SOS images. The interval size was selected based upon how sensitive this photoacoustic system is to SOS errors. For other systems, it is likely that the SOS interval size will be different depending upon the equipment and arrangement of the system collecting the image. A system less sensitive to SOS errors could use larger intervals or could consider a smaller range of SOS to reduce the size of the reference library built at the beginning of the algorithm to save computational time. While beyond the scope of this analysis, an iterative search algorithm applied in 2D or 3D could further increase the computational efficiency of this approach. Additionally, the reconstructions were performed on a single GPU with a CUDA compute capability of 1.3, which is considerably slower than newer GPU alternatives. The computational time for reconstruction has been reduced by

approximately a third by using multiple, higher-quality GPUs in parallel to process data collected by this same PAM system [403].

In this study, the photoacoustic mammography transducer array had a high degree of overall aperture symmetry since the array was arranged in a hemispherical bowl. It is believed that this symmetry aided in the success of the 2D adaptive approach to produce higher quality images by the nature in which the blurring occurred. It was observed that point targets that where reconstructed with an incorrect SOS would appear relative to the transducer array as either a bowl located closer to the array than the point if the SOS was too high, or an inverted bowl further away from the actual point if the SOS was too low. In addition to blurring, the point would appear to travel along the axis where optical illumination was provided (coordinate Z), which was the only axis that lacked symmetry in regards to acoustic detecting array. However, the center of the point did not travel in the directions that did have symmetry (coordinates X and Y) as the SOS was adjusted. Thus by taking the MIP in the Z-direction, the centroid of the point would not appear to travel (provided the point did not travel across the boundary of the imaging volume along the Z-direction) without the need for any volumetric warping to compensate for signal travel and re-align local focus metrics for comparison between different SOS.

The 2D and 3D adaptive SOS approaches produce speed-of-sound maps (CMAPs) that were used for inputs for a beamforming algorithm to reconstruct the image volume for a better image. Since the approach is based on determining which SOS produces the most focused image (as determined by the Brenner gradient), it should be clarified that the CMAPs do not represent the actual SOS within the scanned environment. While it is likely one may determine the estimates of the actual sound speed within the scanned environment using the CMAP, it would require further processing to obtain this information. The intended purpose of the CMAP is to

provide image quality enhancement rather than report diagnostic information by quantifying tissue SOS heterogeneities, but it is likely that this approach could be used to determine this information from the CMAP.

The behavior of the adaptive SOS approach on the two numerical phantoms provides insight into the inherent trade-off a spatially varying autofocusing approach. In the grid phantom, automated SOS selection provided better image metrics with increasing kernel size while the reverse was true for the wheel phantom. The autofocusing approach inherently assumes that there is a detectible feature within the field of view at the time of its application, however this depends upon the distribution of signal sources within the imaged region. If no source of photoacoustic signal is within the region of the summing kernel, the autofocusing approach produces an estimate of SOS based on noise. Likewise if multiple signal sources exist within the kernel during summing, then the SOS estimate for that region will likely be erroneous if the two signal sources do not have the same SOS. For this reason, the performance of the algorithm depends upon not only the SOS itself, but also its distribution within the imaging field. Selection of an appropriately sized kernel (large kernel in sparse signal regions, small kernels in densely packed signal regions) is necessary to obtain optimal performance of this approach. For this reason, it is suggested that spatially varying automatic SOS selection approaches like this one could be improved by applying scale space filtering approaches [408] to combine SOS estimates across multiple kernel sizes.

8.2.5 Conclusions

This section introduced and described an automated method of estimating the SOS distribution in acoustic images relying on assuming a SOS for image reconstruction using a modified autofocusing approach. The method does not require simulation to provide its answer,

and its performance depends mainly upon choosing an appropriate kernel size. Both 2D and 3D versions of this algorithm were evaluated and compared in numerical phantoms, graphite fiber phantoms, and in photoacoustic mammography of a whole breast. The 2D version of this algorithm produced higher SNR and targets with smaller FWHM than images produced using a constant SOS or the 3D version of this approach. The size of the kernel greatly affected the outcome of the SOS estimation and the performance of this algorithm. Ideally, the kernel size would match the spatial distributions of the photoacoustic signal sources so that the summing kernel used for local variation in SOS estimate could be evaluated without overlapping estimates from signals with different sound speeds. Local SOS estimation using an autofocusing approach is feasible and can be a good alternative for determining and correcting for SOS variations that would otherwise severely reduce image quality through blurring.

CHAPTER 9

DISCUSSION AND CONCLUSIONS

The work presented in this dissertation outlines the effort of translating superharmonic contrast imaging into intravascular ultrasound applications for the detection of microvascular flow. Acoustic angiography is an imaging methods that is characterized by having high CTR and increased resolution of vessels by detecting the higher-order nonlinear harmonics generated by microbubble contrast agents. While research is still being performed to better understand this new contrast imaging method, the work presented herein has shown that it can be translated into intravascular ultrasound to detect microvascular flow which would be valuable in determining plaque vulnerability in atherosclerotic lesions.

In Chapter 5, we developed a prototype dual-frequency IVUS transducer capable of acoustic angiography. We showed that this transducer was capable of producing pressures in excess of 1 MPa at a low frequency while simultaneously capable of detecting the weak, superharmonic response scattered by microbubbles.

The combined effects of reducing the aperture while creating images from low energy superharmonics reduced the SNR compared to acoustic angiography seen in previous work. The loss of SNR was partially mitigated by designing and fabricating appropriate transducer hardware in Chapter 6. Challenges of translating the technique to IVUS were several, but the most noticeable issue pertained to the low SNR seen in early studies. The SNR was improved 10

dB by reducing the noise of the excitation and acquisition system by designing a printed circuit board for use with dual-frequency transducers.

In Chapter 7 the prototype transducer was evaluated in terms of the images it could make in several imaging environments. Tissue mimicking phantoms were used to quantify the CTR, TNR, and SNR of IVUS images to determine the maximum range (7 mm) that it could detect microvascular flow in an attenuating medium. We showed how the high degree of tissue suppression can be advantageous for producing 3D renderings of vessel patterns in complex geometries in tissue-mimicking materials. Excised porcine arteries were used as a human surrogate to show that DF-IVUS can be used to detect the presence of a microvessel of similar size to primary human *vasa vasorum* in a histologically similar environment that would be seen *in vivo*. Volumetric pullbacks using the prototype DF-IVUS system were used to demonstrate the ability of the system to register 3D volumes of vessel segments in both B-mode and acoustic angiography. Finally, experiments in the chorioallantoic membrane showed that DF-IVUS can detect microvascular flow *in vivo* in vessels optically measured to be less than 150 μm in diameter.

Chapter 8 concludes the dissertation by describing post-processing methods that are advantageous to vascular medical imaging derived from acoustic detectors. In this chapter, a multi-dimensional autofocusing algorithm is developed to determine the appropriate speed of sound and correct for phase errors associated in beamforming. It was shown that the algorithm performance was dependent upon the spatial distribution of the signal sources located in the imaging field and that 2D focusing metrics perform better than assuming a single speed of sound as is done in conventional beamforming. Another study in this chapter introduced beamforming applications in DF-IVUS that can address the low SNR of acoustic angiography when

implemented with IVUS catheters. Adaptive beamforming methods include minimum variance and phase coherence were applied to phantom, *ex vivo*, and *in vivo* DF-IVUS images of vessels. We found that adaptive beamforming methods work well for our application in terms of improving resolution and reducing off-axis noise contributions due to the greater degree of tissue suppression seen in our data.

The results of these studies indicate the acoustic angiography can be translated into the intravascular ultrasound environment to detect microvascular flow in arteries and may provide prognostic value in future studies determining to assess atherosclerotic plaque vulnerability. This technology was enabled by using a novel dual-frequency design prototype IVUS transducer and the collaboration efforts of a team of researchers.

9.1 Future directions

Future directions of acoustic angiography include reducing the form factor to an even smaller dimension while curtailing some of the spurious inhomogeneities when fabricating a device required for prototyping. Ultimately, the DF-IVUS will only work as well as the transducer will allow so increased transducer performance is a must to increase signal quality, and thus image quality. This will likely happen if this research is given the opportunity to have commercial collaboration as the fabrication of the transducers used in this study were conducted by graduate students without specialty equipment that would normally be used in an industrial setting. This would allow for tighter tolerances, more uniform performance between transducers, and would reduce the number of possible reasons why one design factor worked better than another, which current designs can frequently attribute to slight variations between fabrications. Instances of this variation are exemplified by times where all transducers were made according

to the same specification in a single batch, but cutting individual elements from a single block of piezo-material would yield 4-6 transducers with highly different bandwidths and sensitivities.

Typically in IVUS, single element transducer are required to rotate and acquire scans of the artery at rates exceeding 1000 rpm. Images are formed with a large amount of scan lines for a high degree of spatial sampling that tends to make images appear better. The rotational rate and number of angular samples used in this work could be increased to match commercial equivalents in B-mode. A lower framerate was used in these studies to aid in signal detection of superharmonics. Early studies showed that the pressures used to generate the nonlinear signal from MCAs would also cause some degree of microbubble destruction which would lower the signal upon repeated insonations. However, by decreasing the effective framerate, contrast agents had enough time to reperfuse the areas where destruction occurred. Future work with DF-IVUS single element transducers may experience an impasse if higher framerates are desired.

The fabrication of DF-IVUS arrays was already initiated by the time this manuscript was drafted. Intravascular arrays are already used in the clinic and have some advantages over the single element prototype used in this work. While it is possible to use single element transducers with beamforming, beamforming was originally designed to optimize array-based detection from a single transmission event rather than the beamforming methods applied in Chapter 8, which used a multitude of transmission events through time. Arrays can also perform focusing in both transmission and reception. Focusing on transmission would allow for higher pressures to be delivered to individual regions within the image which would be useful for increasing the SNR without having to physically adjust the placement of the device relative to the object being imaged. Focusing on receive can tighten the beam width to improve the lateral resolution and can reduce off-axis scattering. While dynamic receive focusing can be performed on single element

devices already, some advance receive beamforming techniques such as synthetic aperture requires an actual array in order to work properly. A DF-IVUS array does present some added challenges in terms of fabrication, but it also loses some. Single element components requires rotational translation to place the aperture in a new location for acoustic interrogation. It must use a drive cable and time firing rate with a given location mechanically. Additionally, single element IVUS devices have to have rotary transformer or a slip ring in order to allow the device to indefinitely rotate while still maintaining electrical connectivity between the transducer and the scanner. Arrays have a larger data bus and must carry more electrical connections, but there are no rotational requirements which heavily simplify the design of such a transducer.

9.2 Other applications for dual-frequency transducers

Dual-frequency IVUS can be used in other applications that extend beyond superharmonic imaging of microbubble contrast agents. The symbiotic roles of research and industry gives commercialization opportunities through designing, developing, and demonstrating in the former and optimizing, controlling, expanding in the latter. In the following sections, the authors have proposed various ways that a dual-frequency transducer designed for intravascular applications may be used for additional applications relevant to needs already encountered in today's clinic.

9.2.1 Blood effusion detection

Intravascular ultrasound is already used clinically to verify the location of a stent after deployment and advocated to be used prior to stent placement. Interventional procedures can benefit by including IVUS into their routine and can perform better than radiographic approaches in complex lesions [409]. IVUS is a powerful tool in assessing vascular health both before [410] and after a stent placement [411]. Many complications are associated with endovascular stent

grafts; blood flowing around stents used in fusiform aneurysm repair (such as abdominal aortic aneurysms) presents a deadly problem both in the immediate and long term and requires accurate detection. Abdominal aortic aneurysms (AAA) are lethal and have a high mortality rate in general populations (0.042% male, 0.022% female) [412].

Endoleaks, defined as the flow of blood between the graft and the vessel wall [413], are normally detected by angiographical flow of contrast, even though IVUS may be available during the stent placement in AAA repair. Endoleaks incidence has been reported to be as high as 22.7% of repairs and complications from endoleaks include aneurysm growth and rupture [414]. Currently, IVUS cannot visualize the flow of blood external to the stent since the high frequencies used by IVUS limit depth of penetration. Additionally, grafted aneurysm repairs are supported using a metal stent which greatly reflects sound waves making the region behind the stent difficult to image when using IVUS. Furthermore, it has been shown that IVUS is poor at locating endoleaks in comparison to other techniques such as transesophageal ultrasound or angiography [415]. However, when ultrasound imaging is combined with contrast agents, it becomes comparable to or better than other imaging modalities at detecting endoleaks [414, 416, 417].

A dual-frequency IVUS transducer designed to image contrast agents using superharmonics could have a considerable impact on detecting vascular flow in undesired locations. IVUS transducers utilizing harmonic approaches can severely reduce near-field artifacts that arise from specular reflections of metal stents to increase the field of view [418]. The size of most of our prototypes currently can be housed in an 8F catheter which can easily be used in the abdominal aortic to detect small or slow blood flow after repair. In coronary vessels, the detection of perivascular blood effusion caused by perforation or guidewire exiting can be

identified accurately with radiographic approaches. With a dual-frequency probe, it is likely that this detection can be enhanced using ultrasound for low flow or small leaks that may be difficult to detect using other modalities. The dual-frequency transducer proposed may be useful in other environments, but not in smaller vessels since the incorporation of the design uses a low frequency element which must have a minimum material thickness in order to operate, making it unlikely to further reduce the size below 3F. Additionally, the use of IVUS in tortuous vessels can be difficult since adding bends into the catheter increases frictional losses and retards transducer rotation which may limit its use in the circle of Willis or other similarly tortuous or small vessels networks. Translating the technique into an array would reduce the rotation requirement and may make it more manageable to maneuver in smaller vessels.

9.2.2 Localized therapy

Microbubbles are both diagnostic and therapeutic agents. The general structure of a microbubble includes a perfluorocarbon gas core encapsulated by a shell material such as a phospholipid layer. While the gas core generally has low solubility for most drugs, drugs can be conjugated to the shell material externally through bonding or dissolved into the phospholipid layer [87]. While the shell can only carry a small amount of drug, microbubble formulation strategies such as the inclusion of a drug loaded oil layer can increase dosing if necessary [419]. Local drug delivery as opposed to systemic delivery is advantageous when therapies include chemotherapeutic drugs such as paclitaxel. Microbubbles loaded with agents can be pushed to the vessel endothelium and then burst using ultrasound for localized drug delivery [205, 208] or gene transfection [420] at lower doses than would be administered systemically for the same outcome.

The pushing of microbubbles with acoustic radiation force (ARF) has been shown to increase drug delivery efficacy some researchers have explored doing this in IVUS [421]. One of the major challenges in local drug delivery in IVUS is that ARF used to push microbubbles needs to have high pulse repetition frequency, low frequency, and low pressures which cannot be performed in commercial systems [236]. Additionally, maximum bubble displacement occurs when exciting with a frequency that is close to the microbubble's natural resonance [118]. The dual-frequency transducer we have designed has a low frequency element that is capable of delivering ARF near the microbubble resonance frequency of commercially available Definity® microbubbles, [338] which we expect to be ideal for drug delivery enhancement. Reduction of neointimal formation in rat carotid arteries following balloon angioplasty has been reported to use a tenth of the required dose to achieve equal therapeutic response, using the combination of ultrasound and rapamycin loaded microbubbles [205]. In this study, ARF and bubble bursting had to be performed transcutaneously using two separate transducers. A dual-frequency transducer could be used to do both therapy and monitoring in coronary arties as well as carotid arteries given the previously discussed dimensions of the transducer. Since IVUS catheters are invasive, this approach would likely be limited to situations where guidewires were necessary or when IVUS imaging would be indicated such as plaque visualization or stent monitoring.

APPENDIX A

IEEE MAY 2014 COVER IMAGE

A Preliminary Engineering Design of Intravascular Dual-Frequency Transducers for Contrast-Enhanced Acoustic Angiography and Molecular Imaging

Caption: The cover shows a dual-frequency intravascular ultrasound (IVUS) transducer designed for superharmonic contrast imaging and acoustic angiography. (A) A graphical explanation of the theoretical mode of operation for the dual-frequency transducer. Transmission of acoustic signals uses the lower frequency (6.5 MHz) element to excite microbubble contrast agents while high-frequency backscattered energy is received with the higher frequency (30 MHz) element. (B) A photo of the fabricated transducer mounted in a commercial housing (Boston Scientific, Natick, MA) demonstrates the required form factor for integration. The smallest increment on the ruler is 0.5 mm. (C) The bandwidths of the transmit and receive elements are separated for reduced tissue signal background. (D) Microbubble contrast agents imaged while flowing through a cellulose tube embedded in a phantom with fully developed speckle. The contrast signal has a high signal-to-noise ratio compared with the phantom background because of the dual-frequency imaging approach. For further reading, please see the accompanying article on page 870 of this issue. Images courtesy of Jianguo Ma, K. Heath Martin, Paul A. Dayton, and Xiaoning Jiang.

IEEE TRANSACTIONS ON

ULTRASONICS, FERROELECTRICS, AND FREQUENCY CONTROL

A PUBLICATION OF THE IEEE ULTRASONICS, FERROELECTRICS, AND FREQUENCY CONTROL SOCIETY

MAY 2014 VOLUME 61 NUMBER 5 ITUCER (ISSN 0885-3010)

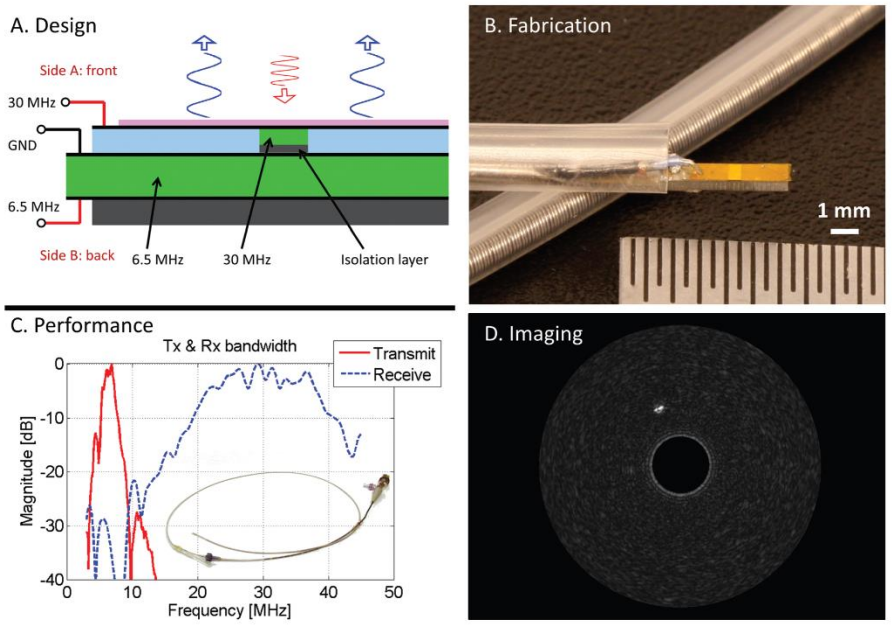

Access the journal with its multimedia contents online at: http://www.ieee-uffc.org/tr/

DOI http://dx.doi.org/10.1109/TUFFC.2014.2961

APPENDIX B

SCHEMATICS FOR FABRICATED COMPONENTS

Drawing schematics are provided for some of the equipment fabricated in order to conduct the studies presented in this dissertation. The schematics were produced using an Academic license of SolidWorks.

B.1 Three channel phantom mold for *in vitro* studies

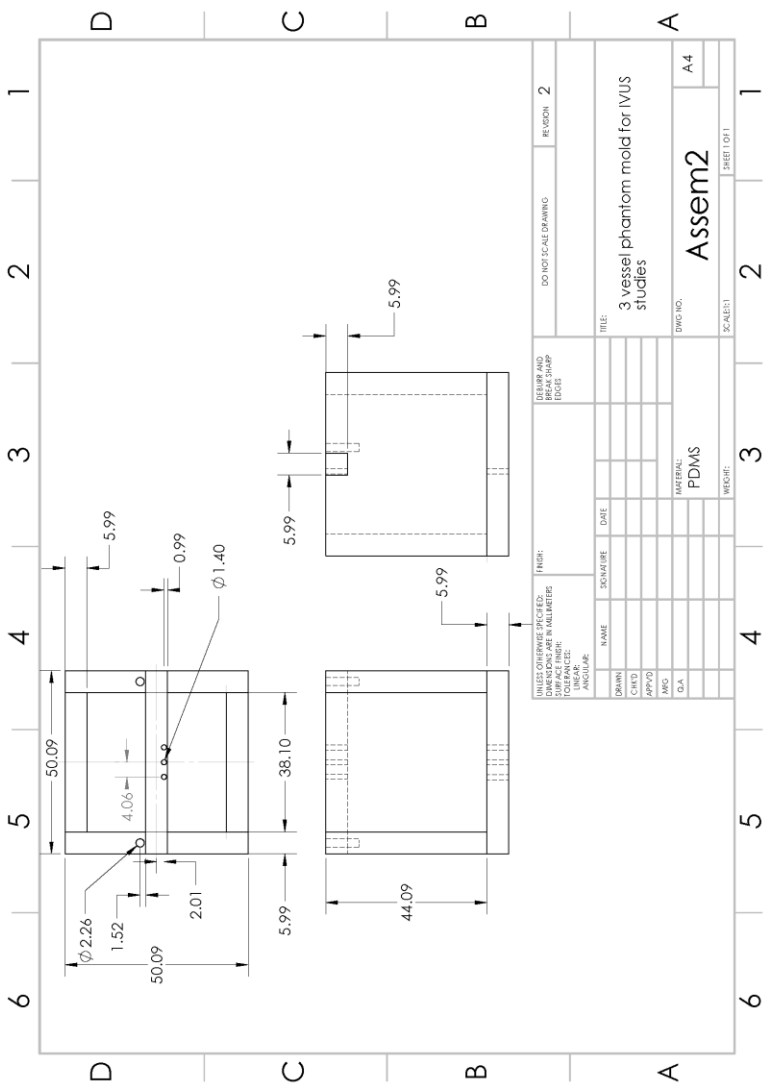

B.2 Intravascular array transducer wrapping tool

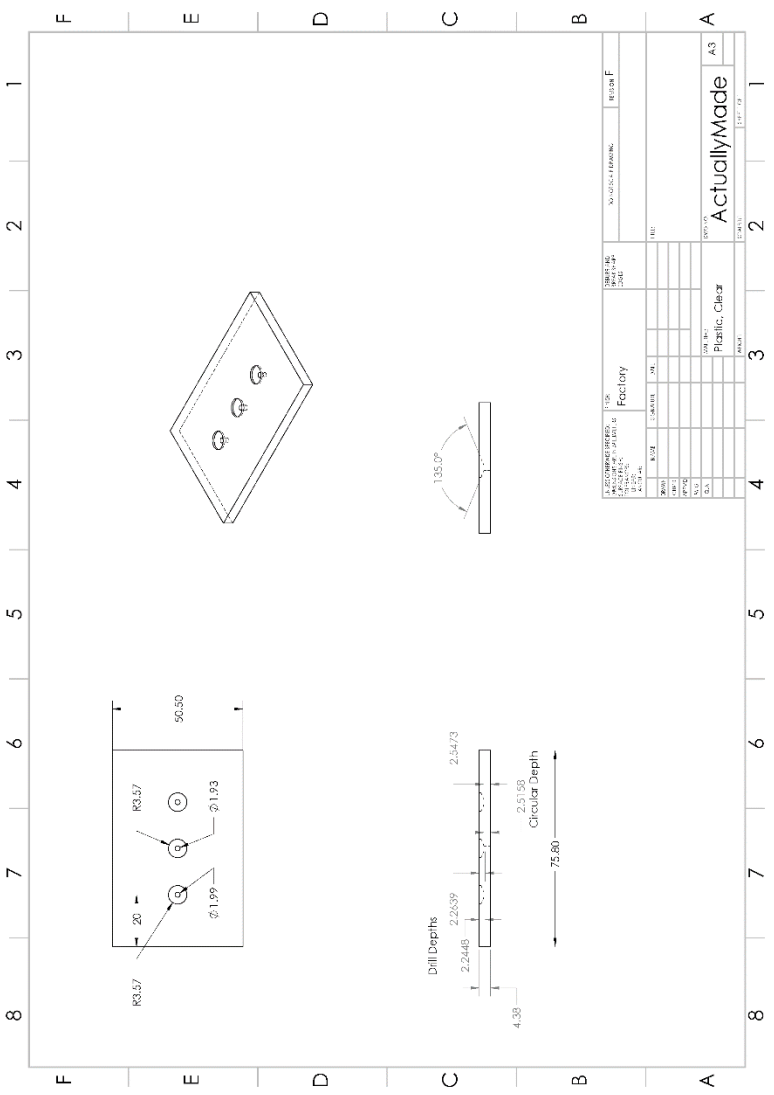

B.3 Intravascular array transducer prototype fixture for 3-axis motion stage

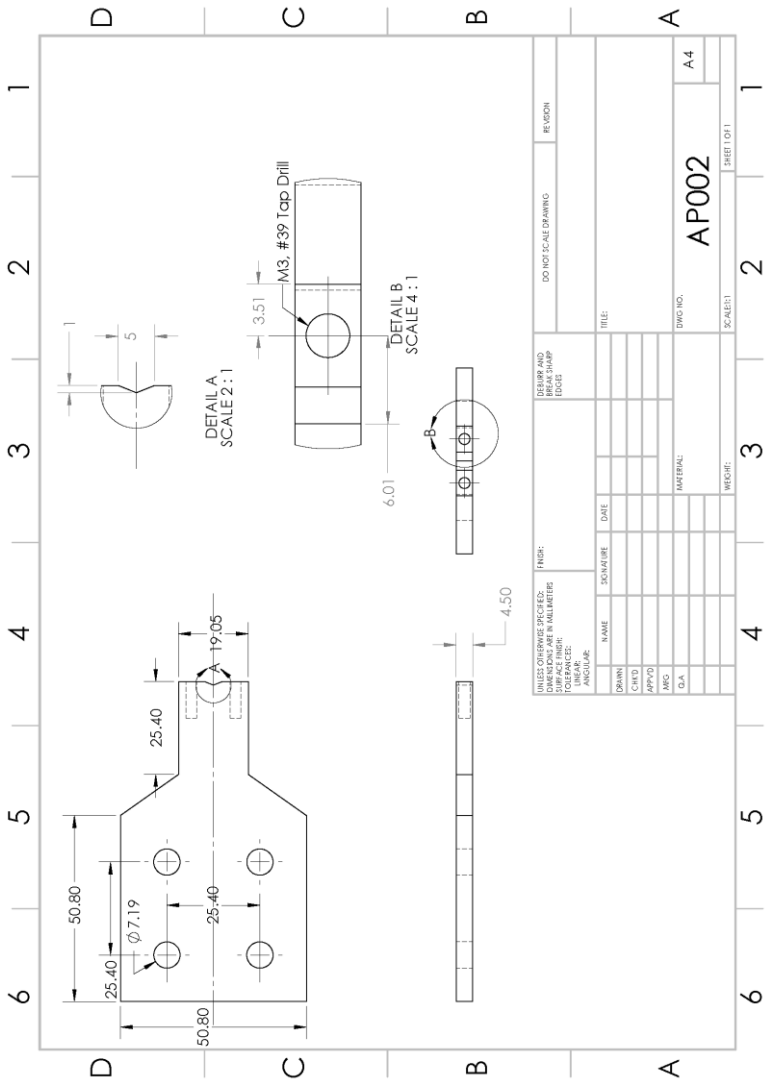

B.4 Head-piece for AP002 seen in Chapter B.3

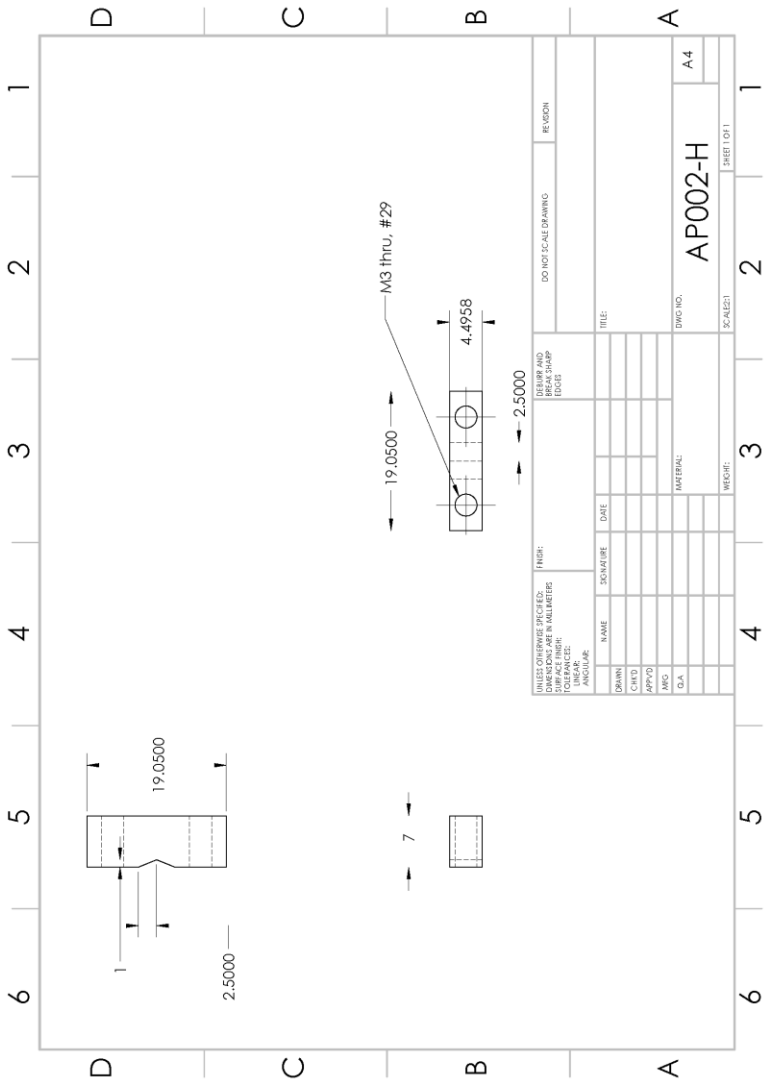

B.5 Phantom mold for depth study. Shallow depth range

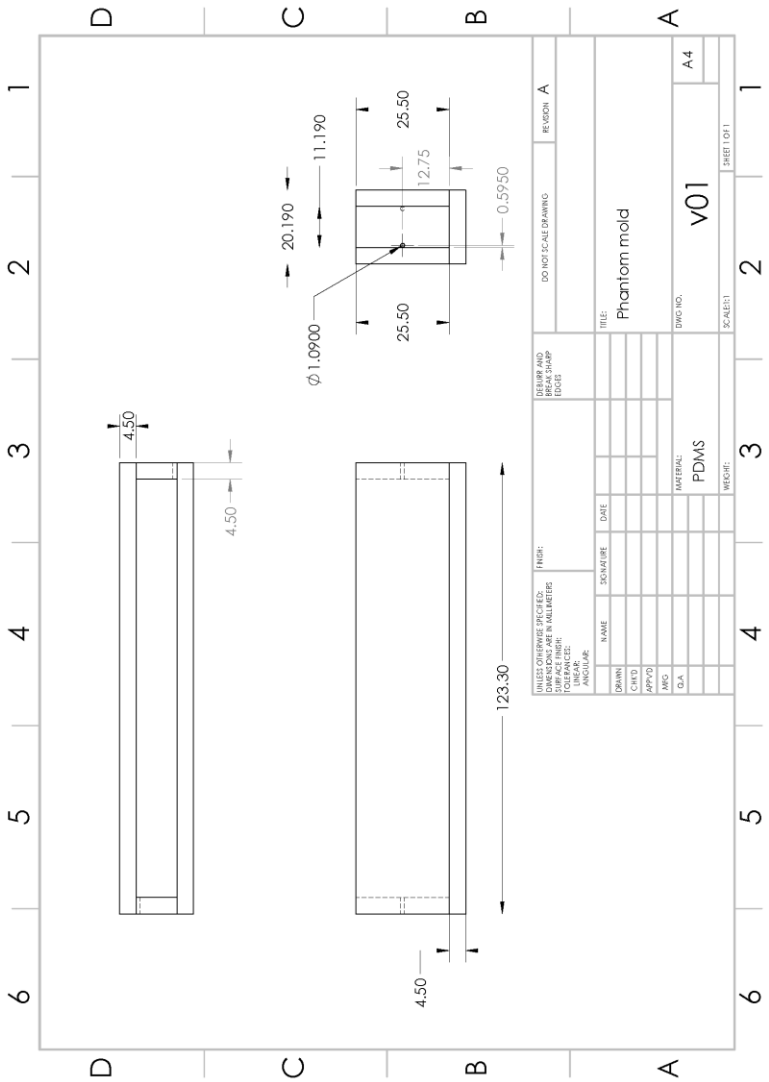

B.6 Phantom mold for depth study. Deep depth range

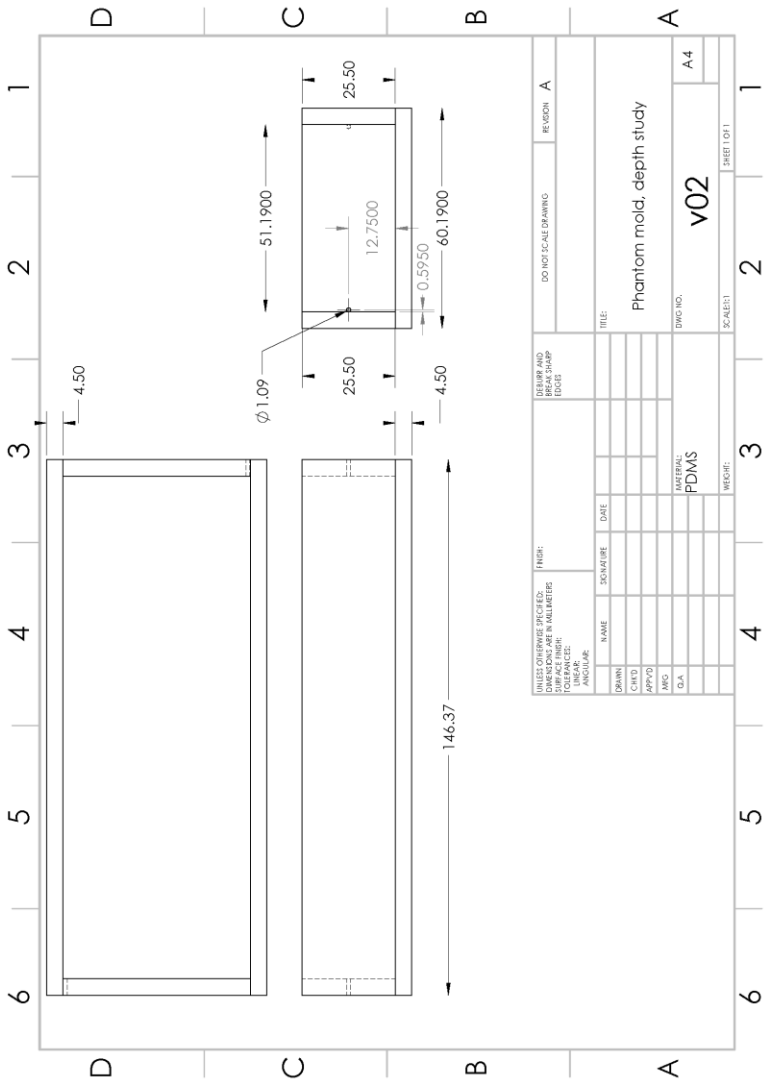

BIBLIOGRAPHY

[1] M. Naghavi, P. Libby, E. Falk, S. W. Casscells, S. Litovsky, J. Rumberger, J. J. Badimon, C. Stefanadis, P. R. Moreno, G. Pasterkamp, Z. Fayad, P. H. Stone, S. Waxman, P. Raggi, M. Madjid, A. Zarrabi, A. P. Burke, C. Yuan, P. J. Fitzgerald, D. S. Siscovick, C. L. de Korte, M. Aikawa, K. E. J. Airaksinen, G. Assmann, C. R. Becker, J. H. Chesebro, A. Farb, Z. S. Galis, C. Jackson, I.-K. Jang, W. Koenig, R. A. Lodder, K. March, J. Demirovic, M. Navab, S. G. Priori, M. D. Rekhter, R. Bahr, S. M. Grundy, R. Mehran, A. Colombo, E. Boerwinkle, C. Ballantyne, W. Insull, R. S. Schwartz, R. Vogel, P. W. Serruys, G. K. Hansson, D. P. Faxon, S. Kaul, H. Drexler, P. Greenland, J. E. Muller, R. Virmani, P. M. Ridker, D. P. Zipes, P. K. Shah, and J. T. Willerson, "From vulnerable plaque to vulnerable patient: a call for new definitions and risk assessment strategies: Part I.," *Circulation,* vol. 108, pp. 1664-72, 2003.

[2] A. P. Burke, A. Farb, G. T. Malcom, Y.-h. Liang, J. Smialek, and R. Virmani, "Coronary risk factors and plaque morphology in men with coronary disease who died suddenly," *N Engl J Med,* vol. 336, pp. 1276-1282, 1997.

[3] P. Constantinides, "Cause of thrombosis in human atherosclerotic arteries," *The American Journal of Cardiology,* vol. 66, pp. G37-G40, 1990.

[4] M. Naghavi, *Asymptomatic atherosclerosis: pathophysiology, Detection and Treatment*: Springer Science & Business Media, 2010.

[5] D. Vancraeynest, A. Pasquet, V. Roelants, B. L. Gerber, and J.-L. J. Vanoverschelde, "Imaging the vulnerable plaque," *J Am Coll Cardiol,* vol. 57, pp. 1961-1979, 2011.

[6] R. C. Gessner, S. R. Aylward, and P. A. Dayton, "Mapping Microvasculature with Acoustic Angiography Yields Quantifiable Differences between Healthy and Tumor-bearing Tissue Volumes in a Rodent Model.," *Radiology,* vol. 264, pp. 733-40, 2012.

[7] M. J. Mulligan-Kehoe, "The vasa vasorum in diseased and nondiseased arteries," *Am J Physiol Heart Circ Physiol,* vol. 298, pp. H295-305, Feb 2010.

[8] E. L. Ritman and A. Lerman, "The dynamic vasa vasorum," *Cardiovasc Res,* vol. 75, pp. 649-658, 2007.

[9] H. Wolinsky and S. Glagov, "Nature of species differences in the medial distribution of aortic vasa vasorum in mammals," *Circulation Research,* vol. 20, pp. 409-21, Apr 1967.

[10] K. Okuyama, G. Yaginuma, T. Takahashi, H. Sasaki, and S. Mori, "The development of vasa vasorum of the human aorta in various conditions. A morphometric study," *Arch Pathol Lab Med,* vol. 112, pp. 721-5, Jul 1988.

[11] Anatomical Chart Company, *Anatomy and Pathology,* 4th ed.: Lippincott Williams & Wilkins, 2005.

[12] D. Y. Li, B. Brooke, E. C. Davis, R. P. Mecham, L. K. Sorensen, B. B. Boak, E. Eichwald, and M. T. Keating, "Elastin is an essential determinant of arterial morphogenesis," *Nature,* vol. 393, pp. 276-280, 1998.

[13] P. Libby, "Molecular bases of the acute coronary syndromes," *Circulation,* vol. 91, pp. 2844-2850, 1995.

[14] D. Hackett, G. Davies, and A. Maseri, "Pre-existing coronary stenoses in patients with first myocardial infarction are not necessarily severe," *Eur Heart J,* vol. 9, pp. 1317-1323, 1988.

[15] J. A. Ambrose, M. A. Tannenbaum, D. Alexopoulos, C. E. Hjemdahl-Monsen, J. Leavy, M. Weiss, S. Borrico, R. Gorlin, and V. Fuster, "Angiographic progression of coronary artery disease and the development of myocardial infarction," *J Am Coll Cardiol,* vol. 12, pp. 56-62, 1988.

[16] M. Nobuyoshi, M. Tanaka, H. Nosaka, T. Kimura, H. Yokoi, N. Hamasaki, K. Kim, T. Shindo, and K. Kimura, "Progression of coronary atherosclerosis: is coronary spasm related to progression?," *J Am Coll Cardiol,* vol. 18, pp. 904-10, 1991.

[17] D. Giroud, J. M. Li, P. Urban, B. Meier, and W. Rutishauser, "Relation of the site of acute myocardial infarction to the most severe coronary arterial stenosis at prior angiography," *The American Journal of Cardiology,* vol. 69, pp. 729-732, 1992.

[18] R. Ross, "Atherosclerosis--an inflammatory disease.," *N Engl J Med,* vol. 340, pp. 115-26, 1999.

[19] R. Virmani, A. P. Burke, A. Farb, and F. D. Kolodgie, "Pathology of the Vulnerable Plaque," *J Am Coll Cardiol,* vol. 47, pp. C13-C18, 2006.

[20] M. Sawabe, T. Arai, I. Kasahara, A. Hamamatsu, Y. Esaki, K. Nakahara, K. Harada, K. Chida, H. Yamanouchi, T. Ozawa, K. Takubo, S. Murayama, and N. Tanaka, "Sustained progression and loss of the gender-related difference in atherosclerosis in the very old: a pathological study of 1074 consecutive autopsy cases," *Atherosclerosis,* vol. 186, pp. 374-9, Jun 2006.

[21] J. C. Wang, "Coronary Artery Spatial Distribution of Acute Myocardial Infarction Occlusions," *Circulation,* vol. 110, pp. 278-284, 2004.

[22] D. N. Ku, D. P. Giddens, C. K. Zarins, and S. Glagov, "Pulsatile flow and atherosclerosis in the human carotid bifurcation. Positive correlation between plaque location and low oscillating shear stress," *Arterioscler Thromb Vasc Biol,* vol. 5, pp. 293-302, 1985.

[23] A. M. Malek, S. L. Alper, and S. Izumo, "Hemodynamic shear stress and its role in atherosclerosis," *JAMA,* vol. 282, pp. 2035-2042, 1999.

[24] C. J. Slager, J. J. Wentzel, F. J. H. Gijsen, A. Thury, A. C. van der Wal, J. A. Schaar, and P. W. Serruys, "The role of shear stress in the destabilization of vulnerable plaques and related therapeutic implications," *Nat Clin Pract Cardiovasc Med,* vol. 2, pp. 456-464, 2005.

[25] Y. S. Chatzizisis, A. U. Coskun, M. Jonas, E. R. Edelman, C. L. Feldman, and P. H. Stone, "Role of endothelial shear stress in the natural history of coronary atherosclerosis and vascular remodeling: molecular, cellular, and vascular behavior," *J Am Coll Cardiol,* vol. 49, pp. 2379-2393, 2007.

[26] H. C. Stary, D. H. Blankenhorn, A. B. Chandler, S. Glagov, W. Insull Jr, M. Richardson, M. E. Rosenfeld, S. A. Schaffer, C. J. Schwartz, and W. D. Wagner, "A definition of the intima of human arteries and of its atherosclerosis-prone regions. A report from the Committee on Vascular Lesions of the Council on Arteriosclerosis, American Heart Association," *Circulation,* vol. 85, p. 391, 1992.

[27] H. C. Stary, A. B. Chandler, S. Glagov, J. R. Guyton, W. Insull, M. E. Rosenfeld, S. A. Schaffer, C. J. Schwartz, W. D. Wagner, and R. W. Wissler, "A definition of initial, fatty streak, and intermediate lesions of atherosclerosis. A report from the Committee on Vascular Lesions of the Council on Arteriosclerosis, American Heart Association," *Arterioscler Thromb Vasc Biol,* vol. 14, pp. 840-856, 1994.

[28] H. C. Stary, A. B. Chandler, R. E. Dinsmore, V. Fuster, S. Glagov, W. Insull, M. E. Rosenfeld, C. J. Schwartz, W. D. Wagner, and R. W. Wissler, "A definition of advanced types of atherosclerotic lesions and a histological classification of atherosclerosis A report from the Committee on Vascular Lesions of the Council on Arteriosclerosis, American Heart Association," *Circulation,* vol. 92, pp. 1355-1374, 1995.

[29] A. P. Burke, F. D. Kolodgie, A. Farb, D. K. Weber, G. T. Malcom, J. Smialek, and R. Virmani, "Healed plaque ruptures and sudden coronary death evidence that subclinical rupture has a role in plaque progression," *Circulation,* vol. 103, pp. 934-940, 2001.

[30] R. Virmani, F. D. Kolodgie, A. P. Burke, A. Farb, and S. M. Schwartz, "Lessons From Sudden Coronary Death," *Arterioscler Thromb,* pp. 1262-1275, 2000.

[31] E. Arbustini, B. Dal Bello, P. Morbini, A. Burke, M. Bocciarelli, G. Specchia, and R. Virmani, "Plaque erosion is a major substrate for coronary thrombosis in acute myocardial infarction," *Heart,* vol. 82, pp. 269-272, 1999.

[32] J. E. Muller, G. Tofler, and P. Stone, "Circadian variation and triggers of onset of acute cardiovascular disease," *Circulation,* vol. 79, pp. 733-743, 1989.

[33] B. A. Kaufmann, J. M. Sanders, C. Davis, A. Xie, P. Aldred, I. J. Sarembock, and J. R. Lindner, "Molecular imaging of inflammation in atherosclerosis with targeted ultrasound detection of vascular cell adhesion molecule-1.," *Circulation,* vol. 116, pp. 276-84, 2007.

[34] P. A. Schumann, J. P. Christiansen, R. M. Quigley, T. P. McCreery, R. H. Sweitzer, E. C. Unger, J. R. Lindner, and T. O. Matsunaga, "Targeted-microbubble binding selectively to GPIIb IIIa receptors of platelet thrombi.," *Invest Radiol,* vol. 37, pp. 587-93, 2002.

[35] S. B. Feinstein, "Contrast ultrasound imaging of the carotid artery vasa vasorum and atherosclerotic plaque neovascularization.," *J Am Coll Cardiol,* vol. 48, pp. 236-43, 2006.

[36] S. Glagov, E. Weisenberg, C. K. Zarins, R. Stankunavicius, and G. J. Kolettis, "Compensatory enlargement of human atherosclerotic coronary arteries," *N Engl J Med,* vol. 316, pp. 1371-1375, 1987.

[37] S. Vallabhajosula and V. Fuster, "Atherosclerosis: imaging techniques and the evolving role of nuclear medicine," *Journal of nuclear medicine : official publication, Society of Nuclear Medicine,* vol. 38, pp. 1788-96, 1997.

[38] J. H. F. Rudd, K. S. Myers, S. Bansilal, J. Machac, C. A. Pinto, C. Tong, A. Rafique, R. Hargeaves, M. Farkouh, V. Fuster, and Z. A. Fayad, "Atherosclerosis inflammation imaging with 18F-FDG PET: carotid, iliac, and femoral uptake reproducibility, quantification methods, and recommendations," *Journal of nuclear medicine : official publication, Society of Nuclear Medicine,* vol. 49, pp. 871-878, 2008.

[39] D. A. Bluemke, S. Achenbach, M. Budoff, T. C. Gerber, B. Gersh, L. D. Hillis, W. G. Hundley, W. J. Manning, B. F. Printz, and M. Stuber, "Noninvasive coronary artery imaging magnetic resonance angiography and multidetector computed tomography angiography: a scientific statement from the American Heart Association Committee on Cardiovascular Imaging and Intervention of the Council on Cardiovascular Radiology and Intervention, and the Councils on Clinical Cardiology and Cardiovascular Disease in the Young," *Circulation,* vol. 118, pp. 586-606, 2008.

[40] L. Saba, M. Anzidei, B. C. Marincola, M. Piga, E. Raz, P. P. Bassareo, A. Napoli, L. Mannelli, C. Catalano, and M. Wintermark, "Imaging of the carotid artery vulnerable plaque," *Cardiovasc Intervent Radiol,* vol. 37, pp. 572-585, 2014.

[41] E. B. Diethrich, M. P. Margolis, D. B. Reid, A. P. Burke, V. Ramaiah, J. A. Rodriguez-Lopez, G. Wheatley, D. Olsen, and R. Virmani, "Virtual histology intravascular ultrasound assessment of carotid artery disease: the Carotid Artery Plaque Virtual Histology Evaluation (CAPITAL) study," *Journal of endovascular therapy : an official journal of the International Society of Endovascular Specialists,* vol. 14, pp. 676-86, 2007.

[42] M. Naghavi, P. Libby, E. Falk, S. W. Casscells, S. Litovsky, J. Rumberger, J. J. Badimon, C. Stefanadis, P. R. Moreno, G. Pasterkamp, Z. Fayad, P. H. Stone, S. Waxman, P. Raggi, M. Madjid, A. Zarrabi, A. P. Burke, C. Yuan, P. J. Fitzgerald, D. S. Siscovick, C. L. de Korte, M. Aikawa, K. E. J. Airaksinen, G. Assmann, C. R. Becker, J. H. Chesebro, A. Farb, Z. S. Galis, C. Jackson, I.-k. Jang, W. Koenig, R. A. Lodder, K. March, J. Demirovic, M. Navab, S. G. Priori, M. D. Rekhter, R. Bahr, S. M. Grundy, R. Mehran, A. Colombo, E. Boerwinkle, C. Ballantyne, W. Insull, R. S. Schwartz, R. Vogel, P. W. Serruys, G. K. Hansson, D. P. Faxon, S. Kaul, H. Drexler, P. Greenland, J. E. Muller, R. Virmani, P. M. Ridker, D. P. Zipes, P. K. Shah, and J. T. Willerson, "From vulnerable plaque to vulnerable patient: a call for new definitions and risk assessment strategies: Part II.," *Circulation,* vol. 108, pp. 1772-8, 2003.

[43] M. Okubo, M. Kawasaki, Y. Ishihara, U. Takeyama, S. Yasuda, T. Kubota, S. Tanaka, T. Yamaki, S. Ojio, K. Nishigaki, G. Takemura, M. Saio, T. Takami, H. Fujiwara, and S. Minatoguchi, "Tissue Characterization of Coronary Plaques," *Circulation Journal,* vol. 72, pp. 1631-1639, 2008.

[44] S. Sathyanarayana, S. G. Carlier, W. Li, and L. Thomas, "Characterisation of atherosclerotic plaque by spectral similarity of radiofrequency intravascular ultrasound signals," *EuroIntervention,* vol. 5, pp. 133-139, 2009.

[45] R. Yamada, H. Okura, T. Kume, Y. Neishi, T. Kawamoto, Y. Miyamoto, K. Imai, K. Saito, A. Hayashida, and K. Yoshida, "A comparison between 40 MHz intravascular ultrasound iMap imaging system and integrated backscatter intravascular ultrasound," *Journal of cardiology,* vol. 61, pp. 149-54, 2013.

[46] R. H. Behler, T. J. Czernuszewicz, C.-D. Wu, T. C. Nichols, H. Zhu, J. W. Homeister, E. P. Merricks, and C. M. Gallippi, "Acoustic radiation force beam sequence performance for detection and material characterization of atherosclerotic plaques: preclinical, ex vivo results," *IEEE Trans Ultrason Ferroelectr Freq Control,* vol. 60, pp. 2471-87, 2013.

[47] C. L. de Korte, G. Pasterkamp, A. F. W. van der Steen, H. A. Woutman, and N. Bom, "Characterization of plaque components with intravascular ultrasound elastography in human femoral and coronary arteries in vitro," *Circulation,* vol. 102, pp. 617-623, 2000.

[48] C. L. de Korte, A. F. W. van der Steen, E. I. Céspedes, and G. Pasterkamp, "Intravascular Ultrasound Elastography in Human Arteries: Initial Experience In Vitro," *Ultrasound Med Biol,* vol. 24, pp. 401-408, 1998.

[49] S. Rosenzweig, M. Palmeri, and K. Nightingale, "GPU-based real-time small displacement estimation with ultrasound," *Ultrasonics, Ferroelectrics, and Frequency Control, IEEE Transactions on,* vol. 58, pp. 399-405, 2011.

[50] G. L. ten Kate, E. J. G. Sijbrands, R. Valkema, F. J. ten Cate, S. B. Feinstein, A. F. W. van der Steen, M. J. Daemen, and A. F. L. Schinkel, "Molecular imaging of inflammation and intraplaque vasa vasorum: a step forward to identification of vulnerable plaques?," *J Nucl Cardiol,* vol. 17, pp. 897-912, Oct 2010.

[51] D. H. Simpson, C. T. Chin, and P. N. Burns, "Pulse inversion Doppler: a new method for detecting nonlinear echoes from microbubble contrast agents.," *IEEE Trans Ultrason Ferroelectr Freq Control,* vol. 46, pp. 372-82, 1999.

[52] F. A. Duck, "Nonlinear acoustics in diagnostic ultrasound," *Ultrasound Med Biol,* vol. 28, pp. 1-18, Jan 2002.

[53] N. de Jong, A. Bouakaz, and F. J. ten Cate, "Contrast harmonic imaging.," *Ultrasonics,* vol. 40, pp. 567-73, 2002.

[54] H. J. Vos, M. E. Frijlink, E. Droog, D. E. Goertz, G. Blacquière, A. Gisolf, N. de Jong, and A. F. W. van der Steen, "Transducer for harmonic intravascular ultrasound imaging.," *IEEE Trans Ultrason Ferroelectr Freq Control,* vol. 52, pp. 2418-22, 2005.

[55] D. E. Goertz, M. E. Frijlink, D. Tempel, V. Bhagwandas, A. Gisolf, R. Krams, N. de Jong, and A. F. W. van der Steen, "Subharmonic contrast intravascular ultrasound for vasa vasorum imaging," *Ultrasound Med Biol,* vol. 33, pp. 1859-72, Dec 2007.

[56] M. E. Frijlink, D. E. Goertz, L. C. A. van Damme, R. Krams, and A. F. W. van der Steen, "Intravascular ultrasound tissue harmonic imaging in vivo," *IEEE Trans Ultrason Ferroelectr Freq Control,* vol. 53, pp. 1844-52, 2006.

[57] D. Maresca, G. Renaud, G. van Soest, X. Li, Q. Zhou, K. K. Shung, N. de Jong, and A. F. W. van der Steen, "Contrast-enhanced intravascular ultrasound pulse sequences for bandwidth-limited transducers," *Ultrasound Med Biol,* vol. 39, pp. 706-13, Apr 2013.

[58] F. Yu, F. S. Villanueva, and X. Chen, "Radial modulation contrast imaging using a 20-MHz single-element intravascular ultrasound catheter.," *IEEE Trans Ultrason Ferroelectr Freq Control,* vol. 61, pp. 779-91, 2014.

[59] R. Hansen, S.-E. Måsøy, T. A. Tangen, and B. A. Angelsen, "Nonlinear propagation delay and pulse distortion resulting from dual frequency band transmit pulse complexes," *J Acoust Soc Am,* vol. 129, pp. 1117-1127, 2011.

[60] H. M. Garcia-Garcia, M. A. Costa, and P. W. Serruys, "Imaging of coronary atherosclerosis: intravascular ultrasound.," *Eur Heart J,* vol. 31, pp. 2456-69, 2010.

[61] J. V. Frangioni, M. Bawendi, S. Kim, and Y. Lim, "Materials and methods for near-infrared and infrared intravascular imaging," ed: Google Patents, 2004.

[62] R. Puri, M. I. Worthley, and S. J. Nicholls, "Intravascular imaging of vulnerable coronary plaque: current and future concepts.," *Nature reviews Cardiology,* vol. 8, pp. 131-9, 2011.

[63] B. H. Li, A. S. O. Leung, A. Soong, C. E. Munding, H. Lee, A. S. Thind, N. R. Munce, G. A. Wright, C. H. Rowsell, V. X. D. Yang, B. H. Strauss, F. S. Foster, and B. K. Courtney, "Hybrid intravascular ultrasound and optical coherence tomography catheter for imaging of coronary atherosclerosis.," *Catheterization and cardiovascular interventions : official journal of the Society for Cardiac Angiography & Interventions,* vol. 000, 2012.

[64] R. Garrett and C. Grisham, *Biochemistry*: Cengage Learning, 2012.

[65] A. M. Noyes and P. D. Thompson, "A systematic review of the time course of atherosclerotic plaque regression," *Atherosclerosis,* vol. 234, pp. 75-84, 2014.

[66] M. Crisby, G. Nordin-Fredriksson, P. K. Shah, J. Yano, J. Zhu, and J. Nilsson, "Pravastatin treatment increases collagen content and decreases lipid content, inflammation, metalloproteinases, and cell death in human carotid plaques implications for plaque stabilization," *Circulation,* vol. 103, pp. 926-933, 2001.

[67] G. Brown, J. J. Albers, L. D. Fisher, S. M. Schaefer, J. T. Lin, C. Kaplan, X. Q. Zhao, B. D. Bisson, V. F. Fitzpatrick, and H. T. Dodge, "Regression of coronary artery disease as a result of intensive lipid-lowering therapy in men with high levels of apolipoprotein B," *N Engl J Med,* vol. 323, pp. 1289-98, 1990.

[68] K. S. Moulton, K. Vakili, D. Zurakowski, M. Soliman, C. Butterfield, E. Sylvin, K.-M. Lo, S. Gillies, K. Javaherian, and J. Folkman, "Inhibition of plaque neovascularization reduces macrophage accumulation and progression of advanced atherosclerosis," *Proceedings of the National Academy of Sciences of the United States of America,* vol. 100, pp. 4736-41, 2003.

[69] J. K. Williams, M. L. Armstrong, and D. D. Heistad, "Vasa vasorum in atherosclerotic coronary arteries: responses to vasoactive stimuli and regression of atherosclerosis," *Circulation research,* vol. 62, pp. 515-523, 1988.

[70] S. H. Wilson, "Simvastatin Preserves the Structure of Coronary Adventitial Vasa Vasorum in Experimental Hypercholesterolemia Independent of Lipid Lowering," *Circulation,* vol. 105, pp. 415-418, 2002.

[71] G. M. Kindberg, H. Tolleshaug, N. Roos, and T. Skotland, "Hepatic clearance of Sonazoid perfluorobutane microbubbles by Kupffer cells does not reduce the ability of liver to phagocytose or degrade albumin microspheres.," *Cell and tissue research,* vol. 312, pp. 49-54, 2003.

[72] J. K. Willmann, Z. Cheng, C. Davis, A. M. Lutz, M. L. Schipper, C. H. Nielsen, and S. S. Gambhir, "Targeted microbubbles for imaging tumor angiogenesis: assessment of whole-body biodistribution with dynamic micro-PET in mice.," *Radiology,* vol. 249, pp. 212-9, 2008.

[73] J. E. Macioch, C. D. Katsamakis, J. Robin, P. R. Liebson, P. M. Meyer, C. Geohas, J. S. Raichlen, M. H. Davidson, and S. B. Feinstein, "Effect of contrast enhancement on measurement of carotid artery intimal medial thickness," *Vascular Medicine,* vol. 9, pp. 7-12, 2004.

[74] Y. Kono, S. P. Pinnell, C. B. Sirlin, S. R. Sparks, B. Georgy, W. Wong, and R. F. Mattrey, "Carotid arteries: contrast-enhanced US angiography--preliminary clinical experience," *Radiology,* vol. 230, pp. 561-8, 2004.

[75] S. Del Vecchio, A. Zannetti, R. Fonti, L. Pace, and M. Salvatore, "Nuclear imaging in cancer theranostics," *The Quarterly Journal of Nuclear Medicine and Molecular Imaging,* vol. 51, p. 152, 2007.

[76] F. Kiessling, S. Fokong, P. Koczera, W. Lederle, and T. Lammers, "Ultrasound microbubbles for molecular diagnosis, therapy, and theranostics.," *Journal of nuclear medicine : official publication, Society of Nuclear Medicine,* vol. 53, pp. 345-8, 2012.

[77] M. G. Pomper and J. G. Gelovani, *Molecular imaging in oncology*: Informa Health Care, 2008.

[78] S. S. Abdelmoneim, M. Bernier, C. G. Scott, A. Dhoble, S. A. C. Ness, M. E. Hagen, S. Moir, R. B. McCully, P. A. Pellikka, and S. L. Mulvagh, "Safety of contrast agent use during stress echocardiography: a 4-year experience from a single-center cohort study of 26,774 patients.," *JACC Cardiovascular imaging,* vol. 2, pp. 1048-56, Sep 2009.

[79] M. S. Dolan, S. S. Gala, S. Dodla, S. S. Abdelmoneim, F. Xie, D. Cloutier, M. Bierig, S. L. Mulvagh, T. R. Porter, and A. J. Labovitz, "Safety and efficacy of commercially available ultrasound contrast agents for rest and stress echocardiography a multicenter experience.," *J Am Coll Cardiol,* vol. 53, pp. 32-8, 2009.

[80] K. Shaikh, S. M. Chang, L. Peterson, K. Rosendahl-Garcia, M. A. Quinones, S. F. Nagueh, K. M. Kurrelmeyer, and W. A. Zoghbi, "Safety of contrast administration for endocardial enhancement during stress echocardiography compared with noncontrast stress.," *The American journal of cardiology,* vol. 102, pp. 1444-50, 2008.

[81] K. J. Tay, H. Ho, A. Low, and C. Cheng, "Is contrast enhanced ultrasound a valid alternative diagnostic modality for renal cell carcinoma in patients with renal impairment?," *Ann Acad Med Singapore,* vol. 41, pp. 127-128, 2012.

[82] R. Gramiak and P. M. Shah, "Echocardiography of the Aortic Root," *Invest Radiol,* vol. 3, pp. 356-366, 1968.

[83] M. W. Keller, W. Glasheen, and S. Kaul, "Albunex: a safe and effective commercially produced agent for myocardial contrast echocardiography," *J Am Soc Echocardiogr,* vol. 2, pp. 48-52, 1989.

[84] P. A. Dayton, K. E. Morgan, A. L. Klibanov, G. H. Brandenburger, and K. W. Ferrara, "Optical and acoustical observations of the effects of ultrasound on contrast agents," *Ultrasonics, Ferroelectrics, and Frequency Control, IEEE Transactions on,* vol. 46, pp. 220-232, 1999.

[85] S. Mayer and P. A. Grayburn, "Myocardial contrast agents: recent advances and future directions," *Prog Cardiovasc Dis,* vol. 44, pp. 33-44, 2001.

[86] F. J. ten Cate, S. B. Feinstein, W. Zwehl, S. Meerbaum, M. Fishbein, P. M. Shah, and E. Corday, "Two-dimensional contrast echocardiography. II. Transpulmonary studies," *J Am Coll Cardiol,* vol. 3, pp. 21-27, 1984.

[87] A. L. Klibanov, "Microbubble contrast agents: targeted ultrasound imaging and ultrasound-assisted drug-delivery applications.," *Invest Radiol,* vol. 41, pp. 354-62, 2006.

[88] B. B. Goldberg, J. S. Raichlen, and F. Forsberg, *Ultrasound contrast agents: basic principles and clinical applications*: Informa Healthcare, 2001.

[89] S. R. Sirsi and M. A. Borden, "Microbubble compositions, properties and biomedical applications," *Bubble science engineering and technology,* vol. 1, p. 3, 2009.

[90] A. L. Klibanov, "Ligand-carrying gas-filled microbubbles: ultrasound contrast agents for targeted molecular imaging.," *Bioconjugate chemistry,* vol. 16, pp. 9-17, 2005.

[91] J. P. Christiansen, B. A. French, A. L. Klibanov, S. Kaul, and J. R. Lindner, "Targeted tissue transfection with ultrasound destruction of plasmid-bearing cationic microbubbles.," *Ultrasound Med Biol,* vol. 29, pp. 1759-67, 2003.

[92] N. G. Fisher, J. P. Christiansen, A. L. Klibanov, R. P. Taylor, S. Kaul, and J. R. Lindner, "Influence of microbubble surface charge on capillary transit and myocardial contrast enhancement.," *J Am Coll Cardiol,* vol. 40, pp. 811-9, 2002.

[93] H. Leong-Poi, M. A. Kuliszewski, M. Lekas, M. Sibbald, K. Teichert-Kuliszewska, A. L. Klibanov, D. J. Stewart, and J. R. Lindner, "Therapeutic arteriogenesis by ultrasound-mediated VEGF165 plasmid gene delivery to chronically ischemic skeletal muscle.," *Circulation research,* vol. 101, pp. 295-303, 2007.

[94] J. J. Rychak, J. R. Lindner, K. F. Ley, and A. L. Klibanov, "Deformable gas-filled microbubbles targeted to P-selectin.," *Journal of controlled release : official journal of the Controlled Release Society,* vol. 114, pp. 288-99, 2006.

[95] E. C. Unger, E. Hersh, M. Vannan, T. O. Matsunaga, and T. McCreery, "Local drug and gene delivery through microbubbles," *Prog Cardiovasc Dis,* vol. 44, pp. 45-54, 2001.

[96] C. C. Chen and M. A. Borden, "The role of poly (ethylene glycol) brush architecture in complement activation on targeted microbubble surfaces," *Biomaterials,* vol. 32, pp. 6579-6587, 2011.

[97] M. A. Borden, M. R. Sarantos, S. M. Stieger, S. I. Simon, K. W. Ferrara, and P. A. Dayton, "Ultrasound radiation force modulates ligand availability on targeted contrast agents.," *Molecular imaging,* vol. 5, pp. 139-47, 2006.

[98] J. Wible Jr, J. Wojdyla, J. Bugaj, and G. Brandenburger, "Effects of inhaled gases on the ultrasound contrast produced by microspheres containing air or perfluoropropane in anesthetized dogs," *Invest Radiol,* vol. 33, pp. 871-879, 1998.

[99] S. Qin and K. W. Ferrara, "The natural frequency of nonlinear oscillation of ultrasound contrast agents in microvessels.," *Ultrasound Med Biol,* vol. 33, pp. 1140-8, 2007.

[100] K. E. Morgan, J. S. Allen, P. A. Dayton, J. E. Chomas, A. L. Klibanov, and K. W. Ferrara, "Experimental and theoretical evaluation of microbubble behavior: effect of transmitted phase and bubble size.," *IEEE Trans Ultrason Ferroelectr Freq Control,* vol. 47, pp. 1494-509, 2000.

[101] M. Kaya, S. B. Feinstein, K. Hettiarachchi, A. P. Lee, and P. A. Dayton, "Acoustic responses of monodisperse lipid-encapsulated microbubble contrast agents produced by flow focusing.," *Bubble science engineering and technology,* vol. 2, pp. 33-40, 2010.

[102] J. A. Feshitan, C. C. Chen, J. J. Kwan, and M. A. Borden, "Microbubble size isolation by differential centrifugation.," *J Colloid Interface Sci,* vol. 329, pp. 316-24, 2009.

[103] J. E. Streeter, R. C. Gessner, I. Miles, and P. A. Dayton, "Improving sensitivity in ultrasound molecular imaging by tailoring contrast agent size distribution: in vivo studies.," *Molecular imaging,* vol. 9, pp. 87-95, 2010.

[104] E. Talu, K. Hettiarachchi, S. Zhao, R. L. Powell, A. P. Lee, M. L. Longo, and P. A. Dayton, "Tailoring the size distribution of ultrasound contrast agents: possible method for improving sensitivity in molecular imaging.," *Molecular imaging,* vol. 6, pp. 384-92, 2008.

[105] J. E. Chomas, P. A. Dayton, D. May, and K. W. Ferrara, "Threshold of fragmentation for ultrasonic contrast agents.," *J Biomed Opt,* vol. 6, pp. 141-50, 2001.

[106] J. J. Choi, J. A. Feshitan, B. Baseri, S. Wang, Y.-s. Tung, M. A. Borden, and E. E. Konofagou, "Microbubble-size dependence of focused ultrasound-induced blood-brain barrier opening in mice in vivo.," *IEEE transactions on bio-medical engineering,* vol. 57, pp. 145-54, 2010.

[107] G. Samiotaki, F. Vlachos, Y. S. Tung, and E. E. Konofagou, "A quantitative pressure and microbubble-size dependence study of focused ultrasound-induced blood-brain barrier opening reversibility in vivo using MRI," *Magn Reson Med,* vol. 67, pp. 769-777, 2012.

[108] E. Talu, M. M. Lozano, R. L. Powell, P. A. Dayton, and M. L. Longo, "Long-term stability by lipid coating monodisperse microbubbles formed by a flow-focusing device.," *Langmuir : the ACS journal of surfaces and colloids,* vol. 22, pp. 9487-90, 2006.

[109] K. Hettiarachchi, E. Talu, M. L. Longo, P. A. Dayton, and A. P. Lee, "On-chip generation of microbubbles as a practical technology for manufacturing contrast agents for ultrasonic imaging," *Lab Chip,* vol. 7, pp. 463-468, 2007.

[110] U. Farook, H. B. Zhang, M. Edirisinghe, E. Stride, and N. Saffari, "Preparation of microbubble suspensions by co-axial electrohydrodynamic atomization.," *Medical engineering & physics,* vol. 29, pp. 749-54, 2007.

[111] D. Goertz, M. E. Frijlink, M. Voormolen, N. de Jong, and A. F. W. van der Steen, "High frequency attenuation measurements of lipid encapsulated contrast agents," *Ultrasonics,* vol. 44, pp. e131-e134, 2006.

[112] E. Talu, R. L. Powell, M. L. Longo, and P. A. Dayton, "Needle size and injection rate impact microbubble contrast agent population," *Ultrasound Med Biol,* vol. 34, pp. 1182-1185, 2008.

[113] N. de Jong, L. Hoff, T. Skotland, and N. Bom, "Absorption and scatter of encapsulated gas filled microspheres: theoretical considerations and some measurements.," *Ultrasonics,* vol. 30, pp. 95-103, 1992.

[114] N. de Jong, P. J. Frinking, A. Bouakaz, M. Goorden, T. Schourmans, X. Jingping, and F. Mastik, "Optical imaging of contrast agent microbubbles in an ultrasound field with a 100-MHz camera," *Ultrasound Med Biol,* vol. 26, pp. 487-492, 2000.

[115] J. E. Chomas, P. A. Dayton, D. May, J. Allen, A. Klibanov, and K. W. Ferrara, "Optical observation of contrast agent destruction," *Appl Phys Lett,* vol. 77, pp. 1056-1058, 2000.

[116] J. E. Chomas, P. A. Dayton, J. S. Allen, K. E. Morgan, and K. W. Ferrara, "Mechanisms of contrast agent destruction," *IEEE Trans Ultrason Ferroelectr Freq Control,* vol. 48, pp. 232-248, 2001.

[117] P. A. Dayton, A. L. Klibanov, G. H. Brandenburger, and K. W. Ferrara, "Acoustic radiation force in vivo: a mechanism to assist targeting of microbubbles.," *Ultrasound Med Biol,* vol. 25, pp. 1195-201, 1999.

[118] P. A. Dayton, K. E. Morgan, A. L. Klibanov, G. H. Brandenburger, K. R. Nightingale, and K. W. Ferrara, "A preliminary evaluation of the effects of primary and secondary radiation forces on acoustic contrast agents," *IEEE Trans Ultrason Ferroelectr Freq Control,* vol. 44, pp. 1264-1277, 1997.

[119] R. C. Gessner, J. E. Streeter, R. Kothadia, S. B. Feinstein, and P. A. Dayton, "An in vivo validation of the application of acoustic radiation force to enhance the diagnostic utility of molecular imaging using 3-d ultrasound.," *Ultrasound Med Biol,* vol. 38, pp. 651-60, 2012.

[120] J. J. Rychak, A. L. Klibanov, K. F. Ley, and J. A. Hossack, "Enhanced targeting of ultrasound contrast agents using acoustic radiation force.," *Ultrasound Med Biol,* vol. 33, pp. 1132-9, 2007.

[121] M. J. Shortencarier, P. A. Dayton, S. H. Bloch, P. A. Schumann, T. O. Matsunaga, and K. W. Ferrara, "A method for radiation-force localized drug delivery using gas-filled lipospheres.," *IEEE Trans Ultrason Ferroelectr Freq Control,* vol. 51, pp. 822-31, 2004.

[122] A. Kheirolomoom, P. A. Dayton, A. F. H. Lum, E. Little, E. E. Paoli, H. Zheng, and K. W. Ferrara, "Acoustically-active microbubbles conjugated to liposomes: characterization of a proposed drug delivery vehicle.," *Journal of controlled release : official journal of the Controlled Release Society,* vol. 118, pp. 275-84, 2007.

[123] A. F. H. Lum, M. A. Borden, P. A. Dayton, D. E. Kruse, S. I. Simon, and K. W. Ferrara, "Ultrasound radiation force enables targeted deposition of model drug carriers loaded on microbubbles.," *Journal of controlled release : official journal of the Controlled Release Society,* vol. 111, pp. 128-34, 2006.

[124] L. Mullin, R. C. Gessner, J. J. Kwan, M. Kaya, M. A. Borden, and P. A. Dayton, "Effect of anesthesia carrier gas on in vivo circulation times of ultrasound microbubble contrast agents in rats.," *Contrast media & molecular imaging,* vol. 6, pp. 126-31, 2011.

[125] A. C. Perkins, M. Frier, A. J. Hindle, P. E. Blackshaw, S. E. Bailey, J. M. Hebden, S. M. Middleton, and M. L. Wastie, "Human biodistribution of an ultrasound contrast agent (Quantison) by radiolabelling and gamma scintigraphy.," *The British journal of radiology,* vol. 70, pp. 603-11, 1997.

[126] M. S. Tartis, D. E. Kruse, H. Zheng, H. Zhang, A. Kheirolomoom, J. Marik, and K. W. Ferrara, "Dynamic microPET imaging of ultrasound contrast agents and lipid delivery.," *Journal of controlled release : official journal of the Controlled Release Society,* vol. 131, pp. 160-6, 2008.

[127] P. Shankar, P. D. Krishna, and V. Newhouse, "Advantages of subharmonic over second harmonic backscatter for contrast-to-tissue echo enhancement," *Ultrasound Med Biol,* vol. 24, pp. 395-399, 1998.

[128] W. T. Shi, F. Forsberg, A. L. Hall, R. Y. Chiao, J.-B. Liu, S. Miller, K. E. Thomenius, M. A. Wheatley, and B. B. Goldberg, "Subharmonic Imaging with Microbubble Contrast Agents: Initial Results," *Ultrasonic Imaging,* vol. 21, pp. 79-94, 1999.

[129] J. E. Chomas, P. A. Dayton, D. May, and K. W. Ferrara, "Nondestructive subharmonic imaging," *IEEE Trans Ultrason Ferroelectr Freq Control,* vol. 49, pp. 883-892, 2002.

[130] P. N. Burns, "Harmonic imaging with ultrasound contrast agents," *Clin Radiol,* vol. 51, pp. 50-55, 1996.

[131] K. Q. Schwarz, X. Chen, S. Steinmetz, and D. Phillips, "Harmonic imaging with Levovist," *J Am Soc Echocardiogr,* vol. 10, pp. 1-10, 1997.

[132] A. Bouakaz, S. Frigstad, F. J. ten Cate, and N. de Jong, "Super harmonic imaging: a new imaging technique for improved contrast detection.," *Ultrasound Med Biol,* vol. 28, pp. 59-68, 2002.

[133] P. L. van Neer, M. G. Danilouchkine, M. D. Verweij, L. Demi, M. M. Voormolen, A. F. W. van der Steen, and N. de Jong, "Comparison of fundamental, second harmonic, and superharmonic imaging: A simulation study," *J Acoust Soc Am,* vol. 130, pp. 3148-3157, 2011.

[134] D. E. Kruse and K. W. Ferrara, "A new imaging strategy using wideband transient response of ultrasound contrast agents.," *IEEE Trans Ultrason Ferroelectr Freq Control,* vol. 52, pp. 1320-9, 2005.

[135] S. Zhao, D. Kruse, K. W. Ferrara, and P. A. Dayton, "Selective imaging of adherent targeted ultrasound contrast agents," *Phys Med Biol,* vol. 52, p. 2055, 2007.

[136] R. C. Gessner, M. Lukacs, M. Lee, E. Cherin, F. S. Foster, and P. A. Dayton, "High-resolution, high-contrast ultrasound imaging using a prototype dual-frequency transducer: in vitro and in vivo studies," *IEEE Trans Ultrason Ferroelectr Freq Control,* vol. 57, pp. 1772-81, Aug 2010.

[137] C. J. Harvey, M. J. Blomley, R. J. Eckersley, R. A. Heckemann, J. Butler-Barnes, and D. O. Cosgrove, "Pulse-inversion mode imaging of liver specific microbubbles: improved detection of subcentimetre metastases," *The Lancet,* vol. 355, pp. 807-808, 2000.

[138] P. Phillips and E. Gardner, "Contrast–agent detection and quantification," *European Radiology Supplements,* vol. 14, pp. P4-P10, 2004.

[139] X. A. Verbeek, L. A. Ledoux, J. M. Willigers, P. J. Brands, and A. P. Hoeks, "Experimental investigation of the pulse inversion technique for imaging ultrasound contrast agents," *J Acoust Soc Am,* vol. 107, pp. 2281-2290, 2000.

[140] K. Wei, A. R. Jayaweera, S. Firoozan, A. Linka, D. M. Skyba, and S. Kaul, "Quantification of myocardial blood flow with ultrasound-induced destruction of microbubbles administered as a constant venous infusion.," *Circulation,* vol. 97, pp. 473-83, 1998.

[141] D. Cosgrove, R. J. Eckersley, M. Blomley, and C. Harvey, "Quantification of blood flow," *European Radiology,* vol. 11, pp. 1338-1344, 2001.

[142] M. Krix, F. Kiessling, S. Vosseler, N. Farhan, M. M. Mueller, P. Bohlen, N. E. Fusenig, and S. Delorme, "Sensitive noninvasive monitoring of tumor perfusion during antiangiogenic therapy by intermittent bolus-contrast power Doppler sonography," *Cancer research,* vol. 63, pp. 8264-8270, 2003.

[143] P. Kogan, K. A. Johnson, S. Feingold, N. Garrett, I. Guracar, W. J. Arendshorst, and P. A. Dayton, "Validation of dynamic contrast-enhanced ultrasound in rodent kidneys as an absolute quantitative method for measuring blood perfusion," *Ultrasound Med Biol,* vol. 37, pp. 900-908, 2011.

[144] R. E. Pollard, P. A. Dayton, K. D. Watson, X. Hu, I. M. Guracar, and K. W. Ferrara, "Motion corrected cadence CPS ultrasound for quantifying response to vasoactive drugs in a rat kidney model.," *Urology,* vol. 74, pp. 675-81, 2009.

[145] K. Wei, E. Le, J.-p. Bin, M. P. Coggins, J. Thorpe, and S. Kaul, "Quantification of renal blood flow with contrast-enhanced ultrasound," *J Am Coll Cardiol,* vol. 37, pp. 1135-1140, 2001.

[146] J. E. Chomas, R. E. Pollard, A. R. Sadlowski, S. M. Griffey, E. R. Wisner, and K. W. Ferrara, "Contrast-enhanced US of microcirculation of superficially implanted tumors in rats.," *Radiology,* vol. 229, pp. 439-46, 2003.

[147] F. S. Foster, P. N. Burns, D. H. Simpson, S. R. Wilson, D. A. Christopher, and D. E. Goertz, "Ultrasound for the visualization and quantification of tumor microcirculation," *Cancer Metastasis Rev,* vol. 19, pp. 131-138, 2000.

[148] N. Lassau, L. Chami, M. Chebil, B. Benatsou, S. Bidault, E. Girard, G. Abboud, and A. Roche, "Dynamic contrast-enhanced ultrasonography (DCE-US) and anti-angiogenic treatments," *Discovery medicine,* vol. 11, pp. 18-24, 2011.

[149] R. E. Pollard, A. R. Broumas, E. R. Wisner, S. V. Vekich, and K. W. Ferrara, "Quantitative contrast enhanced ultrasound and CT assessment of tumor response to antiangiogenic therapy in rats.," *Ultrasound Med Biol,* vol. 33, pp. 235-45, 2007.

[150] R. E. Pollard, A. R. Sadlowski, S. H. Bloch, L. Murray, E. R. Wisner, S. M. Griffey, and K. W. Ferrara, "Contrast-assisted destruction-replenishment ultrasound for the assessment of tumor microvasculature in a rat model.," *Technology in cancer research & treatment,* vol. 1, pp. 459-70, 2002.

[151] S. R. Sirsi, M. L. Flexman, F. Vlachos, J. Huang, S. L. Hernandez, H. K. Kim, T. B. Johung, J. W. Gander, A. R. Reichstein, B. S. Lampl, A. Wang, A. H. Hielscher, J. J. Kandel, D. J. Yamashiro, and M. A. Borden, "Contrast ultrasound imaging for identification of early responder tumor models to anti-angiogenic therapy.," *Ultrasound Med Biol,* vol. 38, pp. 1019-29, 2012.

[152] K. D. Watson, X. Hu, C.-Y. Lai, H. A. Lindfors, D. D. Hu-Lowe, T. A. Tuthill, D. R. Shalinsky, and K. W. Ferrara, "Novel ultrasound and DCE-MRI analyses after antiangiogenic treatment with a selective VEGF receptor inhibitor," *Ultrasound Med Biol,* vol. 37, pp. 909-921, 2011.

[153] M. A. Averkiou, M. Lampaskis, K. Kyriakopoulou, D. Skarlos, G. Klouvas, C. Strouthos, and E. Leen, "Quantification of tumor microvascularity with respiratory gated contrast enhanced ultrasound for monitoring therapy.," *Ultrasound Med Biol,* vol. 36, pp. 68-77, 2010.

[154] N. Lassau, S. Koscielny, L. Albiges, L. Chami, B. Benatsou, M. Chebil, A. Roche, and B. J. Escudier, "Metastatic renal cell carcinoma treated with sunitinib: early evaluation of treatment response using dynamic contrast-enhanced ultrasonography.," *Clinical cancer research : an official journal of the American Association for Cancer Research,* vol. 16, pp. 1216-25, 2010.

[155] S. Lavisse, P. Lejeune, V. Rouffiac, N. Elie, E. Bribes, B. Demers, P. Vrignaud, M.-C. Bissery, A. Brulé, S. Koscielny, P. Péronneau, and N. Lassau, "Early quantitative evaluation of a tumor vasculature disruptive agent AVE8062 using dynamic contrast-enhanced ultrasonography.," *Invest Radiol,* vol. 43, pp. 100-11, 2008.

[156] R. Williams, J. M. Hudson, B. A. Lloyd, A. R. Sureshkumar, G. Lueck, L. Milot, M. Atri, G. A. Bjarnason, and P. N. Burns, "Dynamic microbubble contrast-enhanced US to measure tumor

response to targeted therapy: a proposed clinical protocol with results from renal cell carcinoma patients receiving antiangiogenic therapy.," *Radiology,* vol. 260, pp. 581-90, 2011.

[157] J. Folkman, "Angiogenesis.," *Annu Rev Med,* vol. 57, pp. 1-18, 2006.

[158] J. E. Kennedy, G. R. ter Haar, F. Wu, F. V. Gleeson, I. S. D. Roberts, M. R. Middleton, and D. Cranston, "Contrast-enhanced ultrasound assessment of tissue response to high-intensity focused ultrasound.," *Ultrasound Med Biol,* vol. 30, pp. 851-4, 2004.

[159] C. W. Burke, A. L. Klibanov, J. P. Sheehan, and R. J. Price, "Inhibition of glioma growth by microbubble activation in a subcutaneous model using low duty cycle ultrasound without significant heating.," *J Neurosurg,* vol. 114, pp. 1654-61, 2011.

[160] P. A. Dayton and K. W. Ferrara, "Targeted imaging using ultrasound.," *Journal of magnetic resonance imaging : JMRI,* vol. 16, pp. 362-77, 2002.

[161] J. R. Lindner, "Molecular imaging with contrast ultrasound and targeted microbubbles," *J Nucl Cardiol,* vol. 11, pp. 215-221, 2004.

[162] G. M. Lanza and S. A. Wickline, "Targeted ultrasonic contrast agents for molecular imaging and therapy.," *Current problems in cardiology,* vol. 28, pp. 625-53, 2003.

[163] G. M. Lanza, K. D. Wallace, S. E. Fischer, D. H. Christy, M. J. Scott, R. L. Trousil, W. P. Cacheris, J. G. Miller, P. J. Gaffney, and S. A. Wickline, "High-frequency ultrasonic detection of thrombi with a targeted contrast system," *Ultrasound Med Biol,* vol. 23, pp. 863-870, 1997.

[164] F. S. Villanueva, E. Lu, S. Bowry, S. Kilic, E. Tom, J. Wang, J. Gretton, J. J. Pacella, and W. R. Wagner, "Myocardial ischemic memory imaging with molecular echocardiography," *Circulation,* vol. 115, pp. 345-352, 2007.

[165] J. R. Lindner, J. Song, J. P. Christiansen, A. L. Klibanov, F. Xu, and K. Ley, "Ultrasound assessment of inflammation and renal tissue injury with microbubbles targeted to P-selectin.," *Circulation,* vol. 104, pp. 2107-12, 2001.

[166] N. Deshpande, A. M. Lutz, Y. Ren, K. Foygel, L. Tian, M. Schneider, R. Pai, P. J. Pasricha, and J. K. Willmann, "Quantification and monitoring of inflammation in murine inflammatory bowel disease with targeted contrast-enhanced US.," *Radiology,* vol. 262, pp. 172-80, 2012.

[167] D. B. Ellegala, H. Leong-Poi, J. E. Carpenter, A. L. Klibanov, S. Kaul, M. E. Shaffrey, J. Sklenar, and J. R. Lindner, "Imaging tumor angiogenesis with contrast ultrasound and microbubbles targeted to αvβ3," *Circulation,* vol. 108, pp. 336-341, 2003.

[168] A. Lyshchik, A. C. Fleischer, J. Huamani, D. E. Hallahan, M. Brissova, and J. C. Gore, "Molecular imaging of vascular endothelial growth factor receptor 2 expression using targeted contrast-enhanced high-frequency ultrasonography," *Journal of ultrasound in medicine,* vol. 26, pp. 1575-1586, 2007.

[169] J. E. Streeter, R. C. Gessner, J. Tsuruta, S. B. Feinstein, and P. A. Dayton, "Assessment of Molecular Imaging of Angiogenesis with Three-Dimensional Ultrasonography.," *Molecular imaging,* vol. 10, pp. 460-468, 2011.

[170] G. Korpanty, J. G. Carbon, P. A. Grayburn, J. B. Fleming, and R. A. Brekken, "Monitoring response to anticancer therapy by targeting microbubbles to tumor vasculature.," *Clinical cancer research : an official journal of the American Association for Cancer Research,* vol. 13, pp. 323-30, 2007.

[171] J. E. Streeter, S. Herrera-Loeza, N. Neel, J. J. Yeh, and P. A. Dayton, "A comparative evaluation of ultrasound molecular imaging, perfusion imaging, and volume measurements in evaluating response to therapy in patient-derived xenografts," *Technology in cancer research & treatment,* vol. 12, pp. 311-321, 2013.

[172] J. R. Eisenbrey, N. Joshi, J. K. Dave, and F. Forsberg, "Assessing algorithms for defining vascular architecture in subharmonic images of breast lesions," *Phys Med Biol,* vol. 56, p. 919, 2011.

[173] J. Shiraishi, K. Sugimoto, F. Moriyasu, N. Kamiyama, and K. Doi, "Computer-aided diagnosis for the classification of focal liver lesions by use of contrast-enhanced ultrasonography," *Med Phys,* vol. 35, pp. 1734-1746, 2008.

[174] K. Sugimoto, J. Shiraishi, F. Moriyasu, S. Ichimura, R. Metoki, and K. Doi, "Analysis of intrahepatic vascular morphological changes of chronic liver disease for assessment of liver fibrosis stages by micro-flow imaging with contrast-enhanced ultrasound: preliminary experience," *European Radiology,* vol. 20, pp. 2749-2757, 2010.

[175] F. Molinari, A. Mantovani, M. Deandrea, P. Limone, R. Garberoglio, and J. S. Suri, "Characterization of single thyroid nodules by contrast-enhanced 3-D ultrasound," *Ultrasound Med Biol,* vol. 36, pp. 1616-1625, 2010.

[176] E. Bullitt, M. Ewend, J. Vredenburgh, A. Friedman, W. Lin, K. Wilber, D. Zeng, S. R. Aylward, and D. Reardon, "Computerized assessment of vessel morphological changes during treatment of glioblastoma multiforme: report of a case imaged serially by MRA over four years," *Neuroimage,* vol. 47, pp. T143-T151, 2009.

[177] E. Bullitt, M. G. Ewend, S. R. Aylward, W. Lin, G. Gerig, S. Joshi, I. Jung, K. Muller, and J. K. Smith, "Abnormal vessel tortuosity as a marker of treatment response of malignant gliomas: preliminary report," *Technology in cancer research & treatment,* vol. 3, pp. 577-584, 2004.

[178] P. Carmeliet and R. K. Jain, "Principles and mechanisms of vessel normalization for cancer and other angiogenic diseases," *Nature Reviews Drug Discovery,* vol. 10, pp. 417-427, 2011.

[179] R. Seip, C. T. Chin, C. S. Hall, B. I. Raju, A. Ghanem, and K. Tiemann, "Targeted ultrasound-mediated delivery of nanoparticles: on the development of a new HIFU-based therapy and imaging device.," *IEEE transactions on bio-medical engineering,* vol. 57, pp. 61-70, 2010.

[180] Y. Huang and K. Hynynen, "MR-guided focused ultrasound for brain ablation and blood–brain barrier disruption," *Magnetic Resonance Neuroimaging: Methods and Protocols,* pp. 579-593, 2011.

[181] S.-T. Kang and C.-K. Yeh, "Ultrasound microbubble contrast agents for diagnostic and therapeutic applications: current status and future design.," *Chang Gung medical journal,* vol. 35, pp. 125-39, 2011.

[182] N. A. Geis, H. A. Katus, and R. Bekeredjian, "Microbubbles as a vehicle for gene and drug delivery: current clinical implications and future perspectives.," *Current pharmaceutical design,* vol. 18, pp. 2166-83, 2012.

[183] R. J. Price, D. M. Skyba, S. Kaul, and T. C. Skalak, "Delivery of colloidal particles and red blood cells to tissue through microvessel ruptures created by targeted microbubble destruction with ultrasound.," *Circulation,* vol. 98, pp. 1264-7, 1998.

[184] R. Karshafian, P. D. Bevan, R. Williams, S. Samac, and P. N. Burns, "Sonoporation by ultrasound-activated microbubble contrast agents: effect of acoustic exposure parameters on cell membrane permeability and cell viability.," *Ultrasound Med Biol,* vol. 35, pp. 847-60, 2009.

[185] F. Wang, Y. Cheng, J. Mei, Y. Song, Y.-q. Yang, Y. Liu, and Z. Wang, "Focused ultrasound microbubble destruction-mediated changes in blood-brain barrier permeability assessed by contrast-enhanced magnetic resonance imaging.," *Journal of ultrasound in medicine : official journal of the American Institute of Ultrasound in Medicine,* vol. 28, pp. 1501-9, 2009.

[186] J. J. Choi, S. Wang, T. R. Brown, S. A. Small, K. E. K. Duff, and E. E. Konofagou, "Noninvasive and transient blood-brain barrier opening in the hippocampus of Alzheimer's double transgenic mice using focused ultrasound," *Ultrasonic imaging,* vol. 30, pp. 189-200, 2008.

[187] J. F. Jordão, C. A. Ayala-Grosso, K. Markham, Y. Huang, R. Chopra, J. McLaurin, K. Hynynen, and I. Aubert, "Antibodies targeted to the brain with image-guided focused ultrasound reduces

amyloid-β plaque load in the TgCRND8 mouse model of Alzheimer's disease," *PloS one,* vol. 5, p. e10549, 2010.

[188] S. Fokong, B. Theek, Z. Wu, P. Koczera, L. Appold, S. Jorge, U. Resch-Genger, M. van Zandvoort, G. Storm, F. Kiessling, and T. Lammers, "Image-guided, targeted and triggered drug delivery to tumors using polymer-based microbubbles.," *Journal of controlled release : official journal of the Controlled Release Society,* 2012.

[189] S. Chen, J.-h. Ding, R. Bekeredjian, B.-z. Yang, R. V. Shohet, S. A. Johnston, H. E. Hohmeier, C. B. Newgard, and P. A. Grayburn, "Efficient gene delivery to pancreatic islets with ultrasonic microbubble destruction technology.," *Proc Natl Acad Sci U S A,* vol. 103, pp. 8469-74, 2006.

[190] C. F. Caskey, S. M. Stieger, S. Qin, P. A. Dayton, and K. W. Ferrara, "Direct observations of ultrasound microbubble contrast agent interaction with the microvessel wall.," *J Acoust Soc Am,* vol. 122, pp. 1191-200, 2007.

[191] H. Chen, W. Kreider, A. A. Brayman, M. R. Bailey, and T. J. Matula, "Blood vessel deformations on microsecond time scales by ultrasonic cavitation," *Physical Review Letters,* vol. 106, p. 034301, 2011.

[192] C.-D. Ohl, M. Arora, R. Ikink, N. de Jong, M. Versluis, M. Delius, and D. Lohse, "Sonoporation from jetting cavitation bubbles.," *Biophysical journal,* vol. 91, pp. 4285-95, 2006.

[193] S. M. Stieger, C. F. Caskey, R. H. Adamson, S. Qin, F.-R. E. Curry, E. R. Wisner, and K. W. Ferrara, "Enhancement of Vascular Permeability with Low-Frequency Contrast-enhanced Ultrasound in the Chorioallantoic Membrane Model," *Radiology,* vol. 243, pp. 112-121, 2007.

[194] A. Van Wamel, K. Kooiman, M. Harteveld, M. Emmer, J. Folkert, M. Versluis, and N. De Jong, "Vibrating microbubbles poking individual cells: drug transfer into cells via sonoporation," *Journal of Controlled Release,* vol. 112, pp. 149-155, 2006.

[195] P. Prentice, A. Cuschieri, K. Dholakia, M. Prausnitz, and P. Campbell, "Membrane disruption by optically controlled microbubble cavitation," *Nature Physics,* vol. 1, pp. 107-110, 2005.

[196] Y. Zhou, K. Yang, J. Cui, J. Y. Ye, and C. X. Deng, "Controlled permeation of cell membrane by single bubble acoustic cavitation.," *Journal of controlled release : official journal of the Controlled Release Society,* vol. 157, pp. 103-11, 2012.

[197] S. Bao, B. D. Thrall, and D. L. Miller, "Transfection of a reporter plasmid into cultured cells by sonoporation in vitro.," *Ultrasound Med Biol,* vol. 23, pp. 953-9, 1997.

[198] D. L. Miller and J. Quddus, "Sonoporation of monolayer cells by diagnostic ultrasound activation of contrast-agent gas bodies.," *Ultrasound Med Biol,* vol. 26, pp. 661-7, 2000.

[199] K. Keyhani, H. R. Guzmán, A. Parsons, T. N. Lewis, and M. R. Prausnitz, "Intracellular drug delivery using low-frequency ultrasound: quantification of molecular uptake and cell viability.," *Pharmaceutical research,* vol. 18, pp. 1514-20, 2001.

[200] M. M. Forbes, R. L. Steinberg, and W. D. O'Brien, "Frequency-dependent evaluation of the role of Definity in producing sonoporation of Chinese hamster ovary cells.," *Journal of ultrasound in medicine : official journal of the American Institute of Ultrasound in Medicine,* vol. 30, pp. 61-9, 2011.

[201] Y. Liu, H. Miyoshi, and M. Nakamura, "Encapsulated ultrasound microbubbles: therapeutic application in drug/gene delivery.," *Journal of controlled release : official journal of the Controlled Release Society,* vol. 114, pp. 89-99, 2006.

[202] M. Schneider, "Molecular imaging and ultrasound-assisted drug delivery.," *Journal of endourology / Endourological Society,* vol. 22, pp. 795-802, 2008.

[203] X. Xiong, F. Zhao, M. Shi, H. Yang, and Y. Liu, "Polymeric microbubbles for ultrasonic molecular imaging and targeted therapeutics.," *Journal of biomaterials science Polymer edition,* vol. 22, pp. 417-28, 2011.

[204] I. Lentacker, S. C. de Smedt, and N. N. Sanders, "Drug loaded microbubble design for ultrasound triggered delivery," *Soft Matter,* vol. 5, p. 2161, 2009.

[205] L. C. Phillips, A. H. Dhanaliwala, A. L. Klibanov, J. A. Hossack, and B. R. Wamhoff, "Focused Ultrasound-Mediated Drug Delivery From Microbubbles Reduces Drug Dose Necessary for Therapeutic Effect on Neointima Formation.," *Arterioscler Thromb Vasc Biol,* pp. 2853-2855, 2011.

[206] K. Hettiarachchi, S. Zhang, S. Feingold, A. P. Lee, and P. A. Dayton, "Controllable microfluidic synthesis of multiphase drug-carrying lipospheres for site-targeted therapy," *Biotechnol Prog,* vol. 25, pp. 938-945, 2009.

[207] E. C. Unger, T. P. McCreery, R. H. Sweitzer, V. E. Caldwell, and Y. Wu, "Acoustically active lipospheres containing paclitaxel: a new therapeutic ultrasound contrast agent," *Invest Radiol,* vol. 33, pp. 886-892, 1998.

[208] M. S. Tartis, J. McCallan, A. F. H. Lum, R. LaBell, S. M. Stieger, T. O. Matsunaga, and K. W. Ferrara, "Therapeutic effects of paclitaxel-containing ultrasound contrast agents.," *Ultrasound Med Biol,* vol. 32, pp. 1771-80, 2006.

[209] M. C. Cochran, J. Eisenbrey, R. O. Ouma, M. Soulen, and M. A. Wheatley, "Doxorubicin and paclitaxel loaded microbubbles for ultrasound triggered drug delivery," *Int J Pharm,* vol. 414, pp. 161-170, 2011.

[210] B. Geers, I. Lentacker, N. N. Sanders, J. Demeester, S. Meairs, and S. C. De Smedt, "Self-assembled liposome-loaded microbubbles: The missing link for safe and efficient ultrasound triggered drug-delivery.," *Journal of controlled release : official journal of the Controlled Release Society,* vol. 152, pp. 249-56, 2011.

[211] L. C. Phillips, A. L. Klibanov, B. R. Wamhoff, and J. A. Hossack, "Localized ultrasound enhances delivery of rapamycin from microbubbles to prevent smooth muscle proliferation," *Journal of Controlled Release,* vol. 154, pp. 42-49, 2011.

[212] Z. Hou, L. Li, C. Zhan, P. Zhu, D. Chang, Q. Jiang, S. Ye, X. Yang, Y. Li, and L. Xie, "Preparation and in vitro evaluation of an ultrasound-triggered drug delivery system: 10-Hydroxycamptothecin loaded PLA microbubbles," *Ultrasonics,* vol. 52, pp. 836-841, 2012.

[213] D. J. May, J. S. Allen, and K. W. Ferrara, "Dynamics and fragmentation of thick-shelled microbubbles," *Ultrasonics, Ferroelectrics, and Frequency Control, IEEE Transactions on,* vol. 49, pp. 1400-1410, 2002.

[214] M. A. Borden, C. F. Caskey, E. Little, R. J. Gillies, and K. W. Ferrara, "DNA and polylysine adsorption and multilayer construction onto cationic lipid-coated microbubbles.," *Langmuir : the ACS journal of surfaces and colloids,* vol. 23, pp. 9401-8, 2007.

[215] L. C. Phillips, A. L. Klibanov, D. K. Bowles, M. Ragosta, J. A. Hossack, and B. R. Wamhoff, "Focused in vivo delivery of plasmid DNA to the porcine vascular wall via intravascular ultrasound destruction of microbubbles.," *Journal of vascular research,* vol. 47, pp. 270-4, 2010.

[216] Y. Taniyama, K. Tachibana, K. Hiraoka, T. Namba, K. Yamasaki, N. Hashiya, M. Aoki, T. Ogihara, K. Yasufumi, and R. Morishita, "Local delivery of plasmid DNA into rat carotid artery using ultrasound.," *Circulation,* vol. 105, pp. 1233-9, 2002.

[217] S. D. Tiukinhoy, M. E. Mahowald, V. P. Shively, A. Nagaraj, B. J. Kane, M. E. Klegerman, R. C. MacDonald, D. D. McPherson, and J. S. Matsumura, "Development of echogenic, plasmid-incorporated, tissue-targeted cationic liposomes that can be used for directed gene delivery.," *Invest Radiol,* vol. 35, pp. 732-8, 2000.

[218] J. L. Tlaxca, C. R. Anderson, A. L. Klibanov, B. Lowrey, J. A. Hossack, J. S. Alexander, M. B. Lawrence, and J. J. Rychak, "Analysis of in vitro transfection by sonoporation using cationic and neutral microbubbles.," *Ultrasound Med Biol,* vol. 36, pp. 1907-18, 2010.

[219] N. Nomikou, P. Tiwari, T. Trehan, K. Gulati, and A. P. McHale, "Studies on neutral, cationic and biotinylated cationic microbubbles in enhancing ultrasound-mediated gene delivery in vitro and in vivo.," *Acta biomaterialia,* vol. 8, pp. 1273-80, 2012.

[220] D. Wang, D. R. Robinson, G. S. Kwon, and J. Samuel, "Encapsulation of plasmid DNA in biodegradable poly(D, L-lactic-co-glycolic acid) microspheres as a novel approach for immunogene delivery.," *Journal of controlled release : official journal of the Controlled Release Society,* vol. 57, pp. 9-18, 1999.

[221] S. Seemann, P. Hauff, M. Schultze-Mosgau, C. Lehmann, and R. Reszka, "Pharmaceutical evaluation of gas-filled microparticles as gene delivery system.," *Pharmaceutical research,* vol. 19, pp. 250-7, 2002.

[222] F. Xie, J. M. Tsutsui, J. Lof, E. C. Unger, J. Johanning, W. C. Culp, T. O. Matsunaga, and T. R. Porter, "Effectiveness of lipid microbubbles and ultrasound in declotting thrombosis.," *Ultrasound Med Biol,* vol. 31, pp. 979-85, 2005.

[223] F. Perren, J. Loulidi, D. Poglia, T. Landis, and R. Sztajzel, "Microbubble potentiated transcranial duplex ultrasound enhances IV thrombolysis in acute stroke.," *Journal of thrombosis and thrombolysis,* vol. 25, pp. 219-23, 2008.

[224] C. A. Molina, M. Ribo, M. Rubiera, J. Montaner, E. Santamarina, R. Delgado-Mederos, J. F. Arenillas, R. Huertas, F. Purroy, P. Delgado, and J. Alvarez-Sabín, "Microbubble administration accelerates clot lysis during continuous 2-MHz ultrasound monitoring in stroke patients treated with intravenous tissue plasminogen activator.," *Stroke; a journal of cerebral circulation,* vol. 37, pp. 425-9, 2006.

[225] A. V. Alexandrov, "Ultrasound enhancement of fibrinolysis," *Stroke; a journal of cerebral circulation,* vol. 40, pp. S107-S110, 2009.

[226] S. Kutty, F. Xie, S. Gao, L. K. Drvol, J. Lof, S. E. Fletcher, S. J. Radio, D. A. Danford, J. M. Hammel, and T. R. Porter, "Sonothrombolysis of intra-catheter aged venous thrombi using microbubble enhancement and guided three-dimensional ultrasound pulses," *J Am Soc Echocardiogr,* vol. 23, pp. 1001-1006, 2010.

[227] F. Xie, J. Slikkerveer, S. Gao, J. Lof, O. Kamp, E. Unger, S. J. Radio, T. Matsunaga, and T. R. Porter, "Coronary and microvascular thrombolysis with guided diagnostic ultrasound and microbubbles in acute ST segment elevation myocardial infarction," *J Am Soc Echocardiogr,* vol. 24, pp. 1400-1408, 2011.

[228] W.-S. Chen, C. Lafon, T. J. Matula, S. Vaezy, and L. A. Crum, "Mechanisms of lesion formation in high intensity focused ultrasound therapy," *Acoustics Research Letters Online,* vol. 4, p. 41, 2003.

[229] C. C. Coussios, C. H. Farny, G. R. ter Haar, and R. A. Roy, "Role of acoustic cavitation in the delivery and monitoring of cancer treatment by high-intensity focused ultrasound (HIFU)," *International Journal of Hyperthermia,* vol. 23, pp. 105-120, 2007.

[230] R. G. Holt and R. A. Roy, "Measurements of bubble-enhanced heating from focused, MHz-frequency ultrasound in a tissue-mimicking material.," *Ultrasound Med Biol,* vol. 27, pp. 1399-412, 2001.

[231] B. C. Tran, J. Seo, T. L. Hall, J. B. Fowlkes, and C. A. Cain, "Microbubble-enhanced cavitation for noninvasive ultrasound surgery," *Ultrasonics, Ferroelectrics, and Frequency Control, IEEE Transactions on,* vol. 50, pp. 1296-1304, 2003.

[232] Y.-S. Tung, H.-L. Liu, C.-C. Wu, K.-C. Ju, W.-S. Chen, and W.-L. Lin, "Contrast-agent-enhanced ultrasound thermal ablation," *Ultrasound Med Biol,* vol. 32, pp. 1103-1110, 2006.

[233] K. Hynynen, "The threshold for thermally significant cavitation in dog's thigh muscle in vivo.," *Ultrasound Med Biol,* vol. 17, pp. 157-69, 1991.

[234] S. Peng, Y. Xiong, K. Li, M. He, Y. Deng, L. Chen, M. Zou, W. Chen, Z. Wang, J. He, and L. Zhang, "Clinical utility of a microbubble-enhancing contrast ("SonoVue") in treatment of uterine fibroids with high intensity focused ultrasound: A retrospective study.," *European journal of radiology,* 2012.

[235] K. K. Shung, "In vitro experimental results on ultrasonic scattering in biological tissues," in *Ultrasonic Scattering in Biological Tissues,* K. K. Shung and G. A. Thieme, Eds., ed Boca Raton, FL: CRC Press, 1992.

[236] K. W. Ferrara, R. E. Pollard, and M. A. Borden, "Ultrasound microbubble contrast agents: fundamentals and application to gene and drug delivery.," *Annual review of biomedical engineering,* vol. 9, pp. 415-47, 2007.

[237] M. A. Ainslie and T. G. Leighton, "Review of scattering and extinction cross-sections, damping factors, and resonance frequencies of a spherical gas bubble," *J Acoust Soc Am,* vol. 130, pp. 3184-208, Nov 2011.

[238] W. Lauterborn, "Numerical investigation of nonlinear oscillations of gas bubbles in liquids," *J Acoust Soc Am,* vol. 59, pp. 283-283, 1976.

[239] Q. Chen, J. A. Zagzebski, T. Wilson, and T. Stiles, "Pressure-dependent attenuation in ultrasound contrast agents," *Ultrasound Med Biol,* vol. 28, pp. 1041-51, 2002.

[240] V. Sboros, C. A. MacDonald, S. D. Pye, C. M. Moran, J. Gomatam, and W. N. McDicken, "The dependence of ultrasound contrast agents backscatter on acoustic pressure: theory versus experiment," *Ultrasonics,* vol. 40, pp. 579-83, May 2002.

[241] M. A. Averkiou, "Tissue Harmonic Imaging " presented at the IEEE International Ultrasonics Symposium, San Juan, PR, 2000.

[242] P. T. Christopher and K. J. Parker, "New approaches to nonlinear diffractive field propagation," *J Acoust Soc Am,* vol. 90, pp. 488-99, Jul 1991.

[243] H. G. Flynn, "Physics of Acoustic Cavitation in Liquids," *Physical Acoustics,* vol. 1, pp. 57-172, 1964 1964.

[244] N. de Jong, R. Cornet, and C. T. Lancée, "Higher harmonics of vibrating gas-filled microspheres. Part one: simulations," *Ultrasonics,* vol. 32, pp. 447-453, 1994.

[245] N. de Jong, R. Cornet, and C. T. Lancée, "Higher harmonics of vibrating gas-filled microspheres. Part two: measurements," *Ultrasonics,* vol. 32, pp. 455-459, 1994.

[246] N. de Jong, A. Bouakaz, and P. J. Frinking, "Basic acoustic properties of microbubbles," *Echocardiography,* vol. 19, pp. 229-240, Apr 2002.

[247] G. A. Brock-Fisher, M. D. Poland, and P. G. Rafter, "Means for increasing sensitivity in non-linear ultrasound imaging systems," U.S. Patent 5577505 A, 1996.

[248] R. J. Eckersley, C. T. Chin, and P. N. Burns, "Optimising phase and amplitude modulation schemes for imaging microbubble contrast agents at low acoustic power," *Ultrasound Med Biol,* vol. 31, pp. 213-9, Feb 2005.

[249] B. Haider and R. Y. Chiao, "Higher order nonlinear ultrasonic imaging," presented at the IEEE International Ultrasonics Symposium, Lake Tahoe, NV, 1999.

[250] P. J. Phillips, "Contrast pulse sequences (CPS): imaging nonlinear microbubbles," presented at the IEEE International Ultrasonics Symposium, Atlanta, GA, 2001.

[251] J. W. Hunt, M. Arditi, and F. S. Foster, "Ultrasound Transducers for Pulse-Echo Medical Imaging," *IEEE Trans Biomed Eng,* vol. 30, pp. 453-81, Aug 1983.

[252] C. S. Desilets, J. D. Fraser, and G. S. Kino, "The Design of Efficient Broad-Band Piezoelectric Transducers," *IEEE Transactions on Sonics and Ultrasonics,* vol. SU-25, pp. 115-125, May 1978 1978.

[253] G. S. Kino, *Acoustic Waves: Devices, Imaging, and Analog Signal Processing*. Englewood Cliffs, NJ: Prentice Hall PTR, 1987.

[254] R. E. McKeighen, "Design guidelines for medical ultrasonic arrays," presented at the Medical Imaging 1998: Ultrasonic Transducer Engineering, 1998.

[255] H. L. W. Chan, J. Unsworth, and T. Bui, "Mode coupling in modified lead titanate/polymer 1–3 composites," *Journal of Applied Physics,* vol. 65, p. 1754, 1989.

[256] R. Lerch, "Simulation of Piezoelectric Devices by Two- and Three-Dimensional Finite Elements," *IEEE Trans Ultrason Ferroelectr Freq Control,* vol. 37, pp. 233-247, 1990.

[257] A. Safari, R. E. Newnham, L. E. Cross, and W. A. Schulze, "Perforated PZT-Polymer Composites for Piezoelectric Transducer Applications," *Ferroelectrics,* vol. 41, pp. 197-205, 1982.

[258] W. A. Smith, A. Shaulov, and B. A. Auld, "Tailoring the properties of composite piezoelectric materials for medical ultrasonic transducers," presented at the IEEE International Ultrasonics Symposium, San Francisco, CA, 1985.

[259] W. A. Smith, "The application of 1-3 piezocomposites in acoustic transducers," presented at the IEEE International Symposium on the Applications of Ferroelectrics, Urbana-Champaign, IL, 1990.

[260] K. H. Lam and H. L. W. Chan, "Piezoelectric cement-based 1-3 composites," *Applied Physics A,* vol. 81, pp. 1451-1454, 2005.

[261] K. C. Cheng, H. L. W. Chan, C. L. Choy, Q. Yin, H. Luo, and J. Yin, "Single crystal PMN-0.33PT/epoxy 1-3 composites for ultrasonic transducer applications " *IEEE Trans Ultrason Ferroelectr Freq Control,* vol. 50, pp. 1177-83, 2003.

[262] H. P. Savakus, K. A. Klicker, and R. E. Newnham, "PZT-epoxy piezoelectric transducers: A simplified fabrication procedure," *Materials Research Bulletin,* vol. 16, pp. 677-680, 1981.

[263] J. R. Yuan, S. Rhee, and X. Jiang, "60 MHz PMN-PT based 1-3 composite transducer for IVUS imaging," presented at the IEEE International Ultrasonics Symposium, Beijing, China, 2008.

[264] X. Jiang, J. R. Yuan, A. Cheng, K. Snook, P. J. Cao, P. W. Rehrig, W. S. Hackenberger, G. Lavalelle, X. Geng, and T. R. Shrout, "Microfabrication of piezoelectric composite ultrasound transducers (PC-MUT)," presented at the IEEE International Ultrasonics Symposium, Vancouver, BC, 2006.

[265] F. S. Foster, J. Mehi, M. Lukacs, D. Hirson, C. White, C. Chaggares, and A. Needles, "A new 15-50 MHz array-based micro-ultrasound scanner for preclinical imaging," *Ultrasound Med Biol,* vol. 35, pp. 1700-8, 2009.

[266] A. Novell, M. Legros, N. Felix, and A. Bouakaz, "Exploitation of capacitive micromachined transducers for nonlinear ultrasound imaging," *IEEE Trans Ultrason Ferroelectr Freq Control,* vol. 56, pp. 2733-43, 2009.

[267] A. Novell, J. M. Escoffre, and A. Bouakaz, "Second Harmonic and Subharmonic for Non-Linear Wideband Contrast Imaging Using a Capacitive Micromachined Ultrasonic Transducer Array," *Ultrasound Med Biol,* vol. 39, pp. 1500-12, Aug 2013.

[268] O. Oralkan, A. S. Ergun, J. A. Johnson, M. Karaman, U. Demirci, K. Kaviani, T. H. Lee, and B. T. Khuri-Yakub, "Capacitive Micromachined Ultrasonic Transducers: Next-Generation Arrays for Acoustic Imaging?," *IEEE Trans Ultrason Ferroelectr Freq Control,* vol. 49, pp. 1596-1610, 2002.

[269] A. S. Ergun, G. G. Yaralioglu, and B. T. Khuri-yakub, "Capacitive Micromachined Ultrasonic Transducers: Theory and Technology," *J Aerosp Eng,* vol. 16, pp. 76-84, 2003.

[270] A. S. Ergun, Y. Huang, and S. Member, "Capacitive Micromachined Ultrasonic Transducers : Fabrication Technology," *IEEE Trans Ultrason Ferroelectr Freq Control,* vol. 52, pp. 2242-2258, 2005.

[271] A. Novell, M. Legros, J.-M. Grégoire, P. A. Dayton, and A. Bouakaz, "Evaluation of bias voltage modulation sequence for nonlinear contrast agent imaging using a capacitive micromachined ultrasonic transducer array," *Phys Med Biol,* vol. 59, pp. 4879-96, 2014.

[272] M. E. Frijlink, L. Lovstakken, and H. Torp, "Investigation of transmit and receive performance at the fundamental and third harmonic resonance frequency of a medical ultrasound transducer," *Ultrasonics,* vol. 49, pp. 601-604, Dec 2009.

[273] W. S. Hackenberger, X. Jiang, P. W. Rehrig, G. Xuecang, A. Winder, and F. Forsberg, "Broad band single crystal transducer for contrast agent harmonic imaging," presented at the IEEE International Ultrasonics Symposium, Honolulu, HI, 2003.

[274] A. Bouakaz, B. J. Krenning, W. B. Vletter, F. J. ten Cate, and N. de Jong, "Contrast superharmonic imaging: A feasibility study," *Ultrasound Med Biol,* vol. 29, pp. 547-553, 2003.

[275] A. Bouakaz, F. Cate, and N. de Jong, "A new ultrasonic transducer for improved contrast nonlinear imaging," *Phys Med Biol,* vol. 49, pp. 3515-25, Aug 21 2004.

[276] D. N. Stephens, X. M. Lu, T. Proulx, W. Walters, P. A. Dayton, M. Tartis, D. E. Kruse, A. F. H. Lum, T. Kitano, S. M. Stieger, and K. W. Ferrara, "Multi-frequency Array Development for Drug Delivery Therapies: Characterization and First Use of a Triple Row Ultrasound Probe," presented at the IEEE International Ultrasonics Symposium, Vancouver, BC, 2006.

[277] H. Zheng, D. E. Kruse, D. N. Stephens, K. W. Ferrara, P. L. Sutcliffe, and E. Gardner, "A sensitive ultrasonic imaging method for targeted contrast microbubble detection," presented at the 30th Annual International IEEE EMBS Conference, Vancouver, BC, 2008.

[278] X. Hu, H. Zheng, D. E. Kruse, P. L. Sutcliffe, D. N. Stephens, and K. W. Ferrara, "A sensitive TLRH targeted imaging technique for ultrasonic molecular imaging.," *IEEE Trans Ultrason Ferroelectr Freq Control,* vol. 57, pp. 305-16, 2010.

[279] X. Hu, C. F. Caskey, L. M. Mahakian, D. E. Kruse, J. R. Beegle, A. E. Decleves, J. J. Rychak, P. L. Sutcliffe, K. Sharma, and K. W. Ferrara, "In vivo validation and 3D visualization of broadband ultrasound molecular imaging," *American journal of nuclear medicine and molecular imaging,* vol. 3, pp. 336-49, 2013.

[280] D. N. Stephens, D. E. Kruse, A. S. Ergun, S. H. Barnes, X. M. Lu, and K. W. Ferrara, "Efficient array design for sonotherapy," *Phys Med Biol,* vol. 53, pp. 3943-69, Jul 21 2008.

[281] D. E. Kruse, C. Y. Lai, D. N. Stephens, P. L. Sutcliffe, E. E. Paoli, S. H. Barnes, and K. W. Ferrara, "Spatial and temporal-controlled tissue heating on a modified clinical ultrasound scanner for generating mild hyperthermia in tumors," *IEEE Trans Biomed Eng,* vol. 57, pp. 155-66, Jan 2010.

[282] G. Ferin, M. Legros, N. Felix, C. Notard, and L. Ratsimandresey, "Ultra-Wide Bandwidth Array for New Imaging Modalities " presented at the IEEE International Ultrasonics Symposium, New York, NY, 2007.

[283] P. L. M. J. van Neer, G. M. Matte, M. G. Danilouchkine, M. D. Verweij, and N. de Jong, "A study of phased array transducer topology for superharmonic imaging," presented at the IEEE International Ultrasonics Symposium, San Diego, CA, USA, 2010.

[284] P. L. M. J. van Neer, G. M. Matte, M. G. Danilouchkine, C. Prins, F. van den Adel, and N. de Jong, "Super-harmonic imaging: development of an interleaved phased-array transducer," *IEEE Trans Ultrason Ferroelectr Freq Control,* vol. 57, pp. 455-68, 2010.

[285] K. K. Shung, "High Frequency Ultrasonic Imaging," *Journal of medical ultrasound,* vol. 17, pp. 25-30, 2009.

[286] J.-Z. Zhao, C. H. F. Alves, K. A. Snook, J. M. Cannata, W.-H. Chen, R. J. Meyer, S. Ayyappan, T. A. Ritter, and K. K. Shung, "Performance of 50 MHz transducers incorporating fiber composite, PVDF, PbTiO3, and LiNbO3," presented at the IEEE International Ultrasonics Symposium, Lake Tahoe, NV, 1999.

[287] G. M. Lous, I. A. Cornejo, T. F. McNulty, A. Safari, and S. A. Danforth, "Fabrication of curved ceramic/polymer composite transducer for ultrasonic imaging applications by fused deposition of ceramics," presented at the IEEE International Symposium on the Applications of Ferroelectrics, Montreaux, Switzerland, 1998.

[288] J. A. Brown, F. S. Foster, A. Needles, E. Cherin, and G. R. Lockwood, "Fabrication and performance of a 40-MHz linear array based on a 1-3 composite with geometric elevation focusing," *IEEE Trans Ultrason Ferroelectr Freq Control,* vol. 54, pp. 1888-1894, Sep 2007.

[289] J. A. Brown, E. Cherin, Y. Jianhua, and F. S. Foster, "Fabrication and performance of high-frequency composite transducers with triangular-pillar geometry," *IEEE Trans Ultrason Ferroelectr Freq Control,* vol. 56, pp. 827-836, 2009.

[290] M. Lukacs, M. Lee, E. Cherin, J. Yin, D. Hirson, F. S. Foster, R. C. Gessner, and P. A. Dayton, "Hybrid Dual Frequency Transducer and Scanhead for Micro-Ultrasound Imaging," presented at the IEEE International Ultrasonics Symposium, Rome, Italy, 2009.

[291] B. D. Lindsey, J. D. Rojas, K. H. Martin, S. E. Shelton, and P. A. Dayton, "Acoustic characterization of contrast-to-tissue ratio and axial resolution for dual-frequency contrast-specific acoustic angiography imaging," *IEEE Trans Ultrason Ferroelectr Freq Control,* vol. 61, pp. 1668-1687, 2014.

[292] R. C. Gessner, C. B. Frederick, F. S. Foster, and P. A. Dayton, "Acoustic angiography: a new imaging modality for assessing microvasculature architecture," *Journal of Biomedical Imaging,* vol. 2013, p. 14, 2013.

[293] S. E. Shelton, Y. Z. Lee, F. S. Foster, M. Lee, S. R. Aylward, and P. A. Dayton, "Quantification of microvascular tortuosity during tumor evolution utilizing acoustic angiography," *Manuscript submitted for publication,* 2015.

[294] A. Guiroy, A. Novell, E. Ringgaard, R. Lou-Moeller, J.-M. Grégoire, A.-P. Abellard, T. Zawada, A. Bouakaz, and F. Levassort, "Dual-frequency transducer for nonlinear contrast agent imaging.," *IEEE Trans Ultrason Ferroelectr Freq Control,* vol. 60, pp. 2634-44, 2013.

[295] S. Li, W. Huang, X. Jiang, X. Jian, and Y. Cui, "A Dual-layer Micromachined PMN-PT 1-3 Composite Transducer for Broadband Ultrasound Imaging," presented at the IEEE International Ultrasonics Symposium, Prague, 2013.

[296] K. K. Shung, J. M. Cannata, and Q. Zhou, "Piezoelectric materials for high frequency medical imaging applications: A review," *J Electroceram,* vol. 19, pp. 141-147, Sep 2007.

[297] S. E. Nissen and P. Yock, "Intravascular ultrasound: novel pathophysiological insights and current clinical applications," *Circulation,* vol. 103, pp. 604-16, Jan 30 2001.

[298] H. M. Kwon, G. Sangiorgi, E. L. Ritman, A. Lerman, C. McKenna, R. Virmani, W. D. Edwards, D. R. Holmes, and R. S. Schwartz, "Adventitial vasa vasorum in balloon-injured coronary arteries: visualization and quantitation by a microscopic three-dimensional computed tomography technique," *J Am Coll Cardiol,* vol. 32, pp. 2072-9, Dec 1998.

[299] H. J. Vos, M. E. Frijlink, E. Droog, D. E. Goertz, G. Blacquiere, A. Gisolf, N. de Jong, and A. F. W. van der Steen, "A 20-40 MHz Ultrasound Transducer for Intravascular Harmonic Imaging," presented at the IEEE International Ultrasonics Symposium, Montreal, Canada, 2004.

[300] D. E. Goertz, M. E. Frijlink, D. Tempel, L. C. A. van Damme, R. Krams, J. A. Schaar, F. J. ten Cate, P. W. Serruys, N. de Jong, and A. F. W. van der Steen, "Contrast harmonic intravascular ultrasound: a feasibility study for vasa vasorum imaging.," *Invest Radiol,* vol. 41, pp. 631-8, 2006.

[301] O. T. von Ramm and S. W. Smith, "A multiple frequency array for improved diagnostic imaging," *IEEE Transactions on Sonics and Ultrasonics,* vol. 25, pp. 340-345, 1978.

[302] T. Bui, H. L. W. Chan, and J. Unsworth, "A multifrequency composite ultrasonic transducer system," presented at the IEEE International Ultrasonics Symposium, Chicago, IL, 1988.

[303] S. de Fraguier, J. F. Gelly, L. Wolnerman, and O. Lannuzel, "Novel Acoustic Design For Dual Frequency Transducers Resulting In Separate Bandpass For Color Flow Mapping," presented at the IEEE International Ultrasonics Symposium, Honolulu, HI, 1990.

[304] S. Saitoh, M. Izumi, and Y. Mine, "A dual frequency ultrasonic probe for medical applications," *IEEE Trans Ultrason Ferroelectr Freq Control,* vol. 42, pp. 294-300, 1995.

[305] J. A. Hossack, P. Mauchamp, and L. Ratsimandresy, "A High Bandwidth Transducer Optimized for Harmonic Imaging " presented at the IEEE International Ultrasonics Symposium, San Juan, Puerto Rico, 2000.

[306] J. A. Hossack and B. A. Auld, "Improving the Characteristics of a Transducer Using Multiple Piezoelectric Layers," *IEEE Trans Ultrason Ferroelectr Freq Control,* vol. 40, pp. 131-139, Mar 1993.

[307] T. R. Gururaja, A. Shurland, and J. Chen, "Medical ultrasonic transducers with switchable frequency bands centered about f(0) and 2f(0)," presented at the IEEE International Ultrasonics Symposium, Toronto, Ont., 1997.

[308] S. Takeuchi, M. R. A. Al Zaabi, T. Sato, and N. Kawashima, "Development of ultrasound transducer with double-peak-type frequency characteristics for harmonic imaging and subharmonic imaging," *Jpn J Appl Phys 1,* vol. 41, pp. 3619-3623, May 2002.

[309] H. H. Kim, J. M. Cannata, R. Liu, J. H. Chang, R. H. Silverman, and K. K. Shung, "20 MHz/40 MHz dual element transducers for high frequency harmonic imaging," *IEEE Trans Ultrason Ferroelectr Freq Control,* vol. 55, pp. 2683-91, 2008.

[310] J. S. Jeong, J. H. Chang, and K. K. Shung, "Ultrasound transducer and system for real-time simultaneous therapy and diagnosis for noninvasive surgery of prostate tissue," *IEEE Trans Ultrason Ferroelectr Freq Control,* vol. 56, pp. 1913-22, Sep 2009.

[311] A. J. Casper, D. Liu, J. R. Ballard, and E. S. Ebbini, "Real-time implementation of a dual-mode ultrasound array system: in vivo results," *IEEE Trans Biomed Eng,* vol. 60, pp. 2751-9, Oct 2013.

[312] C. Y. Lai, D. E. Kruse, C. F. Caskey, D. N. Stephens, P. L. Sutcliffe, and K. W. Ferrara, "Noninvasive Thermometry Assisted by a Dual-Function Ultrasound Transducer for Mild Hyperthermia," *IEEE Trans Ultrason Ferroelectr Freq Control,* vol. 57, pp. 2671-2684, Dec 2010.

[313] K. H. Martin and P. A. Dayton, "Current status and prospects for microbubbles in ultrasound theranostics.," *Wiley interdisciplinary reviews Nanomedicine and nanobiotechnology,* vol. 5, pp. 329-345, 2013.

[314] J. E. Kennedy, "High-intensity focused ultrasound in the treatment of solid tumours," *Nature reviews Cancer,* vol. 5, pp. 321-7, Apr 2005.

[315] G. R. ter Haar and C. C. Coussios, "High intensity focused ultrasound: Physical principles and devices," *International Journal of Hyperthermia,* vol. 23, pp. 89-104, 2007.

[316] C. H. Seo, Y. Shi, S. W. Huang, K. Kim, and M. O'Donnell, "Thermal strain imaging: a review," *Interface focus,* vol. 1, pp. 649-64, Aug 6 2011.

[317] T. Azuma, M. Ogihara, J. Kubota, A. Sasaki, S. Umemura, and H. Furuhata, "Dual-frequency ultrasound imaging and therapeutic bilaminar array using frequency selective isolation layer," *IEEE Trans Ultrason Ferroelectr Freq Control,* vol. 57, pp. 1211-24, May 2010.

[318] C.-C. Shih, C.-C. Huang, Q. Zhou, and K. K. Shung, "High-resolution acoustic-radiation-force-impulse imaging for assessing corneal sclerosis," *IEEE Transactions on Medical Imaging,* vol. 32, pp. 1316-24, 2013.

[319] Y. Chen, M. Nguyen, and J. T. Yen, "7.5 MHz dual-layer transducer array for 3-D rectilinear imaging," *Ultrasonic Imaging,* vol. 33, pp. 205-16, Jul 2011.

[320] J. T. Yen, C. H. Seo, S. I. Awad, and J. S. Jeong, "A dual-layer transducer array for 3-D rectilinear imaging," *IEEE Trans Ultrason Ferroelectr Freq Control,* vol. 56, pp. 204-12, Jan 2009.

[321] R. Virmani, F. D. Kolodgie, A. P. Burke, A. V. Finn, H. K. Gold, T. N. Tulenko, S. P. Wrenn, and J. Narula, "Atherosclerotic plaque progression and vulnerability to rupture: angiogenesis as a source of intraplaque hemorrhage.," *Arterioscler Thromb Vasc Biol,* vol. 25, pp. 2054-61, 2005.

[322] F. D. Kolodgie, H. K. Gold, A. P. Burke, D. R. Fowler, H. S. Kruth, D. K. Weber, A. Farb, L. J. Guerrero, M. Hayase, R. Kutys, J. Narula, A. V. Finn, and R. Virmani, "Intraplaque hemorrhage and progression of coronary atheroma.," *N Engl J Med,* vol. 349, pp. 2316-25, 2003.

[323] J. Milei, J. C. Parodi, G. F. Alonso, A. Barone, D. Grana, and L. Matturri, "Carotid rupture and intraplaque hemorrhage: immunophenotype and role of cells involved.," *American heart journal,* vol. 136, pp. 1096-105, 1998.

[324] P. R. Moreno and V. Fuster, "New aspects in the pathogenesis of diabetic atherothrombosis.," *J Am Coll Cardiol,* vol. 44, pp. 2293-300, 2004.

[325] F. A. Jaffer, P. Libby, and R. Weissleder, "Molecular and cellular imaging of atherosclerosis: emerging applications.," *J Am Coll Cardiol,* vol. 47, pp. 1328-38, 2006.

[326] J. D. Kasprzak, B. Paelinck, F. J. ten Cate, W. B. Vletter, N. de Jong, D. Poldermans, A. Elhendy, A. Bouakaz, and J. R. Roelandt, "Comparison of native and contrast-enhanced harmonic echocardiography for visualization of left ventricular endocardial border," *The American Journal of Cardiology,* vol. 83, pp. 211-217, 1999.

[327] J. Ma, X. Jiang, K. H. Martin, and P. A. Dayton, "Small aperture, dual frequency ultrasound transducers for intravascular contrast imaging," presented at the Ultrasonics Symposium (IUS), 2013 IEEE International, 2013.

[328] R. Krimholtz, D. A. Leedom, and G. L. Matthaei, "New equivalent circuits for elementary piezoelectric transducers," *Electronics Letters*, vol. 6, pp. 398-399, 1970.

[329] J. R. Yuan, X. Jiang, P.-J. Cao, A. Sadaka, R. Bautista, K. Snook, and P. W. Rehrig, "High frequency piezo composites microfabricated ultrasound transducers for intravascular imaging," in *Ultrasonics Symposium, 2006 IEEE*, 2006, pp. 264-268.

[330] J. Ma, K. H. Martin, P. A. Dayton, and X. Jiang, "A preliminary engineering design of intravascular dual-frequency transducers for contrast-enhanced acoustic angiography and molecular imaging," *IEEE Trans Ultrason Ferroelectr Freq Control*, vol. 61, pp. 870-80, May 2014.

[331] S. Ricci, E. Boni, F. Guidi, T. Morganti, and P. Tortoli, "A programmable real-time system for development and test of new ultrasound investigation methods," *Ultrasonics, Ferroelectrics, and Frequency Control, IEEE Transactions on*, vol. 53, pp. 1813-1819, 2006.

[332] M. Lewandowski and A. Nowicki, "High frequency coded imaging system with RF," *Ultrasonics, Ferroelectrics, and Frequency Control, IEEE Transactions on*, vol. 55, pp. 1878-1882, 2008.

[333] W. Qiu, Y. Chen, X. Li, Y. Yu, W. F. Cheng, F. K. Tsang, Q. Zhou, K. K. Shung, J. Dai, and L. Sun, "An open system for intravascular ultrasound imaging.," *IEEE Trans Ultrason Ferroelectr Freq Control*, vol. 59, pp. 2201-9, 2012.

[334] H. Choi, M. G. Kim, T. M. Cummins, J. Y. Hwang, and K. K. Shung, "Power MOSFET–Diode–Based Limiter for High-Frequency Ultrasound Systems," *Ultrasonic imaging*, vol. 36, pp. 317-330, 2014.

[335] J. Ma, M. B. Steer, and X. Jiang, "An acoustic filter based on layered structure," *Appl Phys Lett*, vol. 106, p. 111903, 2015.

[336] J. Ma, S. Li, Z. Wang, and X. Jiang, "Anti-matching design for wave isolation in dual frequency transducer for intravascular super-harmonic imaging," in *ASME 2014 International Mechanical Engineering Congress and Exposition*, 2014, pp. V003T03A084-V003T03A084.

[337] E. L. Madsen, J. A. Zagzebski, R. A. Banjavie, and R. E. Jutila, "Tissue mimicking materials for ultrasound phantoms.," *Med Phys*, vol. 5, pp. 391-4, 1978.

[338] D. E. Goertz, N. de Jong, and A. F. W. van der Steen, "Attenuation and size distribution measurements of Definity and manipulated Definity populations," *Ultrasound Med Biol,* vol. 33, pp. 1376-88, Sep 2007.

[339] D. E. Goertz, M. E. Frijlink, A. Bouakaz, C. T. Chin, N. de Jong, and A. F. W. van der Steen, "The effects of bubble size on nonlinear scattering from microbubbles," in *Ultrasonics, 2003 IEEE Symposium on*, 2003, pp. 1503-1506.

[340] A. C. Barger, R. r. Beeuwkes, L. L. Lainey, and K. J. Silverman, "Hypothesis: vasa vasorum and neovascularization of human coronary arteries. A possible role in the pathophysiology of atherosclerosis," *N Engl J Med,* vol. 310, pp. 175-7, Jan 19 1984.

[341] S. P. Jackson, "Arterial thrombosis-insidious, unpredictable and deadly," *Nat Med,* vol. 17, pp. 1423-1436, Nov 2011.

[342] G. W. Stone, A. Maehara, A. J. Lansky, B. de Bruyne, E. Cristea, G. S. Mintz, R. Mehran, J. McPherson, N. Farhat, S. P. Marso, H. Parise, B. Templin, R. White, Z. Zhang, and P. W. Serruys, "A prospective natural-history study of coronary atherosclerosis.," *N Engl J Med,* vol. 364, pp. 226-35, 2011.

[343] B. Doyle and N. Caplice, "Plaque neovascularization and antiangiogenic therapy for atherosclerosis," *J Am Coll Cardiol,* vol. 49, pp. 2073-80, May 29 2007.

[344] A. F. L. Schinkel, C. G. Krueger, A. Tellez, J. F. Granada, J. D. Reed, A. L. Hall, W. Zang, C. Owens, G. L. Kaluza, D. Staub, B. Coll, F. J. ten Cate, and S. B. Feinstein, "Contrast-enhanced ultrasound for imaging vasa vasorum: comparison with histopathology in a swine model of atherosclerosis.," *Eur J Echocardiogr,* vol. 11, pp. 659-64, Sep 2010.

[345] D. E. Goertz, M. E. Frijlink, N. de Jong, and A. F. W. van der Steen, "Nonlinear intravascular ultrasound contrast imaging," *Ultrasound Med Biol,* vol. 32, pp. 491-502, Apr 2006.

[346] D. Maresca, I. Skachkov, G. Renaud, K. Jansen, G. van Soest, N. de Jong, and A. F. W. van der Steen, "Imaging microvasculature with contrast-enhanced ultraharmonic ultrasound," *Ultrasound Med Biol,* vol. 40, pp. 1318-28, 2014.

[347] D. Maresca, K. Jansen, G. Renaud, G. van Soest, X. Li, Q. Zhou, N. de Jong, K. K. Shung, and A. F. W. van der Steen, "Intravascular ultrasound chirp imaging," *Appl Phys Lett,* vol. 100, p. 043703, 2012.

[348] D. E. Goertz, E. Cherin, A. Needles, R. Karshafian, A. S. Brown, P. N. Burns, and F. S. Foster, "High frequency nonlinear B-scan imaging of microbubble contrast agents," *IEEE Trans Ultrason Ferroelectr Freq Control,* vol. 52, pp. 65-79, Jan 2005.

[349] J. D. Thomas and D. N. Rubin, "Tissue harmonic imaging: why does it work?," *J Am Soc Echocardiogr,* vol. 11, pp. 803-8, 1998.

[350] K. H. Martin, B. D. Lindsey, J. Ma, M. Lee, S. Li, F. S. Foster, X. Jiang, and P. A. Dayton, "Dual-frequency piezoelectric transducers for contrast enhanced ultrasound imaging," *Sensors,* vol. 14, pp. 20825-42, 2014.

[351] J. C. Sluimer and M. J. Daemen, "Novel concepts in atherogenesis: angiogenesis and hypoxia in atherosclerosis.," *J Pathol,* vol. 218, pp. 7-29, May 2009.

[352] C. E. Riva, J. E. Grunwald, S. H. Sinclair, and B. L. Petrig, "Blood velocity and volumetric flow rate in human retinal vessels," *Invest Ophthalmol Vis Sci,* vol. 26, pp. 1124-32, Aug 1985.

[353] T. Kubo, T. Imanishi, S. Takarada, A. Kuroi, S. Ueno, T. Yamano, T. Tanimoto, Y. Matsuo, T. Masho, H. Kitabata, K. Tsuda, Y. Tomobuchi, and T. Akasaka, "Assessment of Culprit Lesion Morphology in Acute Myocardial Infarction," *J Am Coll Cardiol,* vol. 50, pp. 933-939, 2007.

[354] C. A. Given, G. F. Attizzani, M. R. Jones, C. N. Ramsey, W. H. Brooks, M. A. Costa, and H. G. Bezerra, "Frequency-domain optical coherence tomography assessment of human carotid atherosclerosis using saline flush for blood clearance without balloon occlusion," *AJNR American journal of neuroradiology,* vol. 34, pp. 1414-8, 2013.

[355] I.-K. Jang, B. E. Bouma, D.-H. Kang, S.-J. Park, S.-W. Park, K.-B. Seung, K.-B. Choi, M. Shishkov, K. Schlendorf, E. Pomerantsev, S. L. Houser, H. T. Aretz, and G. J. Tearney, "Visualization of coronary atherosclerotic plaques in patients using optical coherence tomography: comparison with intravascular ultrasound," *J Am Coll Cardiol,* vol. 39, pp. 604-9, 2002.

[356] J. O. Hasler-Rapacz, H. Ellegren, A. K. Fridolfsson, B. Kirkpatrick, S. Kirk, L. Andersson, and J. Rapacz, "Identification of a mutation in the low density lipoprotein receptor gene associated with recessive familial hypercholesterolemia in swine," *American journal of medical genetics,* vol. 76, pp. 379-86, Apr 13 1998.

[357] K. A. Grunwald, K. Schueler, P. J. Uelmen, B. A. Lipton, M. Kaiser, K. Buhman, and A. D. Attie, "Identification of a novel Arg-->Cys mutation in the LDL receptor that contributes to spontaneous hypercholesterolemia in pigs," *Journal of lipid research,* vol. 40, pp. 475-85, Mar 1999.

[358] J. O. Hasler-Rapacz, T. C. Nichols, T. R. Griggs, D. A. Bellinger, and J. Rapacz, "Familial and diet-induced hypercholesterolemia in swine. Lipid, ApoB, and ApoA-I concentrations and distributions in plasma and lipoprotein subfractions," *Arteriosclerosis and thrombosis : a journal of vascular biology / American Heart Association,* vol. 14, pp. 923-30, Jun 1994.

[359] G. R. Lockwood, L. K. Ryan, J. W. Hunt, and F. S. Foster, "Measurement of the ultrasonic properties of vascular tissues and blood from 35-65 MHz," *Ultrasound Med Biol,* vol. 17, pp. 653-66, 1991.

[360] E. J. Gussenhoven, C. E. Essed, C. T. Lancée, F. Mastik, P. Frietman, F. C. van Egmond, J. Reiber, H. Bosch, H. van Urk, J. Roelandt, and N. Bom, "Arterial wall characteristics determined by intravascular ultrasound imaging: An in vitro study," *J Am Coll Cardiol,* vol. 14, pp. 947-952, 1989.

[361] H.-C. Han and D. N. Ku, "Contractile responses in arteries subjected to hypertensive pressure in seven-day organ culture," *Ann of Biomed Eng,* vol. 29, pp. 467-475, 2001.

[362] NRC, *Committee for the Update of the Guide for the Care and Use of Laboratory Animals. Guide for the Care and Use of Laboratory Animals: Eighth Edition.* Washington, DC: The National Academies Press, 2011.

[363] T. Schomann, F. Qunneis, D. Widera, C. Kaltschmidt, and B. Kaltschmidt, "Improved method for ex ovo-cultivation of developing chicken embryos for human stem cell xenografts," *Stem Cells Int,* vol. 960958, pp. 1-9, 2013.

[364] J. A. Jensen, "Field: A program for simulating ultrasound systems. Paper presented at the 10th Nordic-Baltic Conference on Biomedical Imaging," *Published in Medical & Biological Engineering & Computing,* pp. 351-353, 1996.

[365] J. A. Jensen and N. B. Svendsen, "Calculation of pressure fields from arbitrarily shaped, apodized, and excited ultrasound transducers," *IEEE Trans Ultrason Ferroelectr Freq Control,* vol. 39, pp. 262-7, 1992.

[366] B. D. Lindsey, J. D. Rojas, and P. A. Dayton, "On the relationship between microbubble fragmentation, deflation and broadband superharmonic signal production," *Ultrasound Med Biol,* vol. 41, pp. 1711-25, Jun 2015.

[367] A. Bouakaz, S. Frigstad, F. J. ten Cate, and N. de Jong, "Improved contrast to tissue ratio at higher harmonics.," *Ultrasonics,* vol. 40, pp. 575-8, 2002.

[368] G. Pinton, G. E. Trahey, and J. J. Dahl, "Sources of image degradation in fundamental and harmonic ultrasound imaging using nonlinear, full-wave simulations," *IEEE Trans Ultrason Ferroelectr Freq Control,* vol. 58, pp. 754-765, 2011.

[369] M.-X. Tang and R. J. Eckersley, "Nonlinear propagation of ultrasound through microbubble contrast agents and implications for imaging," *IEEE Trans Ultrason Ferroelectr Freq Control,* vol. 53, pp. 2406-15, 2006.

[370] G. L. ten Kate, G. G. J. Renaud, Z. Akkus, S. C. H. van den Oord, F. J. ten Cate, V. Shamdasani, R. R. Entrekin, E. J. G. Sijbrands, N. de Jong, J. G. Bosch, A. F. L. Schinkel, and A. F. W. van der Steen, "Far-wall pseudoenhancement during contrast-enhanced ultrasound of the carotid arteries: clinical description and in vitro reproduction," *Ultrasound Med Biol,* vol. 38, pp. 593-600, 2012.

[371] B. D. Lindsey, J. D. Rojas, K. H. Martin, S. E. Shelton, and P. A. Dayton, "Optimization of contrast-to-tissue ratio and role of bubble destruction in dual-frequency contrast-specific "acoustic angiography" imaging," presented at the Ultrasonics Symposium (IUS), 2014 IEEE International, 2014.

[372] G. S. Mintz, S. E. Nissen, W. D. Anderson, S. R. Bailey, R. Erbel, P. J. Fitzgerald, F. J. Pinto, K. Rosenfield, R. J. Siegel, E. M. Tuzcu, P. G. Yock, R. A. O'Rourke, J. Abrams, E. R. Bates, B. R. Brodie, P. S. Douglas, G. Gregoratos, M. A. Hlatky, J. S. Hochman, S. Kaul, C. M. Tracy, D. D. Waters, and W. L. Winters, "American College of Cardiology clinical expert consensus document on standards for acquisition, measurement and reporting of intravascular ultrasound studies (IVUS)," *J Am Coll Cardiol,* vol. 37, pp. 1478-1492, 2001.

[373] A. Maehara, G. S. Mintz, and N. J. Weissman, "Advances in intravascular imaging," *Circulation: Cardiovascular Interventions,* vol. 2, pp. 482-490, 2009.

[374] E. Falk, "Why do plaques rupture?," *Circulation,* vol. 86, pp. III30-42, 1992.

[375] A. V. Finn, M. Nakano, J. Narula, F. D. Kolodgie, and R. Virmani, "Concept of vulnerable/unstable plaque," *Arterioscler Thromb Vasc Biol,* vol. 30, pp. 1282-1292, 2010.

[376] A. A. Doinikov, J. F. Haac, and P. A. Dayton, "Resonance frequencies of lipid-shelled microbubbles in the regime of nonlinear oscillations," *Ultrasonics,* vol. 49, pp. 263-268, 2009.

[377] J. A. Mann and W. F. Walker, "A constrained adaptive beamformer for medical ultrasound: initial results," in *2002 IEEE Ultrasonics Symposium, 2002 Proceedings* vol. 2, ed: IEEE, 2002, pp. 1807-1810.

[378] F. Vignon and M. R. Burcher, "Capon beamforming in medical ultrasound imaging with focused beams," *Ultrasonics, Ferroelectrics, and Frequency Control, IEEE Transactions on,* vol. 55, pp. 619-628, 2008.

[379] J.-F. Synnevag, A. Austeng, and S. Holm, "Benefits of minimum-variance beamforming in medical ultrasound imaging.," *IEEE Trans Ultrason Ferroelectr Freq Control,* vol. 56, pp. 1868-79, 2009.

[380] B. M. Asl and A. Mahloojifar, "Contrast enhancement and robustness improvement of adaptive ultrasound imaging using forward-backward minimum variance beamforming," *Ultrasonics, Ferroelectrics, and Frequency Control, IEEE Transactions on,* vol. 58, pp. 858-867, 2011.

[381] B. M. Asl and A. Mahloojifar, "A low-complexity adaptive beamformer for ultrasound imaging using structured covariance matrix," *Ultrasonics, Ferroelectrics, and Frequency Control, IEEE Transactions on,* vol. 59, pp. 660-667, 2012.

[382] B. M. Asl and A. Mahloojifar, "Minimum variance beamforming combined with adaptive coherence weighting applied to medical ultrasound imaging," *Ultrasonics, Ferroelectrics, and Frequency Control, IEEE Transactions on,* vol. 56, pp. 1923-1931, 2009.

[383] I. K. Holfort, F. Gran, and J. A. Jensen, "Broadband minimum variance beamforming for ultrasound imaging.," *IEEE Trans Ultrason Ferroelectr Freq Control,* vol. 56, pp. 314-25, 2009.

[384] J. Camacho, M. Parrilla, and C. Fritsch, "Phase coherence imaging," *IEEE Trans Ultrason Ferroelectr Freq Control,* vol. 56, pp. 958-974, 2009.

[385] H. Hasegawa and H. Kanai, "Effect of subaperture beamforming on phase coherence imaging," *Ultrasonics, Ferroelectrics, and Frequency Control, IEEE Transactions on,* vol. 61, pp. 1779-1790, 2014.

[386] C. Tremblay-Darveau, R. Williams, L. Milot, M. Bruce, and P. N. Burns, "Combined perfusion and doppler imaging using plane-wave nonlinear detection and microbubble contrast agents," *Ultrasonics, Ferroelectrics, and Frequency Control, IEEE Transactions on,* vol. 61, pp. 1988-2000, 2014.

[387] J. Capon, "High-resolution frequency-wavenumber spectrum analysis," *Proceedings of the IEEE,* vol. 57, pp. 1408-1418, 1969.

[388] K. Kim, S. Park, S.-C. Park, J. Kang, Y.-T. Kim, and J.-H. Kim, "Fast transform-based adaptive beamformer for medical ultrasound imaging," in *Image Processing (ICIP), 2013 20th IEEE International Conference on*, 2013, pp. 2329-2333.

[389] T. Szasz, A. Basarab, M.-F. Vaida, and D. Kouamé, "Beamforming with sparse prior in ultrasound medical imaging," in *Ultrasonics Symposium (IUS), 2014 IEEE International*, 2014, pp. 1077-1080.

[390] J. Chen, B. Yiu, H. K.-H. So, and A. C. Yu, "Real-time GPU-based adaptive beamformer for high quality ultrasound imaging," in *Ultrasonics Symposium (IUS), 2011 IEEE International*, 2011, pp. 474-477.

[391] J. P. Asen, J. I. Buskenes, C.-I. C. Nilsen, A. Austeng, and S. Holm, "Implementing capon beamforming on a GPU for real-time cardiac ultrasound imaging," *Ultrasonics, Ferroelectrics, and Frequency Control, IEEE Transactions on,* vol. 61, pp. 76-85, 2014.

[392] M. Xu and L. V. Wang, "Universal back-projection algorithm for photoacoustic computed tomography," *Physical Review E,* vol. 71, p. 016706, 2005.

[393] J. C. Bamber, "Speed of sound," in *Physical Principles of Medical Diagnosis*, C. R. Hill, J. C. Bamber, and G. R. ter Haar, Eds., 2nd ed Chichester, U.K.: Wiley, 2004.

[394] J. Jose, R. G. H. Willemink, W. Steenbergen, C. H. Slump, T. G. van Leeuwen, and S. Manohar, "Speed-of-sound compensated photoacoustic tomography for accurate imaging.," *Med Phys,* vol. 39, pp. 7262-71, 2012.

[395] C. Huang, K. Wang, L. Nie, L. V. Wang, and M. A. Anastasio, "Full-wave iterative image reconstruction in photoacoustic tomography with acoustically inhomogeneous media," *IEEE Transactions on Medical Imaging,* vol. 32, pp. 1097-1110, 2013.

[396] X. Jin and L. V. Wang, "Thermoacoustic tomography with correction for acoustic speed variations," *Phys Med Biol,* vol. 51, pp. 6437-48, 2006.

[397] S. Manohar, R. G. H. Willemink, F. Van Der Heijden, C. H. Slump, and T. G. Van Leeuwen, "Concomitant speed-of-sound tomography in photoacoustic imaging," *Appl Phys Lett,* vol. 91, pp. 1-4, 2007.

[398] N. Duric, P. Littrup, L. Poulo, A. Babkin, R. Pevzner, E. Holsapple, O. Rama, and C. Glide, "Detection of breast cancer with ultrasound tomography: first results with the Computed Ultrasound Risk Evaluation (CURE) prototype," *Med Phys,* vol. 34, pp. 773-785, 2007.

[399] Y. Hristova, P. Kuchment, and L. Nguyen, "Reconstruction and time reversal in thermoacoustic tomography in acoustically homogeneous and inhomogeneous media," *Inverse Problems,* vol. 24, pp. 55006-55006, 2008.

[400] Z. Yuan and H. Jiang, "Three-dimensional finite-element-based photoacoustic tomography: reconstruction algorithm and simulations," *Med Phys,* vol. 34, pp. 538-546, 2007.

[401] X. L. Deán-Ben, V. Ntziachristos, and D. Razansky, "Statistical optoacoustic image reconstruction using a-priori knowledge on the location of acoustic distortions," *Appl Phys Lett,* vol. 98, 2011.

[402] B. E. Treeby, T. K. Varslot, E. Z. Zhang, J. G. Laufer, and P. C. Beard, "Automatic sound speed selection in photoacoustic image reconstruction using an autofocus approach.," *J Biomed Opt,* vol. 16, p. 090501, 2011.

[403] R. A. Kruger, C. M. Kuzmiak, R. B. Lam, D. R. Reinecke, S. P. Del Rio, and D. Steed, "Dedicated 3D photoacoustic breast imaging," *Med Phys,* vol. 40, pp. 113301-113301, 2013.

[404] American National Standards Institute Inc., "ANSI Z136.1-2007: American National Standard for Safe Use of Lasers," ed. Orlando, FL: Laser Institute of America, 2007, p. 81.

[405] R. A. Kruger, R. B. Lam, D. R. Reinecke, S. P. Del Rio, and R. P. Doyle, "Photoacoustic angiography of the breast.," *Med Phys,* vol. 37, pp. 6096-100, 2010.

[406] Y. Wang, D. Xing, Y. Zeng, and Q. Chen, "Photoacoustic imaging with deconvolution algorithm," *Phys Med Biol,* vol. 49, pp. 3117-3124, 2004.

[407] A. Fedorov, R. Beichel, J. Kalpathy-Cramer, J. Finet, J.-C. Fillion-Robin, S. Pujol, C. Bauer, D. Jennings, F. Fennessy, and M. Sonka, "3D Slicer as an image computing platform for the Quantitative Imaging Network," *Magnetic resonance imaging,* vol. 30, pp. 1323-1341, 2012.

[408] A. P. Witkin, "Scale-space filtering: A new approach to multi-scale description," in *Acoustics, Speech, and Signal Processing, IEEE International Conference on ICASSP'84*, 1984, pp. 150-153.

[409] R. Rogacka, A. Latib, and A. Colombo, "IVUS-guided stent implantation to improve outcome: a promise waiting to be fulfilled," *Current cardiology reviews,* vol. 5, p. 78, 2009.

[410] P. J. Fitzgerald, "902-2 Lesion Composition Impacts Size and Symmetry of Stent Expansion: Initial Report from the STRUT Registry," *J Am Coll Cardiol,* vol. 25, p. 49A, 1995.

[411] H. Doi, A. Maehara, G. S. Mintz, N. J. Weissman, A. Yu, H. Wang, L. Mandinov, J. J. Popma, S. G. Ellis, E. Grube, K. D. Dawkins, and G. W. Stone, "Impact of in-stent minimal lumen area at 9 months poststent implantation on 3-year target lesion revascularization-free survival: a serial intravascular ultrasound analysis from the TAXUS IV, V, and VI trials," *Circulation Cardiovascular interventions,* vol. 1, pp. 111-8, 2008.

[412] F. Fowkes, C. Macintyre, and C. Ruckley, "Increasing incidence of aortic aneurysms in England and Wales," *BMJ: British Medical Journal,* vol. 298, p. 33, 1989.

[413] G. H. White, W. Yu, J. May, X. Chaufour, and M. S. Stephen, "Endoleak as a complication of endoluminal grafting of abdominal aortic aneurysms: classification, incidence, diagnosis, and management," 2009.

[414] M. J. Dill-Macky, S. R. Wilson, Y. Sternbach, J. Kachura, and T. Lindsay, "Detecting endoleaks in aortic endografts using contrast-enhanced sonography," *AJR American journal of roentgenology*, vol. 188, pp. W262-8, 2007.

[415] D. H. Koschyk, C. A. Nienaber, M. Knap, T. Hofmann, Y. V. Kodolitsch, V. Skriabina, M. Ismail, O. Franzen, T. C. Rehders, and C. Dieckmann, "How to guide stent-graft implantation in type B aortic dissection? Comparison of angiography, transesophageal echocardiography, and intravascular ultrasound," *Circulation*, vol. 112, pp. I-260-I-264, 2005.

[416] P. J. Bendick, "Clinical efficacy of an ultrasound contrast agent with harmonic imaging in the post-operative evaluation of aortic aneurysm repair," *Proceedings of the Second Joint 24th Annual Conference and the Annual Fall Meeting of the Biomedical Engineering Society] [Engineering in Medicine and Biology*, vol. 2, pp. 949-950, 2002.

[417] V. Napoli, I. Bargellini, S. G. Sardella, P. Petruzzi, R. Cioni, C. Vignali, M. Ferrari, and C. Bartolozzi, "Abdominal aortic aneurysm: contrast-enhanced US for missed endoleaks after endoluminal repair," *Radiology*, vol. 233, pp. 217-25, 2004.

[418] M. E. Frijlink, D. E. Goertz, and A. F. W. van der Steen, "Reduction of stent artifacts using high-frequency harmonic ultrasound imaging," *Ultrasound Med Biol*, vol. 31, pp. 1335-1342, 2005.

[419] K. Kooiman, M. R. Böhmer, M. Emmer, H. J. Vos, C. Chlon, W. T. Shi, C. S. Hall, S. H. de Winter, K. Schroën, and M. Versluis, "Oil-filled polymer microcapsules for ultrasound-mediated delivery of lipophilic drugs," *Journal of Controlled Release*, vol. 133, pp. 109-118, 2009.

[420] P. Hauff, S. Seemann, R. Reszka, M. Schultze-Mosgau, M. Reinhardt, T. Buzasi, T. Plath, S. Rosewicz, and M. Schirner, "Evaluation of gas-filled microparticles and sonoporation as gene delivery system: feasibility study in rodent tumor models.," *Radiology*, vol. 236, pp. 572-8, 2005.

[421] J. P. Kilroy, A. L. Klibanov, B. R. Wamhoff, and J. A. Hossack, "Intravascular ultrasound catheter to enhance microbubble-based drug delivery via acoustic radiation force," *Ultrasonics, Ferroelectrics, and Frequency Control, IEEE Transactions on*, vol. 59, 2012.